ROLE OF MAGNETIC RESONANCE AND WAVE INTERFERENCE IN TAILORING THE RADIATIVE PROPERTIES OF MICRO/NANOSTRUCTURES

A Dissertation
Presented to
The Academic Faculty

By

Liping Wang

In Partial Fulfillment
of the Requirements for the Degree
Doctor of Philosophy in the
School of Mechanical Engineering

Georgia Institute of Technology
December 2011

ROLE OF MAGNETIC RESONANCE AND WAVE INTERFERENCE IN TAILORING THE RADIATIVE PROPERTIES OF MICRO/NANOSTRUCTURES

Approved by:

Dr. Zhuomin Zhang, Advisor
George W. Woodruff School of Mechanical Engineering
Georgia Institute of Technology

Dr. F. Levent Degertekin
George W. Woodruff School of Mechanical Engineering
Georgia Institute of Technology

Dr. Peter J. Hesketh
George W. Woodruff School of Mechanical Engineering
Georgia Institute of Technology

Dr. David S. Citrin
School of Electrical and Computer Engineering
Georgia Institute of Technology

Dr. Phillip N. First
School of Physics
Georgia Institute of Technology

Date Approved: 11/02/2011

ACKNOWLEDGEMENTS

I am very grateful to my Ph.D. advisor, Dr. Zhuomin Zhang, for offering me the great opportunity to work in his research group four years ago that has changed my life. I have benefited a lot from his experience not only from a professional point of view but also in personal aspects. I would also like to thank Dr. Peter Hesketh, Dr. Levent Degertekin, Dr. Phillip First, and Dr. David Citrin, who took their time to serve on my dissertation reading committee and provided valuable advice. Some researches presented in this dissertation were supported by the National Science Foundation and the Department of Energy.

Sincere appreciation is also expressed to my former and current group members, and I learned a lot by collaborating and interacting with them during my Ph.D. study. I want to thank Dr. Bong Jae Lee, Dr. Soumyadipta Basu, and Xiaojia Wang for our fruitful collaborations. I also cherish the interactions with Andrew McNamara, Trevor Bright, Jesse Watjen, Ahmad Haider, Nazli Donmezer, and David Lai. I want to specially thank Dr. Qinghe Li for his help during my first year in Atlanta.

Without the support and encouragement from my family, my Ph.D. study would never be possible. I am indebted to my parents for their love and support, and I thank my parents-in-law for their help and encouragement. Finally, I want to express my deepest gratitude to my wife, Xin Tan, who is willing to stay at home after her graduation to take care of our lovely daughter, Shirley, for her constant love and support.

TABLE OF CONTENTS

LIST OF TABLES

LIST OF FIGURES

LIST OF SYMBOLS AND ABBREVIATIONS

b	slit width, m
C_g	gap capacitance, F
C_m	capacitance of two parallel strips, F
c	speed of light in vacuum, 299 792 458 m/s
D	local density of states, m^{-3} s rad^{-1}
D'	local density of states per unit solid angle, m^{-3} s rad^{-1} sr^{-1}
d	thickness, m
$\mathbf{E}$	electric field vector, V/m
FT-IR	Fourier-transform infrared
f	filling ratio
$\bar{\bar{\mathbf{G}}}$	dyadic Green's function, m^{-1}
$\mathbf{H}$	magnetic field vector, C m^{-1} s^{-1}
h	height, m; convection heat transfer coefficient, W/m^2-K
$\hbar$	Planck constant divided by 2π, 1.055×10^{-34} J s
I_ω	spectral intensity of radiation, W m^{-2} s rad^{-1} sr^{-1}
i	$\sqrt{-1}$
$\mathbf{j}$	electric current density, A m^{-2}
j	jth diffraction order
LC	inductor-capacitor
L_m	inductance of two parallel strips, H
L_e, L_k	kinetic inductance, H
L_{coh}	coherence length, m
l	strip length in the y direction, m
$\mathbf{K}$	wavevector, m^{-1}
k	magnitude of wavevector, m^{-1}; thermal conductivity, W/m-K

k_B	Boltzmann constant, 1.381×10^{-23} J K^{-1}
MP	magnetic polariton
n	refractive index
Q	quality factor
q	order number of cavity resonance
q''_ω	spectral heat flux, W m^{-2} s rad^{-1}
RCWA	rigorous coupled-wave analysis
R	spectral-directional reflectance
R''_c	thermal resistance of the films, m^2-K/W
R''_{films}	thermal resistance of the films, m^2-K/W
r	reflection coefficient
$\mathbf{S}$	spectral Poynting vector, W m^{-2} s rad^{-1}
SPP	surface plasmon/phonon polariton
S	spectral signal from FT-IR
TAAS	three-axis automated scatterometer
TC	thermocouple
TE	traverse electric
TM	traverse magnetic
TPV	thermophotovoltaic
T	spectral-directional transmittance; temperature, K
T_ω	brightness temperature, K
ΔT	temperature difference, K
t	transmission coefficient
u	spectral energy density, J m^{-3} s rad^{-1}
V	volume, m^3
w	width, m

x,y,z space locations, m

Z_{tot} total impedance, Ω

Greek symbols

α spectral-directional absorptance

β phase shift, rad; parallel wavevector component, m^{-1}

Γ scattering rate of Au, rad/s or cm^{-1}

γ wavevector component in the z direction, m^{-1}; scattering rate of SiC, cm^{-1}

Δ lateral shift in complex gratings, m

δ penetration depth, m

ε relative permittivity (dielectric function)

ε_0 electric permittivity of vacuum, 8.854×10^{-12} F/m

ε_S total-hemispherical emittance

ε_∞ high-frequency constant in the dielectric function

ε'_ν, ε'_λ spectral-directional emissivity

Θ mean energy of the Planck oscillator, J

θ zenith (polar) angle, rad

$\Delta\theta$ full width at half minimum (or maximum), rad

κ extinction coefficient

Λ period, m

λ wavelength in vacuum, m

μ (relative) magnetic permeability

μ_0 magnetic permeability of vacuum, $4\pi\times10^{-7}$ N A^{-2}

ν wavenumber, cm^{-1}

$\Delta\nu$ free spectral range, cm^{-1}

$\delta\nu$ full width at half maximum (or minimum), cm^{-1}

ϕ	azimuthal angle, rad; phase angle of the reflection coefficient, rad
ψ	angle between **E** and the plane of incidence, rad; phase shift, rad
Ω	solid angle, sr
ω	angular frequency, rad/s
ω_p	plasma frequency, rad/s
ω_R	resonance frequency, rad/s

Superscripts

*	complex conjugate
inv	inverse
m	*m*th order
ord	ordinary

Subscripts

0	vacuum or at room temperature
1	medium 1
2	medium 2
A	ambient
B	blackbody
c	cavity
d	dielectric
f	film
i	incident
j	*j*th layer
S	sample
sum	summation
s	substrate

SUMMARY

The spectral and directional control of radiative properties by utilizing engineered micro/nanostructures has enormous applications in photonics, microelectronics, and energy conversion systems. The present dissertation aims at: (1) design and analysis of micro/nanostructures based on wave interference and magnetic resonance effects to achieve tunable coherent thermal emission or enhanced optical transmission; (2) microfabrication of the designed structures including multilayered thin films and patterned structures; and (3) development of a high-temperature emissometer to experimentally demonstrate coherent thermal emission from fabricated samples using spectrometric techniques at temperatures from 300 to 800 K.

An asymmetric Fabry-Perot resonant cavity, sandwiched by a thick Au film and an ultra-thin Au film of few nanometers, was studied as a potential coherent emission source based on the wave interference effect. The coherent emission behavior from fabricated samples was successfully demonstrated from room temperature up to 800 K. The reflectance was measured at room temperature using a Fourier-transform infrared spectrometer, and then the emittance can be indirectly obtained from Kirchhoff's law. A high-temperature emissometer was built to measure the thermal emission of fabricated multilayer samples at elevated temperatures, and the temperature effect on the emission peaks was discussed. To facilitate the computation of thermal emission from layered structures with nonuniform temperature distributions, the direct (fluctuational electrodynamics) and indirect (matrix formulation) approaches were analyzed and unified, resulting in a generalized Kirchhoff's law.

A comprehensive investigation was performed to understand and potentially utilize the magnetic resonance effect for tailoring radiative properties in periodic grating microstructures. Contrary to the conventional explanations using the coupled-surface-plasmon-polaritons or Fabry-Perot-cavity resonance effect, the effect of magnetic resonance was identified to be responsible for the resonant transmission/absorption in metallic grating structures. By using capacitor-inductor circuit models and rigorous coupled-wave analysis, good agreement on the resonant conditions was shown, through which the physical mechanism as magnetic resonance was verified. Another finding was to identify phonon-mediated magnetic polaritons (MPs) in microstructures made of polar materials, and to predict extraordinary radiative properties in the infrared region as their counterparts in metallic microstructures. Based on the excitation of MPs, an innovative coherent thermal emitter was designed and extended in particular for thermophotovoltaic (TPV) applications. The spectral selectivity and directional insensitivity associated with MPs offer unique emission spectra favored in TPV systems to improve the conversion efficiency. The unique characteristics of magnetic polaritons were, for the first time, experimentally demonstrated from fabricated microstructured surfaces at room temperature as well as elevated temperatures. Both experimental and theoretical studies suggest that the resonance wavelength can be tuned with strip widths for different applications, and the emittance peak changes little with temperature, indicating that high performance can be achieved without much degradation at elevated temperatures.

The fundamental understanding and experimental results obtained from the dissertation will facilitate the design and applications of micro/nanostructures in energy systems to harvest solar energy as well as recover waster heat.

CHAPTER 1
INTRODUCTION

1.1 Background

Tailoring the spectral and directional radiative properties has enormous applications in photonic and energy conversion systems, such as photodetectors, solar cells and solar absorbers, thermophotovoltaic (TPV) devices, and radiation filters and emitters [1,2]. The radiative properties of subwavelength periodic structures, such as one-dimensional (1D) slit arrays [3], annular apertures [4], and subwavelength apertures [5], have been intensively studied after the observation of significant optical transmission enhancement through 2D hole arrays [6] and directional thermal emission from 1D Si gratings [7]. The extraordinary optical transmission in subwavelength could realize the plasmonic nanolithography beyond the diffraction limit with 2D hole arrays [8] or metallic slit arrays [9]. It is also known that, any object at a temperature above absolute zero will emit thermal radiation due to the random thermal motion of charges, such as electrons in metals or ions in polar materials. In most cases, bulk solids emit thermal radiation in a broad spectrum with quasi-isotropic angular behavior. In other words, thermal emission is usually incoherent. Spectral and directional control of thermal emission could enhance the conversion efficiency and power throughput in energy-harvesting systems, especially TPV devices. The depleting reserves of conventional energy sources and increasing environmental impact such as the greenhouse effect have resulted in an urgent need for high-efficiency renewable energy sources [10]. TPV devices provide a viable solution since they can generate electricity directly from heat which could come from waste heat, the sun, or burning of fossil fuel.

1.2 Literature Study

Micro/nanostructures may enable coherent emission based on several different physical mechanisms such as surface plasmon/phonon polaritons (SPPs/SPhPs), cavity resonance, Wood's anomaly, wave interference and magnetic resonance. Hesketh *et al.* [7] measured selective thermal emission from doped Si gratings due to cavity resonances. Greffet *et al.* [11] showed that SiC gratings exhibit both temporal and spatial coherences due to excitation of SPhPs. Temporal or spatial coherence refers respectively to the spectral or directional selectivity in emittance. Dahan *et al.* [12] reported extraordinary coherent emission observed from SiC microstructures at 770 K, by coupling the resonance cavity modes with SPhPs. Layered structures such as photonic crystal on a Ag film have also been demonstrated to have coherent emission characteristics for both polarizations, arising from excitation of surface waves at the PC-Ag interface [13,14]. However, the coherent emittance peaks associated with SPPs or surface waves are usually very sharp and the amount of radiative energy is quite limited. Narayanaswamy and Chen [15] also theoretically demonstrated the excellent selective emission characteristics from 1D metallodielectric photonic crystals with alternating tungsten and alumina films at optical frequencies. In addition, cavity resonance and Wood's anomaly were also suggested to result in transmission/absorption enhancement in subwavelength nanoslit arrays [16].

Electromagnetic metamaterials have become a hot research area in the recent decade. In order to obtain the metamaterials, or negative index materials, permittivity (ε) and permeability (μ) must be simultaneously negative at the same frequency region [17]. Since most naturally occurring materials do not respond to magnetic fields at optical

frequencies, artificial micro/nanostructures have to be designed to induce magnetic responses at optical frequencies [18-24]. Though metamaterials have potential applications such as optical cloaking [25] and high-resolution imaging beyond diffraction limit [26-28], the role of magnetic resonance in controlling radiative properties is little understood.

Recently, several research groups have investigated the role of magnetic resonance on the extraordinary optical transmission through periodic structures. Ortuno *et al.* [29] pointed out that magnetic response and a negative effective permeability can be achieved in double-layer metallic hole arrays due to the internal SPPs. When the thickness of the dielectric separation layer is less than SPP attenuation length, SPPs at the two inner interfaces can couple with each other inside the dielectric layer, and exhibit different dispersion relation with the traditional SPPs at a single interface. Mary *et al.* [30] showed the resonant magnetic response behavior in double-layer fishnet structures. The electric field counter propagates with strong magnetic field confinement in the dielectric gap between two metal films, which was related to the excitation of so-called gap surface plasmon modes. Similar to the SPP which results from the coupling of surface plasmons or phonons with light, the concept of magnetic (plasmon) polaritons (MPs) was proposed by Li *et al.* [31] to indicate the coupling between the incident light and magnetic resonances inside subwavelength periodic structures. Subsequently, Li *et al.* [32] investigated the optical transmission through hole arrays perforated in trilayer structures and revealed the dispersion property of multiple MP modes. Note that magnetic response has been employed to realize optical negative-index metamaterials, which exhibit exotic properties and potential applications such as cloaking and superlens [33].

Debate on the physical origin of enhanced transmission/absorption in 1D and 2D periodic grating structures has existed over a decade. The physical mechanism of enhanced transmission or emission has been intensively investigated as either due to SPPs [3,34] or due to a Fabry-Perot or cavity-like resonance [35-38]. The theory of coupled SPPs propagating along the slit walls cannot explain the grating height dependence [39]. The oversimplified Fabry-Perot-like model breaks down for very narrow slits [37,40].

Several groups have studied the enhanced optical transmission in double-layer nanoslit arrays. Chan *et al.* [41] experimentally demonstrated extraordinary optical transmission through double nanoslit layers in close proximity with different lateral displacement between the two layers. Cheng *et al.* [42] performed a numerical study of the electromagnetic field distributions to explore the underlying mechanism of the extraordinary optical transmission in double-layer gratings. Both studies concluded that the origin lies in the coupling of evanescent waves between two single grating layers. The Fabry-Perot-like guided mode was also suggested to be responsible for the strong field confinement in the gaps between strips in the same layer [42]. However, the effect of magnetic resonance was not addressed. It should be noted that double-layer grating structure is also a candidate of negative-index metamaterials [43]. Hence, understanding the role of magnetic polaritons in this structure is critical for its future applications.

Wave interference effect has been discovered long time ago, and has facilitated the development and wide application of optics [44,45]. Interference effects in planar structures can also be utilized to achieve coherent emission, such as in a resonance cavity with highly reflective coatings [46-48]. The reflector can be made of a metallic layer,

doped Si, or Bragg mirrors. An asymmetric Fabry-Perot cavity resonator, evolved from the well-known optical etalon, has been indirectly shown to exhibit spectral and directional selectivity of emittance [13]. The Fabry-Perot structure has been widely used in spectroscopy, laser applications, and wavelength and frequency standards [45]. Back to 1940s, similar structures have been theoretically studied as reflection and transmission filters [49]. Laroche *et al.* [50] also analyzed a system called the Salisbury screen to enhance the emission of silicon surfaces. However, experimental observation from such a structure is lacking to further address its potential applications. To practically realize high-temperature coherent emitters based on the Fabry-Perot structures, it is imperative to investigate how the emittance spectrum will change with temperature, especially at elevated temperatures, as well as other issues such as chemical stability and thermal stress. Recently, Zhang and Wang [51] reviewed some measurement results and modeling methods of spectral-directional radiative properties of micro/nanostructures, which can be controlled based on different physical mechanisms.

The determination of the emissivity of layered structures is critical in many applications, such as radiation thermometry, microelectronics, radiative cooling, and energy harvesting [2,52]. Two different approaches, “direct” and “indirect” methods, are commonly used for computing the emissivity of an object. Several studies have directly computed the thermal emission of layered structures by solving Maxwell’s equations with the help of the fluctuation-dissipation theorem and dyadic Green’s functions [15,53-55]. Based on the direct method Narayanaswamy and Chen [15] analyzed thermal emission from one-dimensional (1D) metallodielectric photonic crystals, and excellent selective emission characteristics were seen in the optical frequencies. Luo *et al.* [56]

performed a numerical simulation to directly calculate the normal emissivity of 2D photonic crystals at a uniform temperature with the fluctuation-dissipation theorem, and Kirchhoff's law was validated by the equivalence between the normal emissivity from the direct method and the normal absorptivity from the indirect method. Besides the far-field thermal emission, the direct method has been also extensively used to investigate the near-field radiative heat transfer [57-59] and to trace energy streamlines [60,61]. Although mathematically intensive, the direct method demonstrates the statistical nature of thermal emission and, in principle, can predict thermal emission from a layered structure with a temperature gradient between two semi-infinite media.

On the other hand, emissivity can also be indirectly obtained from Kirchhoff's law, by calculating the absorptivity of a structure under a uniform temperature from the spectral directional-hemispherical reflectance R and transmittance T according to energy conservation [1]. If the structure is opaque, the emissivity ε'_ω is simply $1-R$. The indirect method has been widely used in predicting the emissivity, especially for inhomogeneous structures such as surface relief gratings. Lee *et al.* [62] proposed a coherent thermal emission source by exciting magnetic resonance and the emissivity was indirectly calculated based on rigorous coupled-wave algorithm. Wang *et al.* [63] experimentally investigated the spatial and temporal coherence of thermal emission from an asymmetric Fabry-Perot resonance cavity by measuring the spectral directional-hemispherical reflectance, and the results agree well with theoretical predictions. However, the indirect method used in these studies was under the assumption that all layers are at the same temperature. It has been pointed out by some researchers [53,64] that the indirect method would be problematic in dealing with temperature nonuniformity inside the structure.

When layered structures suffer from temperature non-uniformity, the validity of Kirchhoff's law and the indirect method is under question. For a body in a nonequilibrium environment, the validity of Kirchhoff's law of thermal radiation has been discussed by Baltes [65].

1.3 Objectives

This dissertation is devoted to theoretically and experimentally investigate the roles of wave interference and magnetic resonance in tailoring the radiative properties of micro/nanostructures for energy applications. Two different structures are analyzed, designed, fabricated and characterized, and comparisons are made on their radiative properties between model predictions and experimental data. The first structure is a multilayered thin-film structure, called an asymmetric Fabry-Perot resonant cavity, sandwiched by a thick Au film and an ultra-thin Au film of few nanometers, in which wave interference effect can occur. The other one is a periodic grating structure deposited on layered thin films, in which magnetic resonance can be excited under particular conditions. These structures hold great promises for energy-harvesting applications. The objectives of this thesis are: (1) design and analysis of micro/nanostructures based on wave interference and magnetic resonance effects to achieve tunable coherent thermal emission or enhanced optical transmission; (2) microfabrication of the designed structures including multilayered thin films and patterned structures; and (3) development of a high-temperature emissometer to experimentally demonstrate coherent thermal emission from fabricated samples using spectrometric techniques at temperatures from 300 to 800 K.

This dissertation is organized as follows. Chapter 2 presents the theoretical background for calculating the radiative properties of layered structures and periodic grating structures which the work in sequent chapters is based on, as well as reviews the concepts of magnetic polaritons and surface plasmon/phonon polaritons. Chapter 3 discusses the experimental methods for measuring the radiative properties of microstructures at both room and elevated temperatures with an emphasis on the development of high-temperature emissometry facility. Chapter 4 focuses on the experimental demonstration of coherent thermal emission from fabricated asymmetric Fabry-Perot cavity resonator samples at both room- and high-temperatures along with the discussion based on theoretical calculations. In addition, the validity of Kirchhoff's law in layered structures with nonuniform temperature distributions is verified through unifying the direct and indirect methods on calculating the thermal emission from such structures. Chapter 5 clarifies the role of magnetic resonance in resonant transmission/absorption in simple metallic gratings, double-layer nanoslit arrays and gratings made of polar materials by the theoretical study using the rigorous coupled-wave analysis and LC circuit models. Moreover, coherent thermal emitters by excitation of magnetic polaritons are proposed with unique characteristics suitable for TPV applications. In Chapter 6, fabricated coherent emitters are experimentally demonstrated to possess those unique characteristics based on room- and high-temperature measurements to further ensure their promising practical applications with excellent performance under high temperature environment. Chapter 7 summarizes the major findings and conclusions of this dissertation work as well as recommends some research topics for future studies.

CHAPTER 2
THEORETICAL BACKGROUND

This Chapter provides the formulation, methods, and concepts necessary for the analysis of radiative properties of micro/nanostructures in this dissertation. To start with, the formulae to calculate the reflectance and transmittance of asymmetric Fabry-Perot resonant cavities are presented in Section 2.1. Section 2.2 reviews the direct method based on fluctuational electrodynamics and the indirect method based on matrix formulation for calculating the thermal emission from layered structures. Section 2.3 briefly discusses the rigorous coupled-wave algorithm (RCWA) for calculating the radiative properties of 1D periodic grating structures. Section 2.4 explains the concept of magnetic polaritons and the inductor-capacitor (LC) model to predict magnetic resonance conditions, and finally the dispersion of surface plasmon/phonon polaritons in periodic structures is visited in Section 2.5.

2.1 Radiative Properties of Asymmetric Fabry-Perot Resonant Cavities

Wave interference effect has been extensively applied in optical devices. One excellent example is the Fabry-Perot interferometer, also known as an optical cavity or etalon, which has been widely used in spectroscopy, laser applications, and wavelength and frequency standard [45]. An asymmetric Fabry-Perot resonant cavity with a thick Ag substrate has been theoretically shown as a promising coherent emission source with both spatial and temporal coherency characteristics [13]. The proposed Fabry-Perot resonance cavity is schematically shown in Fig. 2.1. It is different from the conventional Fabry-Perot resonator made of two parallel reflectors separated at a finite distance, because the

bottom metal layer can be treated as semi-infinite and is opaque to incident radiation. In other words, the geometry of proposed structure is asymmetric with respect to the dielectric cavity. In general, high reflection from the boundaries of the resonance cavity is essential for the sharp spectral peak at the resonance condition [45]. In the present study, SiO_2 is employed to form the optical cavity and Au is chosen as the reflective coating on both sides of the cavity.

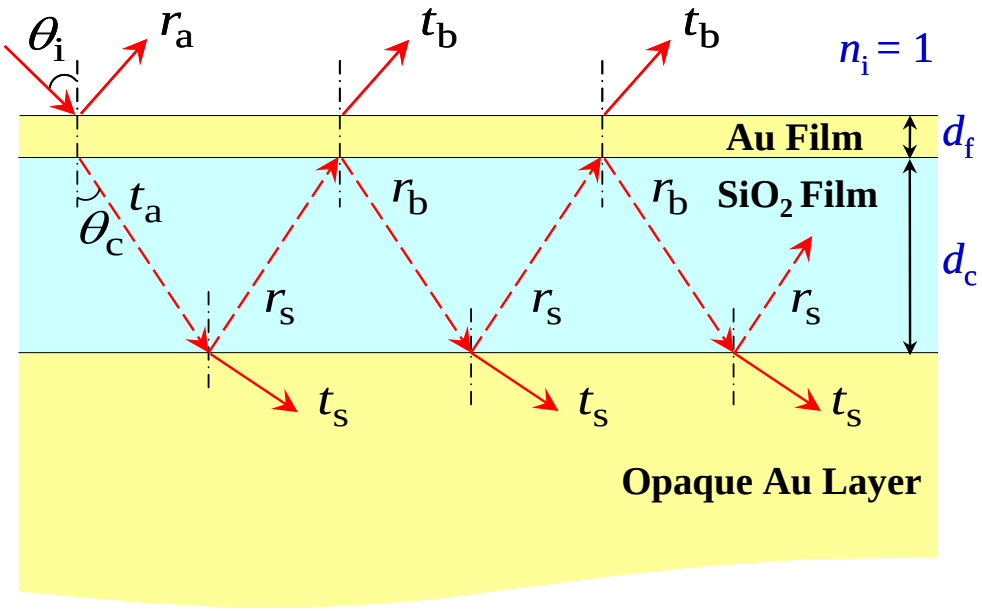

Figure 2.1 Schematic of the asymmetric Fabry-Perot resonance cavity, with illustration of the reflection and transmission coefficients at the boundaries.

Figure 2.1 also illustrates the reflection and transmission coefficients at the boundaries of the Fabry-Perot resonator. It should be noted that t_a and r_a are respectively the transmission and reflection coefficients from air to SiO_2, and t_b and r_b are respectively the transmission and reflection coefficients from SiO_2 to air, assuming that SiO_2 is semi-infinite. These coefficients depend on the complex refractive index and the thickness of Au, according to Airy's formulae. Furthermore, t_s and r_s are the Fresnel

transmission and reflection coefficients at the interface between SiO_2 and Au. All the transmission and reflection coefficients are polarization dependent and the expressions can be found from [1] for either TE wave or TM wave. According to Airy's formulae, the reflection and transmission coefficients of the Fabry-Perot resonator can be expressed after superposition as follows [1,44]

$$r = r_{\mathrm{a}} + \frac{t_{\mathrm{a}} t_{\mathrm{b}} r_{\mathrm{s}} e^{i2\beta}}{1 - r_{\mathrm{b}} r_{\mathrm{s}} e^{i2\beta}} \tag{2.1}$$

and

$$t = \frac{t_{\mathrm{a}} t_{\mathrm{s}} e^{i\beta}}{1 - r_{\mathrm{b}} r_{\mathrm{s}} e^{i2\beta}} \tag{2.2}$$

where $\beta = 2\pi n_{\mathrm{c}} d_{\mathrm{c}} \cos\theta_{\mathrm{c}} / \lambda$ is the phase shift upon traveling inside the cavity with the refractive index n_{c} and the thickness d_{c}. As shown in Fig. 2.1, θ_{c} is the refraction angle in the dielectric cavity. The spectral-directional reflectance and transmittance of the Fabry-Perot cavity can be calculated from the reflection and transmission coefficients as

$$R = rr^{*} \tag{2.3}$$

and

$$T = \frac{\mathrm{Re}\left(\cos\theta_{\mathrm{s}} / n_{\mathrm{s}}\right)}{\mathrm{Re}\left(\cos\theta_{\mathrm{i}} / n_{\mathrm{i}}\right)} tt^{*} \quad \text{for TM waves} \tag{2.4a}$$

or

$$T = \frac{\mathrm{Re}\left(n_{\mathrm{s}} \cos\theta_{\mathrm{s}}\right)}{\mathrm{Re}\left(n_{\mathrm{i}} \cos\theta_{\mathrm{i}}\right)} tt^{*} \quad \text{for TE waves} \tag{2.4b}$$

where Re( ) indicates the real part of a complex quantity, the asterisk denotes the complex conjugate, and n_{i} and n_{s} are the complex refractive indices of air and Au, respectively. The square of the reflection and transmission coefficients can be simplified using Eqs. (2.1) and (2.2) as follows:

$$rr^{*} = \frac{\left(\rho_{\mathrm{a}} + \rho_{\mathrm{s}}\zeta\right)^2 - 4\rho_{\mathrm{a}}\rho_{\mathrm{s}}\zeta \sin^2\psi_1}{\left(1 - \rho_{\mathrm{b}}\rho_{\mathrm{s}}\right)^2 + 4\rho_{\mathrm{b}}\rho_{\mathrm{s}} \sin^2\psi_2} \tag{2.5}$$

and $$tt^* = \frac{\tau_a \tau_s}{(1-\rho_b\rho_s)^2 + 4\rho_b\rho_s \sin^2\psi_2} \tag{2.6}$$

where $\rho = |r_j|$ and $\tau = t_j t_j^*$ with j representing a, b, or s as the corresponding subscript, $\zeta = |t_a t_b - r_a r_b|$, $\psi_1 = (2\beta - \phi_a + \phi_s + \phi_\zeta)/2$ and $\psi_2 = (2\beta + \phi_b + \phi_s)/2$, with $\phi_j = \arg(r_j)$ and $\phi_\zeta = \arg(t_a t_b - r_a r_b)$. In the proposed structure, the thickness of bottom Au layer is set to be much greater than the radiation penetration depth (i.e., photon mean free path); thus the bottom Au layer can be assumed semi-infinite. Note that *T* represents the fraction of energy transmitted into the Au layer and will eventually be absorbed. Since the bottom Au layer is opaque, the spectral emissivity of the Fabry-Perot cavity can be obtained as $\varepsilon'_\lambda = 1 - R$ according to Kirchhoff's law [1], where *R* is calculated from Eq. (2.5). However, the thickness of the top Au film should be on the order of the radiation penetration depth to enable resonance inside the cavity.

2.2 Methods to Calculate Thermal Emission from Layered Structures

Fluctuational electrodynamics, developed by Rytov [66] in 1950s, originates from the stochastic nature of thermal emission, and has been used to directly investigate emission, propagation and absorption of thermal radiation in both near- and far-field regimes. The basic concept is that, at temperatures above absolute zero, the random motion of charges, such as electrons in metals or ions in polar materials, generates a spatial- and time-dependent fluctuating current $\mathbf{j}(\mathbf{x}, t)$ that results in an electromagnetic field. The fluctuating current can be decomposed into the frequency domain $\mathbf{j}(\mathbf{x}, \omega)$ using the Fourier transform. The electromagnetic field at any location is a superposition of

contributions from all point sources in the radiating region. Thus, the induced electric and magnetic fields due to the fluctuating current density can be expressed as volume integrations with the assistance of dyadic Green's function

$$\mathbf{E}(\mathbf{x},\omega) = i\omega\mu_0 \int_{V'} \bar{\bar{\mathbf{G}}}(\mathbf{x},\mathbf{x}',\omega)\cdot\mathbf{j}(\mathbf{x}',\omega)d^3\mathbf{x}' \tag{2.7}$$

$$\mathbf{H}(\mathbf{x},\omega) = \int_{V'} \nabla\times\bar{\bar{\mathbf{G}}}(\mathbf{x},\mathbf{x}',\omega)\cdot\mathbf{j}(\mathbf{x}',\omega)d^3\mathbf{x}' \tag{2.8}$$

where ω is the angular frequency, μ_0 is the permeability of vacuum, V' is the volume that contains the fluctuating sources, $\bar{\bar{\mathbf{G}}}(\mathbf{x},\mathbf{x}',\omega)$ is the dyadic Green's function for the electric field, and $\mathbf{x}$ is the space variable. The dyadic Green's function is a spatial transfer function between a current source $\mathbf{j}$ at location $\mathbf{x}'$ and the resultant electric field at $\mathbf{x}$. The spectral radiative energy flux can be expressed by the time-averaged Poynting vector as [1]

$$\left\langle \mathbf{S}(\mathbf{x},\omega)\right\rangle = \frac{1}{2}\left\langle \mathrm{Re}[\mathbf{E}(\mathbf{x},\omega)\times\mathbf{H}^*(\mathbf{x},\omega)]\right\rangle \tag{2.9}$$

where <> is ensemble average and * denotes complex conjugate. To obtain the spectral energy flux, it is important to know the ensemble average of the spatial correlation of fluctuating currents, which is given by the fluctuation-dissipation theorem. Thermal emission into the vacuum from a layered structure with a known temperature distribution can thus be calculated. As shown in Fig. 2.2(a), each layer is assumed to be at a temperature T_j with a frequency-dependent dielectric function ε_j and a thickness d_j. Detailed discussion about the direct approach can be found in several references [15,53,57,59,67]. The emphasis of the present study is on how to deduce the spectral directional emissivity, through which the direct and indirect methods can be related.

By substituting the electric and magnetic fields given in Eqs. (2.7) and (2.8) into Eq. (2.9), the time-averaged Poynting vector can be expressed in terms of Green's functions after replacing the time-averaged fluctuational currents $\langle j_m(\mathbf{x}',\omega) j_n(\mathbf{x}'',\omega)\rangle$ with the fluctuation-dissipation theorem. Following Ref. [59], the spectral energy heat flux from any arbitrary emitting layer *j* to vacuum, which is basically the time-averaged Poynting vector, has a form of

$$q''_{\omega,j} = \frac{1}{\pi^2}\Theta\left(\omega,T_j\right)\int_0^{\omega/c} Z_j\left(\omega,\beta\right)\beta d\beta \tag{2.10}$$

Here, β is the parallel component of wavevector and is the same for all layers due to the phase-matching condition; $Z_j(\omega,\beta)$ is called the *exchange function* [59], which must be evaluated by the dyadic Green's functions for multilayered structures [15,53,58,68] rather than the Green function for two parallel semi-infinite media [59,69]; and $\Theta(\omega,T_j)$ is the mean energy of a Planck oscillator at frequency ω at thermal equilibrium temperature T_j and is given by [59]

$$\Theta(\omega,T_j) = \frac{\hbar\omega}{\exp(\hbar\omega/k_{\mathrm{B}}T_j)-1} \tag{2.11}$$

where $2\pi\hbar$ is the Planck constant and k_{B} is the Boltzmann constant. Only thermal emission in the far field is considered, therefore the upper limit of integration in Eq. (2.10) is set to ω/c to include propagating waves only and *c* is the speed of light in vacuum.

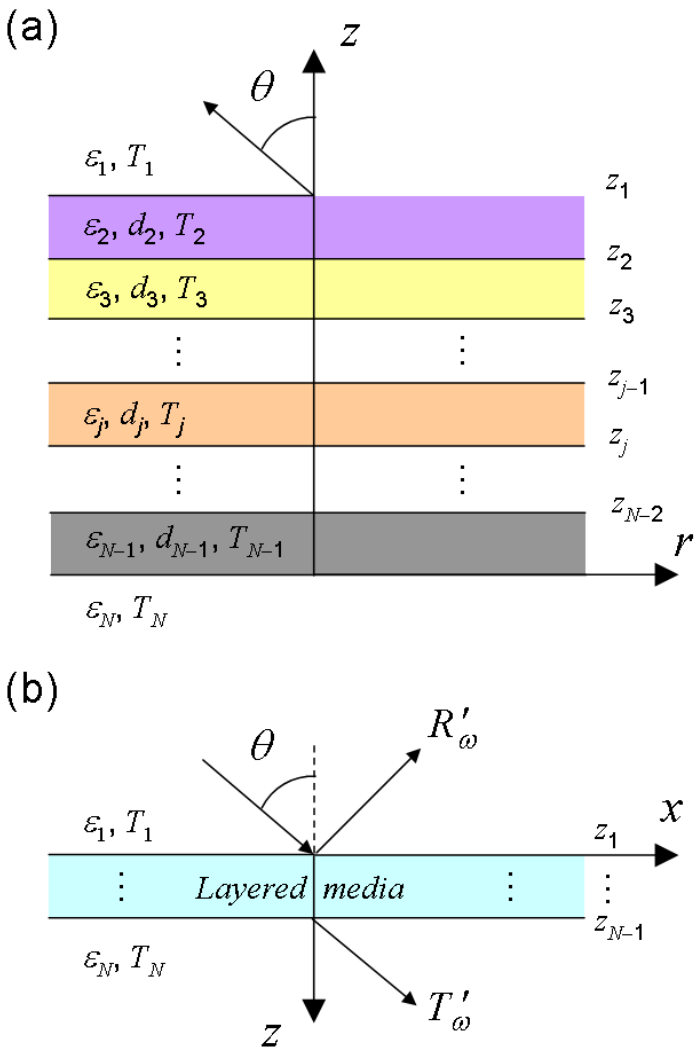

Figure 2.2 Schematic representation of a multilayered structure for the study of thermal emission based on (a) the direct method and (b) the indirect method.

Though the direct method provides a valuable way to investigate thermal emission from layered structures, numerical solutions can be computationally intensive. Alternatively, the indirect method only involves the calculation of reflectance and transmittance of a considered structure and this can be much easier to use and faster to compute for complicated structures. This is particularly true for a structure with a uniform temperature. In order to establish the equivalence between the indirect and direct

methods for nonuniform-temperature structures, detailed derivation of how to calculate the spectral directional absorptivity of an individual layer is given as follows based on the matrix formulation [1].

Consider a linearly polarized electromagnetic wave incident at a polar angle θ from vacuum to the multilayered structure shown in Fig. 2.2(b). Each layer is assumed to be isotropic and homogeneous as in the direct method. Furthermore, the complex permeabilities μ_j are included in the following, so that the formulation for TE waves can be easily extended to TM waves later. For a TE wave at an angular frequency ω, the electric field in the *j*th layer can be written as

$$\mathbf{E}_j = E_{y,j}\hat{\mathbf{y}} = E_j(z)e^{i(\beta x-\omega t)}\hat{\mathbf{y}} \tag{2.12}$$

where $E_1(z) = A_1 e^{i\gamma_1 z} + B_1 e^{-i\gamma_2 z}$ and $E_j(z) = A_j e^{i\gamma_j(z-z_{j-1})} + B_j e^{-i\gamma_j(z-z_{j-1})}$, $j = 2,3,...,N$. Note that A_j and B_j are the amplitudes of the forward and backward waves at the interfaces; d_j is the *j*th layer thickness; $z_j = z_{j-1} + d_j$ $(j = 2,3,...,N-1)$; and γ_j is the *z*-component of the wavevector which can be solved from $\beta^2 + \gamma_j^2 = \varepsilon_j \mu_j \omega^2 / c^2$. The magnetic field can be obtained from the Maxwell equation,

$$\mathbf{H} = \frac{1}{i\omega\mu\mu_0}\nabla\times\mathbf{E} = \frac{1}{i\omega\mu\mu_0}\left(-\frac{\partial E_y}{\partial z}\hat{\mathbf{x}} + \frac{\partial E_y}{\partial x}\hat{\mathbf{z}}\right) \tag{2.13}$$

After obtaining the electric and magnetic fields, the Poynting vector can be calculated. The *z*-component Poynting vectors in each layer can be expressed as

$$S_{1z} = \frac{\gamma_1}{2\omega\mu_0}\left(A_1 A_1^* - B_1 B_1^*\right)$$

and $$S_{jz} = \frac{1}{2}\mathrm{Re}\left[\frac{\gamma_j^*}{\omega\mu_0\mu_j^*}\left(\psi_1 - \psi_2 - \psi_3\right)\right] \tag{2.14}$$

where $\psi_1 = \left|A_j\right|^2 e^{2\mathrm{Re}\left(i\gamma_j\right)\left(z-z_{j-1}\right)}$, $\psi_2 = \left|B_j\right|^2 e^{-2\mathrm{Re}\left(i\gamma_j\right)\left(z-z_{j-1}\right)}$, and $\psi_3 = 2i\,\mathrm{Im}\left[A_j B_j^* e^{i2\mathrm{Im}\left(i\gamma_j\right)\left(z-z_{j-1}\right)}\right]$. After applying the boundary conditions, the field amplitudes of adjacent layers are related by

$$\begin{pmatrix} A_j \\ B_j \end{pmatrix} = \mathbf{P}_j \mathbf{D}_j^{-1} \mathbf{D}_{j+1} \begin{pmatrix} A_{j+1} \\ B_{j+1} \end{pmatrix} \tag{2.15}$$

Here, $\mathbf{P}_j$ is called the propagation matrix and is given by

$$\mathbf{P}_j = \begin{pmatrix} 1 & 0 \\ 0 & 1 \end{pmatrix}, \text{ when } j = 1$$

and $$\mathbf{P}_j = \begin{pmatrix} e^{-i\gamma_j d_j} & 0 \\ 0 & e^{i\gamma_j d_j} \end{pmatrix}, \text{ when } j = 2, 3, ..., N-1 \tag{2.16}$$

$\mathbf{D}_j$ is the dynamical matrix and is given (for TE waves) by

$$\mathbf{D}_j = \begin{pmatrix} 1 & 1 \\ \gamma_j/\mu_j & -\gamma_j/\mu_j \end{pmatrix}, \; j = 1, 2, ..., N \tag{2.17}$$

From Eq. (2.15), it can be shown that

$$\begin{pmatrix} A_1 \\ B_1 \end{pmatrix} = \mathbf{M} \begin{pmatrix} A_N \\ B_N = 0 \end{pmatrix}, \text{ where } \mathbf{M} = \prod_{l=1}^{N-1} \mathbf{P}_l \mathbf{D}_l^{-1} \mathbf{D}_{l+1} \tag{2.18}$$

The transmission and reflection coefficients can be expressed as

$$t = \frac{A_N}{A_1} = \frac{1}{\mathbf{M}_{11}} \quad \text{and} \quad r = \frac{B_1}{A_1} = \frac{\mathbf{M}_{21}}{\mathbf{M}_{11}} \tag{2.19}$$

Thus, the spectral directional-hemispherical reflectance and transmittance can be obtained as

$$R'_\omega = rr^* = \left|\frac{\mathbf{M}_{21}}{\mathbf{M}_{11}}\right|^2 \tag{2.20a}$$

and

$$T'_\omega = \frac{\mathrm{Re}\left(\gamma_N / \mu_N\right)}{\mathrm{Re}\left(\gamma_1 / \mu_1\right)} tt^* = \frac{\mathrm{Re}\left(\gamma_N / \mu_N\right)}{\mathrm{Re}\left(\gamma_1 / \mu_1\right)} \left|\frac{1}{\mathbf{M}_{11}}\right|^2 \tag{2.20b}$$

For TM waves, Eqs. (2.14) through (2.20) are still applicable by interchanging μ to ε. According to Kirchhoff's law, the emittance of the layered structure at a uniform temperature is

$$\varepsilon'_\omega = \alpha'_\omega = 1 - R'_\omega - T'_\omega \tag{2.21}$$

2.3 Rigorous Coupled-Wave Analysis

The rigorous coupled-wave analysis (RCWA) is a numerical modeling algorithm for calculating diffraction efficiencies of periodic gratings by solving Maxwell's equations for different polarization, angle of incidence and wavelength. The dielectric function of the inhomogeneous grating region is expanded with Fourier series, and the number of Fourier terms is coupled with the total number of the considered diffraction order. A brief algorithm on the RCWA for the conical diffraction on 1D grating is given below, and details can be found in Refs. [16,70].

Figure 2.3 shows a plane wave with wavevector **k** incident on a binary grating, where the space is divided into three regions: Region I (vacuum), Region II (grating), and Region III (substrate). Since the grating region is composed of media A and B, its dielectric function, composed of ε_A and ε_B, is a periodic function of x. The geometry of

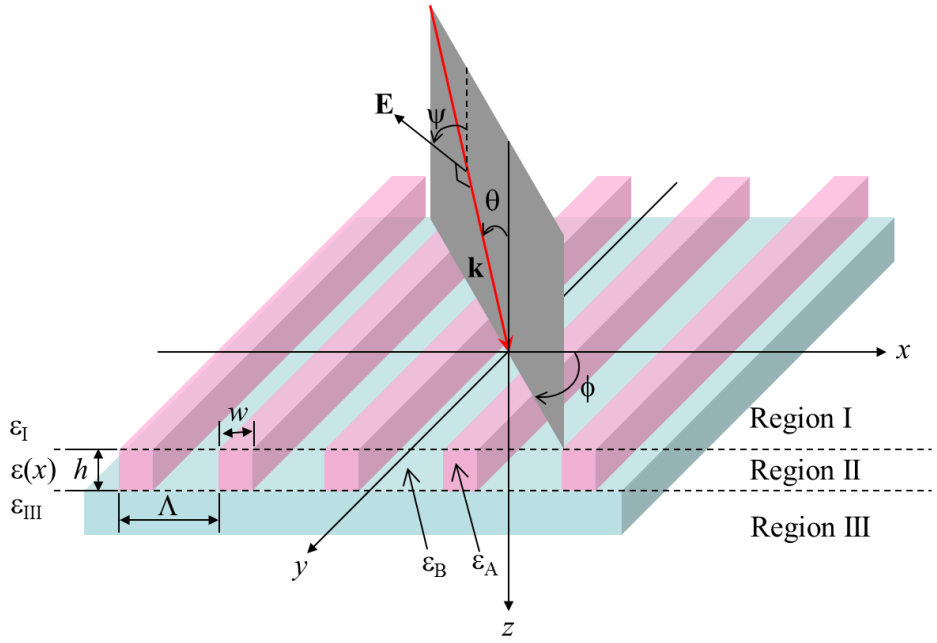

Figure 2.3 Schematic of a 1D grating with a period Λ, width *w*, and height *h* for arbitrary plane wave incidence [16].

gratings is defined by the period (Λ), thickness or height (*h*), and the width (*w*). The filling ratio of medium A is given by $f = w/\Lambda$. The direction of incident wave is expressed by the azimuthal angle (ϕ) and the zenith angle (θ). The plane of incidence is defined by the direction of incidence and the *z* axis, except at normal incidence when the *y*-*z* plane is taken as the plane of incidence. For linearly polarized incident wave, the polarization status is determined by ψ, the angle between the electric field vector and the plane of incidence. In Region I, after omitting the time harmonic term $\exp(i\omega t)$, the incident electric-field vector **E** is given by

$$\mathbf{E} = \mathbf{E}_{\mathrm{i}} \exp\left(ik_x x + ik_y y + ik_z z\right) \tag{2.22}$$

where $\mathbf{E}_{\mathrm{i}}$ is the incident electric field vector at the origin, and the components of the incident wavevector are given by $k_x = k\sin\theta\cos\phi$, $k_y = k\sin\theta\sin\phi$, and $k_z = k\cos\theta$,

with $k = 2\pi / \lambda$. The incident electric field can be normalized so that

$$\begin{aligned}\mathbf{E}_{\mathrm{i}} = &\left(\cos\psi\cos\theta\cos\phi - \sin\psi\sin\phi\right)\hat{\mathbf{x}} \\ &+ \left(\cos\psi\cos\theta\sin\phi + \sin\psi\cos\phi\right)\hat{\mathbf{y}} - \cos\psi\sin\theta\,\hat{\mathbf{z}}\end{aligned} \tag{2.23}$$

According to the Bloch-Floquet condition [44], the wavevector components of the *j*th diffraction order in Region I are given by

$$k_{xj} = \frac{2\pi}{\lambda}\sin\theta\cos\phi + \frac{2\pi}{\Lambda}\,j \tag{2.24a}$$

$$k_y = \frac{2\pi}{\lambda}\sin\theta\sin\phi \tag{2.24b}$$

$$k_{zj}^r = \begin{cases} \sqrt{k^2 - k_{xj}^2 - k_y^2}, & k^2 > k_{xj}^2 + k_y^2 \\ i\sqrt{k_{xj}^2 + k_y^2 - k^2}, & k_{xj}^2 + k_y^2 > k^2 \end{cases} \tag{2.24c}$$

As required by the phase-matching condition, the parallel components of wavevector k_{xj} and k_y must be the same for the diffracted waves in all three regions. In Eq. (2.24c), superscript r refers to the reflected diffraction. We may denote the reflected wavevectors by $\mathbf{k}_{rj} = (k_{xj}, k_y, k_{zj}^r)$ and the transmitted wavevectors by $\mathbf{k}_{tj} = (k_{xj}, k_y, k_{zj}^t)$. For transmitted diffraction, k_{zj}^r can be replaced by k_{zj}^t after substituting $k_{\mathrm{III}} = k\sqrt{\varepsilon_{\mathrm{III}}}$ for k in Eq. (2.24c). From Eq. (2.24b), the y component of the wavevector is the same for all diffraction orders. Hence, the wavevectors for all diffracted waves end on the semi-circles, which are intersects of the plane of constant k_y and the hemispherical surfaces with a radius k_{I} and k_{III} in each half plane. Taking $z < 0$ or Region I for example, the reflected wavevectors form a half-conical surface. Furthermore, the x components of the wavevectors vary by multiples of $2\pi / \Lambda$ according to Eq. (2.24a). For higher diffraction

orders, the z component of the wavevector becomes purely imaginary, such that the diffracted waves are evanescent. If $\phi = 0^\circ$ or 180°, all the reflected and transmitted diffraction rays lie in the same plane as the plane of incidence. The electric field in region I can be expressed as the sum of the incidence and all reflected waves (including evanescent waves) and that in region III can be expressed as a sum of all transmitted waves (including evanescent waves).

The magnetic fields in Regions I and III can be obtained from Maxwell's equation, $\mathbf{H} = (i\omega\mu_0)^{-1}\nabla\times\mathbf{E}$. In Region II, the electric and magnetic fields can be expressed as a Fourier series. Due to the periodicity, the dielectric function in Region II can also be expressed in a Fourier expansion

$$\varepsilon^{\text{ord}}(x) = \varepsilon(x) = \sum_p \varepsilon_p^{\text{ord}} \exp\left(i\frac{2p\pi}{\Lambda}x\right) \tag{2.25a}$$

It is essential to express the inverse of the dielectric function in Region II as a separate Fourier expansion, i.e.,

$$\varepsilon^{\text{inv}}(x) = \frac{1}{\varepsilon(x)} = \sum_p \varepsilon_p^{\text{inv}} \exp\left(i\frac{2p\pi}{\Lambda}x\right) \tag{2.25b}$$

where $\varepsilon_p^{\text{ord}}$ and $\varepsilon_p^{\text{inv}}$ are the pth Fourier coefficient for the ordinary and inverse of $\varepsilon(x)$ as defined in Eqs. (2.25a) and (2.25b), respectively; and in general, $\varepsilon_p^{\text{inv}} \neq 1/\varepsilon_p^{\text{ord}}$. In the numerical calculation, an upper limit of p can be set such that $p = 0, \pm 1, \pm 2, \ldots \pm 2q$, which means that there are a total of $4q+1$ terms in the Fourier series.

Sufficient diffraction orders must be employed in the RCWA calculation. A total of 101 Fourier components are demonstrated to be sufficient and thus are used to represent the dielectric function in the grating region for the calculations in Chapters 5

and 6 [16]. The spectral-directional reflectance R of the grating can be obtained as the sum of the diffraction efficiencies for all reflected diffraction orders, while the transmittance T is the sum of the diffraction efficiencies for all transmitted diffraction orders. The absorptance is thus $\alpha = 1 - R - T$. Other methods, such as the finite-difference time domain, have also been used to compute the radiative properties of micro/nanostructures [71]. In this dissertation, RCWA is used to calculate the radiative properties of grating structures.

2.4 Magnetic Polaritons and Inductor-Capacitor Model

Magnetic polaritons, referring to the coupling of the magnetic resonance inside a micro/nanostructure with the external electromagnetic waves, have been brought into attention recently due to the fast advancement in the metamaterial research area. It is known that, when a time-varying magnetic field is introduced parallel to the axis of a spiral metallic coil, an oscillating current will be produced in the structure and an induced magnetic field is created according to Lenz's law.

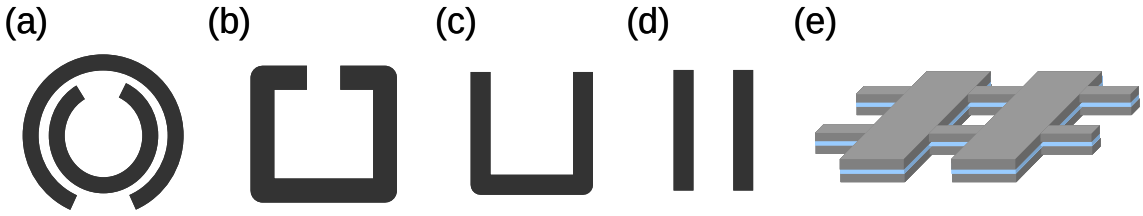

Figure 2.4 Structures that serve as "magnetic atoms": (a) split-ring resonators [18]; (b) single split-ring resonators [19]; (c) U-shape resonators [20]; (d) short-wire, short-rod, or short-strip pairs [21-23]; (e) fishnet structures [24].

Based on this diamagnetic response, Pendry *et al.* [18] proposed a split-ring resonator, the first structure to possess negative μ in the microwave region as shown in

Fig. 2.4(a). Single-split-ring [19] and U-shape [20] unit cells as shown in Figs. 2.4(b) and 2.4(c) were later introduced to scale the magnetic resonance to the near infrared. Researchers also showed that, such a diamagnetic response can be achieved in a short-strip (or short-rod, short-wire) pair, as shown in Fig. 2.4(d), with anti-parallel currents induced in the strips. Podolskiy *et al.* [21] showed that from paired-wire composites both negative ε and μ can exist in the near-infrared and visible frequencies, resulting in negative refractive indices. With the rapid development in nanofabrication techniques, negative refractive index was also experimentally observed from a double-layer periodic gold nanorod array [22] and a paired-copper-wire structure [23], respectively. Fishnet structures [24] consisting of perforated metal films separated by a dielectric spacer as shown in Fig. 2.4(e), were also shown to exhibit negative refractive indices, and negative refraction in the near infrared was experimentally demonstrated with a similar structure composed of 21 alternating Ag and MgF_2 layers [72].

To excite the magnetic resonance or to achieve negative refractive indices at desired frequencies, the accurate prediction on the resonant conditions is very important. Equivalent optical circuitry theory has been widely used recently to predict the electric and magnetic resonant conditions in facilitating the design and analysis of metamaterials [73]. The inductor-capacitor (LC) model is usually employed where the resistance elements are usually neglected. The kinetic inductance accounting for the contributions from the drifting charge carriers cannot be neglected for micro/nanostructures since their critical dimension is comparable with or even smaller than the wavelength of interest [74].

Figure 2.5(a) schematically illustrates the charge distribution between two conducting metal strip separated with a vacuum gap of *b* when the fundamental mode of

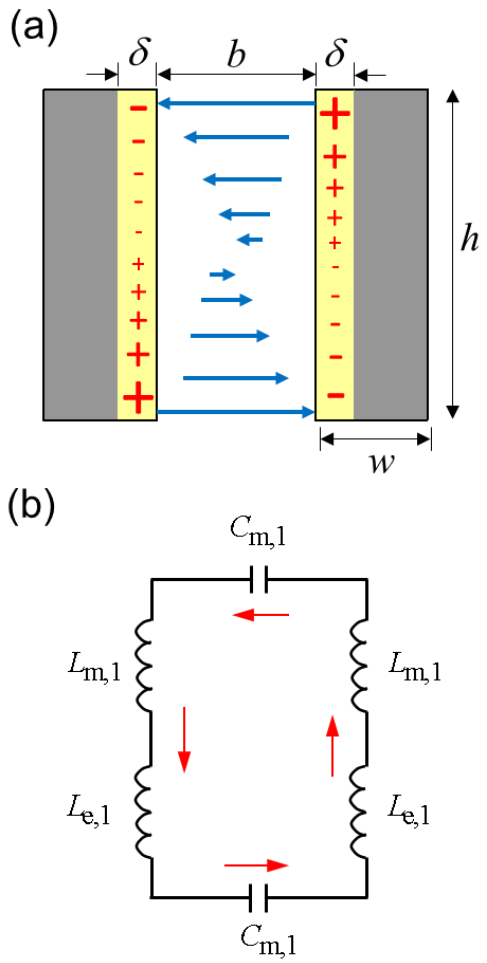

Figure 2.5 (a) Schematic of the charge distribution when the fundamental mode of magnetic resonance is excited between two conducting metal strips; (b) the equivalent LC model at magnetic resonance, where red arrows indicate the induced currents.

magnetic resonance is excited. The strips have a height *h*, width *w*, and length *l* in the direction perpendicular to the paper. Note that the magnetic resonance can only be excited when there is an oscillating magnetic field perpendicular to the paper according to Lenz's law. The magnetic resonance will induce electric currents flowing at the opposite surfaces of the metal strips with opposite directions. Due to the induced currents, charges will not distribute uniformly but with a gradient at the surface, and negative and positive charges will accumulated at two ends, indicated by "–" and "+" markers in the

figure, respectively. The equivalent LC circuit model is shown in Fig. 2.5(b). The capacitance between two strips can be expressed as that between two parallel plates by

$$C_{\mathrm{m},1} = c_1 \varepsilon_{\mathrm{d}} \varepsilon_0 hl / b \tag{2.26}$$

where ε_{d} is the relative permittivity of the filling dielectric ($\varepsilon_{\mathrm{d}} = 1$ for vacuum in this case), ε_0 is the free-space permittivity, and c_1 is a numerical factor accounting for the nonuniform charge distribution at the metal surfaces. Typically, $0.2 \le c_1 \le 0.3$ and in the calculation c_1 is set to be 0.22 following Ref. [75]. $L_{\mathrm{m},1}$ represents the inductance of two parallel strips and can be expressed as

$$L_{\mathrm{m},1} = 0.5 \mu_0 hb / l \tag{2.27}$$

where μ_0 is the vacuum permeability and l is the strip length in the y direction. The contribution of the drifting electrons towards the inductance is given by

$$L_{\mathrm{e},1} = h / (\varepsilon_0 \omega_{\mathrm{p}}^2 S') \tag{2.28}$$

where ω_{p} is the plasma frequency (e.g., 1.364×10^{16} rad/s for Ag) [74]. If the width w is larger than the power penetration depth $\delta = \lambda / 4\pi\kappa$ where κ is the extinction coefficient of the metal, the effective cross-sectional area of the metal strip is approximated as $S' = \delta l$ by assuming that all induced electric current flows at the depths within δ near the metal surface; otherwise, $S' = wl$. The total impedance of the LC circuit is given by

$$Z_{\mathrm{tot},1} = 2i \left[\omega (L_{\mathrm{m},1} + L_{\mathrm{e},1}) - (\omega C_{\mathrm{m},1})^{-1} \right] \tag{2.29}$$

By setting $Z_{\mathrm{tot},1} = 0$, the magnetic resonance frequency for the fundamental mode is

$$\omega_{\mathrm{R},1} = \left[(L_{\mathrm{m},1} + L_{\mathrm{e},1}) C_{\mathrm{m},1} \right]^{-1/2} \tag{2.30}$$

which is independent of l. Furthermore, if $w \gg \delta$, the resonance frequencies for higher orders can be approximated by doubling or tripling the fundamental resonance frequency.

The study of metamaterials nowadays mainly focuses on the invisible cloaking [25] and subwavelength imaging beyond diffraction limit by using superlenses [26] and hyperlenses [28], and little has been addressed on the optical properties and the application of energy conversion and harvesting. Magnetic polaritons have been employed to achieve extraordinary optical transmission through a diatomic chain of slit-hole resonators [76], and their effect on the optical transmission through hole arrays perforated in trilayer structures was investigated [31,32,77]. However, whether or not magnetic polaritons exist in 1D periodic grating structure and how the radiative properties would be affected is still not known.

2.5 Surface Plasmon/Phonon Polaritons

Plasmons are quasiparticles associated with oscillations of plasma, which is a collection of charged particles such as electrons in a metal or semiconductor [78]. Plasmons are longitudinal excitations that can occur either in the bulk or at the interface. The field associated with a plasmon is confined near the surface, while the amplitude decays away from the interface. Such a wave propagates along the surface, and it is called a surface electromagnetic wave. Surface plasmons can be excited by electromagnetic waves and are important for the study of optical properties of metallic materials, especially near the plasma frequency, which usually lies in the ultraviolet. The excitation of SPPs has been intensively studied and is responsible for the extraordinary optical transmission through 2D hole arrays [6] and the thermal emission peaks observed

from the 1D Si gratings [7]. SPPs also play important roles in near-field microscopy [79], plasmonic nanolithography [8], and biosensing applications [80].

The requirement of evanescent waves on both sides of the interface prohibits the coupling of propagating waves in air to the surface plasmons. Prisms and gratings are commonly used to couple propagating waves in air with surface plasmons. In addition to the requirement of evanescent waves on both sides of the interface, the polariton dispersion relations given below must be satisfied [81]:

$$\frac{k_{1z}}{\varepsilon_1} + \frac{k_{2z}}{\varepsilon_2} = 0 \quad \text{for TM waves} \tag{2.31a}$$

$$\frac{k_{1z}}{\mu_1} + \frac{k_{2z}}{\mu_2} = 0 \quad \text{for TE waves} \tag{2.31b}$$

This means that the sign of permittivity must be opposite for media 1 and 2 in order to couple a surface polariton with a TM wave. A negative Re(ε) exists in the visible and near infrared for metals like Al, Ag, W, and Au. When Eq. (2.31a) is satisfied, the excitation of surface plasmon polariton (SPP) interacts with the incoming radiation and causes a strong absorption. Lattice vibration in some dielectric materials like SiC and SiO_2 can result in a negative Re(ε) in the middle infrared. The associated surface electromagnetic wave is called a surface phonon polariton (SPhP). On the other hand, a magnetic material with negative permeability is necessary for a TE wave to be able to couple with a surface polariton. Some metamaterials can exhibit negative permeability in the optical frequencies and negative index materials exhibit simultaneously negative permittivity and permeability in the same frequency region. Therefore, both TE and TM waves may excite SPPs with negative index materials [81] or with bilayer materials of alternating negative ε and μ, the so-called single negative materials [82].

The condition for the excitation of surface polaritons is that the denominator of Fresnel's reflection coefficient be zero. A pole in the reflection coefficient is an indication of a resonance. One can solve Eq. (2.31a) for a TM wave to obtain [1]

$$k_x = \frac{\omega}{c}\sqrt{\frac{\mu_1/\varepsilon_1 - \mu_2/\varepsilon_2}{1/\varepsilon_1^2 - 1/\varepsilon_2^2}} \tag{2.32}$$

This equation is called the polariton dispersion relation, which relates the frequency with the parallel component of the wavevector. For nonmagnetic materials, it becomes

$$k_x = \frac{\omega}{c}\sqrt{\frac{\varepsilon_1\varepsilon_2}{\varepsilon_1 + \varepsilon_2}} \tag{2.33}$$

One should bear in mind that the permittivities are in general functions of the frequency. For a metal with a negative real permittivity, the normal component of the wavevector is purely imaginary for any real k_x, because $\mu\varepsilon\omega^2/c^2 < 0$. Thus, evanescent waves exist in metals regardless of the angle of incidence. Figure 2.6(a) shows the dispersion curve (the unfolded one) to excite the SPP at a Ag/vacuum interface. Note that the optical constant of Ag is taken from the data in Ref. [83] at room temperature.

When the plane of incidence is perpendicular to grooves, only TM waves can excite SPPs in metallic gratings. Figure 2.6(b) is a schematic of a free-standing 1D binary grating structure in vacuum, with a period Λ, strip width w, slit width b, and grating height h. Due to the periodicity, the Bloch-Floquet condition [1] gives the parallel component of wavevectors of the jth diffraction order as $k_{x,j} = k_x + 2\pi j/\Lambda$, where $k_x = (\omega/c)\sin\theta$ is the parallel component of the wavevector in vacuum and θ is the angle of incidence. Based on the Bloch-Floquet condition, the dispersion relation of SPPs can be folded at $k_x = j\pi/\Lambda$ into the region $k_x \le \pi/\Lambda$, as the dash curve shown in Fig. 2.6(a) for a

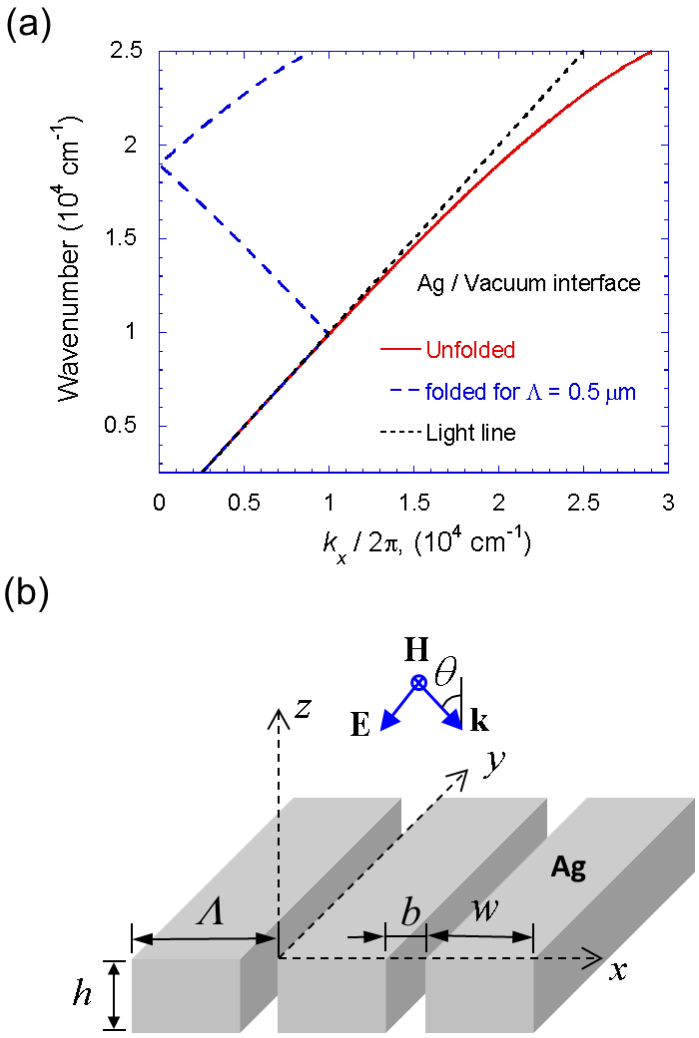

Figure 2.6 (a) Dispersion curves for the excitation of SPPs at an Ag/vacuum interface (the folded curve for grating period Λ = 0.5 um); (b) Schematic of a free-standing binary Ag grating structure with a period Λ, grating height *h*, strip width *w*, and slit width *b*.

Ag grating with Λ = 0.5 μm. The excitation condition for SPPs can be determined by the intersection location of the dispersion curve with a specific angle of incidence. Therefore, the excitation condition for SPPs in grating structures is strongly dependent on the grating period and direction.

CHAPTER 3
INSTRUMENTATION FOR ROOM- AND HIGH-TEMPERATURE MEASUREMENTS OF RADIATIVE PROPERTIES

This Chapter describes the instrumentation and experimental methods used in following chapters for characterizing the radiative properties of fabricated micro/nanostructure samples at both room and elevated temperatures, such as asymmetric Fabry-Perot resonant cavities and subwavelength grating structures as coherent thermal emitters. Section 3.1 presents how the spectral specular reflectance is measured with a Fourier-transform infrared (FT-IR) spectrometer at specific angles by using different reflectance accessories. Section 3.2 briefly introduces a laser scatterometer which measures the reflectance with various angles of incidence at a single wavelength. A high-temperature emissometry facility is developed as one of the main tasks and contributions of this dissertation. The experimental setup and procedures are discussed in detail in Section 3.3 along with some theoretical analysis. Finally, Section 3.4 presents the emittance of a SiC sample at 800 K measured with the emissometer, based on which the accuracy of the direct emittance measurement facility is demonstrated.

3.1 Spectral Reflectance Measurements

An FT-IR spectrometer (ABB Bomen FTLA2000), as shown in Fig. 3.1(a), was used to measure the spectral reflectance of the samples at near normal incidence (10°), as well as incidence angles of 30° and 45° using suitable specular reflectance accessories. Figure 3.1(b) shows the near normal incidence reflectance accessory. At 10° incidence, the difference between TE and TM waves is negligibly small and the beam from the FT-

IR source is assumed to be unpolarized (i.e., average of the two polarizations). A wire-grid IR polarizer was used to measure the reflectance for TE and TM waves at different angles of incidence, as shown in Fig. 3.1(c) along with the 30 °reflectance accessory. The polarizer was intentionally tilted during the measurements to eliminate multiple reflections [84].

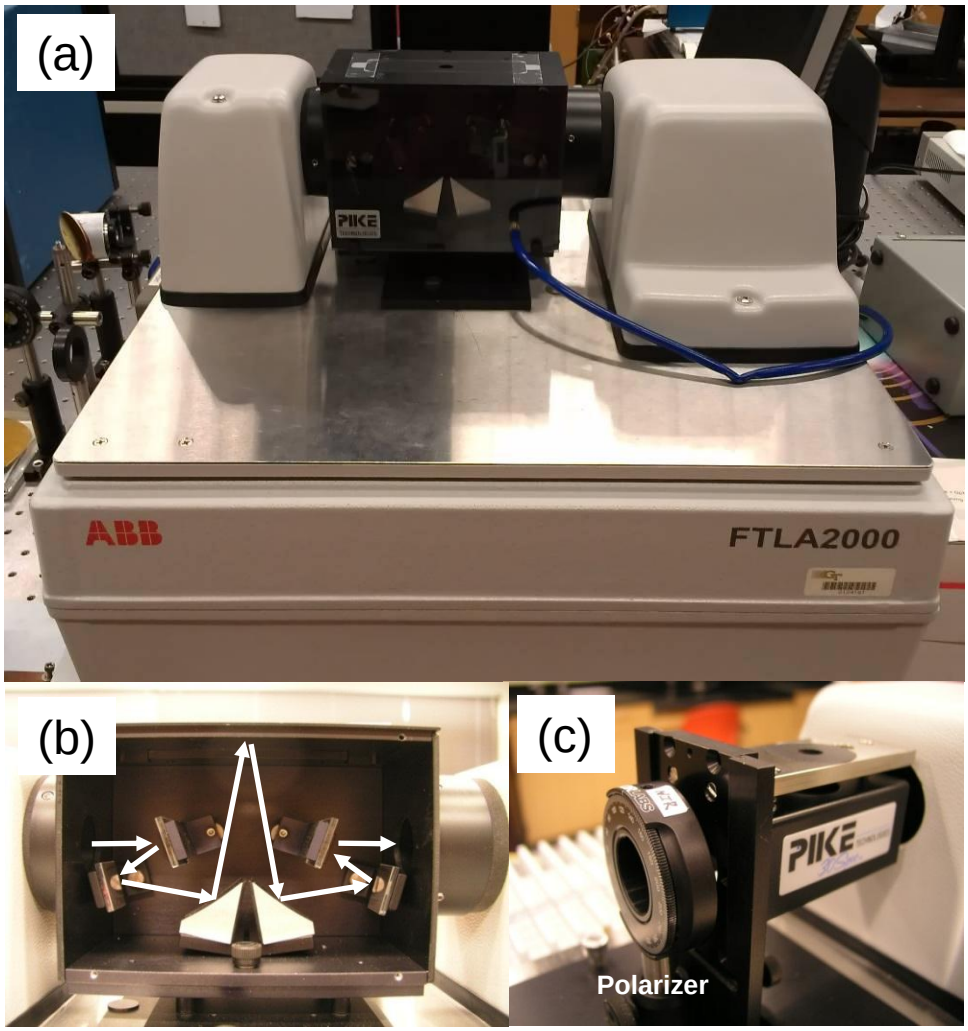

Figure 3.1 Pictures of (a) the FT-IR spectrometer, (b) 10 °and (c) 30 °specular reflectance accessory. Note that a polarizer can be mounted on the accessory to select different incident wave polarizations.

An internal near-IR source (a quartz-halogen lamp with a tungsten filament) and an infrared source (SiC Globar) were used with a deuterated triglycine sulfate (DTGS) pyroelectric detector, which has an excellent linearity from 500 cm^{-1} up to 13000 cm^{-1} in wavenumber. Before the measurement, the sources were turned on for more than one hour to reach thermal stability. The optical path of the spectrometer, including the reflectance accessory, was purged with N_2 gas to reduce water vapor and CO_2 absorption. A mirror made of a 200-nm-thick Au film deposited on a Si substrate was used as the reference. To ensure the radiometric accuracy of FT-IR spectrometers, several procedures were conducted such as taking 100% line and background signal measurement. The stability of the IR signal from 2 to 19 μm with the mirror was within ±0.5%, and the background signal (with an open aperture of 9-mm diameter when removing the mirror) was less than 0.5% of the reference signal with the mirror. During the experiment, the sample and Au mirror were interchanged to measure the relative reflectance of the sample with respect to that of the Au mirror. Each spectrum was the average of 32 scans with a resolution of 4 cm^{-1}. The reflectance of the sample was obtained by averaging five repeated measurements and then corrected by multiplying the Au mirror reflectance of 0.985, calculated from the optical constants of Au in Ref. [83]. The overall uncertainty in reflectance was estimated to be 0.02, considering various possible sources of error, such as beam divergence, misalignment, background signal, and repeatability.

3.2 Angle-Resolved Reflectance Measurements

To experimentally study the directional radiative properties of the constructed Fabry-Perot resonance cavities, a laser scatterometer [85,86] was used to measure the

specular reflectance at different incidence angles for each polarization. The scatterometer is also called three-axis automated scatterometer (TAAS) since it has three movable stages to change the incidence and observation directions, which can be automatically controlled by a computer under the LabVIEW environment.

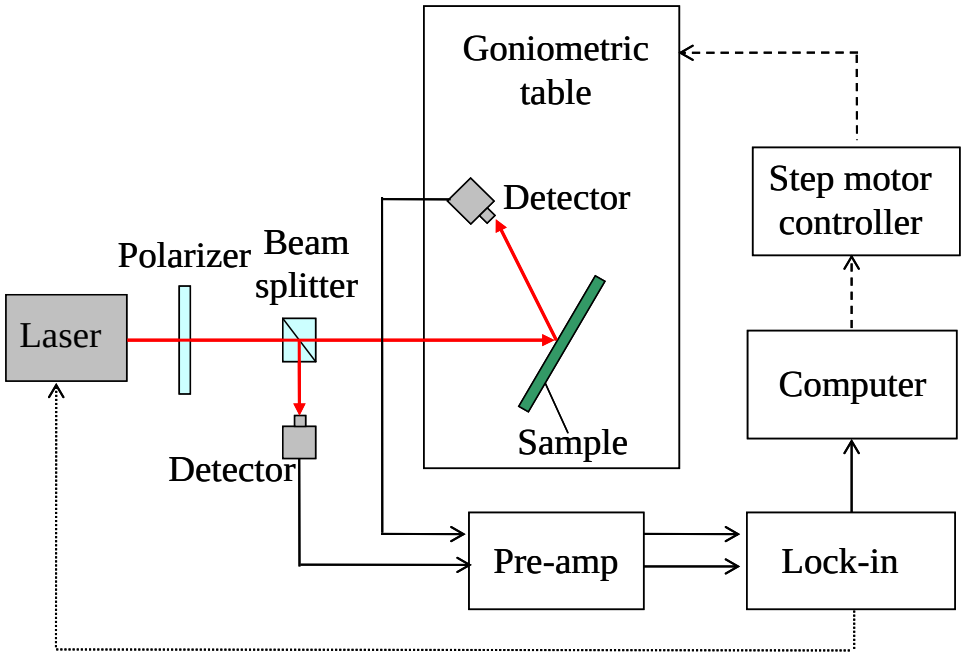

Figure 3.2 Schematic of the laser scatterometer system.

The experimental setup is illustrated in Figure 3.2. A thermoelectric-cooled diode laser system was employed using a laser diode at the wavelength of 891 nm with a full-width-at-half-maximum (FWHM) bandwidth of 3 nm. A lock-in amplifier connected with a diode laser controller modulates the output power at 400 Hz. The output laser power is approximately 1 mW with a stability of a few tenths of a percent. The laser beam passed through a small iris and was collimated through a pair of lenses before going through a near-IR polarizer. A beamsplitter divided the ray into two beams: a transmitted beam that was in the same direction as the incidence and a reflected beam that was in the horizontal plane but perpendicular to the incidence. The transmitted beam

was incident on the sample and the signal reflected by the sample was received by a movable Si detector. The reflected beam from the beamsplitter was sent to a stationary reference Si detector. The majority of the laser power is transmitted with a transmittance of about 85% for the TE wave and 95% for the TM wave. The synchronous voltage signals from the two detectors were collected by the lock-in amplifier through a trans-impedance preamplifier. The effect of background radiation (i.e., stray light) can be eliminated by only picking up the phase-locked signals at 400 Hz. The specular reflectance of the Fabry-Perot sample was measured at the incidence angles from 2 ° to 75 ° with 1 ° increment, except that in the range between 32 ° and 50 °, where the increment was set at 0.2 ° in order to resolve the reflectance valley (emissivity peak). The uncertainty of the angle-resolved reflectance measurement was estimated to be 0.02 by calibration using a bare Si sample and by evaluation of the standard deviation of repeated measurements.

3.3 High-Temperature Emissometry Facility

FT-IR spectrometers have been frequently used for direct emittance measurements [87-93] and sometimes also for radiometric temperature measurements [89,92,93]. The optical layout of the high-temperature emissometry facility is presented in Fig. 3.3(a), and the main components include a heater assembly, blackbody source, optical components, and FT-IR, which was used to collect the emission spectra from either the sample or the blackbody [94]. Figure 3.3(b) shows the configuration of the heat assembly. The sample was compressed on a copper disk, which was nickel-plated to prevent oxidation. The nickel-plated copper disk maintained a uniform temperature

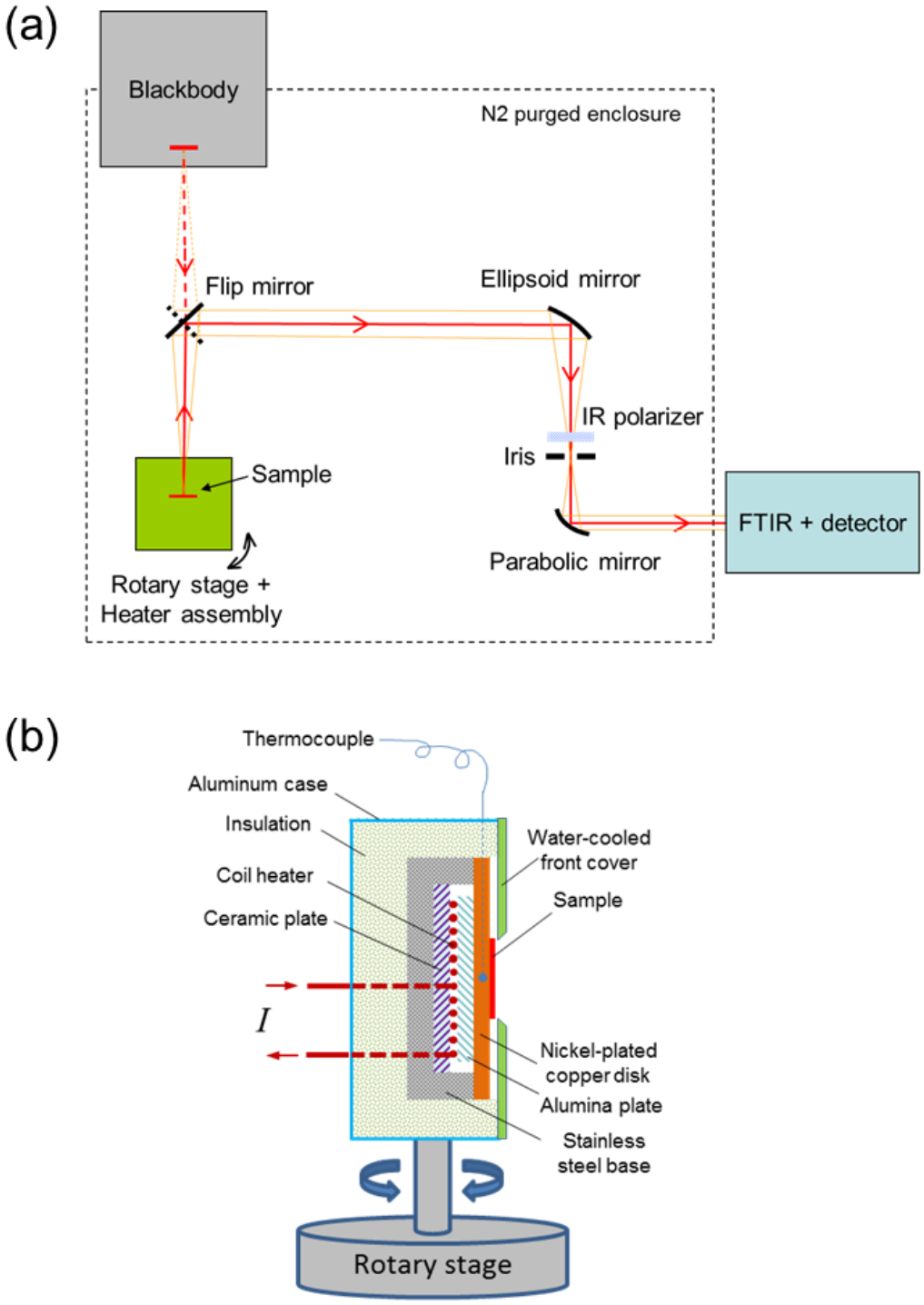

Figure 3.3 (a) Optical layout of the high-temperature emissometer, consisting of a blackbody, a heater assembly mounted on a rotary stage, an FT-IR spectrometer, and optical components; (b) Schematic of the heater assembly.

underneath the sample. Note that the wafers used in the present study were double-side polished with high smoothness. The copper surface was also polished before nickel plating to reduce thermal contact resistance (TCR). A coil heater was located at the back of the copper disk with an alumina plate inserted in between for electrical insulation. A K-type thermocouple probe (Omega KMTXL) with oxidation-resistive sheathing up to 1150 ℃ was embedded inside the copper disk for sample temperature measurement. A PID temperature controller maintained the sample temperature within ±1 K of the set point. The heater assembly was placed in refractory materials and mounted in a metal box. The sample temperature can reach 1000 K with a power input around 140 W, about 15% of which leaves the sample surface by convection and radiation. The front cover of the heater assembly was water-cooled with an aperture of 25-mm diameter to expose the sample. The heater assembly was mounted on a rotary stage to change the emission angle. The rotary stage was computer controlled with LabVIEW for rotation on both sides with a step resolution of 0.01 º.

A blackbody (MIKRON M360), with an accuracy of ±1 K and a stability of ±0.5 K, was used as the reference source. A flip mirror with 90 º rotation was used to interchange the emission source between the sample and the blackbody. The optical setup used an ellipsoidal reflector and an off-axis paraboloidal reflector similar to the work of Zhang *et al.* [95]. The longer focus of the ellipsoid was on either the sample surface or the opening of the blackbody cavity. The shorter focus of the ellipsoid overlaps with that of the paraboloid. The emitted ray from either the sample or the blackbody, after being reflected by the flip mirror, the ellipsoidal reflector, and the paraboloidal reflector, became collimated with about 25 mm in diameter and was then directed into the FT-IR

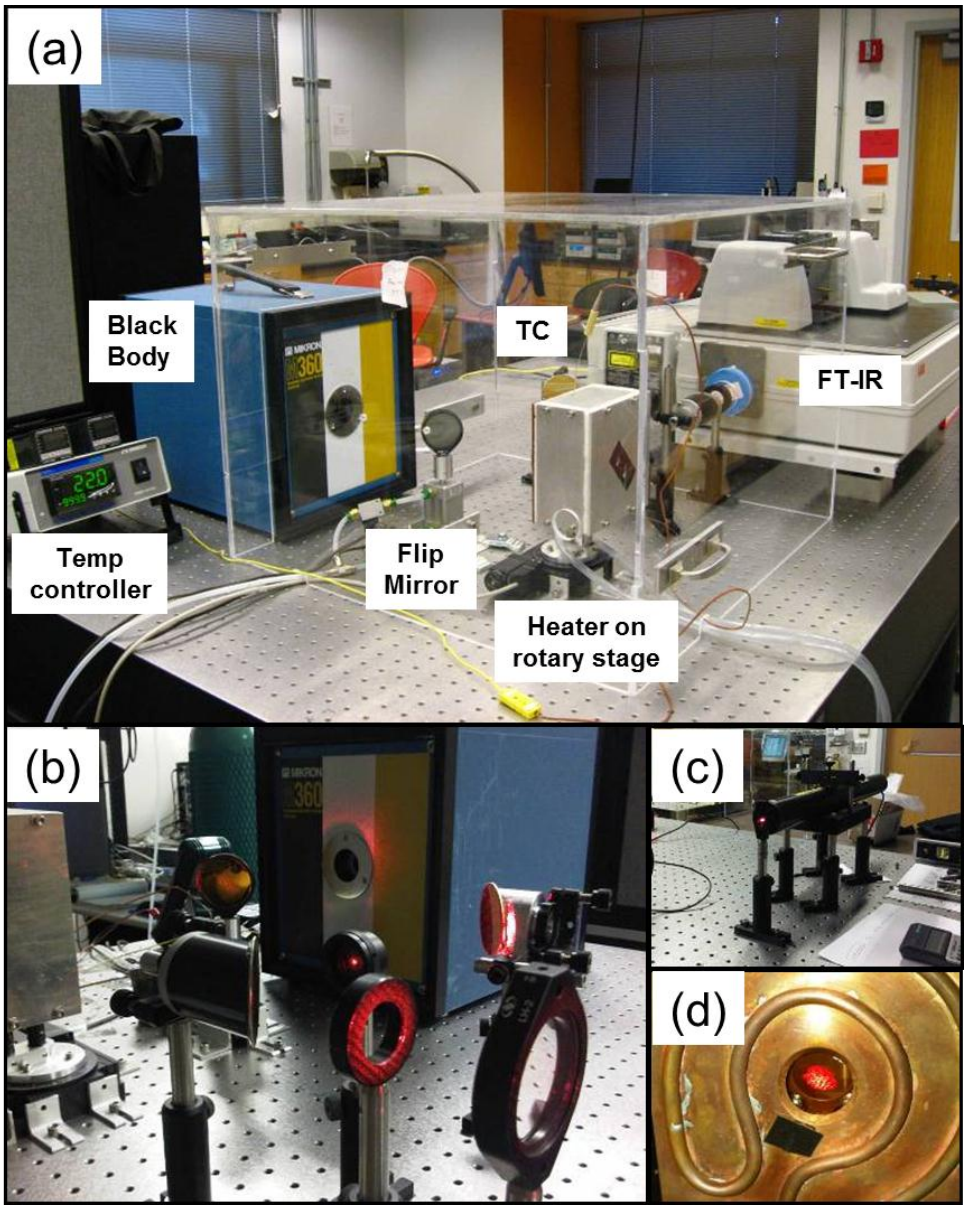

Figure 3.4 Pictures of (a) the entire high-temperature emissometry facility; (b) the optical parts; (c) the He-Ne laser used for optics alignment; and (d) the laser spot on the sample surface which approximates the emitted area from sample to be collected.

through a side port. The distance between the ellipsoidal foci is 514 mm and the paraboloid focal length is about 60 mm. The half-cone angle of the collected beam from the sample is approximately 3°. An iris was placed at the focus of the paraboloidal reflector to limit the collecting area on the sample and adjusted the amount of radiation

going into the spectrometer. An IR polarizer next to the iris was used to allow either transverse electric (TE) waves, where the electric field is perpendicular to the optical table, or transverse magnetic waves, where the magnetic field is perpendicular to the optical table, to pass through. The DTGS detector can be used at temperatures higher than about 700 K. A liquid-nitrogen cooled indium antimonite (InSb) detector with a higher detectivity can be used at temperatures above 500 K in the spectral range from 2.0 μm to 5.5 μm. Before the direct emission measurement, the internal IR source inside the FT-IR was turned off for a couple of hours for cooling down. Figure 3.4(a) shows a picture of the entire high-temperature emissometry facility.

The optics alignment turned out to be challenging for IR optics. Hence, a He-Ne laser at wavelength of 632 nm, as shown in Fig. 3.4(c), was placed at the spectrometer's position by removing the FT-IR to align the optical components shown in Fig. 3.4(b). The laser beam was first expanded to approximately 25 mm in diameter with two convex lenses, and then the collimated beam was sent to the paraboloidal reflector. The optical components were aligned by tracing the laser beam backwards from the paraboloidal reflector to the sample surface or the blackbody. Figure 3.4(d) shows the laser spot during the alignment on the sample surface, which approximates the active area from which the thermal radiation from the sample surface is collected.

To ensure uniform heating and protect the sample from thermal shock, the heating process was divided into several intermediate steps with incremental set temperatures, and the temperature was maintained for 30 min after each set point was reached before proceeding to the next step. The stability of the thermal radiation from the blackbody or the sample surface was checked to be within ±0.5% before measuring the emission

spectrum. An average of 100 scans with a resolution of 4 cm^{-1} was used for each emission spectrum. By turning the flip mirror, the emission spectrum from the sample surface or the blackbody can be individually collected with the spectrometer. The blackbody spectrum and the sample spectrum are denoted as $S_B(\nu, T_B)$ and $S_S(\nu, T_S)$, respectively, where T_S and T_B are the sample and blackbody temperatures, and ν is the frequency or wavenumber. The background spectrum $S_A(\nu, T_A)$, where T_A = 21 ℃ is the room (ambient) temperature, was collected by removing the heater assembly. An alternative way is to turn the heater off and let it cool down to ambient temperature. Assuming that $T_B = T_S$, one obtains the spectral emittance of the sample from the following measurement equation:

$$\varepsilon'_\nu(\nu) = \frac{S_S(\nu, T_S) - S_A(\nu, T_A)}{S_B(\nu, T_S) - S_A(\nu, T_A)} \tag{3.1}$$

During the experiment, the blackbody was set at the same temperature with the thermocouple (TC) reading, i.e., $T_B = T_{TC}$; however, the surface temperature of the sample would be somewhat lower than that of the copper plate underneath the sample. Based on the one-dimensional heat transfer model, the temperature difference $\Delta T = T_{TC} - T_S$ can be obtained from the energy balance at the steady state,

$$\frac{\Delta T}{0.5 d_{Cu}/k_{Cu} + R''_c + d_{Sub}/k_{Sub} + R''_{films}} = h(T_S - T_A) + \varepsilon_S \sigma (T_S^4 - T_A^4) \tag{3.2}$$

where h is the convection coefficient at the sample surface, ε_S is the total-hemispherical emissivity of the sample, R''_c is the TCR between the sample and the copper disk, d_{Cu} and k_{Cu} are the thickness and the thermal conductivity of the copper disk, d_{Sub} and k_{Sub} are the thickness and the thermal conductivity of the substrate, and R''_{films} accounts for the

thermal resistance of the multilayered films including thermal boundary resistances between the films and that between the film and the substrate. In Eq. (3.2), since TC was inserted in the middle of the copper disk, the thermal resistance of copper is based on half the thickness only. With the estimated natural convection coefficient $h = 15\ \text{W/m}^2\text{-K}$ and taking $\varepsilon_S = 0.85$ (which is near the higher end of measured samples), the heat loss from the sample surface is less than 20 W for $T_{TC} = 800\ \text{K}$. The lateral dimensions of the sample were $25.4 \times 25.4\ \text{mm}^2$. The copper plate thickness is 3.2 mm and, with its thermal conductivity exceeding 360 W/m-K, one obtains $0.5 d_{Cu}/k_{Cu} < 4.4\ \text{mm}^2\text{-K/W}$. For a substrate thickness of less than 400 μm and thermal conductivity higher than 40 W/m-K, one obtains $d_{Sub}/k_{Sub} < 10\ \text{mm}^2\text{-K/W}$. Note that for Si, the thermal conductivity is around 40 W/m-K at 800 K; on the other hand, SiC would have a much higher thermal conductivity exceeding 200 W/m-K at 800 K [96]. For the Fabry-Perot structure, R''_{films} includes both the contact resistance and the resistance of the films, especially the SiO_2 layers. The thermal boundary resistance for the deposited films is on the order 0.001 to $0.02\ \text{mm}^2\text{-K/W}$ for each interface [97] and thus can be neglected. The resistance estimated by the SiO_2 films gives $R''_{films} \approx 1\ \text{mm}^2\text{-K/W}$. For bare Si on polished copper with applied pressure, the value of $R''_c = 50\ \text{mm}^2\text{-K/W}$ is taken from the room-temperature measurement [98] and is expected to decrease as temperature increases. Clearly, the dominant resistance is R''_c, which could give rise to a temperature difference up to 1.3 K at $T_{TC} = 800\ \text{K}$, while a temperature difference ΔT less than 1.6 K was obtained taking into accounts all the resistances. In the present study, due to the

difficulties in determining the TCR between the sample and the copper plate, no correction for the surface temperature of the sample is made. The temperature error will result in an uncertainty in emittance of less than 1.5% for wavelengths from 2.5μm to 20μm. The overall uncertainty of the emittance measurement is estimated to be 0.03.

3.4 High-Temperature Emittance of SiC

To test the setup, a 6H-SiC wafer (n-type doped with a resistivity of 0.02 to 0.1 Ω-cm) was used as a reference [94]. The thickness of the SiC wafer is 330 μm, and the lateral dimensions are 20 × 20 mm^2. The SiC wafer appears greenish due to doping. Figure 3.5 shows the measured spectral emittance of the SiC wafer at both room temperature (10 º, indirect) and 800 K (0 º, direct) from 700 to 1200 cm^{-1}, where the SiC wafer is essentially opaque. The emittance at the room temperature was measured before and after heating. The slightly increased emittance may be explained by the formation of a thin oxide layer at the surface when heating in air [92], along with the uncertainty in the reflectance measurement. The emittance at room and elevated temperatures has a similar trend. The peak emittance is 0.986 at room temperature and 0.962 at 800 K, respectively. Note that the SiC wafer used in the present study was doped, and the peak emittance for SiC with high resistivity (i.e., low doping concentration) is expected to be essentially unity [83,99]. The corresponding wavelength when the emittance approaches unity is called the Christiansen wavelength, which can be used for calibration of emittance measurements [1,100]. Emittance peaks of a few percent below unity have also been observed by others for SiC samples with different crystalline structures [92].

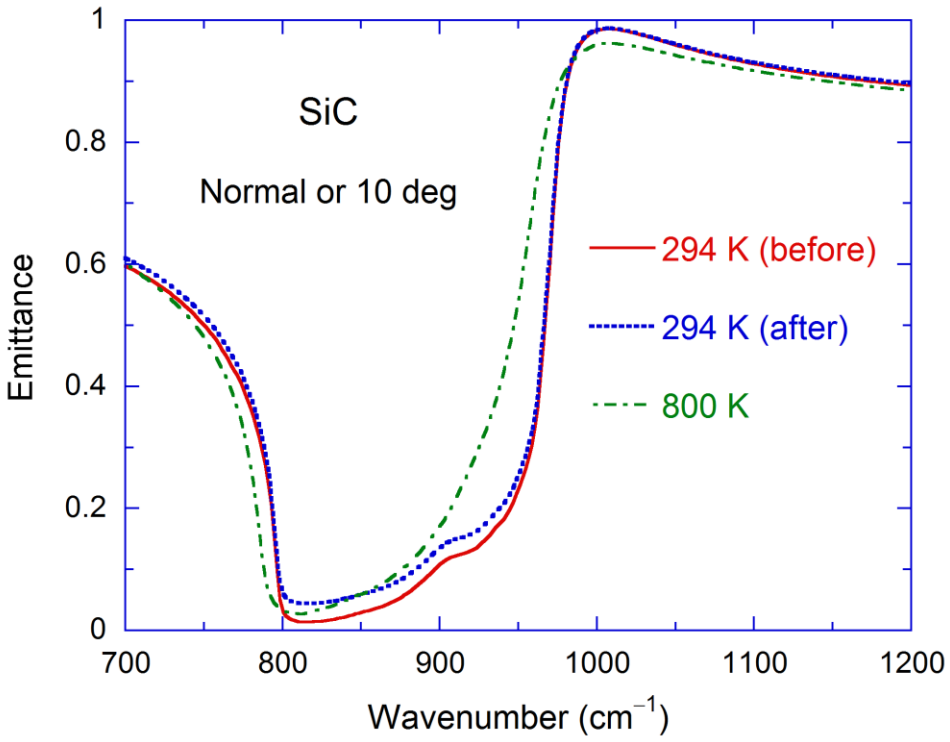

Figure 3.5 Measured emittance spectra of the SiC sample for 10 deg at 294 K (before and after heating) and for normal direction at 800 K. The emittance at 294 K is obtained indirectly from the measured reflectance using Kirchhoff's law, while the emittance at 800 K is directly measured with the emissometer.

The variation in the emittance of SiC at different temperatures is mainly due to the temperature-dependent scattering rate [90]. While emissivity and reflectivity are often used for a smooth semi-infinite medium [101], reflectance and emittance are used in the present study without distinguishing the surface conditions. At normal incidence, the spectral reflectance can be calculated from [1]

$$R_{\mathrm{SiC}} = \frac{(n-1)^2 + \kappa^2}{(n+1)^2 + \kappa^2} \tag{3.3}$$

where the refractive index n and extinction coefficient κ of SiC can be obtained from the Lorentz model for phonon oscillators as

$$\varepsilon_{\mathrm{SiC}}(\nu) = (n + i\kappa)^2 = \varepsilon_\infty \left(1 + \frac{\nu_{\mathrm{LO}}^2 - \nu_{\mathrm{TO}}^2}{\nu_{\mathrm{TO}}^2 - i\gamma\nu - \nu^2} \right) \tag{3.4}$$

The parameters at room temperature are taken from [1,99] as follows: the high-frequency constant $\varepsilon_\infty = 6.7$, longitudinal optical-phonon frequency $\nu_{\mathrm{LO}} = 969\,\mathrm{cm}^{-1}$, transverse optical-phonon frequency $\nu_{\mathrm{TO}} = 793\,\mathrm{cm}^{-1}$, and scattering rate $\gamma = 4.76\,\mathrm{cm}^{-1}$ (N.B., $1\,\mathrm{cm}^{-1} = 1.884\times10^{11}$ rad/s). Following Ref. [90], the scattering rate was used as the only adjustable parameter to minimize the sum of the squared differences between the theoretical and experimental emittance,

$$f = \sum_{i=1}^{N} \left(\varepsilon_{i,\mathrm{theo}} - \varepsilon_{i,\mathrm{exp}} \right)^2 \tag{3.5}$$

where *N* is the number of experimental data points. The scattering rates obtained from the least-squares fitting are 7.98 cm^{-1} at 294 K (before heating) and 20.96 cm^{-1} at 800 K, respectively. The scattering rate increases with temperature almost proportionally; this agrees with the observation made by [90] and is consistent with the phonon scattering mechanism [1]. The slightly higher scattering rates obtained in the present study at both temperatures may be attributed to the higher doping concentration which gives rise to additional impurity scattering.

The emittance of SiC for TE or TM waves was also measured at 800 K for 30 º emission angle to demonstrate the capability of the emissometer to measure the polarization-dependent emittance, as shown in Fig. 3.6. The directional symmetry of the emissometer was checked by measuring the emittance at both +30 º and –30 º angles of emission, and the largest difference is 0.009 for TE waves and 0.024 for TM waves, respectively. The average emittance at +30 º and –30 º is shown in Fig. 3.6 for each

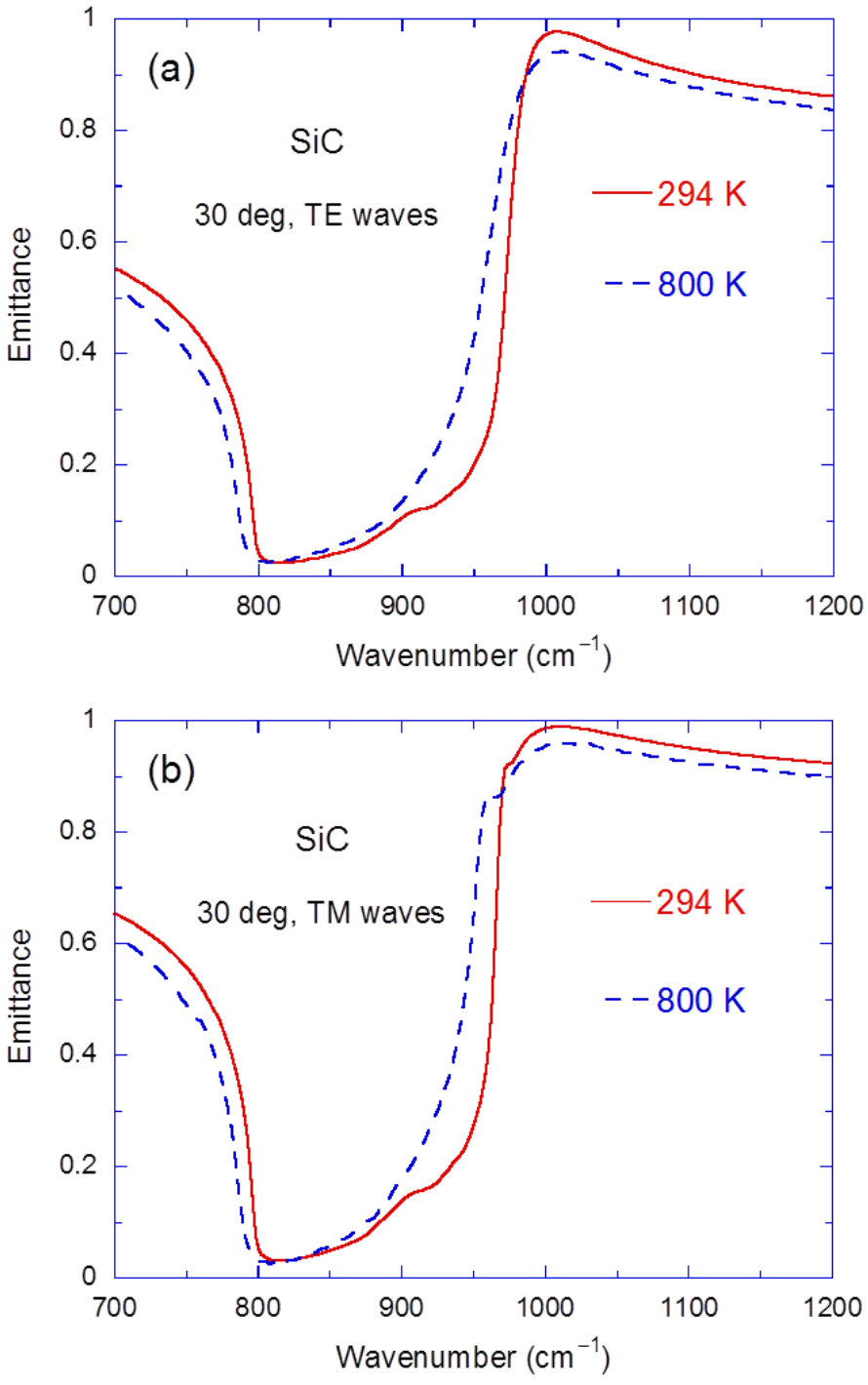

Figure 3.6 The measured 30 ° emittance of the SiC sample at 294 K (before heating) and 800 K: (a) TE waves; (b) TM waves.

polarization. Note that the emittance at room temperature (before heating) was obtained with the indirect method and also shown for comparison. The temperature dependence at 30 º for both polarizations is similar as that for normal direction. The difference can be attributed to the temperature effect on the scattering rate of SiC. Also, the peak emittance is somewhat higher for TM waves than TE waves due to the relatively smaller reflectivity of TM waves between SiC and air at 30 º.

CHAPTER 4
COHERENT THERMAL EMISSION FROM ASYMMETRIC FABRY-PEROT RESONANT CAVITIES

This Chapter experimentally demonstrates the coherent thermal emission from asymmetric Fabry-Perot resonant cavity samples through room- and high-temperature measurements, along with the theoretical discussion on the underlying physics of wave interference effect. Section 4.1 describes the fabrication process of the Fabry-Perot cavity samples. The spectral-directional reflectance of fabricated samples at room temperature was measured in the near-infrared region with the FT-IR spectrometer and the scatterometer to demonstrate both temporal and spatial coherences of thermal emission, which is discussed in detail in Section 4.2. To further investigate the thermal properties under high temperature environment, Section 4.3 presents the high-temperature measurement results as well as the modeling results to facilitate understand the behaviors. At last, Section 4.4 shows that the direct and indirect methods on predicting the thermal emission from layered structures suffering from a temperature gradient are theoretically unified and a generalized Kirchhoff's law is obtained. The equivalence is demonstrated with a Fabry-Perot cavity structure under nonuniform temperature distributions.

4.1 Sample Fabrication

To experimentally demonstrate that the proposed Fabry-Perot cavity structure shown in Fig. 2.1 can be used as a coherent emission source, several samples were fabricated on Si substrates and their spectral and directional radiative properties were measured [63]. The Si wafers are of 100 mm in diameter and 400 μm in thickness. A thin

Ti film and a 200-nm Au film were subsequently deposited on the polished side of the Si substrate, after proper surface cleaning, using an e-beam evaporator without breaking its vacuum environment. A quartz crystal microbalance monitored the deposition thickness. The thin Ti film (about 20 nm) serves as an adhesive layer to prevent the Au film from peeling off. As long as the thickness is much greater than the penetration depth, this Au film can be treated as an opaque layer or a semi-infinite medium. Thus, the exact thicknesses of these bottom layers are not important. After the sample was cooled down in the e-beam evaporator, it was taken out and placed into a plasma-enhanced chemical vapor deposition (PECVD) chamber. SiO_2 thin film was deposited at 250℃ on the sample and on a bare Si piece as well. The thickness of the dielectric layer was measured from the reference Si piece using a reflectometer (Nanospec Film Analyzer 3000). The measurements indicate that the SiO_2 layer has less than 5% variation in thickness relative to the designed value. Afterwards, the sample was placed back into the e-beam evaporator and coated with a thin Au film (less than 30 nm). Because the quartz crystal monitor could not precisely determine the deposited thickness for very thin Au films, several trial-and-error tests were made in order to find the appropriate Au thickness for the Fabry-Perot resonance cavities. Because the resonance frequency and the minimum reflectance value are very sensitive to the thicknesses of the SiO_2 cavity and top Au film, the exact thicknesses of dielectric layer and Au film are determined later by fitting the reflectance measured by the FT-IR spectrometer. Three samples (1, 2, and 3) with different SiO_2 cavity thickness and Au film thickness were fabricated to study the thickness effect. The samples were diced into 25 mm by 25 mm square pieces for measurements of the radiative properties.

4.2 Room-Temperature Reflectance Measurements

The measured reflectance spectra of the three samples at near normal incidence ($\theta_i = 10°$) are shown in Fig. 4.1. At this incidence angle, polarization effect is negligible. In the frequency range from 3000 cm^{-1} to 13000 cm^{-1} in wavenumber, there are two sharp reflectance dips arising from resonances in the dielectric cavity. It should be noted that due to the low signal-to-noise ratio at high frequencies, the spectra beyond 11000 cm^{-1} exhibit large fluctuations. To further reduce the measurement noise, the reflectance at frequencies above the second valley was averaged over 21 consecutive data points (i.e., 10 points on the left and 10 points on the right) with respect to their central frequency. The plots shown in Fig. 4.1 are the spectra after the noise reduction. In order to determine the dielectric and Au film thicknesses of each sample, Eq. (2.5) was used to calculate the spectral reflectance at $\theta_i = 10°$ with d_c and d_f as the adjustable parameters. In the calculation, the optical constants of Au and SiO_2 were taken from Ref. [83]. The initial values were obtained from the measured film thicknesses. The location of the resonance frequency is more sensitive to the SiO_2 thickness, while the magnitude of the reflectance minimum is more sensitive to the Au film thickness. The best fitting results can be obtained by iteratively modifying d_c and d_f and comparing the calculated spectra with that measured. The fitting parameters are tabulated in Table 4.1 for each sample, along with the free spectral range and the quality factor of the resonance as discussed below.

The free spectral range $\Delta\nu$ is the frequency interval between the two consecutive resonance dips. It can be seen that Samples 2 and 3 have similar SiO_2 thickness and free spectral range. For a dielectric film inside air, the free spectral range is determined by resonances inside the film and can be calculated from $\Delta\nu = 1/(2n_c d_c \cos\theta_c)$, assuming

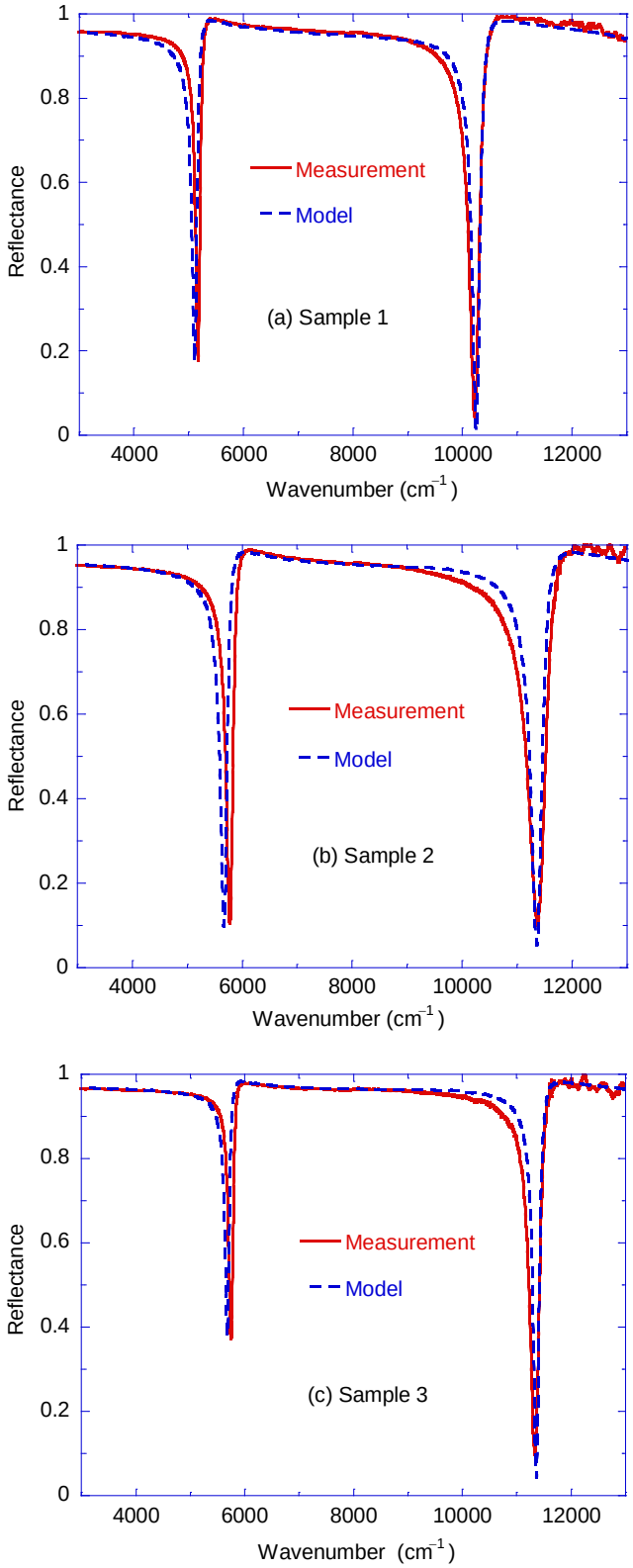

Figure 4.1 Spectral reflectance of the fabricated Fabry-Perot resonators in the near-IR spectral region at $\theta_i = 10°$: (a) Sample 1; (b) Sample 2; (c) Sample 3.

the refractive index of the dielectric is frequency independent [1]. Taking the average refractive index of SiO_2 as 1.44, the above equation gives for Sample 1 $\Delta\nu$ = 5623 cm^{-1}, which is more than 10% greater than the actual $\Delta\nu$ of 5050 cm^{-1}. This is caused by the phase shift upon reflection at the SiO_2 cavity boundaries. From Eqs. (2.5) and (2.6), the modulation of the transmittance and reflectance is determined by the modified phase angles ψ_1 and ψ_2. The maxima of T occur when the denominator of Eq. (2.6) is at its minima, that is,

$$2\psi_2 = 2\beta + \phi_b + \phi_s = 2m\pi \tag{4.1}$$

where m is an integer. Equation (4.1) states that the resonance occurs if total phase shift in the cavity are multiples of 2π, where standing waves exist in the cavity.

Table 4.1 The measured free spectral range and quality factors, along with the fitted SiO_2 and Au film thicknesses based on the measurement results at an angle of incidence of 10°

Sample No.	Free spectral range $\Delta\nu$ (cm^{-1})	SiO_2 thickness d_c (nm)	Au film thickness d_f (nm)	Quality factor Q at the 1st resonance	Quality factor Q at the 2nd resonance
1	5050	622	21	49.5	21.7
2	5576	553	20	34.4	13.9
3	5587	559	30	53.2	25.3

As mentioned earlier, the absorptance of the bottom Au layer is $\alpha_s = T$ because it is opaque. The multiple reflections result in strong absorption in the top Au film as well, though at a nearby frequency. The absorptance of the top Au film is $\alpha_f = 1 - R - T$ because the SiO_2 layer is nonabsorbing in the spectral range of interest. The absorptance of the top Au film and bottom Au layer is shown in Fig. 4.2, which was calculated based

on the fitting parameters for Sample 1. Interestingly, the absorptance α of the Fabry-Perot structure has a minimum on the right of the maximum, this explains why the reflectance *R* exhibits a maximum on the right of the minimum and the reflectance dip is asymmetric, as can be seen from Fig. 4.1. One can see from Eq. (2.5) that the reflectance minimum is determined by its numerator at the frequency that satisfies $\psi_1 = (m+1/2)\pi$. It can be shown that the phase difference between ψ_1 and ψ_2 is close to $\pi/2$. Hence, the reflectance minimum occurs near the resonance condition given in Eq. (4.1). It should be noted that while there exist minima in T at frequencies where $\psi_2 = (m+1/2)\pi$, it does not significantly affect α (or *R*) as can be seen from Fig. 4.2. As a matter of fact, away from the resonance condition, very little of the incident energy can reach the bottom Au layer; subsequently, the reflectance of the Fabry-Perot resonator is essentially the same as the reflectance when the SiO_2 layer is semi-infinite; that is, $R \approx R_a = r_a r_a^*$.

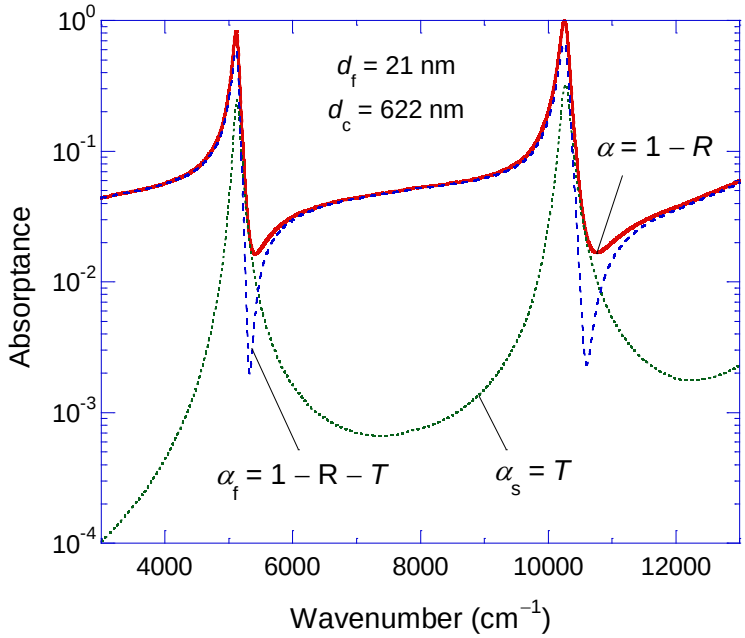

Figure 4.2 Absorptance spectra calculated based on the geometric parameters for Sample 1 ($d_c = 622\,\text{nm}$ and $d_f = 21\,\text{nm}$) for unpolarized waves at $\theta_i = 10°$.

The existence of reflectance dips suggests that the Fabry-Perot resonators can be used to construct coherent emission sources, since $\varepsilon'_\lambda = 1 - R$. A measure of the sharpness of the emissivity peak, or the reflectance dip, is the quality factor defined as $Q = \Delta\nu/\delta\nu$ for Fabry-Perot resonance cavities, where $\delta\nu$ is the full width at half maximum, or minimum [45]. The Q factors for 10 ºangle of incidence at the two resonance frequencies are tabulated in Table 4.1 for each sample. Generally speaking, the peak width tends to broaden towards higher frequencies. This is why the quality factor at the second resonance frequency is about half of that at the first resonance frequency. Because Sample 2 has a thinner SiO_2 layer, the resonance frequencies increase, resulting in a lower Q factor for Sample 2. Samples 2 and 3 have similar SiO_2 thickness but Sample 3 has a thicker Au film. It can be seen that the Q factor is enhanced with increasing Au film thickness. However, the peak emissivity for Sample 3 at the first resonance frequency is not as high as can be seen from Fig. 4.1.

The effect of Au film thickness on the peak emissivity is further investigated near the resonance frequencies. The absorptance at the resonance wavenumbers around 5500 cm^{-1} and 11000 cm^{-1} is calculated for different film thickness d_f for given d_c = 560 nm at $\theta_i = 10°$. Note that the exact resonance frequency will vary somewhat with d_f. As shown in Fig. 4.3, there exist thickness values where the absorptance peak is maximized. However, the maxima of α_f, α_s, and α do not occur at the same d_f. It is interesting to see that more energy is absorbed by the thin Au film than by the bottom Au layer. For the first resonance, the spectral-directional emissivity is close to unity when d_f = 12.5 nm. In this case, about 80% of the energy is absorbed by the Au film. For the second resonance near 11000 cm^{-1}, a close-to-unity emissivity peak is achieved when d_f = 25 nm. In this

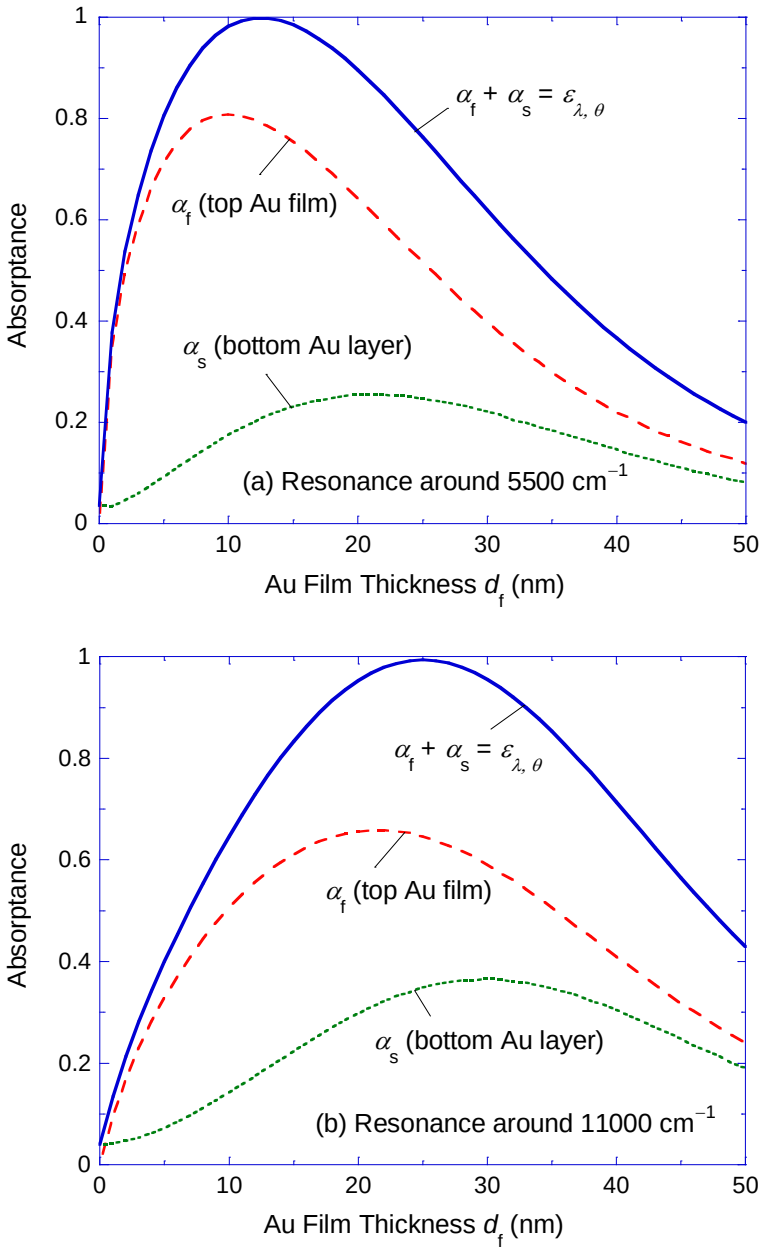

Figure 4.3 Absorptance for unpolarized waves at $\theta_i = 10°$, with respect to the top Au film thickness d_f, by the thin Au film and by the opaque Au layer for d_c = 560 nm at the resonance wavenumber: (a) around 5500 cm^{-1}; (b) around 11000 cm^{-1}.

case, about 60% of the energy is absorbed by the Au film. Because the deposited Au film thickness for the three samples is closer to 25 nm than 12.5 nm, the first reflectance dip is more sensitive to the Au film thickness than the second dip as seen from Fig. 4.1.

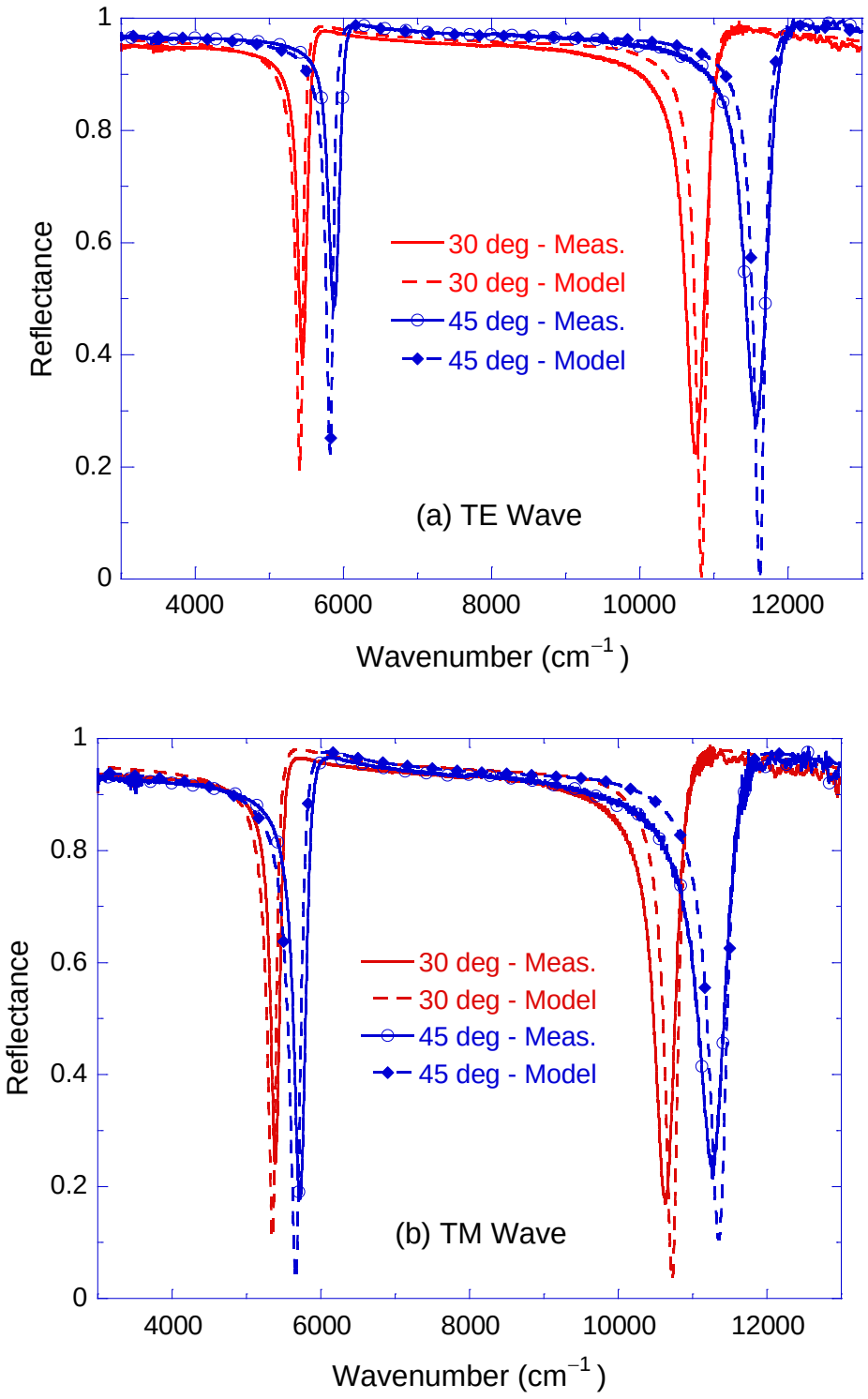

Figure 4.4 Spectral reflectance of Sample 1 in the near-IR spectral region at 30 ° and 45 ° incidence, respectively: (a) TE wave; (b) TM wave.

The spectral reflectance of the Fabry-Perot resonator at other incidence angles is also investigated. Figure 4.4 shows the measurements of Sample 1 at 30 °and 45 °angles of incidence for TE and TM waves, respectively. The model prediction based on the previously obtained thicknesses d_c and d_f for Sample 1 agree with the experiments well. However, the predicted reflectance minima are much lower than those measured. This may be due to partial coherence of the FT-IR spectrometer caused by beam divergence [102]. The resonance frequencies shift toward high frequencies for both polarizations. This is mainly due to the $\cos\theta_c$ terms in the phase shift β. The free spectral range $\Delta\nu$ is tabulated in Table 4.2 for both the measurement and prediction for each case. The relative difference between the measured and predicted $\Delta\nu$ is within 2.5%, suggesting that the fitting results are pretty reliable. Similar to the resonance frequencies, $\Delta\nu$ also increases with the angle of incidence. It can also be seen that toward large incidence angles, $\Delta\nu$ is larger for TE wave than for TM wave; this is due to the phase shifts associated with the reflection at the cavity boundaries.

Table 4.2 Comparison of the free spectral range $\Delta\nu$ (cm^{-1}) obtained from the spectral reflectance measurement and from the model at θ_i = 10 °, 30 °, and 45 °for Sample 1

	$\theta_i = 10°$	30 °TE	30 °TM	45 °TE	45 °TM
Experiment $\Delta\nu$ (cm^{-1})	5050	5306	5246	5692	5546
Model $\Delta\nu$ (cm^{-1})	5142	5422	5376	5798	5688
Relative difference	1.8%	2.1%	2.4%	1.8%	2.5%

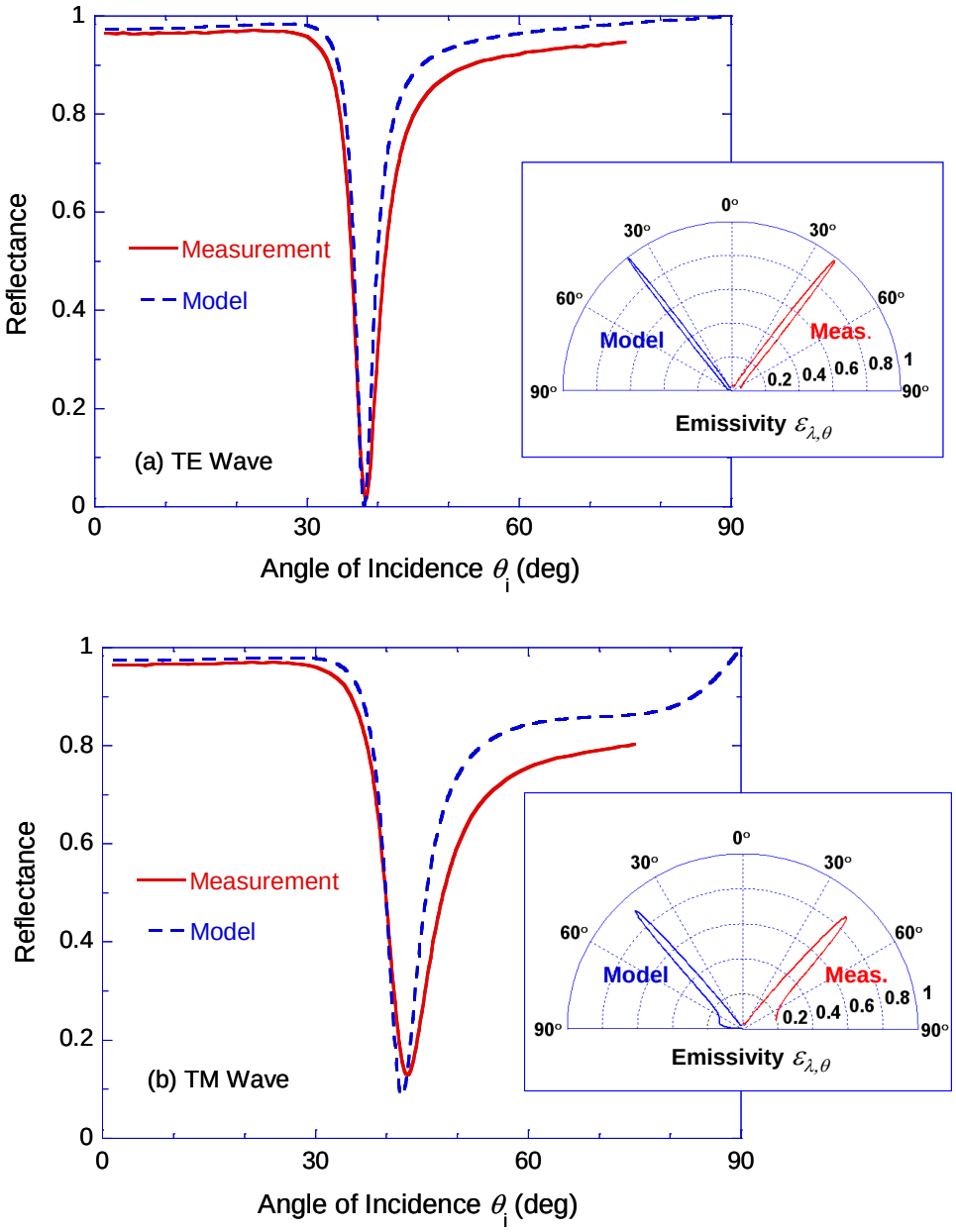

Figure 4.5 Spectral reflectance of Sample 1 at λ = 891 nm: (a) TE wave; (b) TM wave. The insets show the polar plots of the spectral emissivity, $\varepsilon'_\lambda = 1 - R$.

Besides temporal coherence demonstrated by the spectral reflectance measurement, the spatial coherence for Sample 1 is shown in Fig. 4.5 by the angle-resolved reflectance measurement at λ = 891 nm. Reflectance dips are clearly observed at

the resonance polar angle: $\theta_0 = 38.4°$ for the TE wave and $43.0°$ for the TM wave. The polarization-dependent reflection and transmission coefficients at the boundaries are responsible for the variation of resonance angle between the two polarizations. The spectral-directional emissivity, calculated from $\varepsilon'_\lambda = 1 - R$ is shown as insets, where the right side is from the measurement and the left side is from model calculation using the same fitting parameters for Sample 1. Contrary to the FT-IR measurement at large incidence angles, due to the highly collimated laser beam and the high angular resolution, the reflectance dips or emissivity peaks match very well with those predicted. The relative difference between the measurement and model in terms of the resonance angle is within 2%. It can also be observed that the resonance is much sharper for TE waves than for TM waves. The narrow angular lobes of the spectral-directional emissivity shown in the polar plots clearly demonstrate spatial coherence of the considered Fabry-Perot resonance cavity. The coherence length, defined as $L_{\text{coh}} = \lambda / \left(\pi \Delta\theta \cos\theta_{\text{c}}\right)$, is used as a measure of the spatial coherence [102,103]. Note that $\Delta\theta$ is the FWHM of the emissivity peak, and the estimated $\Delta\theta$ from the directional measurement is $4.8°$ and $9.8°$ for TE and TM waves, respectively. Thus, the calculated coherence length is 4.85λ and 2.54λ for TE and TM waves respectively, suggesting that TE waves have better spatial coherence than TM waves for the considered Fabry-Perot resonance cavity structure.

To further investigate the frequency and directional dependence of the emissivity of the proposed structure, the contour plots of the calculated emissivity based on the fitting parameters of Sample 1 are shown in Fig. 4.6 for TE and TM waves. In Fig. 4.6, darker colors represent lower emissivity, whereas brighter colors correspond to higher emissivity. The multiple emissivity peaks due to the resonance can be clearly seen as the

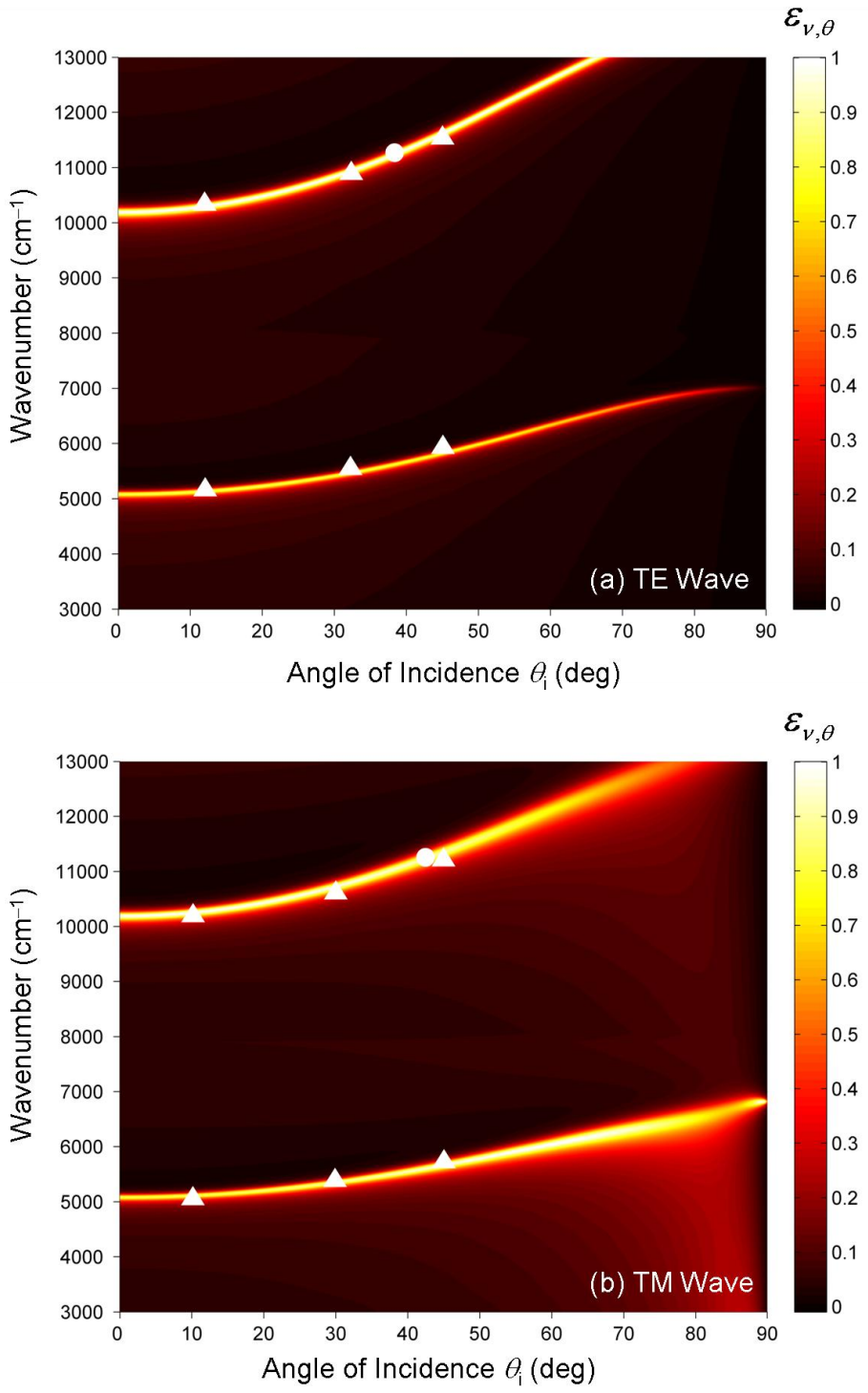

Figure 4.6 Contour plots of the spectral-directional emissivity of the considered Fabry-Perot resonator with the fitting parameters of Sample 1: (a) TE wave; (b) TM wave. The triangles represent the reflectance dips measured by the FT-IR spectrometer, while the circles indicate the reflectance dips obtained by the laser scatterometer.

brightest curves called resonance bands, which exhibit strong spectral and directional selectivity. For comparison, the measurement results of Sample 1 are also plotted as triangles (FT-IR) and circles (TAAS), and very good agreement between the measurement and model can be seen.

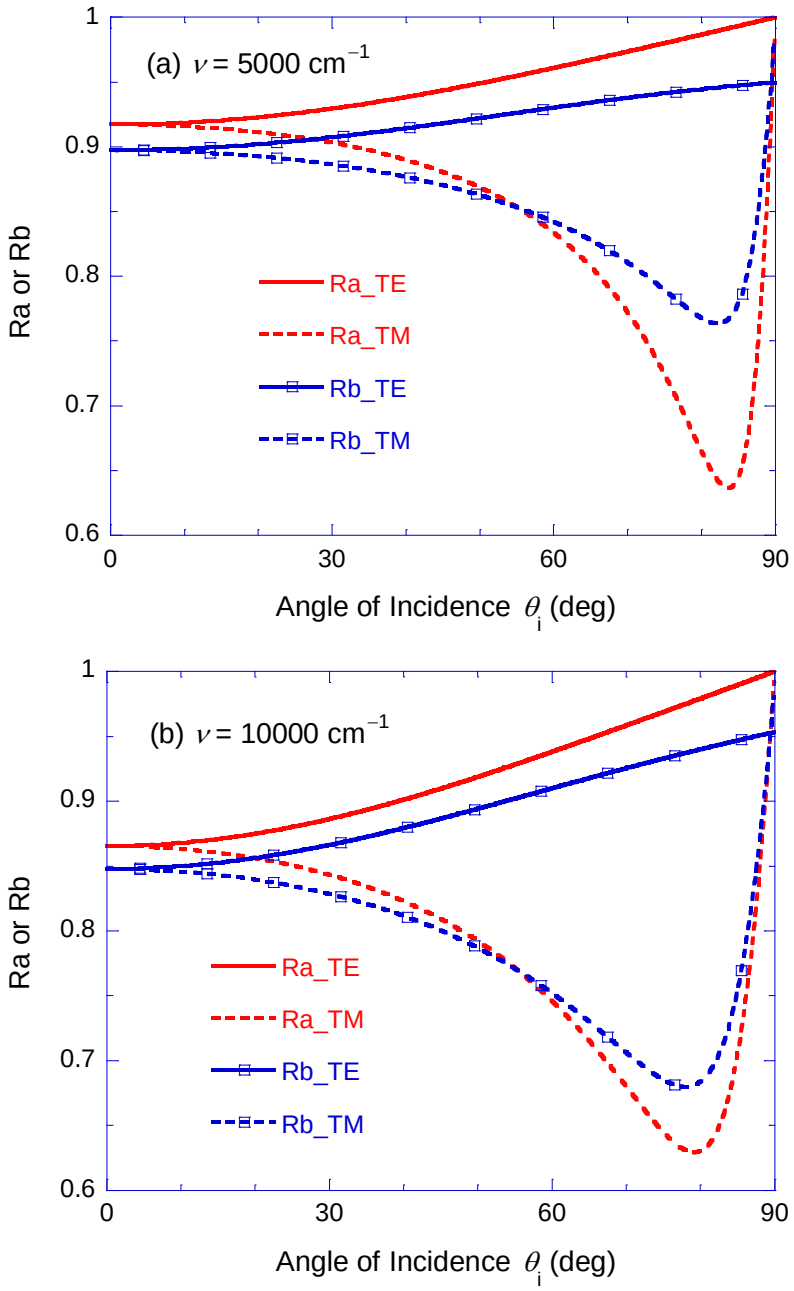

Figure 4.7 Calculated reflectance for each polarization at the interface as a function of incidence angle for Au film thickness of 21 nm: (a) at 5000 cm^{-1}; (b) at 10000 cm^{-1}.

As the incidence angle increases, the resonance bands are getting narrower for TE waves but wider for TM waves. Besides, there are regions beyond the resonance bands where the emissivity for TM waves is noticeably larger, especially at large incident angles. This is due to polarization-dependent reflectivity at each interface since larger reflectivities at the cavity boundaries would result in sharper resonance peaks [1,45]. To further explain this, the reflectivities, $R_a = r_a r_a^*$ and $R_b = r_b r_b^*$, are plotted in Fig. 4.7 as functions of the incidence angle θ_i for both polarizations at $\nu = 5000$ cm^{-1} and $\nu = 10000$ cm^{-1}, respectively. While the reflectivity $R_s = r_s r_s^*$ between SiO_2 and the bottom Au layer is also important, it does not change very much, since the refraction angle inside SiO_2 is limited to approximately 44 °when $\theta_i = 90°$. At the air-Au film and SiO_2-Au film interfaces, there exist large differences in the reflectivity between TE and TM waves at incidence angles greater than 60°. While the reflectance for TE wave increase monotonically with the incidence angle, the reflectance for TM wave is reduced significantly as the incidence angle increases. This is why the resonance bands are much sharper for TE waves than for TM waves. The broader resonance bands of TM waves result from the lower R_b; on the other hand, the reduction of R_a of TM waves at large incidence angles is responsible for the increase in the emissivity outside the resonance bands. It can be seen by comparing Figs. 4.7(a) with 4.7(b) that the reflectivity (R_a or R_b) for given polarization and incidence angle is relatively larger at lower frequency, which can explain why the resonance band at the first resonance (lower frequency) is narrower than that at the second resonance (higher frequency) shown in Figs. 4.1, 4.4,

and 4.6. Since a thicker Au film will result in higher R_a or R_b, this is why Sample 3 has a smaller $\delta\nu$ than Sample 2.

4.3 Direct Emittance Measurements at Elevated Temperatures

To practically realize high-temperature coherent emitters based on the Fabry-Perot structures, it is imperative to investigate how the emittance spectrum will change with temperature, especially at elevated temperatures, as well as other issues such as chemical stability and thermal stress. The high-temperature emissometry facility was employed to measure the spectral emittance of a Fabry-Perot cavity resonator at 600 K and 800 K for different emission angles and polarization states [94]. Modifications were made to the sample structure for improved chemical stability over diffusion and oxidation. The emittance spectra at room temperature were indirectly obtained by measuring the spectral reflectance using a Fourier-transform infrared (FT-IR) spectrometer. Theoretical modeling was carried out to help understand how temperature affects the emission characteristics of the Fabry-Perot structure.

The fabrication process is similar to that described earlier using thin-film deposition techniques. PECVD was used to grow the SiO_2 cavity, while an electron-beam evaporator with different sources was used to thermally deposit the metallic layers under the vacuum condition. Several modifications were made to the previous design to ensure high-temperature stability, as described in the following.

The structure of the fabricated Fabry-Perot cavity resonator is depicted in Fig. 4.8. For emittance measurements, wavevector **K** is reversed to indicate the angle of emission with respect to the surface normal. It should be noted that the radiative properties are

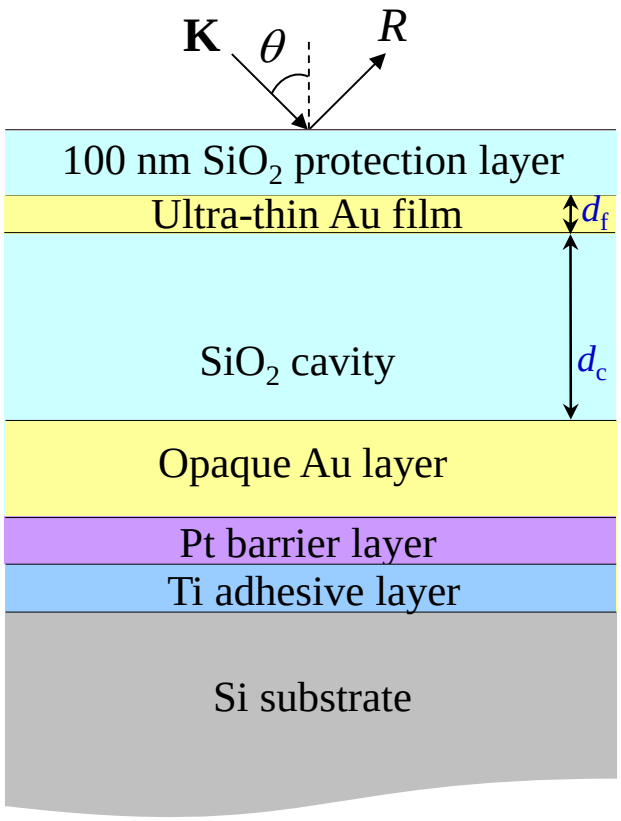

Figure 4.8 Schematic of the fabricated Fabry-Perot cavity resonator (not to scale), indicating the directions for indirect measurements. For direct emittance measurement, the direction of emission follows the reversed wavevector **K**.

independent of the azimuthal angle. The multilayered films were deposited on a double-side polished Si wafer whose thickness is about 400 μm. The polished front side is required to create the Fabry-Perot structures and the polished back side helps reduce TCR between the sample and the copper disk. After depositing a 30-nm Ti adhesive layer, a 40-nm Pt layer was deposited as a barrier layer to prevent the diffusion of Au into Si at temperatures higher than 360 ℃. The existence of the Pt layer is crucial to ensure that the structure stays intact at high temperatures. A 200-nm Au layer was then deposited in the same e-beam evaporator, by rotating the sources without breaking the vacuum. The peak

wavelengths of the emittance spectrum are mainly determined by the thickness of the cavity. In order to obtain high signal-to-noise ratio in the thermal emission measurement, the cavity thickness d_c was designed to be around 1.5 μm for the emittance peak to lie between 3.5 and 5 μm, where the blackbody emission peak occurs for temperatures from 600 to 800 K according to Wien's displacement law. On the other hand, the amplitude of the peak emittance is sensitive to the thickness of the top thin Au layer d_f and it was optimized to be around 10 nm to maximize the emission peak. To prevent Au film from degradation in the ambient (even with nitrogen gas purge, it cannot completely remove the oxygen and other traces in air), a 100-nm SiO_2 layer was deposited on top of the thin Au film. Since the SiO_2 films were deposited with a PECVD system, the sample had to be transferred between the two systems. A number of tests were performed to come out with the present design that appears to be stable at temperatures up to 1000 K even in ambient air. The thickness of the SiO_2 cavity was measured *ex situ* with a reflectometer (Nanometrics NanoSpec 3000) to be 1550 nm $\pm$ 50 nm.

Figure 4.9 depicts the emittance of the Fabry-Perot cavity resonator sample for near-normal direction (10°) at 294 K and that for normal direction at 600 K and 800 K from both measurement and model prediction. Note that the results at 600 K from the emissometry measurement are limited from 1800 to 4000 cm^{-1} due to the cut-off frequencies of the InSb detector. There exist two emission peaks which are located according to the approximate Fabry-Perot equation, $\nu_m^{(q)} = q/(2n_c d_c)$, where n_c (≈ 1.5) is the refractive index of SiO_2 and q is the order of the cavity resonance. The predicted emission peaks for $d_c = 1.55\ \mu$m are at about 2200 and 4400 cm^{-1}, respectively. The actual resonance conditions also depend on the phase shifts at the interfaces and will be

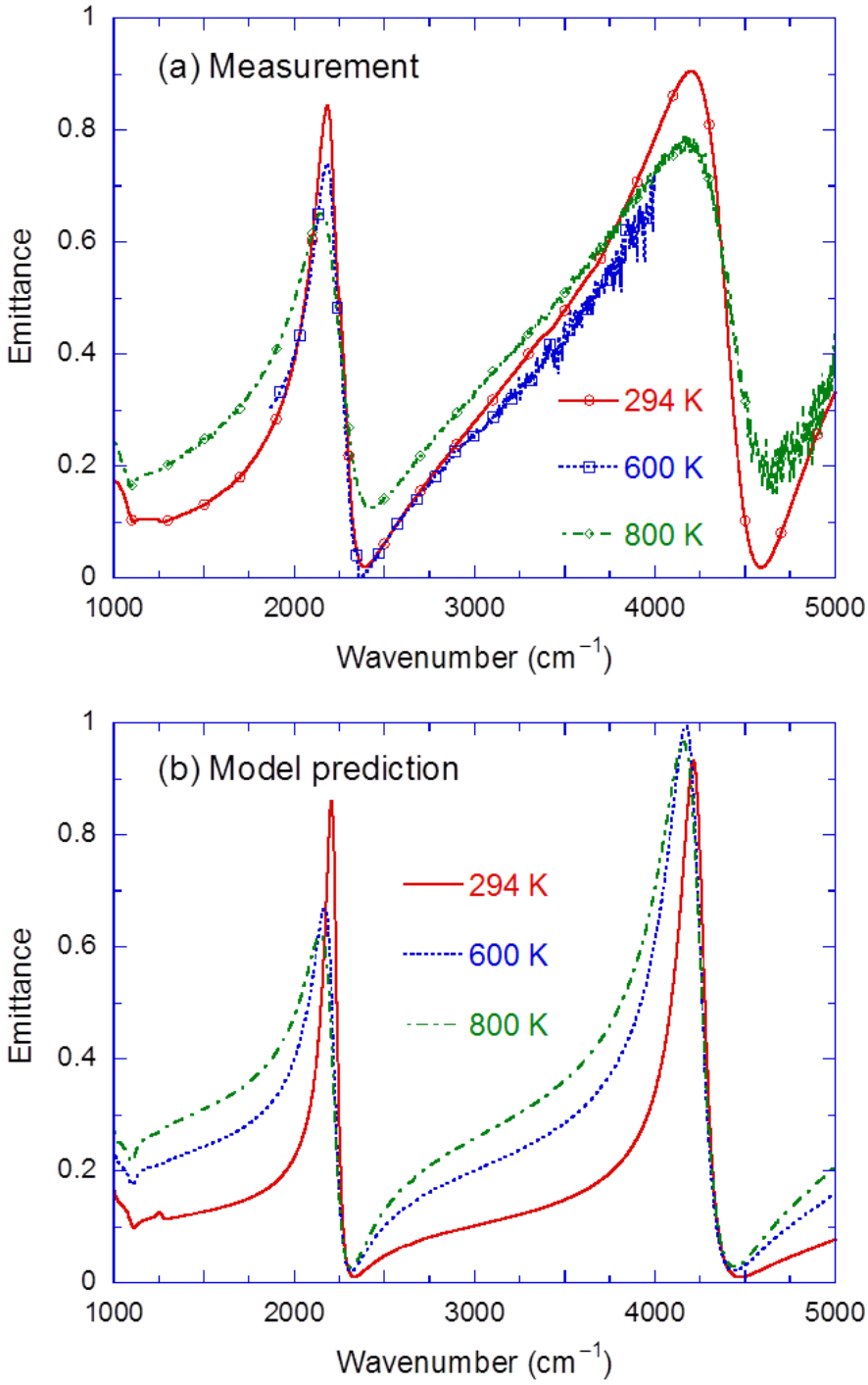

Figure 4.9 The emittance spectra of the Fabry-Perot cavity resonator sample for 10 ° at 294 K and for normal direction at 600 K and 800 K from (a) measurement and (b) modeling. The emittance was directly measured at 600 K with an InSb detector and 800 K with a DTGS detector.

discussed later. Both the experiment and prediction demonstrate the two emission peaks, whose frequencies vary somehow with temperature, indicating the spectral selectivity of thermal emission. From the experimental results, it can be seen that the width of the emittance peaks is broadened and peak value is lowered at elevated temperatures. For example, the emittance maximum at the first peak (q = 1) is 0.845 at room temperature, and decreases to 0.742 at 600 K and 0.652 at 800 K. Besides, the peak location tends to shift toward lower frequencies from 2183 cm^{-1} at 294 K to 2149 cm^{-1} at 800 K.

A theoretical model considering the temperature-dependent properties is developed to better understand the temperature effect. The matrix formulation method was used to calculate the spectral directional reflectance of a multilayered structure as well as the emittance according to Kirchhoff's law [1]. Since the 200-nm Au film is essentially opaque within the frequency range of interest, the Pt and Ti layers and the Si substrate have no influence on the reflectance or emittance of the structure. The calculation was thus simplified by assuming the thick Au layer to be semi-infinite. The frequency-dependent optical constants of SiO_2 were taken from the tabulated data in Ref. [83], and were assumed temperature-independent. Similar assumptions were used previously and found to be reasonable [104]. For the Au film, the Drude model was used to describe its dielectric function as

$$\varepsilon_{\mathrm{Au}}(\nu) = \varepsilon_1 + i\varepsilon_2 = 1 - \frac{\nu_{\mathrm{p}}^2}{\nu^2 + i\Gamma\nu} \tag{4.2}$$

where ν_{p} is the plasma frequency and Γ is the scattering rate [1]. The plasma frequency is proportional to the square root of the electron number density, and was taken as 1.37×10^{16} rad/s (i.e., 72700 cm^{-1}) for bulk Au. The bottom Au layer can be treated as a

bulk; however, ultra-thin Au films from the thermal evaporation process are usually not continuous. This suggests a smaller electron number density, resulting in a lower effective plasma frequency [105]. Thus, the plasma frequency for the 10-nm Au film was estimated to be 1×10^{16} rad/s in the calculation. To better approximate the losses in the thermally deposited thick Au film, its scattering rate at room temperature was obtained by fitting the imaginary part of the dielectric function ε'' which accounts for the losses with the tabulated data from Palik [83]. The scattering rate for the bulk Au at room temperature was obtained as 7.31×10^{13} rad/s , which agrees with the value in the literature [106]. On the other hand, additional losses due to the electron-boundary scattering must be considered for the 10-nm Au film, since the film thickness is comparable to the electron mean free path and there also exist grain boundaries. The scattering rate for the ultra-thin Au film at room temperature was taken as 1.10×10^{14} rad/s , which is 50% higher than the value for the bulk. Furthermore, the plasma frequencies were assumed independent of temperature, whereas the scattering rates were estimated by a linear relationship, i.e., $\Gamma(T)/\Gamma_0 = T/294$, where Γ_0 is the scattering rate at 294 K, because the electron-phonon scattering rate increases linearly with temperature above room temperature [1,107].

The predicted normal emittance at different temperatures is shown in Fig. 4.9(b). The peak location can be determined by Eq. (4.1) at resonances. Note that the phase shift β in the dielectric cavity depends little on temperature. Interestingly, the emittance peaks of the designed structure show asymmetric shapes, comparing with the nearly symmetric transmittance peaks of the conventional Fabry-Perot cavities which are widely used in interferometers [45]. This is due to the different phase shifts involved respectively in the

emittance (or reflectance since $\varepsilon'_\nu = 1 - R$) and transmittance, rather than due to the structural asymmetry. The asymmetric reflectance dips or absorptance peaks of the asymmetric Fabry-Perot structures were also observed and discussed previously at room temperature measurements. The predicted emittance spectra for the first peak exhibit peak broadening, shifting, and reduction as temperature increases. The temperature effect on the emittance can be understood by the increased scattering in the Au films. Additional calculation indicates that the emittance peak is more sensitive to the scattering rate of the thin Au film than that of thick Au layer, since more losses occur within the ultra-thin layer [63]. From the modeling, the shift of the emittance peak location with higher temperatures is apparent, and can be explained by the change of phase angles ϕ_b and ϕ_s since both r_b and r_s vary with temperature.

The trend agrees well with the experimental observation, however, the measured spectra contain broader peaks. This may be due to a number of reasons such as the inhomogeneity of the thin Au film, surface roughness, as well as beam divergence. More interestingly, the first peak at 294 K almost has the same width with the one at 600 K from the measurements, but the calculation shows the increasing scattering rate at higher temperatures would broaden the peak. This indicates some mechanisms which may reduce the scattering at high temperatures during the experiment, such as the annealing effect which enlarges the grain size in the ultra-thin film and makes the film smoother. It appears that the peak shift is not as clear in the experiments due to partial coherence. The calculation also suggests peak broadening and shifting with higher temperatures at the second resonance peak, similar to the temperature effect on the first peak. It should be noted that, the increasing temperature will not necessarily cause the diminishing of the

emittance peak. At the second resonance peak, the predicted peak maximum increases when temperature is changed from 294 K to 600 K. In addition, the measurement results show much broader peaks than the calculation at the second resonance peak, which is mainly due to the partial coherence effect resulting from the inhomogeneity of the ultra-thin Au film. As observed previously, the partial coherence effect tends to be stronger at shorter wavelengths [108]. In fact, the peak broadening may be beneficial for energy system such as TPV emitters in which a sharp emission peak is not preferred due to limited radiative energy and low throughput [10].

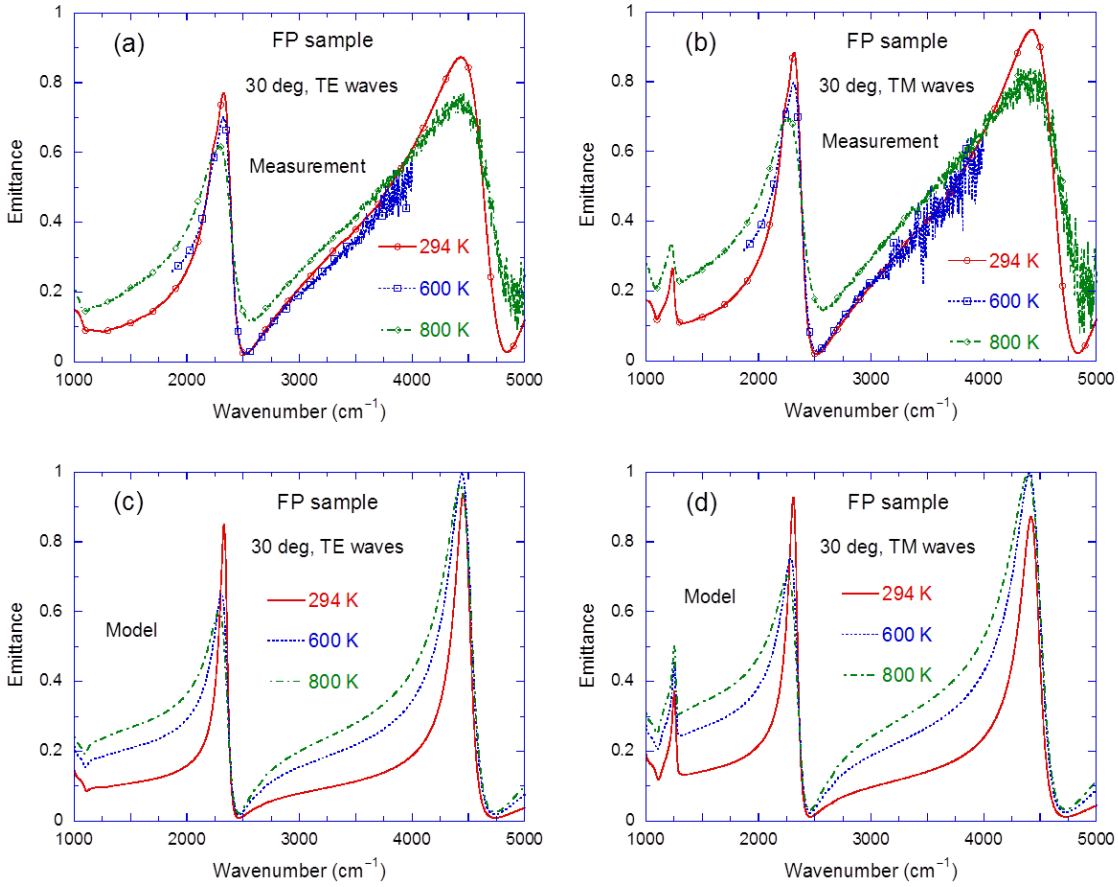

Figure 4.10 The emittance of the Fabry-Perot cavity resonator sample at 30 °. (a) Measurement for TE waves; (b) Measurement for TM waves; (c) Prediction for TE waves; (d) Prediction for TM waves.

The emittance of the Fabry-Perot cavity resonator sample was also studied at 30 ° emission angle with different temperatures. Figures 4.10(a) and 4.10(b) show the measurement results for TE and TM waves, respectively, and emittance peaks were observed as well for both polarizations. Clearly, when the temperature increases from 294 K to 800 K, the emittance peaks become broader and the resonance frequencies also slightly shift to lower wavenumbers. The resonance frequencies are higher than those for normal direction, due to the cosine term in the phase shift. From 0 ° to 30 °, the emittance maximum for TM waves increases but that for TE waves decreases. Take 800 K as an example. The emittance peaks at 2149 cm^{-1} with a maximum of 0.652 at normal incidence, while the maximum at 30 ° is 0.617 at 2299 cm^{-1} for TE waves and 0.695 at 2270 cm^{-1} for TM waves, respectively. The change of the resonance frequency with emission angles indicates the selectivity of spatial direction, i.e., spatial coherence. Figures 4.10(c) and 4.10(d) present the calculated emittance for both polarizations at 30 ° with the same parameters used for the normal direction. The peak broadening with increasing temperature can be seen from the modeling, which arises from the increased scattering rates of Au films. The peak maximum also decreases as the temperature increases at the first resonance but slightly increases at the second resonance.

Interestingly, an additional emittance peak can be seen at 1250 cm^{-1} only for TM waves, as shown in Figs. 4.10(b) and 4.10(d). To help understand the occurrence of this peak, the emittance at room temperature was calculated for TM waves at 30 ° when $d_c \to \infty$, that is, the thick Au layer and Si substrate are replaced with a semi-infinite SiO_2 layer. This structure contains the top SiO_2 layer, the thin Au film, and a semi-infinite SiO_2 medium, which is labeled as the SiO_2-Au-SiO_2 structure. Figure 4.11(a) compares

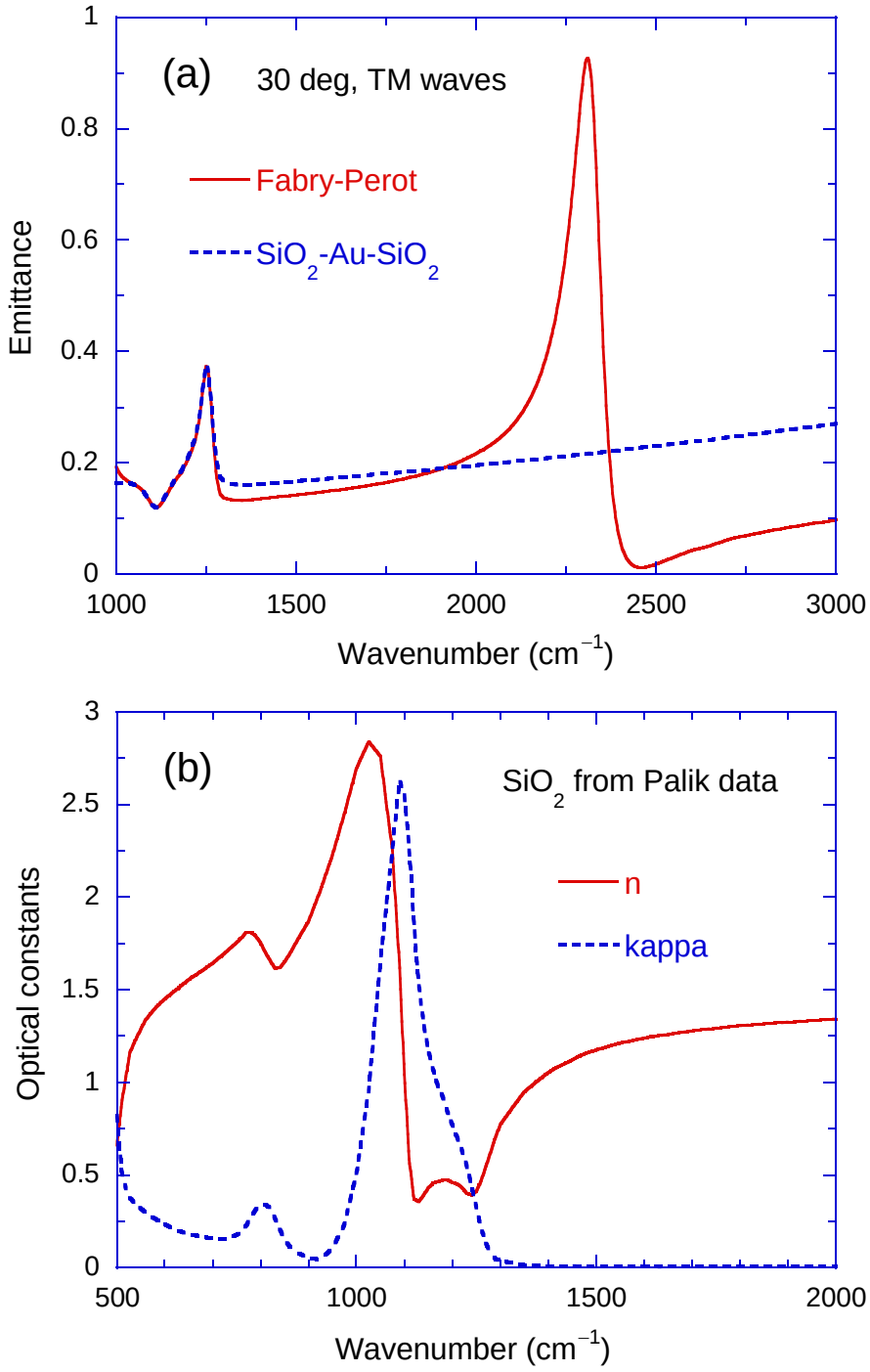

Figure 4.11 (a) Comparison of the calculated emittance of a three-layer structure with SiO_2-Au-SiO_2 (semi-infinite) and the considered Fabry-Perot structure at 30 deg for TM waves; (b) The optical constants of SiO_2 from Palik [83].

the calculated emittance for the SiO_2-Au-SiO_2 structure with that for the Fabry-Perot structure from 1000 to 3000 cm^{-1}. It can be seen that the Fabry-Perot resonance around 2270 cm^{-1} disappears for the SiO_2-Au-SiO_2 structure, but the peak at 1250 cm^{-1} exists in both structures. Additional calculations show that when the emission angle increases, this peak location shifts slightly and the peak amplitude increases to a maximum when the emission angle reaches 73 °. Therefore, the emission peak at 1250 cm^{-1} is attributed to a cancelling effect of the reflection coefficients at the air-SiO_2 and SiO_2-Au interfaces, as a result of the unique optical constants of SiO_2 in this region. In addition, an emission dip can be seen around 1100 cm^{-1} for both normal direction and 30 ° measurements regardless of the polarization state. The cause of this dip is the frequency-dependent optical constants of the SiO_2. Figure 4.11(b) plots the refractive index n and extinction coefficient κ of SiO_2 from Palik [83]. Due to the phonon absorption, the extinction coefficient κ peaks around 1100 cm^{-1}, where $\kappa >> n$. Therefore, only the SiO_2 near the surface emits due to the small penetration depth, which results in a reduction of emittance.

After the sample was heated to 800 K, some cracks occurred in the Fabry-Perot sample as shown in Fig. 4.12(a), which is an image from a 3D confocal microscope (Olympus LEXT OLS4000). Those cracks are spaced about half a millimeter apart and intersect with each other. The formation of the cracks was due to the excess thermal stress induced by the coefficient of thermal expansion (CTE) mismatch among different materials. The CTEs at room temperature are 2.5×10^{-6} 1/K for Si, 0.4×10^{-6} 1/K for SiO_2, and 14×10^{-6} 1/K for Au, respectively [109]. To address whether or not the cracks degrade the sample's performance as a selective emitter, the emittance of the Fabry-Perot sample was indirectly measured at room temperature after cooling. Figure 4.12(b) compares the

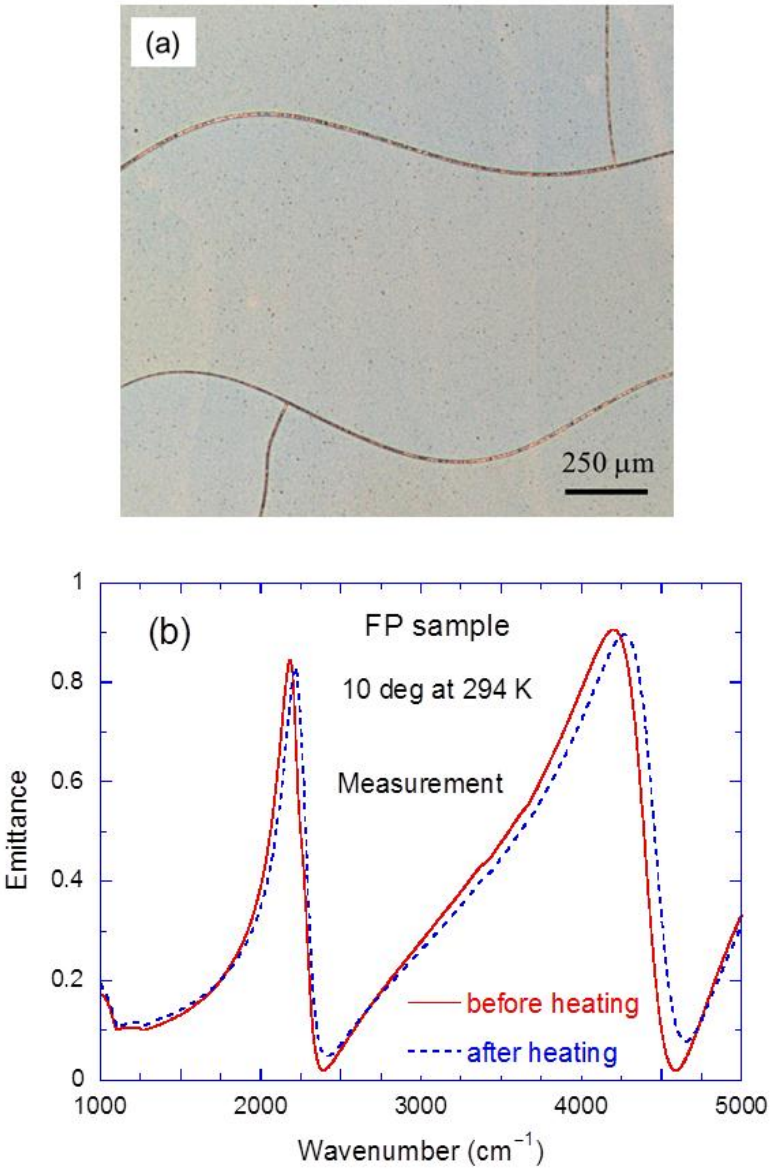

Figure 4.12 (a) An image of the cracks in the Fabry-Perot cavity resonator sample after the heating at 800 K from a 3D confocal microscope; (b) Measured emittance (10 °) of the Fabry-Perot sample at room temperature before and after heating up to 800 K.

near-normal emittance at 300 K before and after the heating. It can be seen that the coherent emission characteristics remain after heating, but the peaks slightly shift toward higher frequencies. This should be mainly due to the annealing effect on the material properties rather than cracking.

4.4 Generalized Kirchhoff's Law

The room- and high-temperature measurements have clearly shown that the temporal and spatial coherence characteristic of the Fabry-Perot resonant cavity as a coherent emission source. However, in practice under high temperature environment, coherent sources may endure nonuniform temperature distribution. Therefore, whether or not the indirect method from Kirchhoff's law $\varepsilon'_\lambda = 1 - R$ is still valid under such a condition must be clarified.

To derive the spectral directional emissivity from each layer at a uniform temperature T_j shown in Fig. 2.2, let us start with the spectral heat flux given in Eq. (2.10) from the direct method in Section 2.2 [110]. Due to $\beta = (\omega/c)\sin\theta$, the spectral heat flux can be re-written as

$$q''_{\omega,j} = \frac{\omega^2}{2\pi^3 c^2}\Theta\left(\omega, T_j\right)\int_0^{2\pi} d\phi \int_0^{\pi/2} Z_j\left(\omega,\beta\right)\cos\theta\sin\theta d\theta \tag{4.3}$$

where ϕ is the azimuthal angle, and $\sin\theta d\theta d\phi = d\Omega$ is the differential solid angle. Note that the spectral heat flux can also be obtained by integrating the spectral intensity I_ω over the hemisphere, that is, $q''_\omega = \int_0^{2\pi} d\phi \int_0^{\pi/2} I_\omega \cos\theta\sin\theta d\theta$. Hence, the spectral intensity from the *j*th layer to vacuum can be extracted by comparison of these two expressions, giving

$$I_{\omega,j}\left(\omega,\theta\right) = \frac{\omega^2}{2\pi^3 c^2}\Theta\left(\omega, T_j\right) Z_j\left(\omega,\beta\right) \tag{4.4}$$

in watts per square meter per unit frequency interval (rad s^{-1}) per unit solid angle (sr), i.e., [W m^{-2} s rad^{-1} sr^{-1}]. The spectral directional emissivity of the *j*th layer can be defined as the ratio of the spectral intensity to that of a blackbody at the same temperature T_j, viz.

$$\varepsilon'_{\omega,j} = \frac{I_{\omega,j}\left(\omega,\theta\right)}{I_{\omega,\mathrm{b}}\left(\omega,T_j\right)} = 4Z_j\left(\omega,\beta\right) \tag{4.5}$$

where $I_{\omega,\mathrm{b}}\left(\omega,T_j\right) = \omega^2\Theta\left(\omega,T_j\right)/8\pi^3c^2$ is the blackbody intensity for one polarization in vacuum.

On the other hand, by using the transfer matrix method introduced in Section 2.2, the absorptivity for the *j*th layer at a uniform temperature T_j can be obtained as well. Similar to Eq. (2.18), the amplitudes of the forward and backward waves in the *j*th layer can be related to those in the incident medium through

$$\begin{pmatrix} A_1 \\ B_1 \end{pmatrix} = \mathbf{Q}\begin{pmatrix} A_j \\ B_j \end{pmatrix} \text{ where } \mathbf{Q} = \prod_{l=1}^{j-1}\mathbf{P}_l\mathbf{D}_l^{-1}\mathbf{D}_{l+1} \tag{4.6}$$

From Eq. (2.19), we know $r = B_1/A_1$, so the amplitudes A_j and B_j in the *j*th layer can be related to A_1 by

$$A_j = C_{j1}A_1, \text{ where } C_{j1} = \mathbf{Q}_{11}^{-1} + r\mathbf{Q}_{12}^{-1} \tag{4.7a}$$

and

$$B_j = C_{j2}A_1, \text{ where } C_{j2} = \mathbf{Q}_{21}^{-1} + r\mathbf{Q}_{22}^{-1} \tag{4.7b}$$

The spectral directional absorptivity of *j*th layer $\left(j = 2,3,...,N-1\right)$ can be expressed as

$$\alpha'_{\omega,j} = \frac{S_{jz}\left(z_{j-1}\right) - S_{jz}\left(z_j\right)}{S_{\mathrm{in}}} = \frac{1}{\gamma_1}\mathrm{Re}\left\{\frac{\gamma_j^*}{\mu_j^*}\left[\zeta_1\left|C_{j1}\right|^2 - \zeta_2\left|C_{j2}\right|^2 - 2i\,\mathrm{Im}\left(\zeta_3 C_{j1}C_{j2}^*\right)\right]\right\} \tag{4.8}$$

where $S_{\mathrm{in}} = \dfrac{\gamma_1}{2\omega\mu_0}A_1A_1^*$ is the incident radiant flux in the z direction, and $\zeta_1 = 1 - e^{2\mathrm{Re}\left(i\gamma_j\right)d_j}$, $\zeta_2 = 1 - e^{-2\mathrm{Re}\left(i\gamma_j\right)d_j}$ and $\zeta_3 = 1 - e^{i2\mathrm{Im}\left(i\gamma_j\right)d_j}$. Note that $\alpha'_{\omega,N} = T'_\omega$. For TM waves, Eqs. (4.6) through (4.8) are still applicable by interchanging μ to ε. It

should be noted that $\alpha'_{\omega,j}$ depends on the angle of incidence, even though only the *z*-component of the Poynting vector appears Eq. (4.8). The absorptance of the multilayered structure is

$$\alpha'_{\omega} = \sum_{j=2}^{N-1} \alpha'_{\omega,j} = 1 - T'_{\omega} - R'_{\omega} \tag{4.9}$$

Only if all media are at the same temperature, the conventional Kirchhoff's law can be applied such that $\alpha'_{\omega} = \varepsilon'_{\omega}$, where ε'_{ω} is the summation of $\varepsilon'_{\omega,j}$ given in Eq. (4.5).

The direct method provides a physically sound way to calculate thermal emission from an individual layer, as if the rest of the structure were at absolute zero temperature. The spectral directional emissivity of a layer can be obtained by comparing the spectral intensity to that of a blackbody at the same temperature as given in Eq. (4.5). Furthermore, the emitted intensity of the whole structure can be treated as a superposition of the intensities emitted by each layer. However, analytical expressions of the exchange functions in a multilayer structure are difficult to obtain. Numerous examples have been evaluated and in all cases, it is found that $\varepsilon'_{\omega,j} \equiv \alpha'_{\omega,j}$, within the limitation of computational accuracy, when they are evaluated from Eq. (4.5) using the direct method and Eq. (4.8) using the indirect method, respectively.

Note that the exchange function $Z_j(\omega,\beta)$ is calculated based on the dyadic Green's function $\bar{\bar{\mathbf{G}}}_j(\mathbf{x},\mathbf{x}',\omega)$ between the emitting layer j ($j>1$) and the vacuum ($j=1$). In the expression of $\bar{\bar{\mathbf{G}}}_j(\mathbf{x},\mathbf{x}',\omega)$, there are four coefficients *A*, *B*, *C* and *D* representing different patterns of electric and magnetic field propagation from the source. These coefficients can be determined by the same matrix formulation as that used in the

indirect method [15,53,57,58,68]. Francoeur *et al.* [67] recently gave a detailed derivation for thermal radiation from a 1D layered structure by combining the dyadic Green's functions and the scattering matrix method, which can remedy the numerical instability problem when the traditional transfer matrix method is applied to the near-field thermal radiation. One of the important equalities in all the matrix formulations is the principle of reciprocity. If the exchange function is defined between any two layers *j* and *k*, then one must have $Z_{jk} = Z_{kj}$. This is to say that the absorptivity of each layer should be equal to the emissivity, since vacuum can be treated as a blackbody. Without further ado, it can be asserted that the spectral directional emissivity in Eq. (4.5) must be the same as the spectral directional absorptivity in Eq. (4.8) for the same layer.

This equality $\varepsilon'_{\omega,j} \equiv \alpha'_{\omega,j}$ is referred to as the *generalized Kirchhoff's law*. The thermal emission or the spectral intensity from the entire layered structure can be obtained by the superposition of the contributions from each layer as

$$I_{\omega,\mathrm{sum}}\left(\omega,\theta,T_1,...,T_N\right) = \sum_{j=2}^{N} \varepsilon'_{\omega,j} I_{\omega,\mathrm{b}}(\omega,T_j) \tag{4.10}$$

According to the equality, the spectral intensity can be also calculated from the indirect method with the absorptivity of each layer. Therefore, the direct and indirect methods are unified on predicting the thermal emission from layered structure with nonuniform temperature distributions, and the indirect method may offer a more convenient way since no Green's function is involved.

The emissivity of a nonuniform temperature structure cannot be defined, unless a reference temperature is specified. Such a definition provides an effective emissivity with respect to a blackbody at an arbitrarily specified reference temperature. On the other hand,

the brightness temperature $T_\omega(\omega,\theta)$, at which a blackbody has the same spectral intensity, is a more fundamental property to characterize thermal emission [1]. The brightness temperature is a function of frequency and the direction. It has been used for thermal emission from layered structures in the microwave region [55], where blackbody intensity is approximately proportional to the absolute temperature according to the Rayleigh-Jeans formula. Subsequently, T_ω can be written as a superposition of weighted temperatures of individual layers [111]. In general, the brightness temperature can be calculated from the spectral intensity of the structure obtained from either the direct or indirect method, and can be expressed as [112]

$$\frac{1}{T_\omega}=\frac{k_{\mathrm{B}}}{\hbar\omega}\ln\left[1+\frac{\hbar\omega^3}{8\pi^3c^2I_{\omega,\mathrm{sum}}}\right] \tag{4.11}$$

Besides spectral directional emissivity and spectral intensity, direct method offers a way to calculate other important physical quantities in analyzing thermal emission as well, such as spectral energy density and local density of states [1,59,113]. The spectral energy density of the electromagnetic field in a nonabsorbing layer *k* (which can be vacuum or a lossless dielectric medium) due to the emission from layer *j* is given as [1]

$$u_{jk}\left(\mathbf{x},\omega\right)=\frac{\varepsilon_k(\omega)\varepsilon_0}{4}\left\langle\mathbf{E}_j\left(\mathbf{x},\omega\right)\cdot\mathbf{E}_j{}^*\left(\mathbf{x},\omega'\right)\right\rangle+\frac{\mu_0}{4}\left\langle\mathbf{H}_j\left(\mathbf{x},\omega\right)\cdot\mathbf{H}_j{}^*\left(\mathbf{x},\omega'\right)\right\rangle \tag{4.12}$$

where $\varepsilon_k(\omega)$ is the dielectric function of the *k*th layer. The spectral energy density can be understood as the electromagnetic energy per unit volume per unit angular frequency, and is the product of the local density of states $D_{jk}(\omega)$ and the mean energy of the Planck oscillator, thus,

$$u_{jk}\left(\omega\right)=D_{jk}\left(\omega\right)\Theta(\omega,T_j) \tag{4.13}$$

Here, $D_{jk}(\omega)$ represents the number of modes per unit frequency interval per unit volume. It should be noted that the energy density and LDOS in a nonabsorbing layer is independent of *z* for propagating waves. In other words, the energy density or LDOS is uniform inside the *k*th layer. In the near field where evanescent waves exist, energy density or LDOS is strongly dependent on the location *z* near the surfaces/interfaces [114]. Since $D_{jk}(\omega)$ is integration over all the β's, it can be written in a form similar to Eq. (2.10) as

$$D_{jk}(\omega) = \int_0^{\omega/c} X_{jk}(\omega,\beta)\beta d\beta \tag{4.14}$$

where $X_{jk}(\omega,\beta)$ can be evaluated using the dyadic Green's function between the *j*th and *k*th layer [15,53,58,68], similar to the exchange function $Z_j(\omega,\beta)$ mentioned previously. Let $D'_{jk}(\omega,\theta)$ be the LDOS per unit solid angle so that $D_{jk} = \int_0^{2\pi} d\phi \int_0^{\pi/2} D'_{jk}(\omega,\theta)\sin\theta d\theta$. It can be shown that

$$D'_{jk}(\omega,\theta) = \frac{\omega^2}{2\pi c^2} X_{jk}(\omega,\beta)\cos\theta \tag{4.15}$$

By definition, the unit of $D'_{jk}(\omega,\theta)$ is [m^{-3} s rad^{-1} sr^{-1}]. The definition of LDOS in terms of the solid angle is important for the study of anisotropic thermal emission in a given direction.

Thermal emission from an asymmetric Fabry-Perot resonance cavity as shown in Fig. 2.1 is taken as an example of layered structures with nonuniform temperature. This structure exhibits coherent emission characteristics [63] and may have applications in advanced energy systems. The thicknesses are taken as $d_f = 21\,\text{nm}$ and $d_c = 622\,\text{nm}$ [63].

The dielectric functions of Au and SiO_2 are taken from Palik [83] at room temperature and are assumed to be independent of temperature for the convenience of calculation. In the considered frequency (or wavenumber) range from 3000 cm^{-1} to 13000 cm^{-1}, SiO_2 is essentially lossless and the emission from SiO_2 is negligible. In the simulation, it is assumed that the top Au film and the bottom Au layer are each at a uniform temperature with $T_1 = 800\,\mathrm{K}$ and $T_2 = 1000\,\mathrm{K}$, respectively. This is a reasonable assumption due to the high thermal conductivity of Au and the low thermal conductivity of SiO_2. A relatively large value is chosen for the illustration purposes.

The contribution from each emitting layer to the spectral intensity of the Fabry-Perot resonance cavity can be calculated from the direct method. The spectral intensities from top and bottom Au films calculated from Eq. (4.4) are shown in Fig. 4.13 at $\theta = 0\,\mathrm{deg}$, along with their sum that represents the intensity emitted by the layered structure according to Eq. (4.10). The blackbody intensities at 800 K and 1000 K are also plotted for comparison. In this spectral region, the intensity decreases with increasing frequency according to Planck's law. All the emission spectra contain two peaks at wavenumbers slightly higher than 5000 cm^{-1} and 10000 cm^{-1}, respectively, while the spectrum for the thin Au film exhibit a minimum near each peak. The sharp peaks in the spectral emission are associated with the temporal coherence as discussed extensively previous sections. The intensity from the bottom Au layer dominates at both peaks due to its higher temperature.

The spectral directional absorptivity in each layer can be calculated from Eq. (4.8) based on the indirect method at an arbitrary angle of incidence, and is exactly the same as the corresponding spectral directional emissivity calculated from Eq. (4.5), i.e., the direct

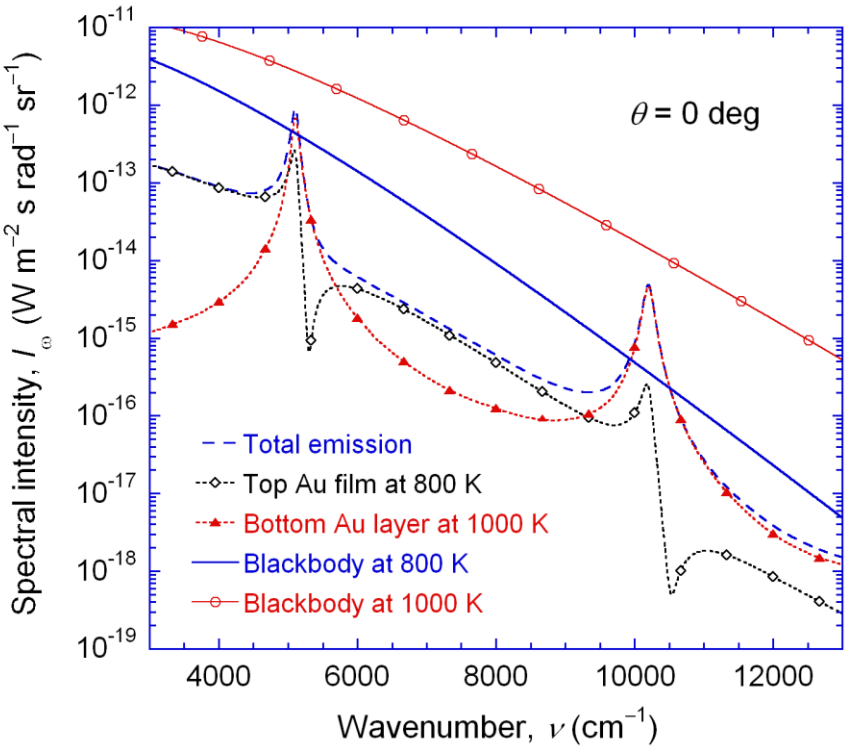

Figure 4.13 Calculated normal spectral intensity emitted by the Fabry-Perot structure shown in Fig. 2.1 from the direct method. Note that $d_f = 21\,\text{nm}$ and $T_1 = 800\,\text{K}$ for the thin Au film, $d_c = 622\,\text{nm}$ for the SiO_2 cavity, and $T_2 = 1000\,\text{K}$ for the bottom Au film.

method. The spectral intensity in Fig. 4.13 can be also obtained from the indirect method by multiplying the absorptivity with the blackbody intensity since the spectral directional absorptivity equals the emissivity at each layer. Figure 4.14(a) shows the emissivity (or absorptivity) spectra at normal incidence for the top and bottom Au films along with that of a 200-nm Au film that can be treated opaque. The emissivity spectra show peaks/valleys similar to the intensity spectra. However, the top Au film has higher peak emissivity values of 0.59 and 0.68, compared with 0.25 and 0.32 for the bottom Au layer. If the temperature were uniform, then the contribution of the thin Au film would be twice as large as that of the opaque Au layer. As shown in Fig. 4.14(a), the normal emissivity

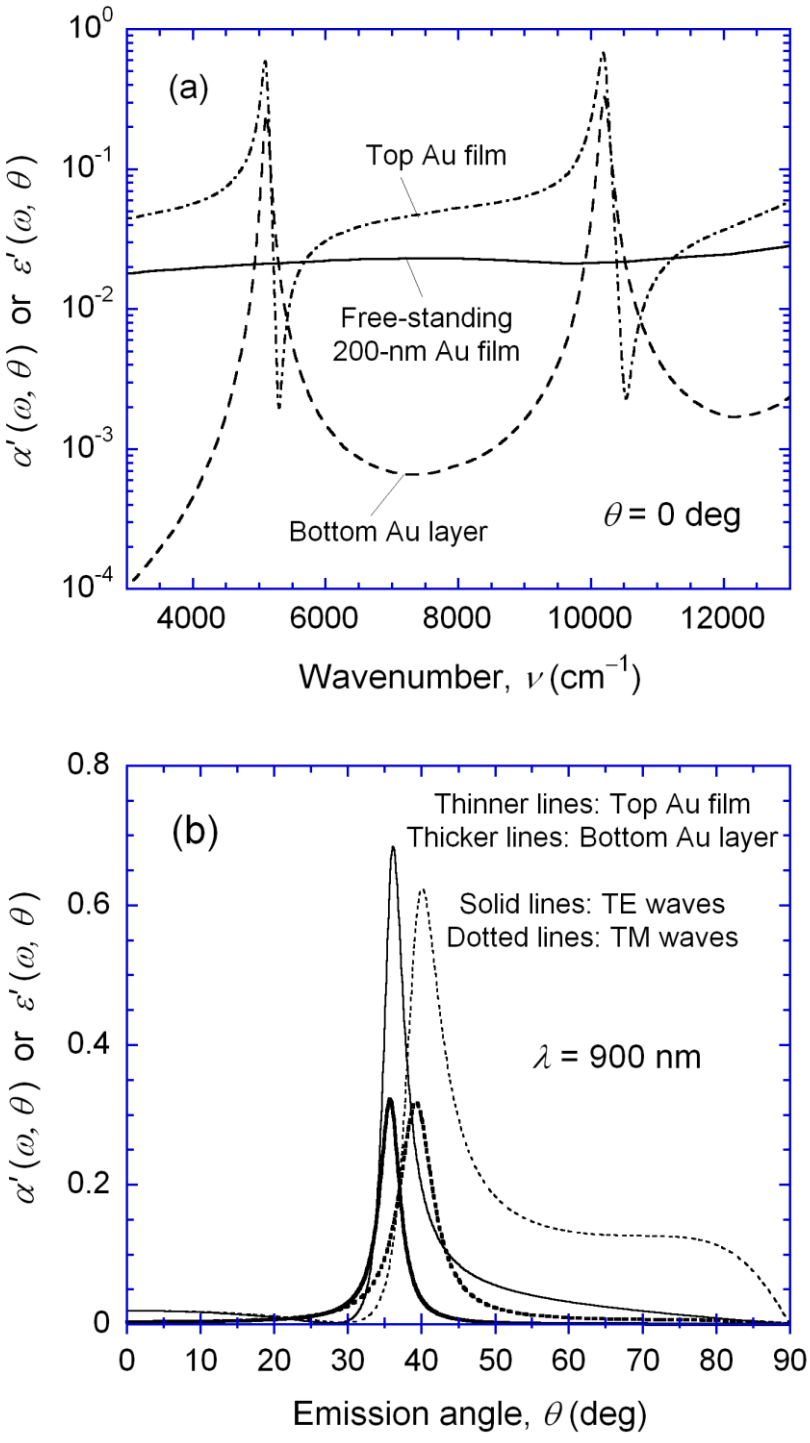

Figure 4.14 (a) The spectral normal absorptivity from the indirect method (or emissivity from the direct method) of each Au film in the Fabry-Perot structure, and that of a free-standing Au film; (b) the spectral directional absorptivity (or emissivity) as a function of emission angles for both polarizations at a wavelength of 900 nm.

of an opaque Au film is between 0.18 and 0.30. With the addition of the SiO_2 and of the thin Au film on top of it, the emissivity of the opaque Au layer is significantly modified. This suggests that the emissivity or absorptivity is not an intrinsic property of the material, but is strongly dependent on the geometry and other materials in the structure.

Figure 4.14(b) plots the directional dependence of the emissivity (or absorptivity) for both polarizations at a wavelength of 900 nm. As is shown, the emissivity for both top and bottom Au layers is enhanced within confined emission angles, around 36 ° for TE waves and 40 ° for TM waves. Similar to the spectral dependence shown in Fig. 4.14(a), the top Au film exhibits higher peak emissivity than the bottom Au layer for both polarizations. The emissivity peaks are sharper for TE waves than that for TM waves, which is because the polarization-dependent reflectivity at the interfaces of the Au film is larger for TE waves, as discussed in Section 4.2.

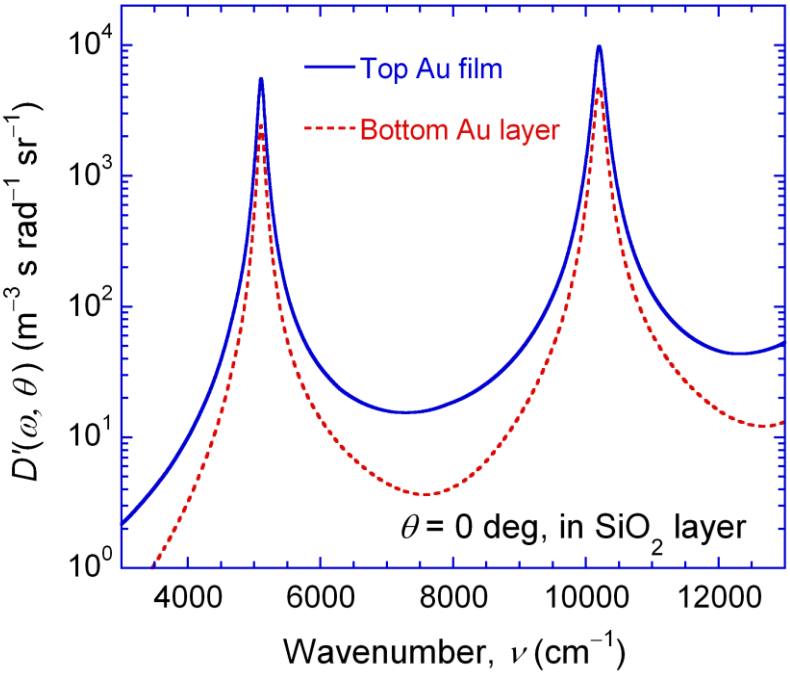

Figure 4.15 Calculated LDOS inside the SiO_2 cavity at $\theta = 0$ deg for contributions from the top Au film and bottom Au layer.

The emission peaks can be understood by wave interferences inside the SiO_2 optical cavity. In near-field radiation, LDOS is often used to explain the surface wave resonance [114], but has never been used to study the interference effect or bulk polaritons [81]. The LDOS inside the SiO_2 film calculated from Eq. (4.15) are plotted in Fig. 4.15 at different wavenumbers at normal direction for the same Fabry-Perot structure. It should be noted that at $\theta = 0$ deg, the LDOS of planar structures is independent of the polarization states. Hence, the result is true for both TE and TM waves. The two curves correspond to the contributions to the LDOS by the thin Au film and by the opaque Au layer, respectively. Since the material properties are assumed to be temperature independent, the LDOS is not a function of temperature. It can be seen that the two peaks in the LDOS match well with the spectral emission peaks. Nearly two orders of magnitude enhancement in LDOS exists in the SiO_2 cavity near 5000 cm^{-1} and 10000 cm^{-1}, suggesting that the increase in LDOS is associated with the emission peaks. It is interesting to notice that the LDOS in SiO_2 contributed by the top Au film layer has no dips, unlike the emissivity or emission spectrum. Additional calculations indicate that the LDOS in vacuum (not shown in the figure) originating from an emitting layer *j* is proportional to $\omega^2 \varepsilon'_{\omega,j}$. Hence, the spectral intensity and energy density are proportional to each other in vacuum as expected for far-field thermal radiation. It should be noted that only the propagating waves are considered in the calculation of LDOS.

Another parameter to characterize thermal emission is the brightness temperature or radiance temperature [1,2,52,55]. Figure 4.16(a) plots the spectral dependence of brightness temperature at $\theta = 0$ deg calculated according to Eq. (4.11). The brightness temperature increases with frequency in general, with two peaks of 871 K near 5000 cm^{-1}

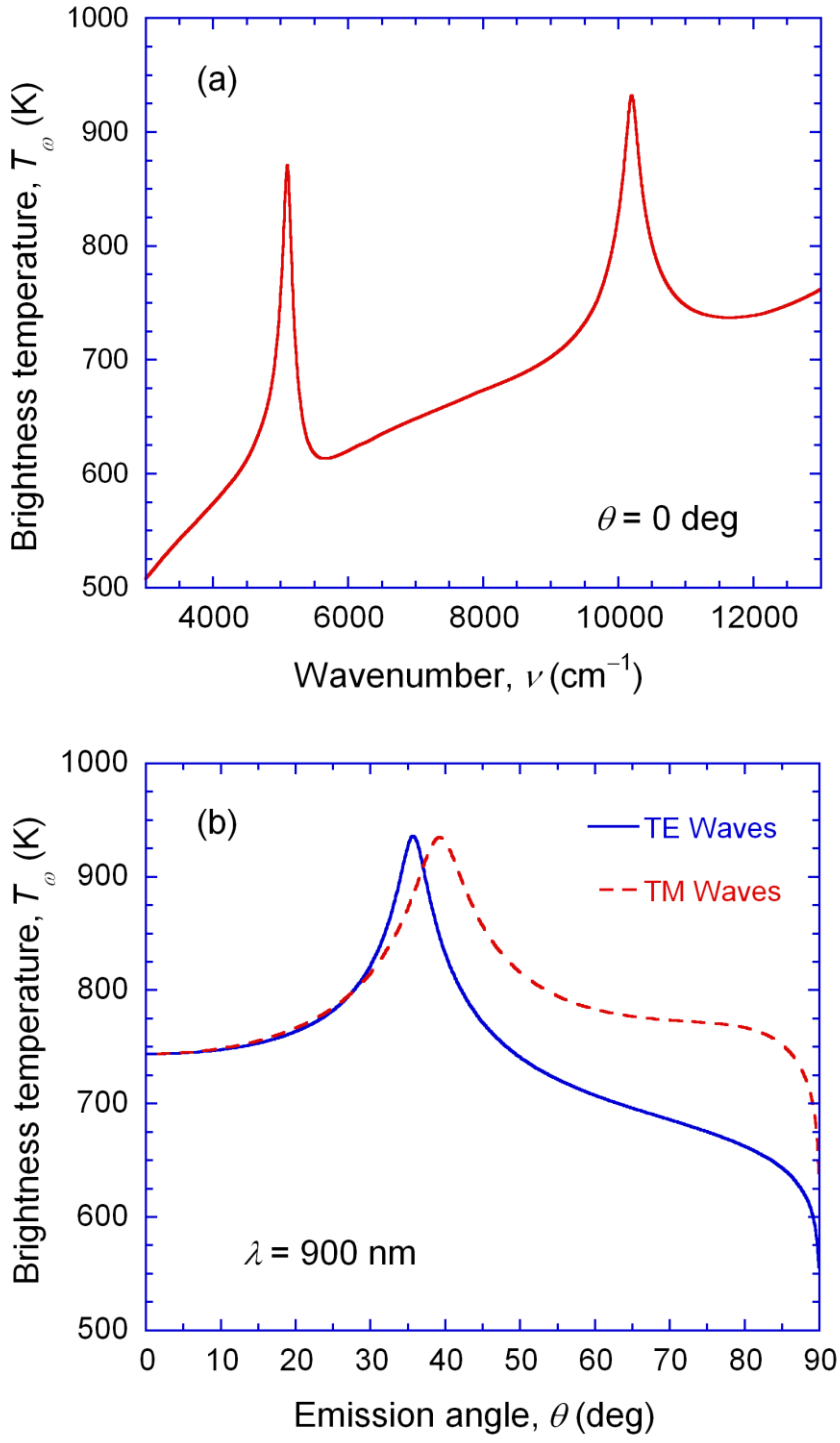

Figure 4.16 The brightness temperature calculated for the Fabry-Perot structure: (a) as a function of wavenumbers at $\theta = 0$ deg; (b) as a function of emission angles for both polarizations at a wavelength of 900 nm.

and 932 K near 10000 cm^{-1}. The first peak is sharper than the second one, similar to the intensity spectrum shown in Fig. 4.13.

The directional dependence of the brightness temperature is calculated at the wavelength of 900 nm for both TE and TM waves, as shown in Fig. 4.16(b). The brightness temperature increases with emission angle from 744 K (at $\theta = 0\,\text{deg}$) up to a peak value of 935 K or so for both polarizations. The peak location corresponds to the peak intensity of the layered structure and is different for different polarizations. Note that the brightness temperature for TE waves exhibits a sharper peak at smaller emission angles. At $\theta > 40\,\text{deg}$, the brightness temperature for TE waves is much smaller than that for TM waves. The brightness temperature finally reduces to zero at the grazing angle for both polarizations.

CHAPTER 5
MAGNETIC POLARITONS IN GRATING MICRO/NANOSTRUCTURES

This Chapter theoretically investigates the role of magnetic resonance in tailoring the radiative properties, such as extraordinary optical transmission and coherent thermal emission. To begin with, Section 5.1 clarifies the physical mechanism of magnetic polaritons (MPs) rather than coupled SPPs or Fabry-Perot-like cavity resonance on resonant transmission or absorption in 1D simple metallic grating structures. Section 5.2 further elucidates the effect of MPs in double-layer slit arrays to achieve extraordinary optical transmission at specific wavelength, and the displacement effect is discussed as well. Based on the similarity between metals and polar materials, MPs can be excited with the assistance of phonons to control radiative properties at infrared regime in grating structures made of SiC, which is discussed extensively in Section 5.3. With the gained fundamental understanding, Section 5.4 proposes a coherent thermal emitter with spectral selectivity by placing a dielectric spacer between a metallic grating layer and a metallic film, where MPs can be excited. With the unique characteristic of MPs, Section 5.5 designs a thermal radiator particularly for TPV applications with wavelength selectivity and directional insensitivity, which are highly desired in TPV systems to improve conversion efficiency and power throughput. In this Chapter, RCWA is used to rigorously calculate the radiative properties of different grating structures, where LC models are employed to predict the magnetic resonance conditions. The behavior and physics with the MPs are extensively discussed from field distributions and dispersion relations, and geometric effects on the MPs are studied as well.

5.1 Resonant Transmission/Absorption through Simple Metallic Gratings

Consider a 1D binary grating surrounded by vacuum as depicted in Fig. 2.6(b), with a height h, period Λ, and slit width b (or the strip width $w = \Lambda - b$) [115]. A TM wave of wavelength λ is incident at a polar angle θ. Rigorous coupled-wave analysis (RCWA) is used to compute the reflectance *R* and transmittance *T*, and the absorptance is $\alpha = 1 - R - T$. Figure 5.1(a) shows the contour plot of the sum of the absorptance and transmittance, i.e., $1 - R$, in the frequency range from 2,500 to 25,000 cm^{-1} for a Ag grating with $h = 400\ \text{nm}$, $\Lambda = 500\ \text{nm}$, and $b = 50\ \text{nm}$. The region outside the light line in the lower-right corner is left blank. The bright bands, at which the reflectance is minimal, indicate resonance behavior. Figure 5.1(b) plots *R*, *T* and α for the same structure at normal incidence. It can be seen that the reflectance minimum is accompanied by the maxima in *T* and α. The first two resonances, denoted by MP1 and MP2, are the fundamental mode and the second harmonic of magnetic polaritons. The next mode is a SPP, followed by the third magnetic polariton, MP3. It appears that the excitation of MP1 results in large transmittance. As the order of MP gets higher, the peak absorption increases, while the transmittance enhancement is weakened. This was also shown similarly in Refs. [40,116]. As seen from Fig. 5.1(a), MP2 and MP3 for this structure interact strongly with SPP excited at the interfaces between the grating and vacuum. As a consequence, MP3 is not clearly observed in Fig. 5.1(b). Because *R* has the largest contrast, $1 - R$ is chosen to show the polariton dispersion relation.

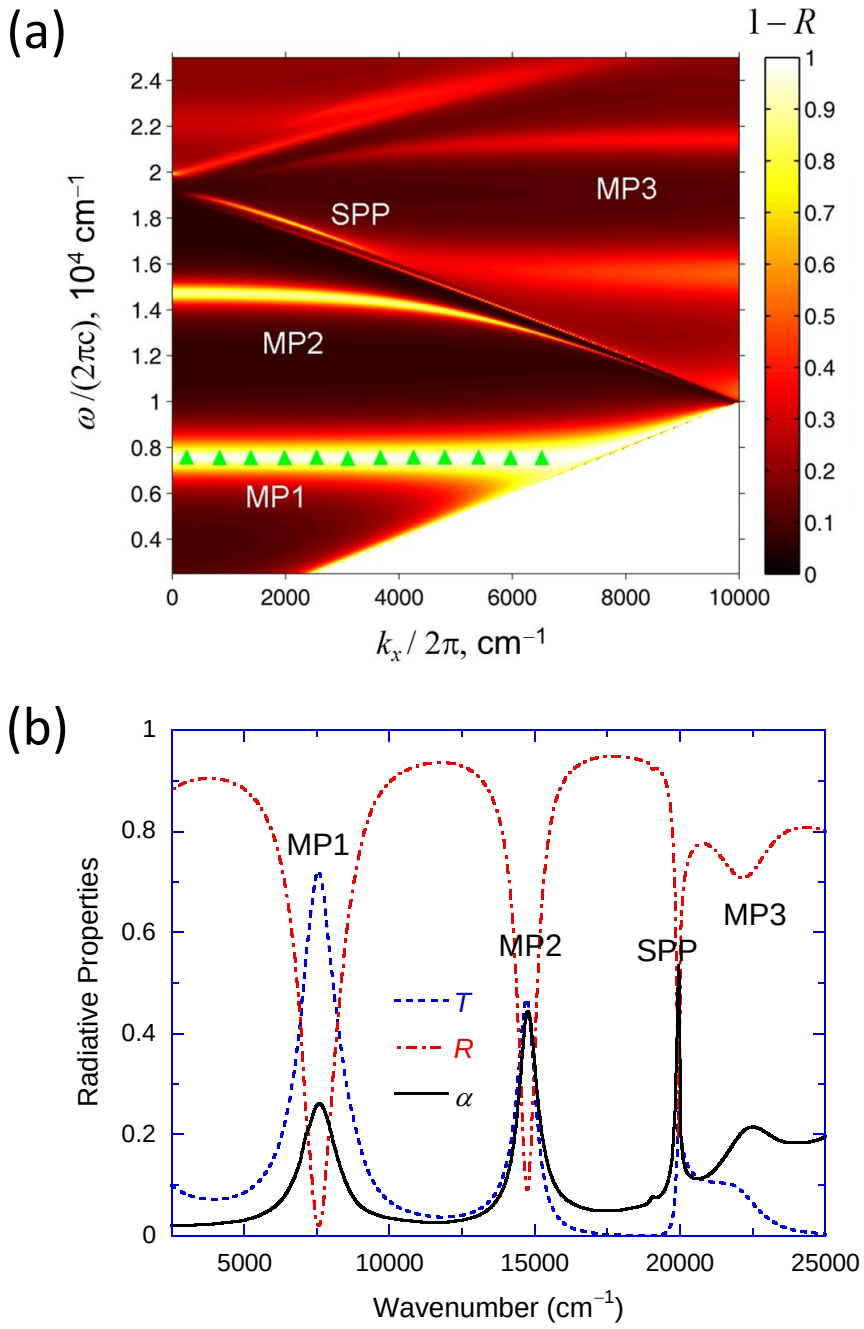

Figure 5.1 (a) Contour plots of the sum of absorptance and transmittance (i.e., 1–*R*) for a Ag grating with period Λ = 500 nm, h = 400 nm, and b = 50 nm. Triangle marks indicate the frequency of the fundamental mode predicted by the LC circuit model according to Eq. (2.30). (b) The radiative properties at normal incidence for TM waves for the same structure.

The SPP dispersion shown in Fig. 5.1(a) is essentially an inclined line close to the light line and then bended due to the Bloch-Floquet condition in the gratings [1]. On the other hand, the nearly flat magnetic polariton curves are similar to those observed for double-layer gratings or gratings over a film [117]. The difference is a $90\,^{\circ}$ rotation of the polar angle θ. These flat dispersion curves cannot be explained by coupled SPPs or the cavity-like resonance. Due to the oscillating magnetic field in the *y*-direction, an electric current is induced in the *x*-*z* plane, resulting in a diamagnetic behavior. The magnetic and electric field distribution is similar to that shown in Ref. [3] and will be discussed in detail in sequent sections. The field distribution reveals that, at the resonance, the magnetic field is strongly localized inside the slit between two neighboring metallic strips, and the induced electric current flows along the metal surface. It is worth mentioning that, due to the interaction of MP and SPP, the curves of MP2 and MP3 in Fig. 5.1(a) split into two branches and are not always flat, especially near intersections with the SPP curve.

The periodic oscillations in the spectral property look indeed like the Fabry-Perot cavity resonance [63]. However, as elaborated below, it is the magnetic polariton that can offer a quantitative explanation of the resonance condition. Equivalent optical nanocircuit theory has been established as a useful tool for the design and analysis of metamaterials [73]. Since the strip width is much larger than the penetration depth δ, the LC circuit model for two parallel strips discussed in Section 2.4 can be employed to predict the magnetic resonance frequency for the fundamental mode. Based on Eq. (2.30), the resonant condition at MP1 for the structure is calculated and presented as triangles in Fig. 5.1(a). Clearly, the prediction by LC model matches well that from RCWA calculations.

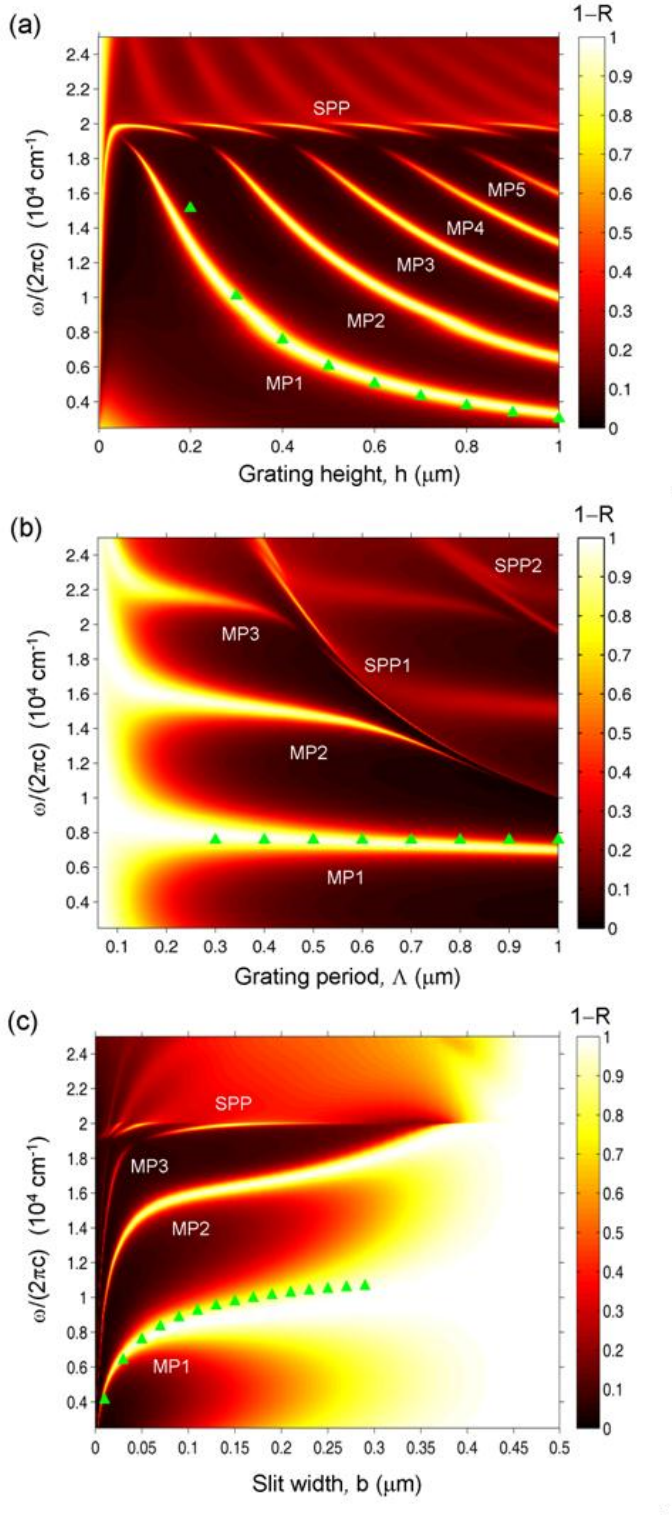

Figure 5.2 Demonstration of the geometric effects on the magnetic resonance conditions: (a) grating height effect, (b) grating period effect, and (c) slit width effect. Triangle marks are calculated from the LC circuit model in Eq. (2.30).

The geometric effects on the resonance conditions are illustrated in Fig. 5.2 for Ag gratings by individually changing *h*, Λ or *b* from the base parameters given in Fig. 5.1, while fixing the other two. The contour plots show $1-R$ at normal incidence. When the grating height is varied, five MPs can be observed in Fig. 5.2(a), and their resonance frequencies decrease as *h* increases. Moreover, SPP is excited about 20,000 cm^{-1} that is nearly independent of *h*, as the SPP excitation frequency should not change for fixed grating period and incidence angle. Because SPP interacts with all five MPs, the resonance frequencies for both SPP and MPs shift near the intersections. The calculated resonance frequencies by LC circuit model for the fundamental mode at several h values are depicted as triangles, which match well with the RCWA result for the dispersion curve of MP1. Hence, the height dependence of enhanced transmission or absorption can be fully explained by MPs. On the contrary, neither coupled SPPs nor Fabry-Perot-like resonance models could quantitatively describe the dispersion of MPs. The relatively large error at $h = 0.2\,\mu\text{m}$ is mainly caused by the strong interaction with the SPP. The inverse proportionality between resonance frequency ω_{R} and the grating height h can be deduced from Eq. (2.30). In addition, nearly evenly spaced MP dispersion curves suggest that the higher-order harmonics can be predicted by multiplying ω_{R} by the order number.

Figure 5.2(b) shows the effect of the grating period on the resonance condition by changing Λ while fixing *b*. Note that this can also be viewed as the strip width effect since $w = \Lambda - b$ also changes. While the period has a strong effect on SPP frequency, the MP resonance frequency is not affected by Λ and *w*. Furthermore, the result from the LC circuit model, again represented by the triangle marks, agrees well with the dispersion curve for MP1. As mentioned before, as long as the metal strip width w is much greater

than the penetration depth δ, it has little effect since the radiation from both the left and right sides cannot penetrate through the strip. Hence, the coupling of localized magnetic polaritons between neighboring slits can be neglected. This is also the reason why the previous analysis for a single slit can apply to periodic subwavelength slit arrays [37,40]. In addition, as Λ further increases, another SPP curve emerges due to the second diffraction order of the gratings. The two SPP branches are indicted as SPP1 and SPP2 in Fig. 5.2(b). The higher orders of magnetic resonance, MP2 and MP3, are truncated by SPP1 and SPP2, and hence, their resonance conditions are altered. Even for MP1, it begins to shift towards lower frequencies for $\Lambda > 0.6\,\mu\text{m}$, where the interaction with SPP becomes stronger. For small grating period, say $\Lambda < 100$ nm, *w* is so small that radiation can penetrate through the gratings, resulting in high transmittance.

The effect of slit width on the magnetic resonance is shown in Fig. 5.2(c). Since the period is kept as 500 nm, the SPP curve is nearly flat around 20000 cm^{-1}, except that it is truncated into several sections due to the interaction with MPs. Although Fabry-Perot-like model considers the slit width dependence [37], the predicted resonance frequency decreases as *b* increases. When *b* approaches zero, the predicted resonance frequency is the highest and equal to the uncorrected Fabry-Perot frequency. From Fig. 5.2(c), the resonance frequency for MPs decreases dramatically as the slit width is reduced to zero. Microwave measurements have confirmed that the resonance frequency should decrease as *b* decreases for very narrow slit [40]. Clearly, the resonance conditions predicted by the LC model compare well with the dispersion curve. However, the LC circuit model starts to deviate from the RCWA calculation for $b > 350$ nm. This is because the period is fixed at $\Lambda = 500$ nm. Further increasing *b* results in a relatively

small *w*, and thus, the coupling of magnetic polaritons between neighboring slits may become significant. In practice, the gratings need to be fabricated on a dielectric substrate, which will slightly modify the dispersion relations of MPs and introduce an additional SPP mode between the grating and the substrate.

5.2 Extraordinary Optical Transmission in Double-Layer Nanoslit Array

In this section, the thermal radiative properties of aligned double-layer nanoslit arrays, shown in Fig. 5.3(a), are numerically studied with the RCWA algorithm in the frequency range from 2,500 cm^{-1} to 25,000 cm^{-1} [118]. The whole structure is assumed to be infinitely extended in the *y* direction. Silver is selected as the material for the strips and SiO_2 is used for the dielectric spacer. Note that *d* is the thickness of the spacer.

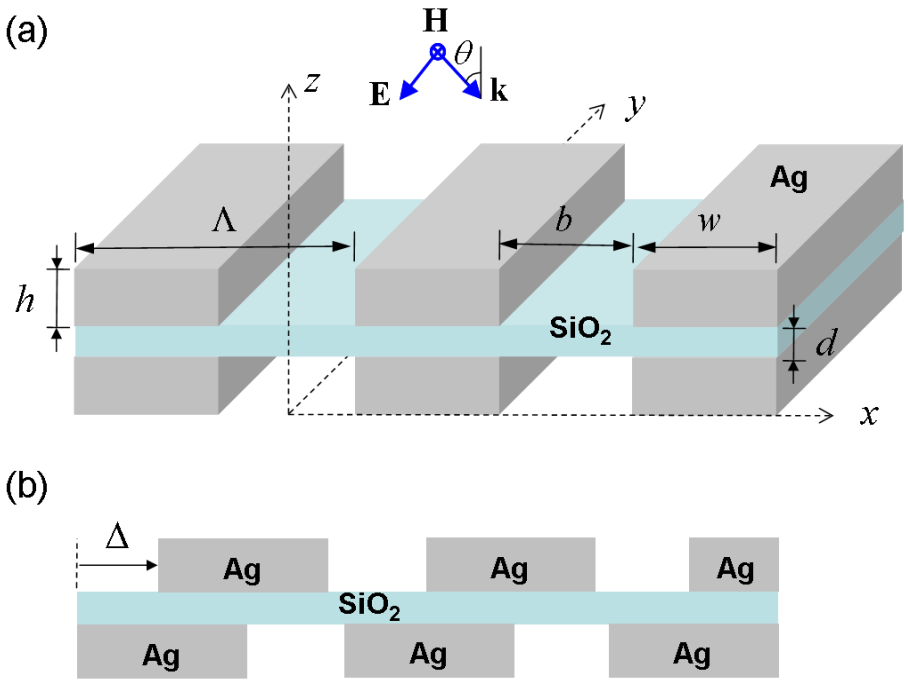

Figure 5.3 (a) Schematic of an aligned double-layer nanoslit array made of Ag with SiO_2 dielectric spacer; (b) cross-sectional view of a misaligned nanoslit array with a lateral displacement Δ.

The radiative properties at normal incidence are discussed first as well as the comparison with the structure without the spacer. With the aid of electric and magnetic field distributions, the behavior at the enhanced transmission or absorption associated with the excitation of magnetic resonances is presented. The dispersion relations are depicted in contour plots to illustrate the behavior of MPs at oblique incidence. The LC model is used to verify the magnetic resonance. The effect of a lateral displacement Δ in misaligned nanoslit arrays, as shown in Fig. 5.3(b), is discussed as well.

5.2.1 Radiative Properties at Normal Incidence

The grating period is taken as Λ = 500 nm and the width of strips is set to be w = 350 nm. The two nanoslit layers have identical thickness of h = 70 nm and are separated by a distance d = 30 nm with the SiO_2 spacer. Only TM waves are considered here. Figure 5.4(a) shows the radiative properties of the structure at normal incidence calculated from the RCWA. Large variations exist in the calculated radiative properties, predominantly with reduced R and enhanced α or T at certain frequencies, such as around 5,286 cm^{-1}, 14,670 cm^{-1}, 17,156 cm^{-1}, and 20,000 cm^{-1} (corresponding to absorption peaks). The one at 20,000 cm^{-1} is due to the excitation of SPP at the air/Ag interface, which has been discussed in Section 2.5. The enhanced absorption and/or transmission at several other frequencies can be explained by the excitation of different MP modes, marked as MP1, MP3, and CMP (coupled MP to be discussed later) in Fig. 5.4(a). Detailed description and explanation of MPs in double-layer nanoslit arrays are given in the following subsections by means of electromagnetic field distributions, dispersion relations, as well as the equivalent LC circuit model.

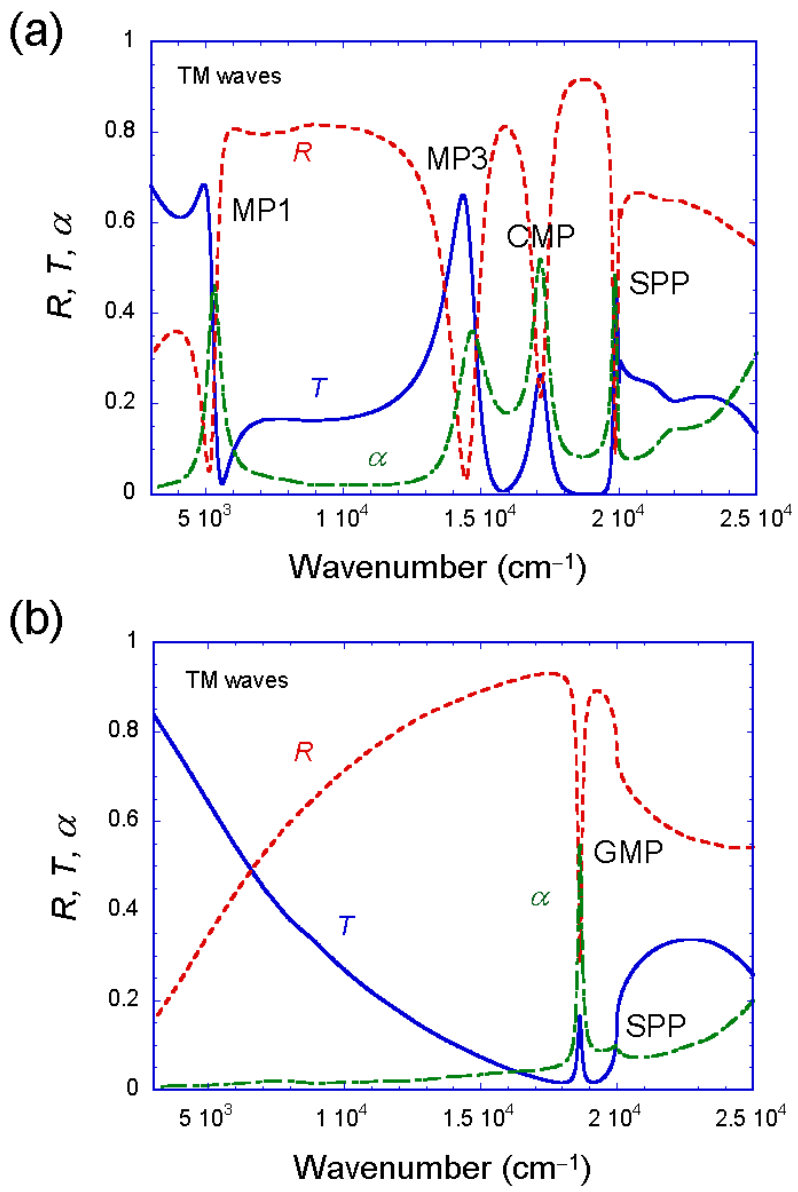

Figure 5.4 Radiative properties at normal incidence. (a) A double-layer nanoslit array with the following parameters: $\Lambda = 500$ nm, $w = 350$ nm, $h = 70$ nm, and $d = 30$ nm; (b) A single-layer nanoslit array with the same grating period, width, and height.

Figure 5.4(b) shows the calculated radiative properties of a single-layer nanoslit array with the same Λ, h, and w as for Fig. 5.4(a). The comparison of Figs. 5.4(a) and 5.4(b) demonstrates how MPs change the radiative properties in the double-layer nanoslit array with great absorption/transmission enhancement at certain frequencies. For instance,

at 14,670 cm^{-1} where MP3 is excited, the transmission is enhanced by six times with the addition of another layer to the single layer. It is worthy of mentioning that MPs can also be excited in the single-layer nanoslit array, because the magnetic field can be strongly localized in the gap between neighboring metal strips, as discussed in Section 5.1. Here, gap magnetic polariton (GMP) is used for the mode at 18,640 cm^{-1}. Multiple GMPs with different anti-nodes of the magnetic field can be excited in deep nanoslit arrays. Moreover, the absorption peak due to SPP also exists at 20,000 cm^{-1} in the single-layer nanoslit array since the period is not changed.

5.2.2 Field Distribution at Magnetic Resonance

The electromagnetic field distributions at the magnetic resonance frequencies are calculated with RCWA, as shown Fig. 5.5, to help understand the physical mechanisms. The metallic strips and dielectric spacer with two unit cells are delineated in the figure. Note that waves are incidence normally from the top to the bottom. The shaded contour (color online) represents the logarithmic of the square of the magnetic field, and arrows indicate the electric field vectors. The circles/ovals indicate the current loops with arrows pointing the electric field direction.

Figure 5.5(a) shows the field distribution at 5,286 cm^{-1}, corresponding to MP1. There exists strong magnetic field confinement in the dielectric spacer between the upper and lower Ag strips, around an order of magnitude greater than that of the incident wave. The electric vector loop suggests the diamagnetic behavior as an eddy current induced by oscillating magnetic fields. By virtue of the eddy current in the metallic strip (near the surfaces adjacent to the dielectric), positive and negative charges are accumulated at two

ends, where the magnetic field decays much faster into the strips than at the center. Since only one anti-node of the magnetic field is formed between the upper and lower Ag strips in a unit cell, the magnetic resonance at this frequency is characterized as the fundamental mode or the first-order MP.

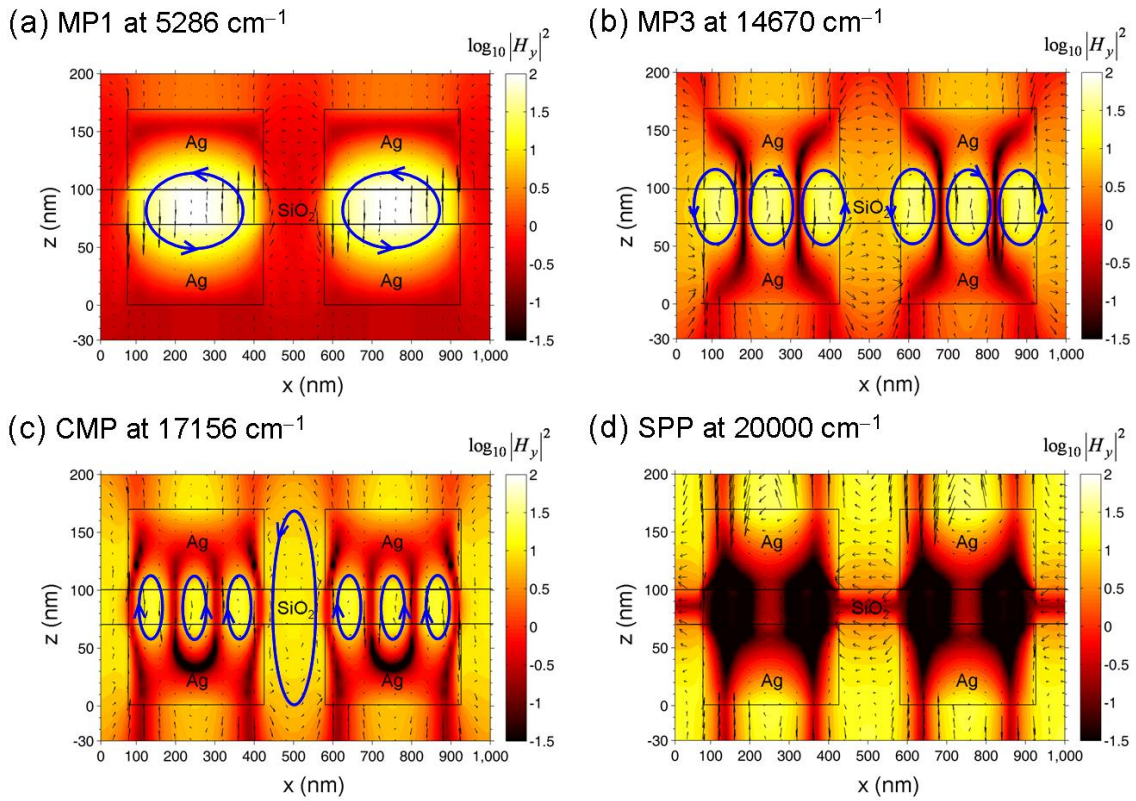

Figure 5.5 Electromagnetic field distributions at different resonance frequencies in the nanoslit array at normal incidence: (a) MP1 at 5,286 cm^{-1}; (b) MP3 at 14,670 cm^{-1}; (c) CMP at 17,156 cm^{-1}; (d) SPP at 20,000 cm^{-1}. The contour represents the logarithmic of the square of magnetic field, arrows indicate electric field vectors, and loops illustrate induced electric currents.

Figure 5.5(b) shows the field distribution at 14,670 cm^{-1}. Three current loops with alternating directions, corresponding to the anti-nodes of magnetic field, are induced in the spacer. This indicates a third harmonic MP mode, denoted as MP3. The maximal

transmission associated with MP3 in the double layer of slits is about 6.6 times of that in a single layer of slits at the same frequency. It should be noted that transmission can also be suppressed to near zero by magnetic resonances at specific frequencies, as can be seen from Fig. 5.4(a).

At 17,156 cm^{-1} where the third absorption peak occurs, an additional anti-node of magnetic field is formed, as indicated in Fig. 5.5(c), with a current loop in the gap between the left and right Ag strips. Consequently, the term coupled magnetic polariton (CMP) is cast to indicate this specific mode since anti-nodes exist both in the gap (between left and right Ag strips) and in the spacer (between upper and lower Ag strips).

It should be pointed out that the electromagnetic field distribution for the SPP is totally different from those of MPs. SPPs are essentially the coupling between the incident electromagnetic waves with collective excitations of charges such as electrons near the surface of a metal. The field associated with SPP is localized at the dielectric/metal interface, and the amplitude decays away from the interface into both the metal and dielectric (which can be air) medium. As shown in Fig. 5.5(d), where SPP is excited between air and the Ag grating, the field amplitude decays into the metal at both top and bottom air/Ag interfaces. The comparison of the field distributions reveals the distinct characteristic of MPs, that is, the field amplitude decays from inside out, since MPs are strongly localized between metal strips in the spacer (or the gap).

The energy density distributions at the magnetic resonance frequencies corresponding to MP1 and MP3 are shown in Figs. 5.6(a) and 5.6(b), respectively. The energy density, calculated in air and the dielectric, is shown as the contour. The arrows represent the Poynting vectors, which indicate the direction of energy flow. The method

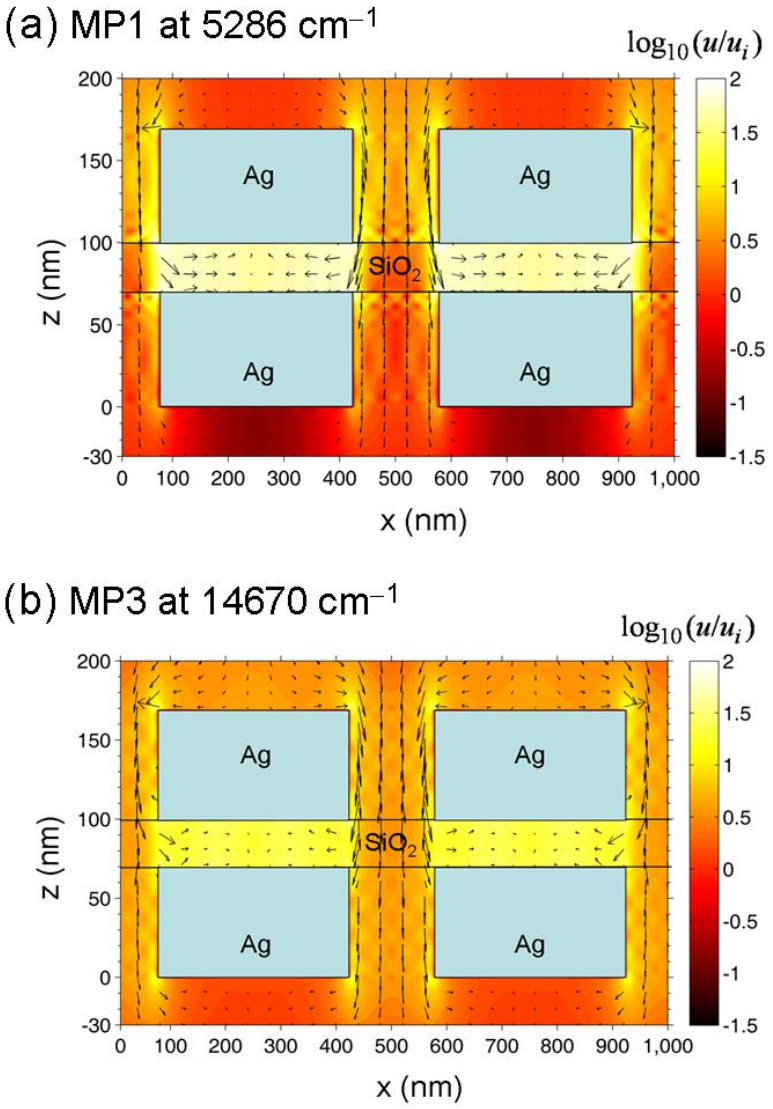

Figure 5.6 Energy density in the nanoslit array outside the Ag strips: (a) MP1 at 5,286 cm^{-1}, and (b) MP3 at 14,670 cm^{-1}. The contour represents energy density and arrows stand for Poynting vectors.

for calculating the energy density and Poynting vector can be found from Refs. [16,119]. As the electromagnetic energy is transmitted through the double-layer nanoslit array, a large amount of energy is trapped in the spacer between the metal strips. The energy density is localized and can be two orders of magnitude higher than that of the incident wave. The strong confinement of the energy density agrees well with the observed

electromagnetic field distribution. This results in strong absorption at the magnetic resonances. In terms of transmission, there exist a maximum and a minimum about each MP, as seen from Fig. 5.4(a).

5.2.3 Dispersion Relation

The spectral-directional absorptance and transmittance of the same structure as for Fig. 5.4(a) is shown in Fig. 5.7(a) and 5.7(b), respectively, as contours in the ω–k_x coordinates. The dispersion relation offers rich information regarding the effects of SPP and MPs on the radiative properties of nanoslit arrays.

The SPP dispersion curve, which can be predicted by coupling Eq. (2.33) with the grating equation, matches well with the inclined narrow band shown in Fig. 5.7(a). Note that the SPP dispersion curve is close to the light line and then folded into the region $k_x \le \pi / \Lambda$ according to the Bloch-Floquet condition. SPP induces notable directional dependence and spectral selectivity. Other dispersion curves with somewhat broader absorption peaks are attributed to the excitation of MPs with different modes. Based on the absorption spectrum at normal incidence, MP1, MP3, and CMP modes can be easily identified, while the second (MP2) and fourth (MP4) harmonic modes are only seen at oblique incidence. The lack of even harmonic modes at normal incidence may be attributed to the symmetric field distribution between the upper and lower Ag strips, leading to zero net current from the two opposite current flows. The flat MP dispersion curves, especially as seen for MP1, is a unique characteristic of MPs. The flat dispersion curve suggests that the resonance frequency is a weak function of k_x or the incidence angle. Note that the dispersion curves of MP2 and MP3 are split and that of CMP is

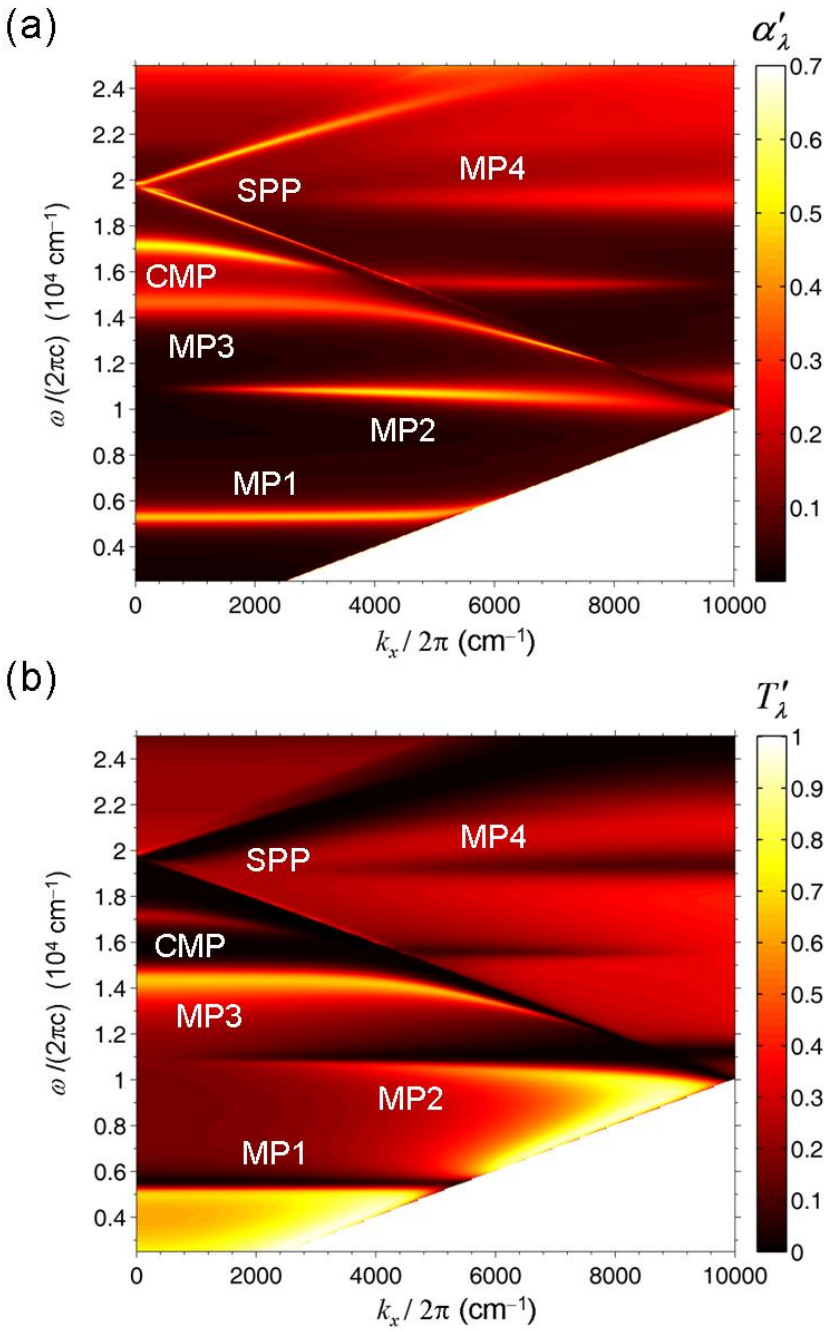

Figure 5.7 Contour plots of the spectral-directional (a) absorptance and (b) transmittance as a function of frequency and the *x*-component wavevector (ω–k_x dispersion relation) for a nanoslit array with the same parameters as those for Fig. 5.4(a).

suppressed at certain ω and k_x due to the intervening of SPP. The insensitiveness to the incidence angle can be understood in terms of diamagnetic response. As long as an

oscillating magnetic field exists along the slits (*y* direction), no matter what angle the electric field is incident on a double-layer nanoslit array, the electric currents can be induced near the surfaces of the metal strips (*x*-*z* plane) to excite the magnetic resonance. Theories like coupled SPPs or coupled evanescent waves cannot fully account for the unusual spectra at oblique angles.

Bright bands in the contour plot of Fig. 5.7(b) indicate enhanced transmission around MPs. This is more prominent for MP3, where a spectral broadening of the enhanced transmission is achieved and the resonance frequency is insensitive to the incidence direction. However, dark bands indicating suppressed transmission are also seen, suggesting that MPs work in both ways. The transmittance can be enhanced to as high as 0.85 or suppressed to near zero at certain frequencies. Therefore, MPs are one of the main physical mechanisms behind the extraordinary optical transmission in double-layer nanoslit arrays. Owing to their unique characteristic of directional independence, MPs may have promising applications in direction-sensitive optical devices, where SPP cannot be implemented. Moreover, MPs hold broader absorption or transmission bands than those associated with SPPs, and may be advantageous in applications of broadband absorption or transmission. In practice, the considered structure can be fabricated on SiO_2 substrate, and the gap in the bottom layer of slit can be filled with SiO_2 rather than air. A similar structure embedded in SiO_2 has already been fabricated by Chan *et al.* [41].

5.2.4 The LC Circuit Model and Geometric Effect

Although the electromagnetic field distribution provides illustrative explanation of magnetic resonances, quantitative evidences are required to further support the

argument. In this section, an equivalent LC circuit is employed to describe the electric current flow for the fundamental mode (MP1) in double-layer nanoslit arrays such that the magnetic resonance frequency can be analytically predicted from the circuitry impedance analysis.

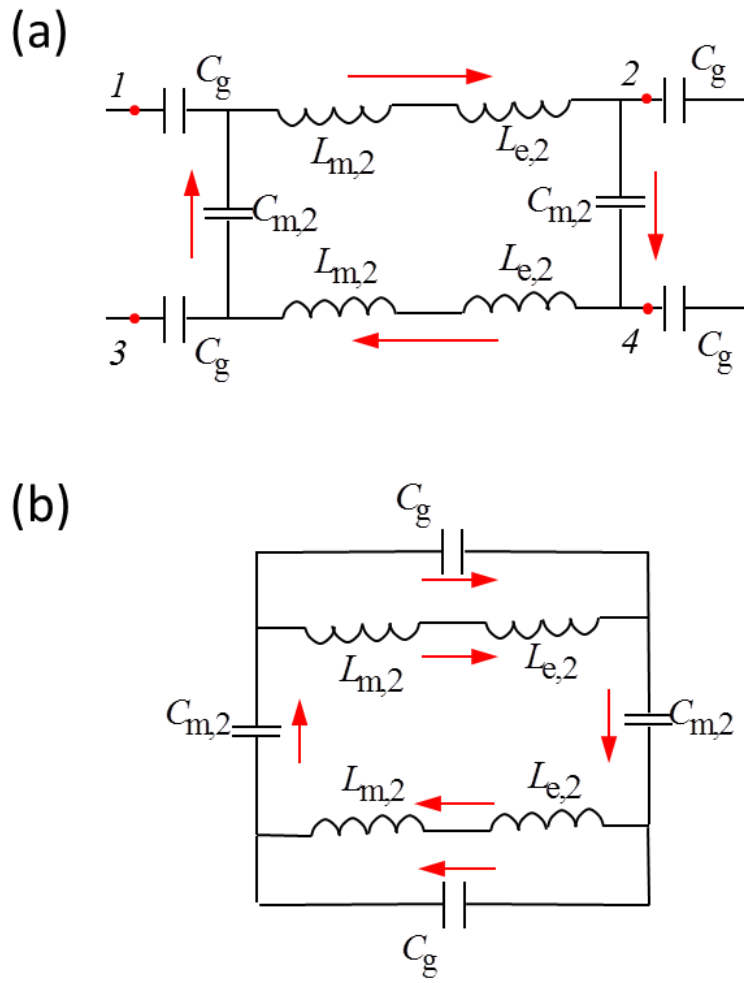

Figure 5.8 An equivalent LC circuit model the double-layer nanoslit array for the prediction of the magnetic resonance condition of the fundamental mode: (a) original circuit corresponding to the periodic structure, (b) simplified circuit for a unit cell. Arrows indicate the current flow direction.

The LC circuit method has provided researchers an effective way to find the magnetic or electric resonance conditions in micro/nano structures [75]. Figure 5.8(a)

shows the equivalent LC circuit for the considered periodic structure where magnetic resonance occurs. Note that in the figure, the LC circuit is periodic and infinitely extended to the both sides, whereas the arrows represent electric current flows in a unit cell of the double-layer nanoslit array. Here, $L_{\mathrm{m},2}$, the inductance of two parallel plates separated by a distance d, has a similar form of Eq. (2.27) as

$$L_{\mathrm{m},2} = \frac{0.5\mu_0 wd}{l} \tag{5.1}$$

The contribution of drifting electrons cannot be neglected for the nanometer structure and is given by

$$L_{\mathrm{e},2} = \frac{w}{\varepsilon_0 \omega_{\mathrm{p}}^2 A} \tag{5.2}$$

where A is the cross-sectional area of the metal strip for current flow. When $h \le \delta$, $A = hl$; but when $h > \delta$, an effective cross-sectional area $A = \delta l$ should be used. Here, δ is set to be 13 nm for simplicity because it only varies by ±1 nm in the considered frequency range. The parallel-plate capacitance between the upper and lower Ag strips is

$$C_{\mathrm{m},2} = \frac{c_1 \varepsilon_{\mathrm{d}} \varepsilon_0 wl}{d} \tag{5.3}$$

The parallel-plate capacitance C_{g} is used in the present study to account for the contribution of the air gap between the left and right Ag strips, viz.

$$C_{\mathrm{g}} = \frac{\varepsilon_0 hl}{b} \tag{5.4}$$

Due to the periodicity, location 1 and 2 are equivalent such that they can be merged together, so are location 3 and 4. As a result, the periodic circuitry is simplified to a closed one as Fig. 5.8(b). Note that, the impedance associated with C_{g} is parallel to that of

($L_{m,2}$+$L_{e,2}$) and their combination is in series with the impedance of $C_{m,2}$. After electric impedance analysis, the total impedance for the closed circuitry can be expressed as

$$Z_{tot,2} = \frac{2i\omega\left(L_{m,2} + L_{e,2}\right)}{1-\omega^2 C_g\left(L_{m,2} + L_{e,2}\right)} - \frac{2i}{\omega C_{m,2}} \tag{5.5}$$

The magnetic resonance occurs when $Z_{tot,2} = 0$, so the magnetic resonance frequency of the fundamental mode can be obtained as

$$\omega_{R,2} = \frac{1}{\sqrt{(L_{m,2} + L_{e,2})(C_{m,2} + C_g)}} \tag{5.6}$$

Since the inductances $L_{m,2}$ and $L_{e,2}$ are inversely proportional to l while the capacitances $C_{m,2}$ and C_g are proportional to l, $\omega_{R,2}$ is independent of the strip length l.

Based on Eq. (5.6), the resonance frequency of MP1 in the double-layer nanoslit array with the same parameters as those for Fig. 5.4(a) is predicted as 4,845 cm^{-1}, which has a relative difference of 8.3% compared to the RCWA calculation. Considering the approximations made in the RCWA with regards to c_1 and A, this agreement is reasonable. Further comparisons are made between RCWA and the LC model by varying the geometric parameters as discussed in the next following.

The geometric effects on the magnetic resonance conditions are illustrated in Fig. 5.9 by individually changing w, b, d, or h from the base values given in Fig. 5.4(a). Note that changing either w or b will affect the period Λ. The contour plots show the absorptance α at normal incidence calculated from the RCWA method. The calculated $\omega_{R,2}$ from the LC model are depicted as filled triangles in Fig. 5.9. Note that the LC circuit model can predict the magnetic resonance condition for the fundamental mode but not the absorptance.

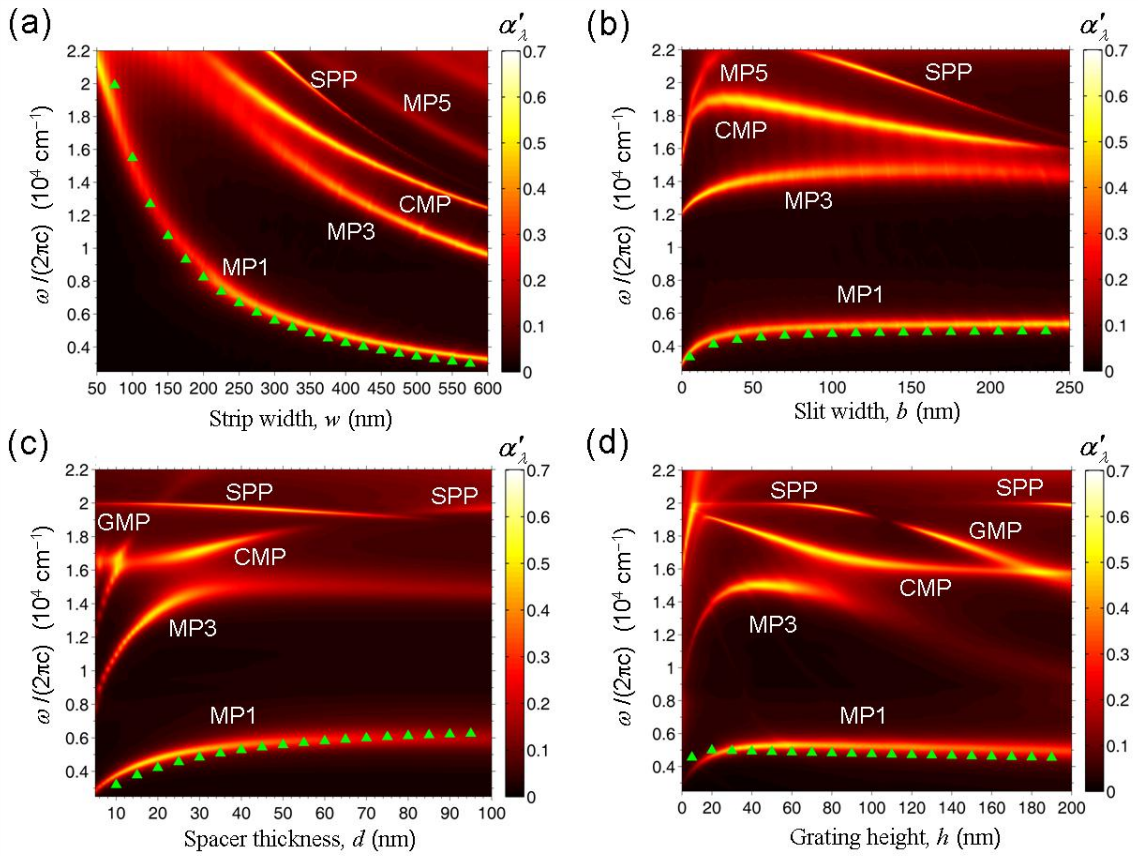

Figure 5.9 Geometric effects on the magnetic resonances in the aligned double-layer nanoslit array indicated by the contour plots of spectral-directional absorptance at normal incidence as a function of frequency ω and one varying geometric parameter: (a) strip width w; (b) slit width b; (c) spacer thickness d; (d) grating height h. Green triangles indicate the MP resonance frequency calculated from the LC circuit model for the fundamental mode.

As shown in Fig. 5.9, the calculation of the resonance frequencies of MP1 based on the LC model generally agree with the RCWA results. In Fig. 5.9(a) where the strip width effect is examined, the reduction of resonance frequency with increasing w shown by the contour plot confirms the prediction from the LC model. Note that increasing w will result in an increase in $L_{m,2}$, $L_{e,2}$, and $C_{m,2}$. At large strip width, say $w = 600$ nm where $C_{m,2}$ is 18 times larger than C_g, the latter can be neglected and thus $\omega_{R,2}$ becomes

inversely proportional to *w*. The higher-order MPs, SPP, and CMP curves are also indicated in Fig. 5.9(a). Recall that the even-order harmonic modes of MPs cannot be excited at normal incidence due to symmetry. Since C_g accounts for the electromagnetic interaction between neighboring unit cells, negligible C_g suggests the decoupling between unit cells. As a result, the resonance frequency for the m^{th}-order MPs can be estimated by $\omega_R^{(m)} = m\omega_{R,2}$. From the RCWA calculation, the ratio of the resonance frequencies between MP3 and MP1 is 2.78 for $w = 350$ nm and 2.95 for $w = 600$ nm. However, since C_g is comparable to $C_{m,2}$ for small *w*, the inverse proportionality between the resonance frequency and *w* does not hold due to the strong coupling across the gap.

The effect of slit width on the resonance frequency of MP1 is shown in Fig. 5.9(b). Since the gap capacitance C_g is inversely proportional to the slit width *b*, $\omega_{R,2}$ will increase with *b*. On the other hand, for *b* further increases, C_g becomes negligible compared to $C_{m,2}$; therefore, the dependence of $\omega_{R,2}$ on *b* diminishes. The slit width is directly related to the coupling between the left and right strips. The further apart the strips, the weaker the interactions between neighboring unit cells. When $b = 200$ nm, C_g is one fifteenth of $C_{m,2}$. The trend of the resonance frequency of MP3 is similar to that of MP1 with nearly triple the frequency. From Figs. 5.9(a) or 5.9(b) one can see that the SPP frequency decreases with increasing *w* or *b*, as a result of increasing grating period.

Figure 5.9(c) illustrates the effect of spacer thickness *d*. The resonance frequency of MP1 rapidly increases with *d* for *d* < 50 nm, but then the trend slows down with further increase in *d*. Note that for very small *d*, $L_{e,2} \gg L_{m,2}$ and $C_{m,2} \gg C_{e,2}$; hence, $\omega_{R,2}$ will increase with *d*. For sufficiently large *d* on the other hand, $L_{e,2} \ll L_{m,2}$ and

$C_{m,2} \ll C_g$; therefore $\omega_{R,2}$ will decrease with increasing d. Calculations show that there is a plateau in $\omega_{R,2}$ for 50 nm < d < 150 nm. Besides, for large d, the absorptance values corresponding to MPs are significantly reduced due to the weak electromagnetic coupling across thick spacers. The excitation frequency of the SPP at the air/Ag interface remains around 20,000 cm^{-1} when d is changed. The SPP curves are truncated due to the interaction between the SPP and other resonance modes. When d > 100 nm, SPP between Ag and SiO_2 as well as bulk polaritons (guided waves) inside the SiO_2 layer between the gratings can be excited in the frequency region of interest. Since the present study focuses on magnetic resonances, these modes are not plotted in Fig. 5.9(c). Note that CMP mode can be identified based on the resonance frequency in Fig. 5.4(a) with the base parameters. Furthermore, GMP mode appears with small spacer thickness or thick nanoslit layers. At d = 0, the double-layer nanoslit array reduces to a single-layer nanoslit array with a thickness of 140 nm, whose GMP mode occurs at 16,544 cm^{-1}. It should be noted that coupled SPP between the SPPs at the Ag/SiO_2 interfaces does not appear in the considered spectral range.

The effect of grating height (or nanoslit layer thickness) h is presented in Fig. 5.9(d). The contour plot of α shows that the resonance frequency of MP1 increases rapidly for thin nanoslit layers and, after reaches a maximum, decreases gradually for thicker nanoslit layers. The LC model predicts the correct trend but with some discrepancies especially for small h values. For $h < \delta$, $C_{m,2} \gg C_g$ and $L_{e,2} \gg L_{m,2}$. The dependence of $\omega_{R,2}$ on h arises from the inverse proportionality between $L_{e,2}$ and A with a relation of $\omega_{R,2} \propto \sqrt{h}$. But for $h > \delta$, A and $L_{e,2}$ are taken as independent of h. Hence,

$\omega_{R,2}$ will slightly decrease as h further increases due to the increase of C_g. Note that $C_{m,2} > C_g$ within the considered range of h. In the LC model calculation, it is simply assumed that the electric current only flows within the depth of δ away from the metal surface when $h > \delta$, or within the entire thickness h otherwise. As a matter of fact, due to the nonuniform charge distribution from the surface into the metal, the assumption seems to underpredict the average current depth for $h > \delta$ and overestimate it for $h \le \delta$, leading to the deviation from the RCWA calculation. This explains why the resonance frequencies of MP1 are underestimated by the LC model in most cases as compared with the contour plots obtained from RCWA shown in Fig. 5.9. Besides, the accuracy of the LC model is subject to the approximation of the factor c_1. As discussed previously, the resonance frequency of MP3 can be estimated by triple that of MP1 when C_g is negligibly small. This agrees well for small h as shown by the contour in Fig. 5.9(d). However, as grating height increases, MP3 becomes weak for h > 70 nm and its resonance frequency drops quickly since C_g becomes comparable to $C_{m,2}$. In fact, LC circuit can also be used to model the electric current loops for MP3 mode, but its resonance condition is not as easy to solve as MP1 from the circuitry impedance analysis. The faster descending MP3 curve may be attributed to the more dominant role of C_g in determining the resonance frequency than that for MP1. In addition, GMP emerges for h > 140 nm and can interact with CMP to enhance absorption around h = 180 nm at some specific frequencies.

5.2.5 Lateral Displacement Effect

The alignment between the layers in a double-layer nanoslit array can significantly affect the radiative properties and may be a useful way in controlling the

radiative properties in practice [41]. Figure 5.10 shows the contour plots of normal absorptance and transmittance in terms of the frequency ω and the normalized lateral displacement Δ/Λ. The results are calculated with RCWA based on the geometry shown in Fig. 5.3(b). The spectral radiative properties at normal incidence for $\Delta = 0.25\Lambda$ and $\Delta = 0.5\Lambda$ are plotted in Fig. 5.11 for clarity.

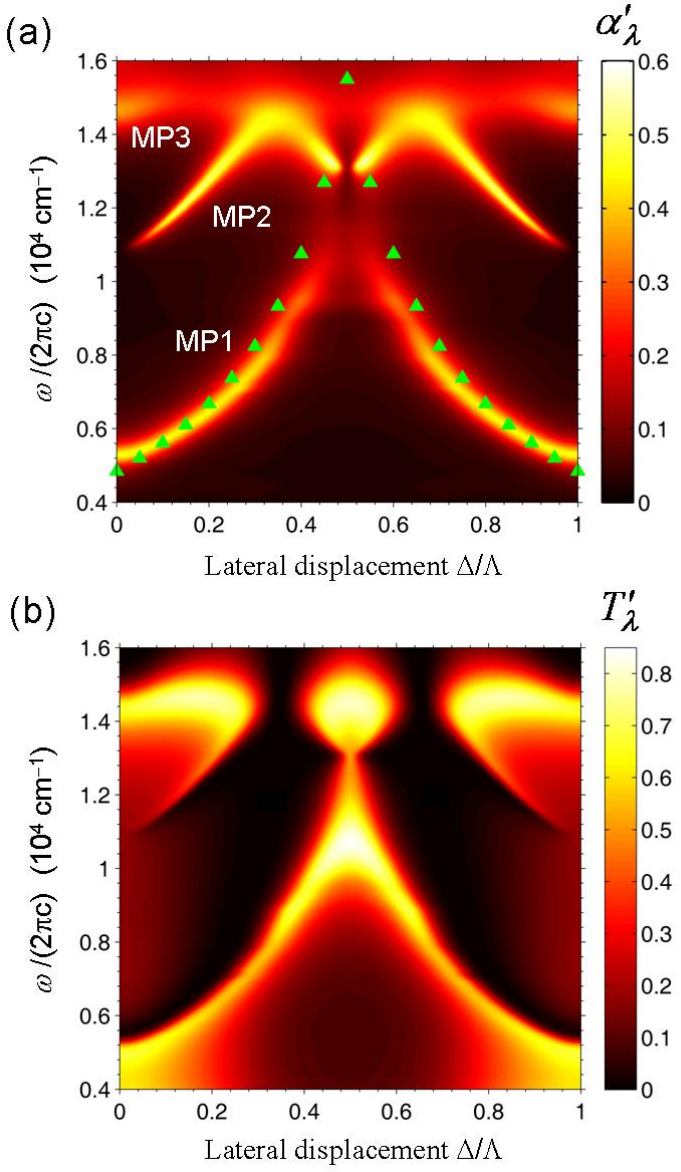

Figure 5.10 Lateral displacement effect on the magnetic resonance for misaligned double-layer nanoslit arrays: (a) absorptance and (b) transmission at normal incidence as contour plots in terms of the frequency ω and lateral displacement Δ.

In Fig. 5.10, the lateral displacement changes from zero to one period, and the contour plots show symmetry with respect to the centerline corresponding to half-period misalignment. Note that only the results at frequencies between 4,000 cm^{-1} and 16,000 cm^{-1} are presented to facilitate the discussion of the lateral displacement effect, since strong interactions among different MP and SPP modes appear at higher frequencies. Three major absorption peaks can be seen in Fig. 5.10(a), two of which are recognized as MP1 and MP3 based on the results for the aligned case (Δ/Λ = 0 or 1). The resonance frequency at MP1 increases with the degree of misalignment, whereas MP3 shows little dependence on Δ. Interestingly, MP2 can also be excited in misaligned double-layer nanoslit arrays, since geometrical symmetry no more exists. The frequency for MP2 first increases with misalignment and then decreases as Δ/Λ approaches 0.5.

It should be noticed that around $\Delta = 0.5\Lambda$ the absorption at all three MP modes are so weak such that extraordinary transmission with a maximum of 0.835 can be achieved with a broad spectral band as shown in Figs. 5.10(b) and 5.10(b). Notice that there is no direct line of sight for this misaligned case and the extraordinary phenomena is indeed a resonance effect caused by the excitation of MPs. Enhanced transmission associated with MPs can be seen in other regions as well with specific frequencies and lateral displacement. When Fig. 5.11(a) is compared with Fig. 5.4(a), the absorptance peaks are shifted to the frequencies of 6,990 cm^{-1}, 13,452 cm^{-1} and 17,656 cm^{-1}, while the SPP mode at 20,000 cm^{-1} is unaffected. For $\Delta = 0.5\Lambda$ as shown in Fig. 5.11(b), a broad transmission band appears with double peaks at 10,690 cm^{-1} and 14,572 cm^{-1} in the near infrared. This is consistent with Fig. 5.10(b).

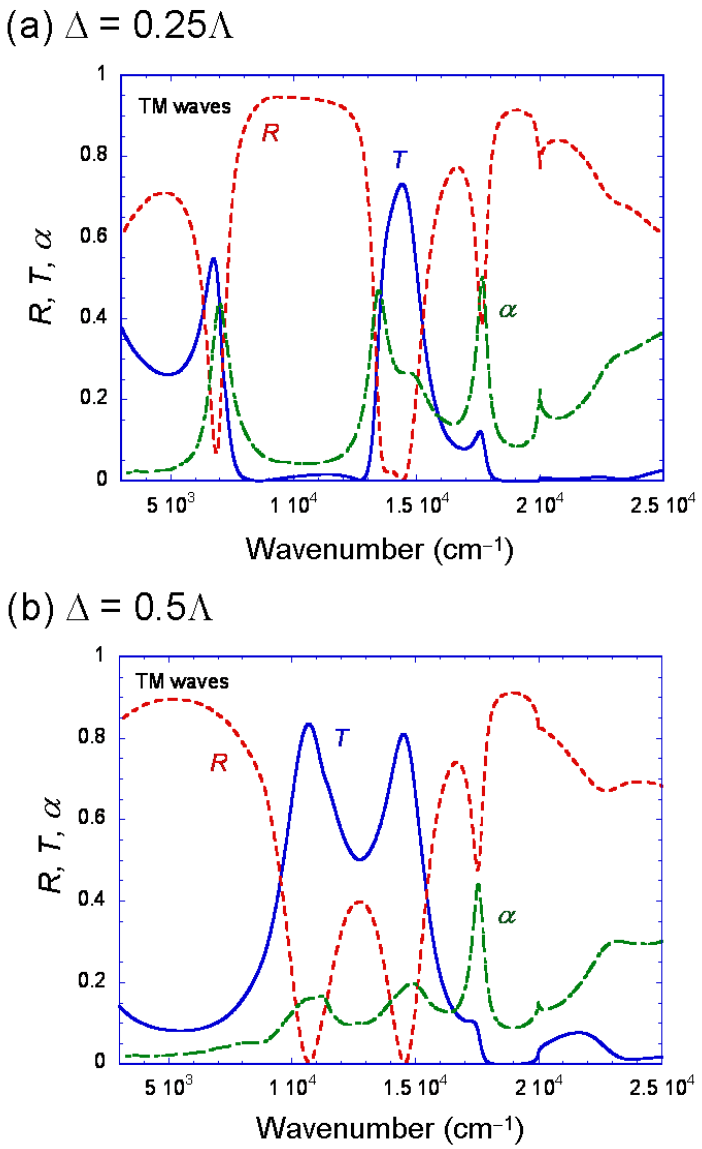

Figure 5.11 Calculated radiative properties at normal incidence when the double-layer nanoslit arrays are misaligned by (a) one-quarter period, and (b) half period.

The field distributions at the absorption peaks for misaligned double-layer nanoslit arrays are shown in Fig. 5.12 for the cases of $\Delta/\Lambda = 0.25$ and 0.5. Recall that the field distributions are shown in Fig. 5.5 for the aligned case. The electromagnetic field at 6,990 cm^{-1} with $\Delta = 0.25\Lambda$ is confined only in the overlapping region between the upper and lower metal strips, as shown in Fig. 5.12(a), indicating a reduced effective metal strip

width. MP1 is identified as the only anti-node in the spacer. Similarly at 13,452 cm^{-1} as shown in Fig. 5.12(b), MP2 mode is confirmed with a reduced effective strip width. The situation is different when $\Delta = 0.5\Lambda$. At 10,690 cm^{-1} as shown in Fig. 5.12(c), the electromagnetic field is confined at the both ends of the strips, and the small overlapping region yields weak field localization that is responsible for the transmission enhancement. At 14,572 cm^{-1}, a GMP mode is visualized by the induced currents in the gaps as shown in Fig. 5.12(d). When one nanoslit layer is laterally displaced, the charge distribution in the misaligned double-layer nanoslit array will change and cause the magnetic resonance condition to vary. As a result, intervention among different modes of MPs, GMPs, and CMPs would occur with lateral displacement.

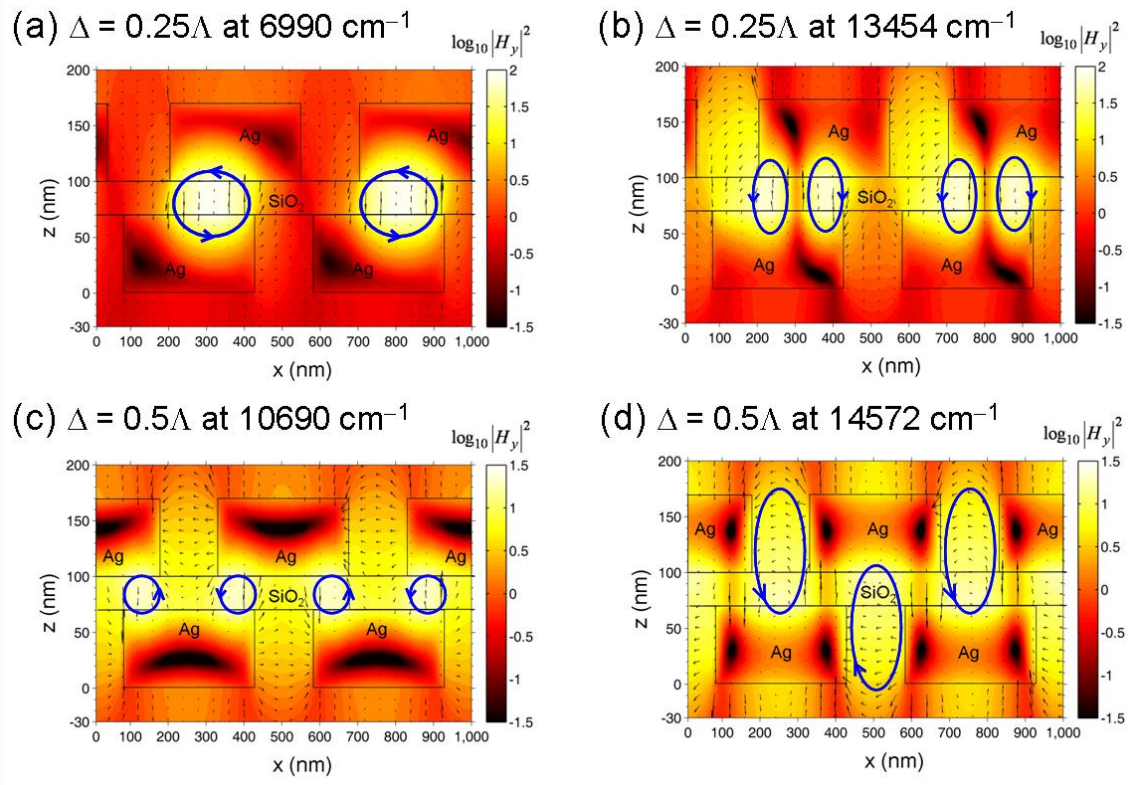

Figure 5.12 Different MP modes illustrated by the electromagnetic fields in misaligned double-layer nanoslit arrays at normal incidence: (a) $\Delta/\Lambda = 0.25$ at 6,990 cm^{-1}; (b) $\Delta/\Lambda = 0.25$ at 13,454 cm^{-1}; (c) $\Delta/\Lambda = 0.5$ at 10,690 cm^{-1}; (d) $\Delta/\Lambda = 0.5$ at 14,572 cm^{-1}.

Based on the observation in the field distribution, an effective metal strip width as $w' = w - \Delta$ (when $\Delta \le 0.5\Lambda$) is used in Eq. (5.6) to estimate the resonance frequency of MP1 with different degrees of lateral displacement, as depicted as triangles in Fig. 5.10(a). The agreement with the RCWA results indicates that the magnetic resonance is indeed responsible to the change of the radiative properties. However, the prediction begins to deviate at $\Delta = 0.3\Lambda$ and the discrepancy reaches the largest at $\Delta = 0.5\Lambda$. This may be due to the fact that the LC model shown in Fig. 5.8 cannot represent the charge distribution when one metal strip starts to overlap with two strips in the other layer.

5.3 Phonon-Mediated Magnetic Polaritons

As the counterpart of surface plasmon polariton, surface phonon polariton has wide applications in coherent thermal emission [90], transmission enhancement [120], near-field radiative heat transfer [121,122], and near-field thermal imaging [79]. An intriguing question arises naturally: whether or not the magnetic polariton has its counterpart in polar materials and what potential applications it may have. Actually polar materials such as SiC exhibit a negative real part of permittivity within the phonon absorption band or called the reststrahlen band [1], based on which the similarity between surface plasmon and phonon polaritons exists.

The geometries of the slit array and the deep grating made of SiC are shown as insets in Figs. 5.13(a) and 5.13(b), respectively [123]. For the deep grating, the underlying SiC is treated as a semi-infinite medium. The RCWA computes the spectral directional reflectance for TM waves. For the deep grating structure, the spectral-directional emittance can be calculated from $\varepsilon'_\lambda = 1 - R$ according to Kirchhoff's law. The

frequency-dependent dielectric function of SiC $\varepsilon_{\text{SiC}}(\nu)=\varepsilon'+i\varepsilon''$ is obtained from the Lorentz-oscillator model, described in Eq. (3.4).

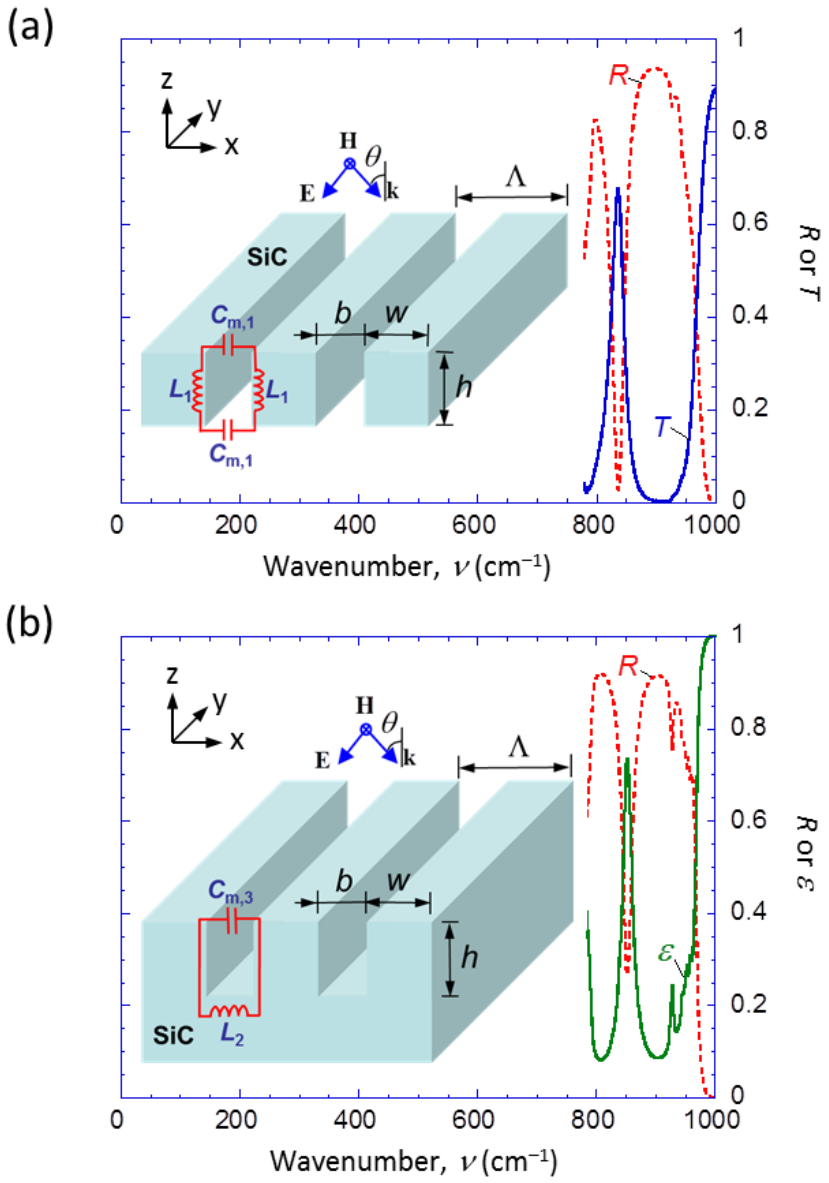

Figure 5.13 Microstructures made of SiC and calculated radiative properties. (a) Calculated spectral-directional reflectance *R* (dashed) and transmittance *T* (solid) at normal incidence for (a) the slit array structure, shown as inset along with the LC circuit model; (b) the deep grating structure, shown as inset along with the LC circuit model.

Figures 5.13(a) and 5.13(b) show the calculated radiative properties for the corresponding structure represented in the insets in the reststrahlen band of SiC at normal incidence. The period Λ is 5 μm and the strip width w is 4.5 μm for both structures, while the height h is 3 μm for the slit array and 1 μm for the deep grating, respectively. Reflectance dips can be seen in the spectra of both structures. A transmittance peak occurs at 836.5 cm^{-1} with a magnitude of 0.676, indicating transmission enhancement by the slit array. Two emittance peaks can be seen in Fig. 5.13(b): the first at 852.5 cm^{-1} has a peak value of 0.734 and the second at 928.7 cm^{-1} has a smaller peak of 0.244. The emission peaks can be applied as selective coherent thermal emission sources. It should be mentioned that both structures are highly reflective for TE waves within the reststrahlen band, similar to those metallic grating [16]. For the case when the plane of incidence is not perpendicular to the grooves, however, both TE and TM waves can have a magnetic field component that is parallel to the grooves. This in turn can result in the excitation of magnetic polaritons.

To gain a better understanding about how the radiative properties vary spectrally and directionally, contour plots of transmittance for the slit array and emittance for the deep grating are shown in Figs. 5.14(a) and 5.14(b), respectively, as functions of the wavenumber and the parallel wavevector component k_x. In Fig. 5.14(a), a flat bright band (labeled as MP1) appears around 836.5 cm^{-1}, implying that the transmission enhancement for the slit array is independent of θ. Similarly, two flat emittance bands, labeled as MP1 and MP2 in Fig. 5.14(b), show up for the deep grating, corresponding to the emittance peaks in Fig. 5.13(b).

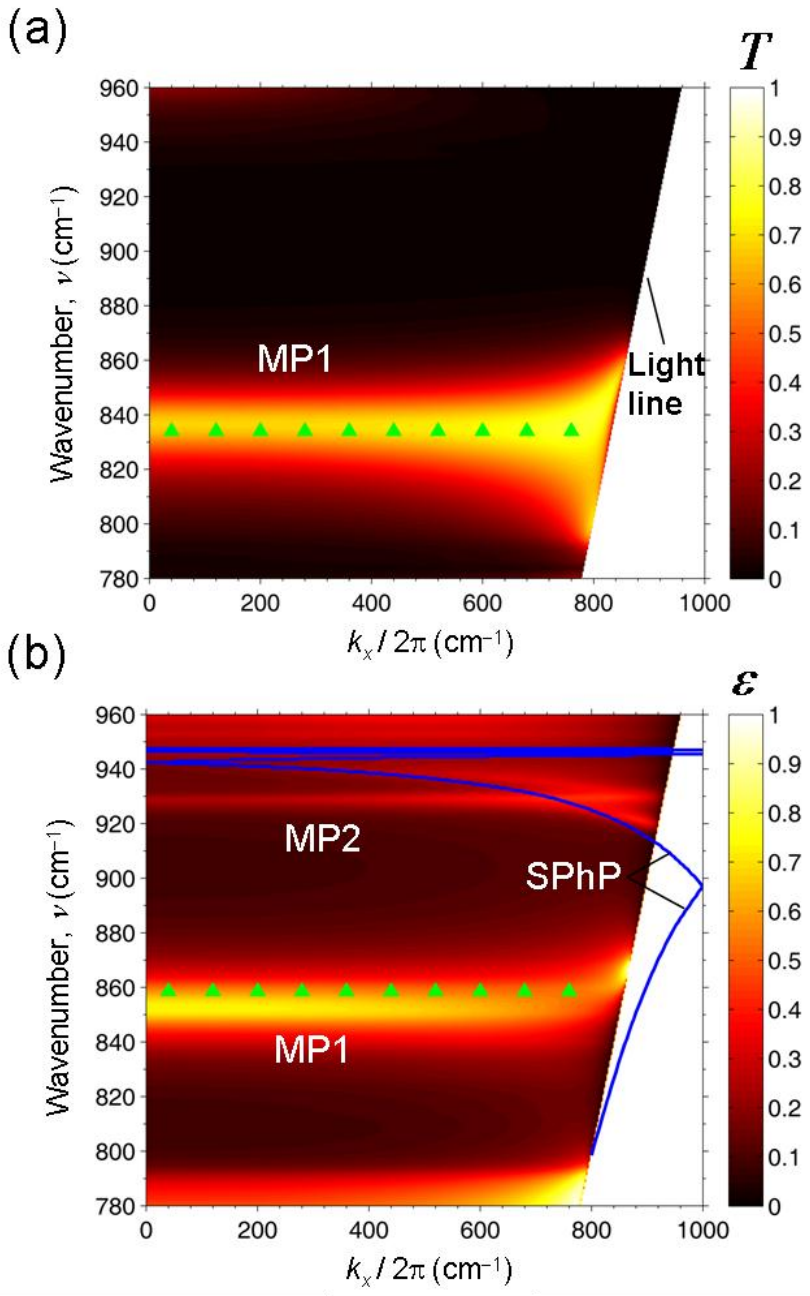

Figure 5.14 Contour plots of the radiative properties as functions of wavenumber and the parallel wavevector component. (a) Transmittance for the slit array shown in Fig. 5.13(a). (b) Emittance for the deep grating shown in Fig. 5.13(b). The dispersion curves of surface phonon polaritons at the SiC-vacuum interface are also shown and indicated as SPhP. Triangles show the frequency of the fundamental mode of magnetic polariton (MP1) predicted from the LC circuit model.

Based on Eq. (2.33), the dispersion of the SPhP can be calculated and agrees reasonably with the inclined band that intersects MP2. Additional bands at higher frequencies are due to multiple folding of SPhP. Obviously, SPhP cannot be excited by propagating waves at frequencies below 913 cm^{-1}. In the following, LC circuit models are used to explain magnetic resonances in the SiC microstructures.

Here, a modified LC model is used considering the dielectric properties of polar materials to verify the magnetic resonance in the SiC microstructures. The equivalent LC circuits for one unit cell are depicted on the structures in the insets of Figs. 5.13(a) and 5.13(b), neglecting resistive elements. Though the structures are periodic, each slit (or groove) can be considered as an isolated unit cell if the width of the strip or ridge is much greater than the radiation penetration depth within the phonon absorption band. Thus, the resonance condition of the entire structure can be obtained simply from the LC circuit for a single slit or groove.

The LC circuits are somewhat different for the two structures shown in Figs. 5.13(a) and 5.13(b). For the slit array, the capacitance between left and right strips can be approximated as a parallel-plate capacitance given by $C_{m,1}$ in Eq. (2.26). The inductance L_1 consists of two contributions. The first one is the mutual inductance obtained from parallel-plate inductance as $L_{m,1}$ given by Eq. (2.27). The other one arises from kinetic inductance that originates from the kinetic energy of mobile charge carriers, such as free electrons in metals or ions (bound electrons) in polar materials. At optical frequencies, the dimension of micro/nanostructures is comparable or smaller than the wavelength, and the contribution from the kinetic inductance becomes comparable to or even larger than the magnetic inductance [74].

The frequency-dependent complex conductivity of SiC can be expressed as $\tilde{\sigma} = \sigma' + i\sigma''$. The complex impedance ($Z_k \equiv R_k - i\omega L_k$) is inversely proportional to the conductivity, i.e., $Z_k = s[(\sigma' + i\sigma'')A_{eff}]^{-1}$. Here, s is the distance the induced current circulates in the open loop and A_{eff} is the effective cross-sectional area for the induced electric current due to the skin effect and nonuniform charge distribution. Since $\sigma' << \sigma''$ for SiC in the absorption band, one obtains $\omega L_k \approx s/(\sigma'' A_{eff})$. Using the relationship $\sigma'' = -\omega\varepsilon_0\varepsilon'$ [1], the kinetic inductance can be approximated as $L_k = -s/(\omega^2\varepsilon_0\varepsilon' A_{eff})$. Note that the real part of the dielectric function of SiC is negative for $\nu_{TO} < \nu < \nu_{LO}$. By assuming that the induced current flows near the strip surface within a depth approximately equal to the power penetration depth δ, the kinetic inductance for the slit array can be expressed as

$$L_{k,1} = -h/(\omega^2\varepsilon_0\varepsilon' l\delta) \tag{5.7}$$

Note that the penetration depth δ for SiC is less than 1 μm in the frequency range from 781.4 cm^{-1} to 953.8 cm^{-1} with a minimum of 53.4 nm at 794.3 cm^{-1}. Similar to Eq. (2.29), the total impedance of the LC circuit shown in Fig. 5.13(a) can be expressed by

$$Z_{tot,1} = i2\omega\left(L_{m,1} + L_{k,1} - \frac{1}{\omega^2 C_{m,1}}\right) \tag{5.8}$$

The magnetic resonance condition $\omega_{R,1}$ for the fundamental mode of magnetic polaritons can be obtained by finding the root of $Z_{tot,1} = 0$. Note that it is an implicit equation since ε' and δ are frequency-dependent. Similarly, the magnetic resonance condition for the deep grating can be solved by zeroing

$$Z_{tot,3} = i\omega\left(L_{m,3} + L_{k,2} - \frac{1}{\omega^2 C_{m,3}}\right) \tag{5.9}$$

where $L_{m,3} = \mu_0 hb/l$ is the magnetic inductance based on the coil inductance, $L_{k,2} = -(2h+b)/(\omega^2 \varepsilon_0 \varepsilon' l \delta)$ is the kinetic inductance of the cavity, and $C_{m,3} = c_2 \varepsilon_0 hl/b$ is the gap capacitance. Again, a numerical factor c_2 is introduced to account for the nonuniform charge distribution between the ridges of the grating. Since there is only one capacitor $C_{m,3}$ in the circuit for the deep grating, rather than two $C_{m,1}$ for the slit array, the reasonable range for c_2 can be estimated as twice of that of c_1. Note that the magnetic resonance conditions are independent of the length l, i.e., the dimension in the y direction.

The exact values of the numerical factors c_1 and c_2 are difficult to determine without knowing the detailed charge distribution near the strip surfaces. Here, $c_1 = 0.22$ and $c_2 = 0.55$ are chosen for the LC models to fit well the resonant conditions of MP1 in Fig. 5.13. It is expected that $c_2 \neq 2c_1$ since the charge distribution in the deep grating should be different from that in the slit array due to the existence of SiC substrate. The fundamental modes of the magnetic polariton predicted by the LC circuit model are at 833.1 cm^{-1} for the slit array and 858.5 cm^{-1} for the deep grating, respectively, and are indicated as triangles in Figs. 5.14(a) and 5.14(b). The magnetic resonance frequency is independent of k_x, and this distinguishes magnetic polaritons from the Fabry-Perot-type cavity resonance.

Figure 5.15 shows how the magnetic resonance frequencies change with one varying geometric parameter such as height h, slit width b or period Λ while other parameters are kept at base values as those in Fig. 5.13. The contour plots obtained from RCWA at normal incidence exhibit multiple bright bands, indicating either transmission or emission enhancement for slit arrays or deep gratings respectively. In Figs. 5.15(a) and 5.15(b), the resonance frequency decreases with increasing height for a specific mode,

suggesting that the frequencies for the enhanced transmission or emission peaks can be tuned by varying the height. The LC model prediction for the fundamental mode (MP1) is shown with triangles, which match well with the resonance band obtained from RCWA.

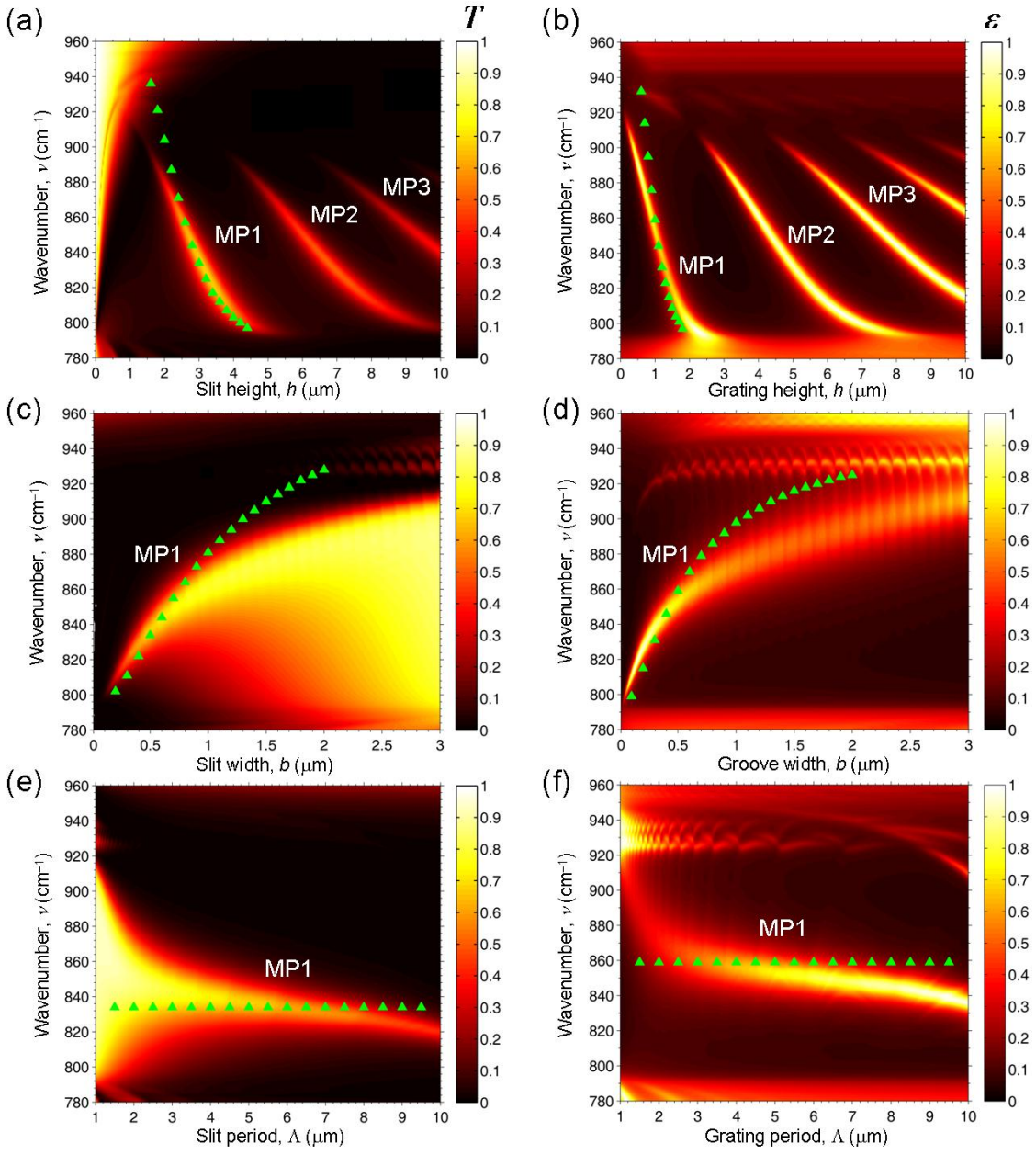

Figure 5.15 Geometric effects on the magnetic polaritons for (a, c, e) the slit array and (b, d, f) the deep grating: (a, b) height *h* effect, (c, d) slit width *b* effect, and (d, f) period Λ effect. The MP1 resonance frequency calculated from the LC model is shown as triangles.

At high frequencies, the LC prediction deviates from the RCWA result, because of the interaction with SPhPs similar to those observed for metallic slit arrays as discussed in Sections 5.1 and 5.2. Higher-order modes of magnetic polaritons also occur for thicker slit arrays or deeper gratings, marked as MP2 and MP3 in the figures.

The slit width effect on the resonance frequency can be seen from Figs. 5.15(c) and 5.15(d) for both structures. Larger slit width will result in increased resonance frequency. The LC circuit model prediction agrees well with RCWA results at low frequencies. However, the existence of SPhPs around 940 cm^{-1} causes the suppression of magnetic polaritons at higher frequencies, resulting in larger discrepancies between RCWA and LC calculations.

Furthermore, under the assumption that the strip width is much larger than the penetration depth, the LC model predicts that the period should have no influence on the resonant condition of magnetic polaritons for both structures. This can be seen from the triangles that are aligned horizontally in Figs. 5.15(e) and 5.15(f) for slit arrays and deep gratings, respectively. However, large deviations between RCWA results and LC model prediction on the resonance frequency of MP1 can be seen for small Λ values. This is because the individual slit or groove cannot be treated isolated anymore for small strip width, and the assumption for the LC model is not valid. As the period increases, the contour plots based on RCWA calculation show that the resonance frequency of MP1 decreases. This again is attributed to the interaction with SPhPs. Due to the folding of SPhP dispersion curves, the excitation condition for SPhPs at normal incidence will shift to lower frequencies for larger grating periods. Even though the simple LC model is not able to consider the interaction with SPhPs, it predicts the resonant condition of MP1

within 3% from RCWA results for the periods from 3 μm to 10 μm. Subsequently, the magnetic polaritons are suppressed to lower frequencies. In general, the LC prediction agrees well with RCWA calculations, demonstrating that magnetic polaritons are indeed responsible for the transmission or emission enhancement in the SiC structures.

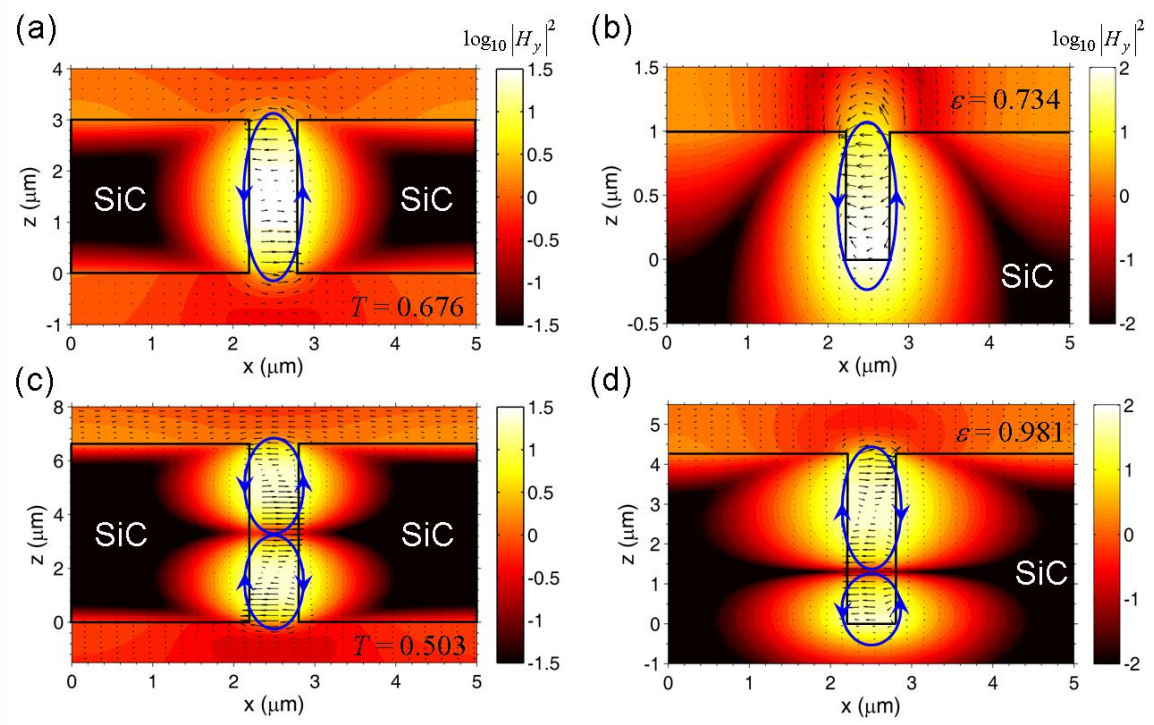

Figure 5.16 Electromagnetic field patterns for magnetic polaritons (not to scale): the fundamental mode (MP1) for (a) the slit array at 836.5 cm^{-1} and (b) the deep grating at 852.5 cm^{-1}; the second harmonic mode (MP2) at the same frequency as MP1 for (c) the slit array but with h = 6.64 μm and (d) the deep grating but with h = 4.28 μm. The corresponding transmittance or emittance values are indicated in the figures.

The electromagnetic field distributions calculated by the RCWA at the excitation frequencies are plotted in Fig. 5.16 at normal incidence. Figures 5.16(a) and 5.16(b) show the field patterns for MP1 excited at 836.5 cm^{-1} for the slit array and at 852.5 cm^{-1} for the deep grating, with the same geometries used in Fig. 5.13. The field distribution reveals strong magnetic field confinement (up to an order of magnitude greater than that of the

incidence wave) inside the slit or groove between the neighboring SiC strips or ridges. The electric field circulates around the slit or groove to form a loop, denoted by ovals with arrows indicating the direction, associated with the antinode of the magnetic field. This is the typical characteristic of the diamagnetic response. The number of induced electric loops or that of antinodes of the magnetic field indicates the order of the magnetic polaritons. The transmission or absorption (emission) enhancement arises as a result of the field confinement.

The field distributions for MP2 are shown in Figs. 5.16(c) and 5.16(d), but with different heights (h = 6.64 μm for the slit array and h = 4.28 μm for the deep grating) in order to obtain the same resonance frequency as MP1 for the corresponding structure. Similar behavior for the magnetic and electric fields can be seen with two antinodes, indicating the second-harmonic mode of magnetic polaritons. It should be emphasized that MP2 helps localize more energy than MP1 into the cavity region, so that emittance as high as 0.981 can be achieved for the deep grating at MP2. Coherent thermal emission using dielectric deep grating structures has been proposed [12], but the underlying mechanism was attributed to cavity resonance modes without considering magnetic polaritons. The insight gained in this work is useful for the design of deep gratings as coherent thermal emission sources.

The field distributions of magnetic polaritons in the SiC microstructures show similar features as that in similar metallic structures: strong magnetic field localization and induced electric currents. Nevertheless, there exists a fundamental difference. In metals, the induced electric current is caused by the motion of free charges such as free electrons, whereas in polar materials, the vibration of ions or bound charges at high

frequencies creates the electric current. In other words, magnetic polaritons excited inside polar materials are mediated by optical phonons. Examples of such materials include SiO_2, CaF_2, GaAs, GaN, MgF_2, MgO, ZnSe, Al_2O_3, TiO_2, $SrTiO_3$, etc. Proper selection of materials will allow tuning the transmittance and reflectance spectra for infrared applications, as well as building coherent thermal emission sources at high temperatures for energy harvesting.

5.4 Coherent Thermal Emission by Excitation of Magnetic Polaritons

From the discussion above, the magnetic resonance has been confirmed as a physical mechanism to control the radiative properties of single- and double-layer grating structures. Based on the excitation of magnetic polaritons, an innovative coherent emission source is designed in the near infrared region by simply replacing the bottom Ag grating layer with an opaque Ag film from the previous double-layer slit array in Fig. 5.3(a) [62]. The thicknesses for the top Ag grating layer and the SiO_2 dielectric spacer are both changed to 20 nm, and the strip width is set to be the half of grating period Λ = 500 nm. Figure 5.17 shows the spectral reflectance at $\theta = 25\,°$ calculated from the RCWA for TM waves, and an oblique angle is considered here to show the second mode of magnetic polaritons. For comparison, the reflectance of a simple Ag grating on the opaque Ag substrate (the case when dielectric spacer thickness d = 0) is also calculated to demonstrate the effect of the existence of the dielectric spacer. The proposed coherent emission source exhibits four reflectance dips, one of which is at the same frequency with that from the simple grating. These two sharp reflectance dips are both due to the excitation of SPP at the Ag/vacuum interface, and their excitation frequency 13780 cm^{-1}

agrees well with the prediction from the SPP dispersion curve as described in Eq. (2.33). Other three reflectance dips at 5670 cm^{-1}, 11490 cm^{-1}, and 16095 cm^{-1} are associated with the fundamental, the second and the third harmonic mode of magnetic polaritons.

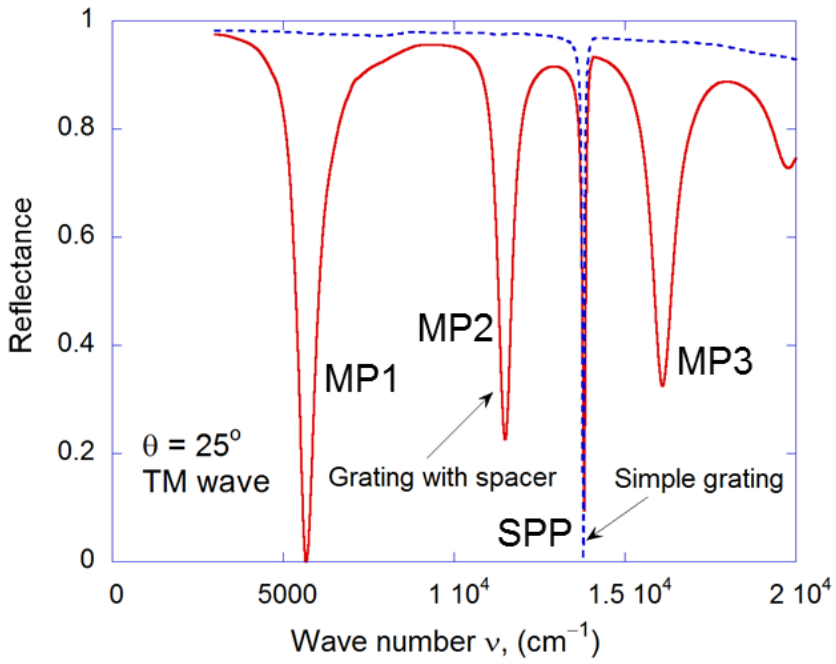

Figure 5.17 The spectral directional reflectance at $\theta = 25\ ^{o}$for the proposed grating with a spacer structure as a coherent emission source; the reflectance for the case without spacer is also plotted for comparison.

The underlying mechanism of magnetic metamaterials can be explained as follows. The oscillating magnetic field produces a current in the metal strip in the *x* direction and another near the surface of the metal film in the opposite direction. The anti-parallel currents result in a diamagnetic response. The diamagnetic response is then coupled to the metallic film to cause a magnetic polariton with a fundamental mode at the wave number around 5,670 cm^{-1}. Magnetic polaritons of the second and higher order harmonics can also be excited. Magnetic polaritons, however, are distinct from the surface plasmon such that the resonance frequencies depend strongly on the strip width

but remain almost unchanged with the grating period Λ. This is because the magnetic polariton is not induced by the diffracted evanescent waves but induced by the magnetic element formed in the modulated structure.

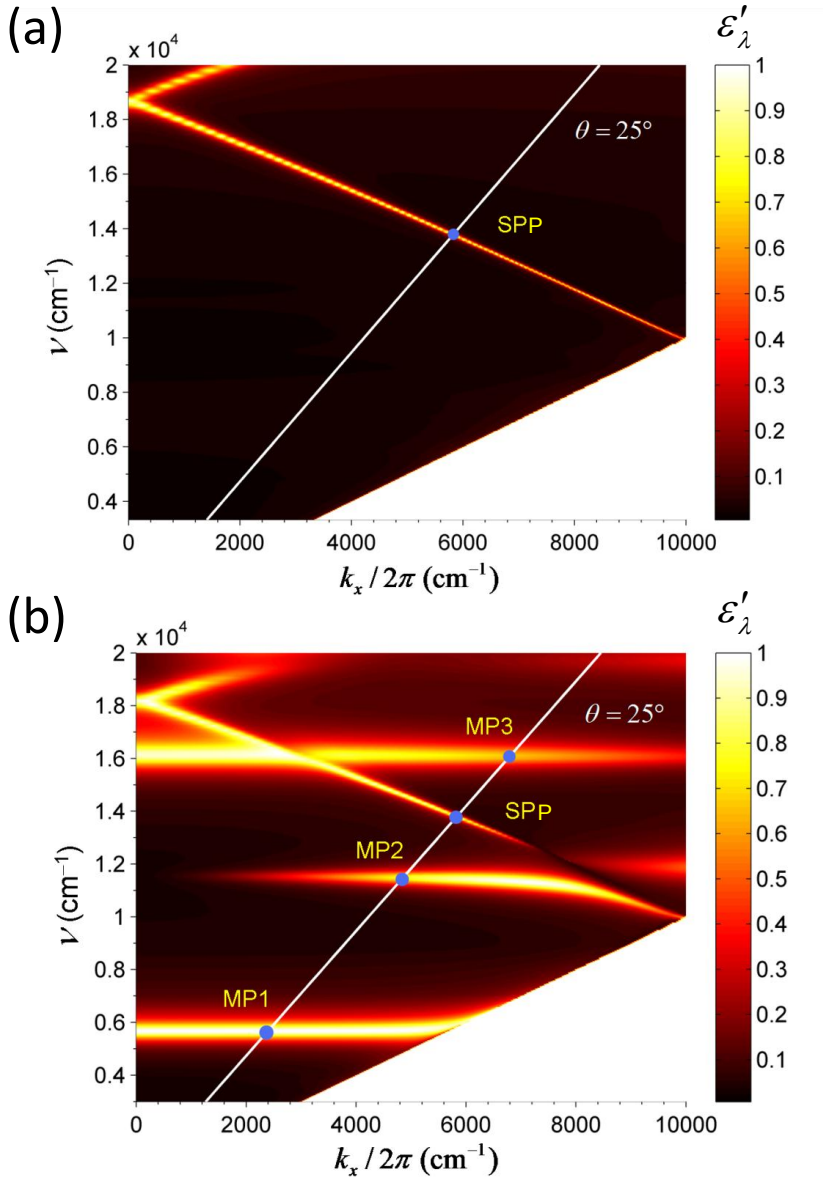

Figure 5.18 Contour plot of the spectral-directional emissivity of (a) the simple grating and (b) the Ag grating and Ag film separated by a SiO_2 spacer. The geometric parameters are the same as those in Fig. 5.17. At $\theta = 25°$, surface plasmon resonance is labeled as SPP, while the magnetic polaritons are labeled as MP1, MP2, and MP3 for the fundamental, second, and third harmonic modes, respectively.

Figure 5.18 shows the contour plot of the spectral-directional emissivity ε'_ν cfor the simple grating (a) and the proposed structure with the spacer (b) in terms of ν and the parallel wavevector component k_x (divided by 2π). As can be seen clearly from Fig. 5.18(a), the grating results in folding of the dispersion curves at $k_x = \pi/\Lambda$, $2\pi/\Lambda$, etc. The emissivity is greatly enhanced when surface plasmons are excited. The branch at $\nu <$ 18,200 cm^{-1} corresponds polaritons coupled with the −1 diffraction order and the high-frequency branch is associated with the +1 diffraction order [78]. The intersection of the surface plasmon dispersion line and the inclined white line, representing $\theta = 25°$, is marked as SPP and corresponding to the reflectance dip shown in Fig. 5.17 due to surface plasmon resonance. In general, the resonance condition of SPPs depends strongly on both ν and k_x; thus, the emissivity peak exhibits the spectral and directional selectivity [11].

The contour plot of the emissivity for the grating with spacer exhibits several additional bands with enhanced emissivity as shown in Fig. 5.18(b). The surface plasmon dispersion is very similar to that shown in Fig. 5.18(a). The multiple magnetic polariton branches correspond to the fundamental, second, and third harmonic resonances and their intersection with the line $\theta = 25°$ are denoted by MP1, MP2, and MP3, which are associated with the reflectance dips at ν = 5,670, 11,490, and 16,095 cm^{-1}, respectively shown in Fig. 5.17(b). In contrast to the surface plasmon, k_x has little effect on resonance conditions for the magnetic polaritons because the magnetic resonance conditions are largely determined by w rather than Λ. Furthermore, the magnetic polaritons are localized in the vicinity of metal strips and are not coupled with each other due to the 250-nm air gap [32]. Hence, the emissivity peak resulted from the magnetic polariton becomes nearly independent of the emission angle and exhibits diffuse characteristic that is desirable for

thermophotovoltaic emitters. It should be noted that the resonance frequency can be easily tuned by varying the strip width w.

Figure 5.18(b) reveals additional interesting aspects of different modes of magnetic responses. The even-order magnetic polaritons (such as the second harmonic mode) can only be excited at oblique incidence, whereas the odd-order magnetic polaritons can be excited at normal incidence. Furthermore, surface plasmons can strongly interact with magnetic polaritons at certain ν and k_x values. The interaction of surface plasmons with magnetic polaritons can result in either enhancement or suppression of the emissivity. It can be inferred from Fig. 5.18(b) that if the surface plasmon dispersion curve intersect an even-order magnetic polariton, the corresponding emissivity is suppressed and the magnetic polariton dispersion line splits in to two curves, as illustrated in Fig. 5.18(b) for the second-harmonic magnetic polariton mode. On the other hand, the odd-order magnetic polaritons constructively interact with the surface plasmon, resulting in high emissivity values and a spectral broadening of the emissivity peak, as illustrated in Fig. 5.18(b) for the third-harmonic magnetic polariton mode. The above conclusions are drawn from numerous calculations with various geometric parameters not shown here.

In order to further investigate the physical mechanism of the magnetic polariton, the magnetic field distribution inside the considered structure is calculated by the RCWA and plotted in Fig. 5.19. The three figures correspond to the resonance conditions MP1, MP2, and MP3 shown in Fig. 5.18(b) at the incidence angle of $\theta = 25°$. Here, the z axis is pointed upwards so that the Ag strips appear to be below the Ag film. As shown in Fig. 5.19(a) for the fundamental mode of the magnetic response, anti-parallel currents in the

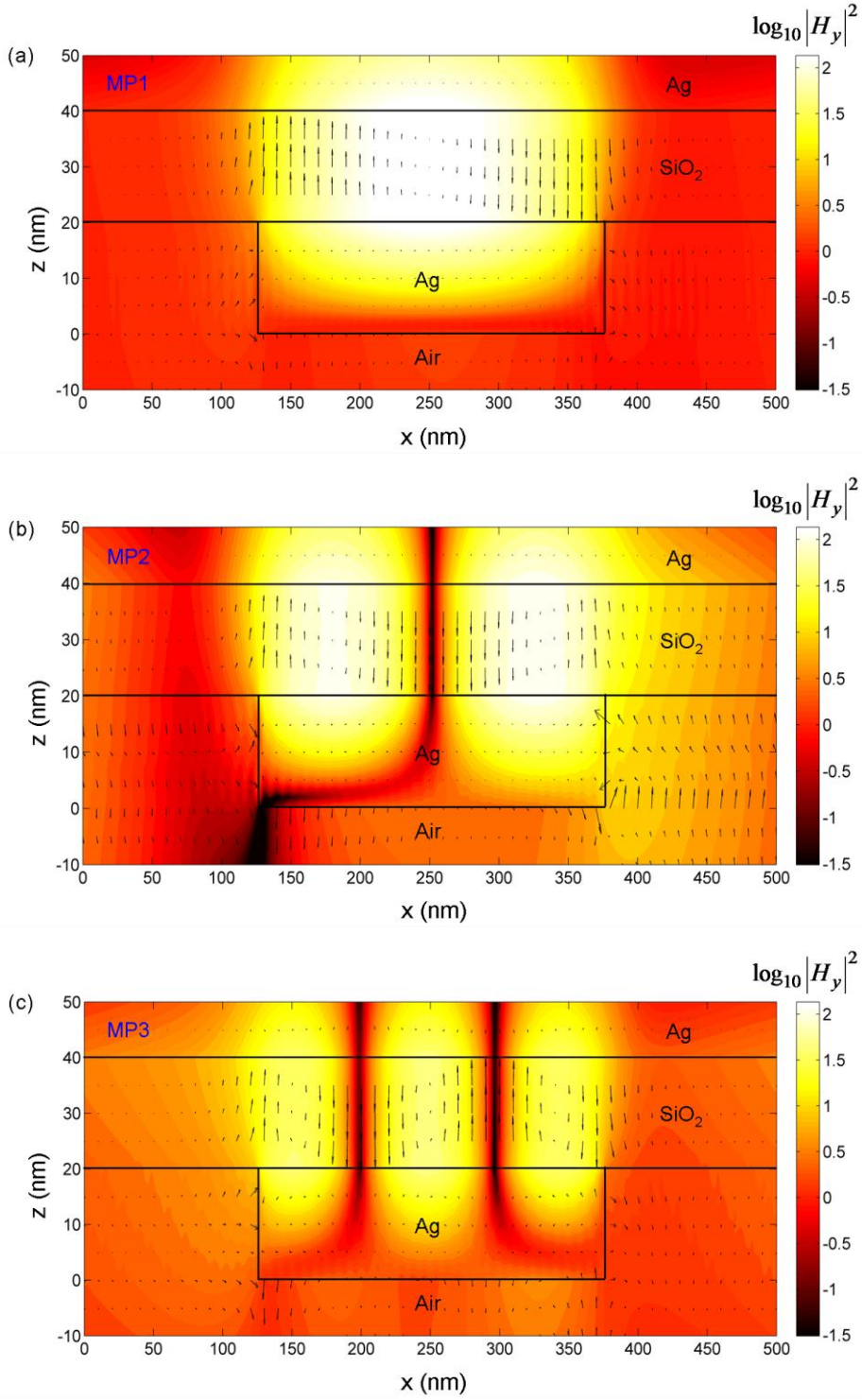

Figure 5.19 Contour shows the square of the magnitude of complex magnetic field in logarithmic scale and the arrows indicate the electric fields when the magnetic polariton is excited for conditions corresponding to MP1, MP2, and MP3 shown in Fig. 5.18(b). (a) MP1, ν = 5,670 cm^{-1}; (b) MP2, ν = 11,490 cm^{-1}; (c) MP3, ν = 16,095 cm^{-1}.

metallic strips and the substrate confine strong magnetic field inside the dielectric spacer. The considered structure acts similarly to the metal strip pairs regarding the magnetic field distribution. However, the semi-infinite metal substrate employed here results in the enhanced absorption at resonance conditions. Although the magnetic field is not symmetric with respect to the center of the metallic strip, the second and third order magnetic resonances are clearly demonstrated such that two and three anti-nodes of the magnetic field are formed in the dielectric spacer underneath the metal strip, respectively. The corresponding electric field distribution further confirms the magnetic induction around the anti-nodes of the magnetic field distribution. Hence, the effective permeability of the considered structure exhibits a resonance like dispersion according to the electric and magnetic fields distribution in the dielectric spacer. It should be noted that the effective permeability can be calculated by averaging the magnetic moment of current loops [124]. As illustrated in Fig. 5.19(b), there are two induced current loops with opposite direction for the second harmonic mode. Therefore, the averaged magnetic moment is zero at normal incidence due to the symmetry, suggesting that even-order harmonic modes can only be excited at oblique incidence. In contrast to the magnetic polariton, the surface plasmon polariton (not shown in Fig. 5.19) generates enhanced magnetic field along the interface between the dielectric and metal film, as well as along the interface between metal strips and air. Furthermore, the field between the metal strips and the film is not enhanced when surface plasmon is excited.

5.5 A Selective and Diffuse Emitter for Thermophotovoltaics

A particular application of coherent thermal emitters is to serve as wavelength-selective emitters in TPV systems to enhance the energy conversion efficiency. A TPV

emitter can be heated up by various sources such as waste heat, the sun, or burning of fossil fuel, and emitted thermal radiation is received by a TPV cell with proper energy bandgap where photocurrent is generated by creating electron-hole pairs. They are also quiet, portable, pollution-free, and low-maintenance. However, low power throughput and poor conversion efficiency are the major challenges for TPV energy converters.

Near-field thermal radiation has been proposed to enhance the power generation by bringing the emitter and receiver in close proximity [58,125], while the conversion efficiency can be improved by controlling the emission spectrum and directions. An ideal emitter should have emittance as high as possible above the bandgap and as low as possible below the bandgap (wavelength-selective) over the whole hemisphere, i.e., insensitive to the direction (diffuse-like). A number of microstructures have been studied to improve the performance of TPV emitters based on different physical mechanisms, such as 1D complex grating [126], 1D photonic crystal (PC) made of tungsten and alumina [15], 2D tungsten grating with thermally excited surface plasmons [127], 2D deep microcavities with cavity resonance modes [128], and 3D woodpile-like PC [129]. Tungsten is usually selected as the emitter material due to high melting point and good corrosion resistance.

Here, a novel TPV emitter consisting of a 1D tungsten grating structure shown in Fig. 5.20(a) with a SiO_2 spacer on a tungsten film is proposed by excitation of MPs. The geometric parameters used to illustrate the MP-enhanced TPV emitter are Λ = 600 nm, h = 60 nm, f = 0.5, and d = 60 nm. The entire structure is deposited on an opaque tungsten film, and can be fabricated with nanoimprint, interference lithography or electron-beam lithography techniques [130]. The spectral-directional emittance can be

calculated with RCWA for TM waves in which MPs can be excited. Optical constants for tungsten and SiO_2 are obtained from tabulated data with interpolation [83].

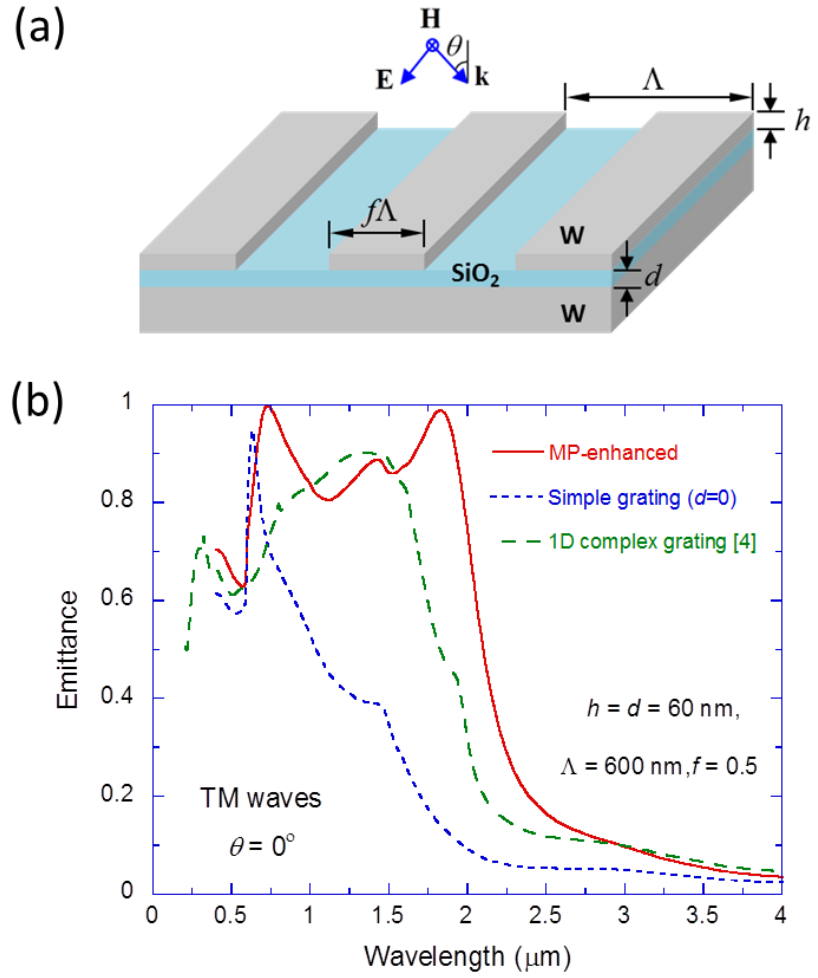

Figure 5.20 (a) Schematic of the TPV emitter made of a tungsten grating and SiO_2 spacer. The parameters used for the calculation are $h = d = 60$ nm, $\Lambda = 600$ nm, and $f = 0.5$. (b) Normal emittance of the proposed emitter, a simple grating, and a 1D complex grating from Ref. [126] for TM waves.

Figure 5.20(b) shows the calculated normal emittance spectra (solid curve) of the proposed TPV emitter. Note that thermal emission for $\lambda < 0.6\,\mu m$ is negligibly small at temperatures lower than 2000 K. The emittance exhibits wavelength-selective behavior with values higher than 0.8 in the spectral range of $0.62\,\mu m < \lambda < 1.98\,\mu m$ but drops

quickly to below 0.2 for $\lambda > 2.4\,\mu\text{m}$. This is highly desired for TPV applications to make use of short-wavelength photons as much as possible while minimizing the thermal leakage due to long-wavelength photons below the TPV cell's bandgap. The high emittance at short wavelength exists due to two close-to-unity peaks: one at 0.73 μm and the other at 1.83 μm. The emittance for a simple grating that does not have a SiO_2 spacer is also shown (dotted curve) for comparison. It peaks at 0.63 μm due to the excitation of SPP at the air-tungsten interface but drops sharply as the wavelength increases. The resonance condition of SPP can be confirmed by its polariton dispersion relation [1]. The peak at 0.73 μm for the emitter is also associated with SPP, while the slight shift is due to the interaction with MPs. By comparison, the importance of the peak at 1.83 μm can be seen as lifting up the emittance spectrum to higher values in a wider spectral range simply by inserting a 60-nm SiO_2 spacer.

For comparison, the emittance of a 1D complex grating discussed by Chen and Zhang [126] is also plotted in Fig. 5.20(b) (dotted curve). The MP-enhanced emitter has higher emittance for $1.55\,\mu\text{m} < \lambda < 2.96\,\mu\text{m}$, indicating better performance when coupled with TPV cells with energy bandgaps around 2 μm. However, it is complicated to obtain actual conversion efficiency and generated electric power, since the radiative heat transfer between the emitter and cell must be analyzed with the coupling of charge transport [58] and heat transport problems [125].

The emittance peak at 1.83 μm plays a crucial role to enhance the radiation energy above the bandgap and thus possible higher power throughput and conversion efficiency. Understanding the mechanism of this peak is critical for the successful TPV emitter design. Figure 5.21(a) presents the electromagnetic field distribution at

wavelength of 1.83 μm and normal direction. The tungsten strip, SiO_2 spacer, and tungsten substrate in one period are delineated in the figure. Clearly, an electric current loop is formed and strong magnetic field is confined between the upper tungsten strip and the lower tungsten film, indicating a diamagnetic response and excitation of the magnetic polaritons, i.e., coupling between the external electromagnetic waves and magnetic resonance inside the structure. Similar MP behaviors have been extensively discussed in preceding sections with different grating structures.

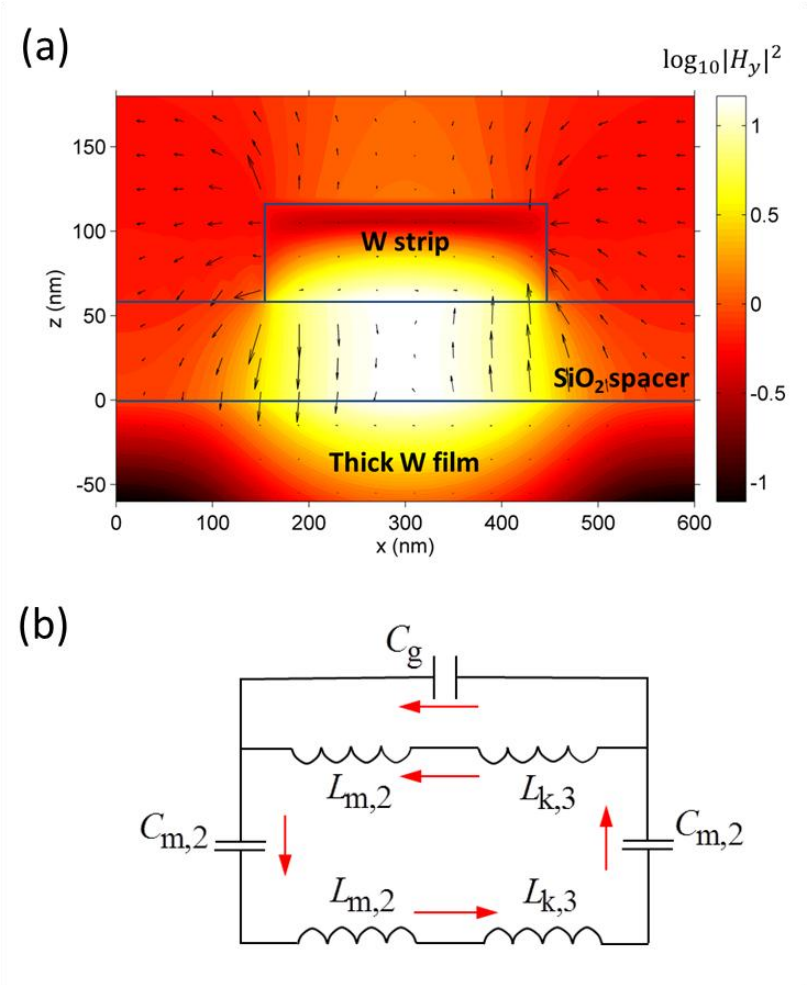

Figure 5.21 (a) Electromagnetic field distribution at wavelength of 1.83 μm and normal direction where MP is excited. (b) The LC circuit model for the fundamental mode.

According to the charge distribution suggested by the field distribution, a LC circuit model can be used to predict the magnetic resonance condition described in Fig. 5.21(b) where arrows indicate the electric currents. Compared with the LC circuit for the double-layer slit array in Fig. 5.8(b), the only difference is the disappearance of the lower gap capacitance C_g since the bottom slit array is replaced with a thin film. Therefore, the parallel-plate inductance $L_{m,2}$, the parallel-plate capacitance $C_{m,2}$, and the gap capacitance C_g can be calculated from Eqs. (5.1), (5.3) and (5.4), respectively. However, the kinetic conductance is obtained with a similar form of Eq. (5.7) as [123]

$$L_{k,3} = -w/(\omega^2 h_{eff} l \varepsilon_0 \varepsilon'_m) \tag{5.10}$$

where ε'_m is the real part of the dielectric function of the metal, the effective thickness h_{eff} for electric currents is assumed to be the power penetration depth δ of tungsten if $\delta < h$ or the grating height h otherwise. The resonance condition for the fundamental MP mode can be found by zeroing the total impedance as

$$Z_{tot,4}(\omega) = \frac{L_{m,2} + L_{k,3}}{1 - \omega^2 C_g (L_{m,2} + L_{k,3})} - \frac{2}{\omega^2 C_{m,2}} + L_{m,2} + L_{k,3} \tag{5.11}$$

Since the penetration depth δ and ε'_m are wavelength-dependent, the resonance condition can only be solved implicitly by setting $Z_{tot,4} = 0$.

The resonance condition for MPs can be tuned by changing the strip width. Figure 5.22(a) shows the normal emittance as a function of wavelength and strip width from the RCWA calculation. One bright resonance band with high emittance values can be seen around the wavelength of 0.7 μm, and its flatness indicates the independence of strip width. This resonance band is associated with the excitation of SPP. The resonance wavelengths for another bright band increase with wider strips, and match well the

resonance condition of MP predicted by the LC model shown as triangular marks. Due to the coupling between SPP and MP, emittance in the spectral range between their resonance wavelengths is enhanced (> 0.7) when $100\,\text{nm} < w < 350\,\text{nm}$, forming a wide high-emittance spectral band. MP and SPP start to decouple when the strip becomes even

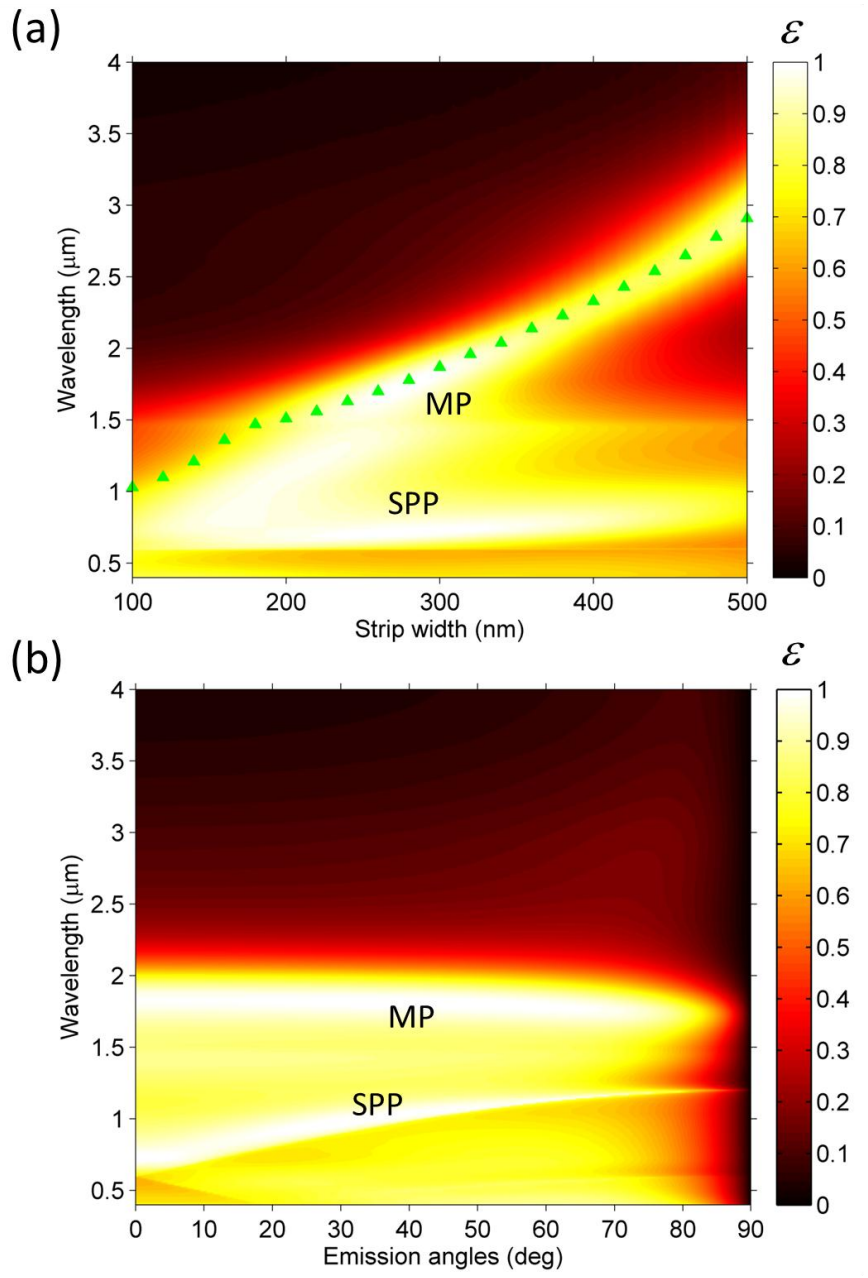

Figure 5.22 Contour plots of emittance of the TPV emitter (a) as a function of wavelength and strip width and (b) as a function of wavelength and emission angle.

wider and as a result, emittance is enhanced only around the resonance wavelengths of MP and SPP. Therefore, the strip width offers tunability of proposed TPV emitter to suit specific TPV cell bandgap and working temperatures. Moreover, by predicting the resonance wavelength of MP, the LC model may provide design guidelines to estimate high/low emittance band edges.

Beside the spectral selectivity in emittance, another important feature for an excellent TPV emitter is directional insensitivity of the emission peaks to maximize the efficiency since the thermal emission is hemispherical in reality. As discussed in preceding sections, the directional independence is an intrinsic characteristic of MPs: the resonance wavelength changes little with emission angles as long as the time-harmonic magnetic field is along the grating grooves. Thus, the excitation of MPs is well suitable for TPV applications. Figure 5.22(b) shows the contour plot of the emittance of the MP-enhanced TPV emitter as a function of wavelength and emission angles. The emittance remains high values (> 0.8 mostly) at shorter wavelength for emission angles up to 75 ºor so and starts to drop beyond 2 μm. The two bright bands indicate emittance peaks. The first one is close to 2 μm and is attributed to the excitation of MP. Its flatness suggests directional independence; hence, high emittance can be obtained in a large range of emission angles. The other one at shorter wavelength has an inclined band, and matches the excitation condition of SPPs at the air-tungsten interface. Again, SPPs are highly sensitive to directions in gratings. The performance of the MP-enhanced emitter is comparable with the multilayer coated triangular gratings [71] but much easier to fabricate.

CHAPTER 6
EXPERIMENTAL DEMONSTRATION OF COHERENT THERMAL EMISSION ENABLED BY MAGNETIC POLARITONS

This Chapter describes an experimental demonstration of coherent emission in the infrared region (1000 – 3000 cm^{-1}) by excitation of MPs inside subwavelength grating structures from room temperature to 800 K. Samples with different patterns are fabricated in order to study the geometric effect on the MPs, as described in Section 6.1. The influence of the geometry on the emittance peak locations and directional behavior is examined in Section 6.2 through room-temperature reflectance measurements. Section 6.3 directly demonstrates the coherent emission characteristics of the MP-enabled emitters at elevated temperatures using the high-temperature emissometer. To help interpret the measurement results and understand the underlying physics, theoretical calculations using the RCWA coupled with a temperature-dependent Drude model and LC model are performed.

6.1 Sample Fabrication

The coherent thermal emitter samples were fabricated with microfabrication techniques in Nanotechnology Research Center at Georgia Tech. A double-sided polished 100-mm silicon wafer with a thickness of 400 μm was used as the substrate due to its high thermal conductivity. As illustrated in Fig. 6.1, the sample fabrication process mainly involved five steps: (a) thin films deposition; (b) pattern transfer with UV light exposure through a photomask; (c) pattern formation after resist development; (d) metallization by evaporating Au onto sample surface; (e) resist stripping or lift-off.

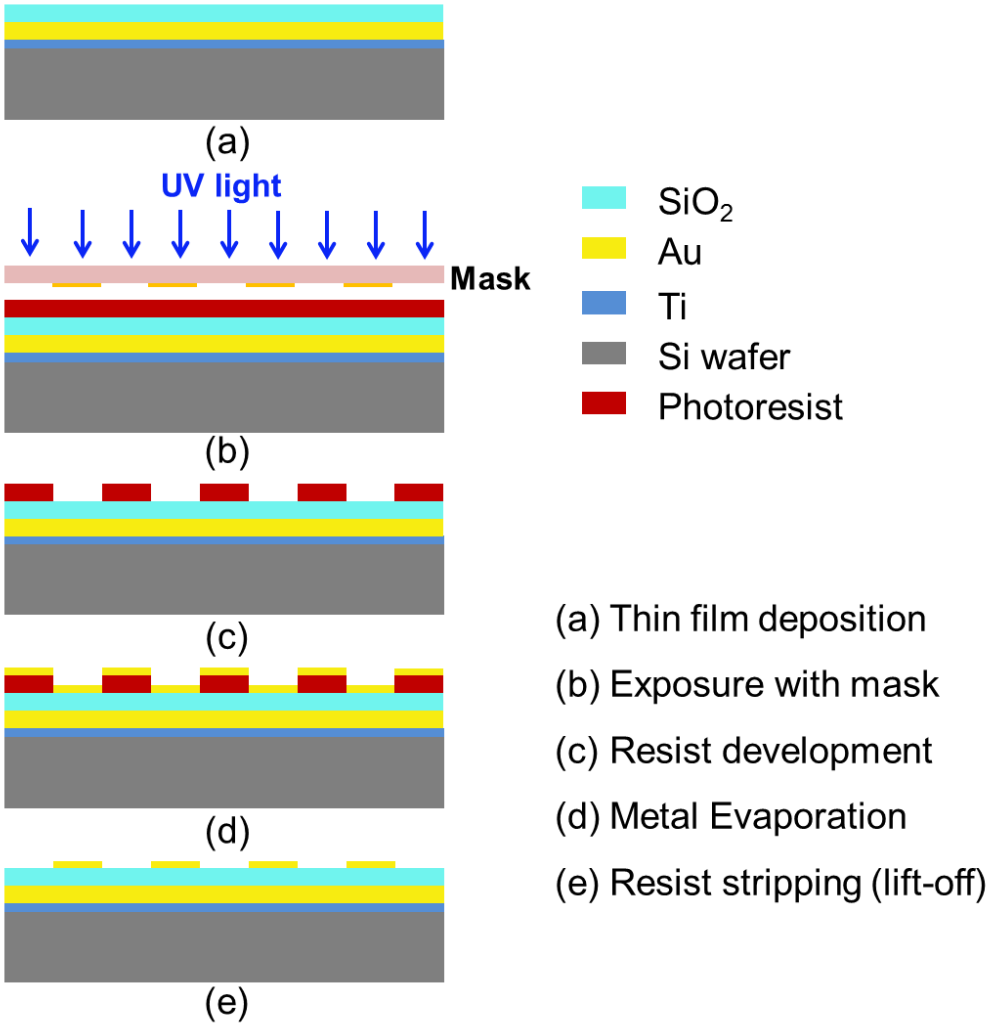

Figure 6.1 Schematic of fabrication process for the subwavelength grating structures as coherent thermal emitters: (a) thin film deposition; (b) exposure with photomask; (c) resist development; (d) metal evaporation; and (e) resist stripping, also called lift-off.

Before the thin films deposition, the wafer surface was thoroughly cleaned with acetone and isopropyl alcohol (IPA) solvents, followed by the DI water rinse and N_2 blow dry, such that the surface is free of any particles. This ensures the success of pattern transfer later. First, an electron-beam evaporator (CVC 5000) was used to deposit 30-nm Ti and 200-nm Au films in sequence onto the sample surface without breaking the vacuum condition. The deposition was performed when the chamber pressure was lower

than 2×10^{-6} Torr, and a quartz crystal sensor was used to control the deposition rate (0.1 nm/s and 0.2 nm/s, respectively) and monitor the film thickness. Note that for high-temperature measurements, an additional 40-nm Pt film was deposited between the Ti and Au as a barrier layer to prevent the inter-diffusion between Si and Au at temperatures higher than 360°C. Then, the sample was removed to a plasma-enhanced chemical vapor deposition (PECVD) chamber, and a layer of SiO_2 of 200 nm was deposited on top of the Au film. The thickness of the SiO_2 layer was measured by a reflectometer (Nanospec Film Analyzer 3000) with a Si piece which was placed in the chamber along with the sample. Next, a layer of negative photoresist (Futurrex NR9-1500PY) was spun coated at 4000 rpm for 45 s. This specific type of photoresist was selected due to its negative-sloping side wall profile which facilitates the lift-off process, superior resolution, fast development time, and easy stripping at room temperature. After prebaked at 150°C for 120 s on a hotplate, the sample was exposed by 365-nm UV light using a mask aligner (Karl Suss MA-6) through a photomask in a hard contact mode. The exposure dose for 1.4-μm-thick photoresist is around 270 mJ/cm^2. The photomask has three different 1D grating patterns intentionally designed to study the grating period and strip width effect on the excitation of magnetic polaritons, and each pattern has an active area of 23.4 mm by 28 mm. After post-baked at 100°C for 120 s on a hotplate, the sample was developed for 10 s in the RD6 solution (Futurrex), followed by the DI water rinse and N_2 blow dry. So far, the grating patterns on the photomask have been transferred to the photoresist. To make the Au grating, the sample was placed into the electron-beam evaporator for metallization with a targeting thickness of 200 nm with a deposition rate of 0.2 nm/s. Note that the top surface of photoresist and the exposed area of SiO_2 layer will be

covered by Au. Lastly, the photoresist along with unwanted Au strips was stripped off by soaking the sample in acetone solvent for 15 min at room temperature. The coherent thermal emitter samples were obtained as the structures shown in Fig. 6.1(e).

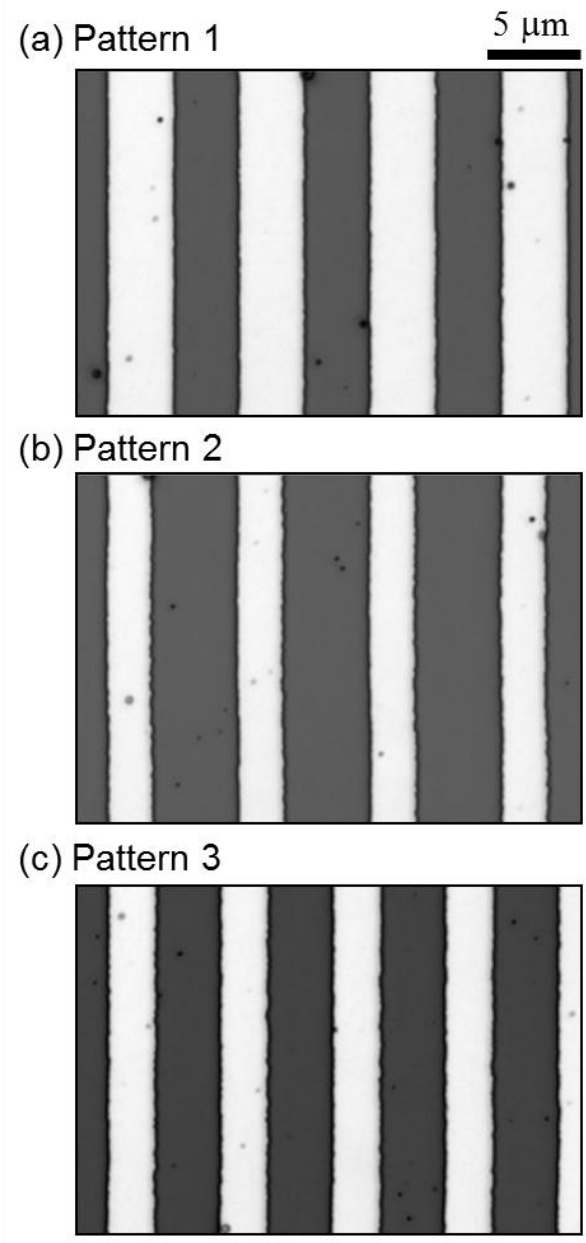

Figure 6.2 Top view images of MP coherent emitter samples with different patters: (a) Pattern 1 with Λ = 7 μm and w = 3.5 μm; (b) Pattern 2 with Λ = 7 μm and w = 2.5 μm; and (c) Pattern 3 with Λ = 6 μm and w = 2.7 μm. Images were taken with a 3D confocal microscope, and the bright regions are the Au grating ridges.

A 3D confocal microscope (Olympus LEXT OLS4000) was used to characterize the grating dimensions in different patterns. Figure 6.2 shows the top views of three different patterns, where the bright regions are the Au grating ridges. Pattern 1 and Pattern 2 have the same grating period ($\Lambda_1 = \Lambda_2 = 7\,\mu\text{m}$) but different strip width ($w_1 = 3.5\,\mu\text{m}, w_2 = 2.5\,\mu\text{m}$), while Pattern 2 and Pattern 3 have almost the same strip width but different period ($\Lambda_3 = 6\,\mu\text{m}, w_3 = 2.7\,\mu\text{m}$).

Table 6.1 Geometry of different samples from characterization which are used for RCWA and LC model calculations

	Pattern 1	**Pattern 2**	**Pattern 3**
Top SiO_2 coating	80 nm		
Au grating period	7 μm	7 μm	6 μm
Au grating strip width	3.5 μm	2.5 μm	2.7 μm
Au grating thickness	170 nm	180 nm	190 nm
SiO_2 spacer thickness	200 nm		
Au film	200 nm		
Ti adhesive layer	30 nm		
Si substrate	400 μm		

The period and strip width values estimated from the images are listed in Table 6.1 along with other geometric values for all three patterns. Note that grating thicknesses are different because the deposition rate in the electron-beam evaporator is not uniform within a large deposition area. Also, the grating profile from the 3D microscope image is not ideally rectangular but more like trapezoidal shape. The top surface of Au strips is not ideally smooth either. Before the measurements for the radiative properties, the sample was coated with 80-nm SiO_2 using PECVD for protecting the top thin Au lines, and was

then diced such that each pattern was 25 mm by 25 mm in size. Note that the fabrication process is highly repeatable such that same patterns from different batches have almost the same geometry.

6.2 Geometric Effect from Reflectance Measurements

Figure 6.3(a) shows the room temperature reflectance of coherent emitter samples with different patterns measured at 10 ° incidence angle for TM waves only using an FT-IR spectrometer. According to previous studies, magnetic polaritons can be only excited at TM waves for 1D gratings, and the grating are basically highly reflective at TE waves, which was observed from the reflectance measurement as well (not shown here). In the figure, reflectance dips with minima less than 0.1 are clearly seen for all three patterns but at different resonance frequencies: 1290 cm^{-1} for Pattern 1, 1408 cm^{-1} for Pattern 2, and 1385 cm^{-1} for Pattern 3. Since all the patterns are opaque, reflectance dips are essentially emittance peaks which indicate the spectral selectivity of the thermal emission. Note that Pattern 1 and Pattern 2 have the same grating period but different strip width, while Pattern 2 and Pattern 3 have close strip with but different period. From the figure, the strip width seems to have much more impact on the resonant frequency than the period since the resonant peaks for Pattern 2 and Pattern 3 are very close considering they have very close strip width. Also, the resonance frequency decreases with longer strips based on the experimental observation from the figure. Besides those major reflectance dips, some small reflectance dips are also noticeable at higher frequencies (from 1650 cm^{-1} to 2000 cm^{-1}) for all the patterns, and the resonance frequencies are also different for each one.

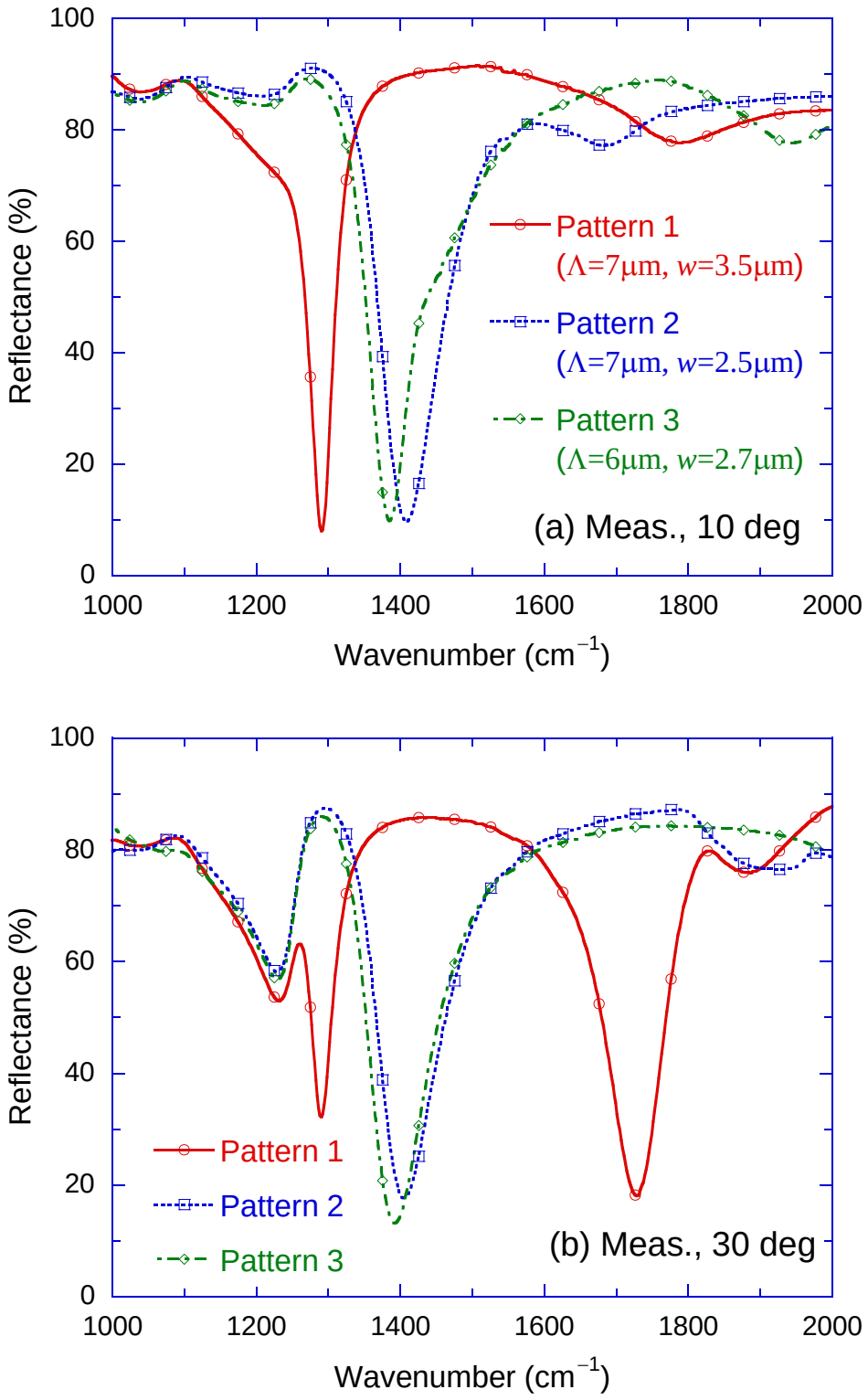

Figure 6.3 The reflectance measurement results at room temperature for MP coherent emitter samples with different patterns at (a) 10 ° and (b) 30 ° incidence angles, respectively. The results are for TM waves only.

The reflectance at 30 ° incidence angle for TM waves was also measured at room temperature to show the behavior at oblique angles. First of all, the major reflectance dips observed at 10 ° incidence angle still exist with little frequency shift: 1290 cm^{-1} for Pattern 1, 1406 cm^{-1} for Pattern 2, and 1393 cm^{-1} for Pattern 3. Interestingly, the reflectance minima for Pattern 2 and Pattern 3 do not change much from those at 10 °, which indicate excellent emission performance with emittance higher than 0.8. The reflectance minima for Pattern 1 increases up to around 0.32, but interestingly, another reflectance dip with the minimum as low as 0.18 appears at 1728 cm^{-1}. In addition, a small reflectance dip occurs at 30 ° incidence angle for all the patterns at the same frequency of 1230 cm^{-1}.

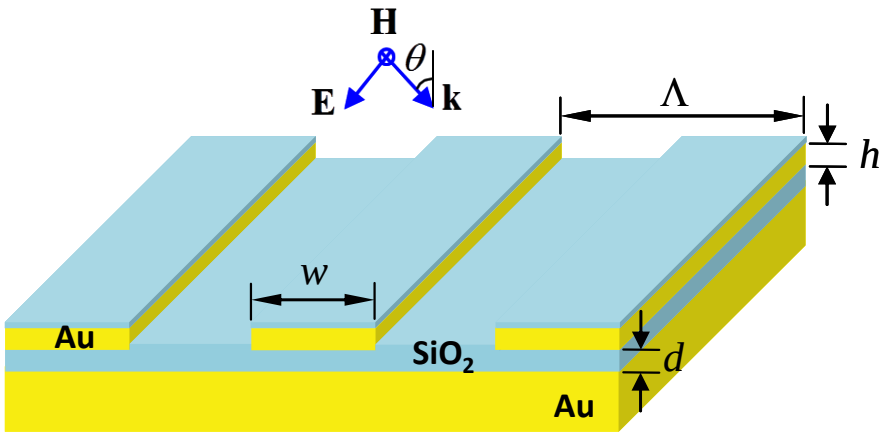

Figure 6.4 The structure used for theoretical modeling. Note that there is a layer of SiO_2 between the Au grating strips, and it has the same thickness (80 nm) with the SiO_2 coating atop of Au strips.

To understand the physical mechanism behind the existence of those reflectance dips (or emission peaks) and the emission behavior of proposed thermal emitters both in temporal and spatial aspects, theoretical modeling is of great necessity. Figure 6.4(a) depicts the grating structures for the calculation. The layers underneath the 200-nm Au

layer can be neglected since it is opaque in the IR region of interest. Note that, the 80-nm SiO_2 coating from PECVD should be on all the surfaces including the sidewalls, but the coating on the sidewalls is much thinner than the strip width such that it can be neglected to simplify the modeling. Note that, the Au grating grooves is filled with 80-nm SiO_2 and air. Also, the profile of the grating ridges, which is actually trapezoidal shape from the 3D microscope imaging, is assumed to be rectangular. The reflectance angle θ_j for the *j*th diffraction order can be calculated from the grating equation [1]:

$$\sin\theta_j = \sin\theta_i + j\lambda/\Lambda \tag{6.1}$$

Calculation based on the above equation indicates that in the $10°$ and $30°$ reflectance measurements, only the specular component (0^{th} diffraction order) is collected by the detector since all other diffraction orders cannot fall into the incident beam cone with a half-cone angle around $3°$. Therefore, only the specular reflectance is calculated from the RCWA for comparison with the experimental data. Note that the surface roughness effect is not considered in the calculation. The geometric values listed in Table 6.1 for three patterns were used for the calculation.

Figures 6.5(a) show the comparison between and measurements (red curve with markers) and the theoretical calculation (blue dash curve) for the reflectance of Pattern 1 at $10°$ incidence. The RCWA predicts a large reflectance dip near the resonant location of the one observed from the measurement with a little offset of 20 cm^{-1}. The predicted dip has a close-to-zero reflectance minimum, which is even smaller than that from the measurement. The difference in the resonance locations and reflectance minima is mainly due to the approximation made in the modeling, such as rectangular ridge profile and neglecting sidewall coating, and some experimental factors such as not 100% TM

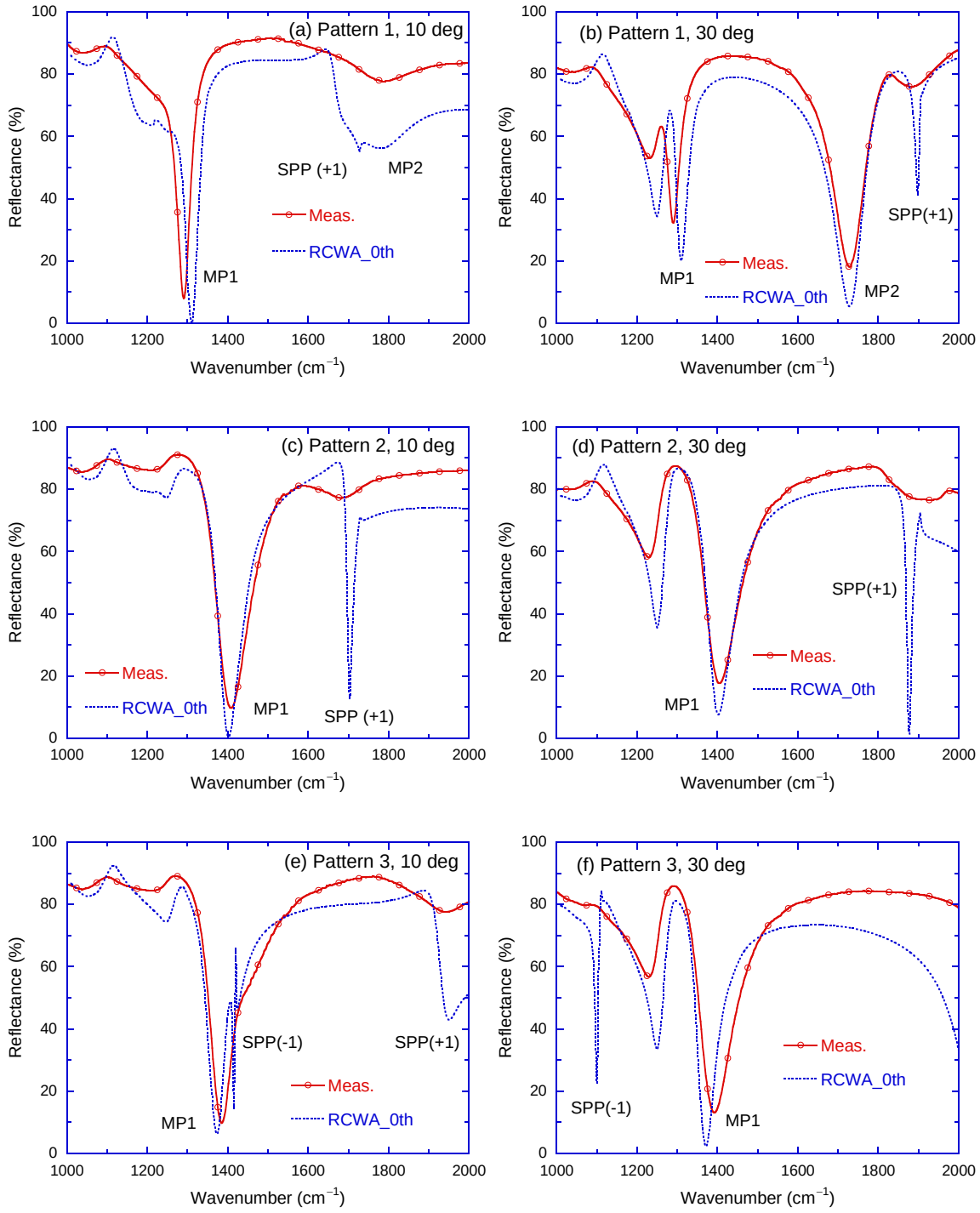

Figure 6.5 The comparison between the measurements (red curve with markers) and the RCWA calculation (dash curve) on the reflectance for (a)(b) Pattern 1, (c)(d) Pattern 2; and (e)(f) Pattern 3. The RCWA calculation is based on the geometric parameters from the fabrication listed in Table 6.1, and specular reflectance (0^{th} order) is only compared.

polarized waves and sample imperfection. This major reflectance dip is actually due to the excitation of the fundamental mode of magnetic polaritons, labeled as "MP1", which will be discussed later. At longer frequency there are two additional small dips from the calculation: a sharp one at 1728 cm^{-1} and the one at 1780 cm^{-1}. The first one is due to the excitation of SPP (+1 order) in the grating structure. The resonant condition for SPP for TM waves at an interface between a dielectric and a metal can be predicted by Eq. (2.33). Due to the periodicity in gratings, SPP dispersion curve can be folded according to the grating period, and multiple SPPs can be excitation due to different diffraction orders. However, this small dip is not seen from the measurement, which is mainly due to the beam divergence in the reflectance measurement since the resonance frequency for SPP changes with the direction. The other dip can be seen from both modeling and measurement around the same location (around 1790 cm^{-1}), and results from the excitation of the second order of magnetic polaritons, namely "MP2", which will be discussed later as well. However, there is a quite deviation at frequencies beyond 1650 cm^{-1} between the calculation and measurements. In general, the modeling agrees well with the measurements on the reflectance spectrum, and their deviations are mainly associated with the approximations in the calculation and some experimental limitations.

For the 30° incidence, a good agreement can be clearly seen between the calculation and measurements in Fig. 6.5(b) with four apparent reflectance dips. The one around 1300 cm^{-1} is MP1 which has the same frequency with that at 10° incidence. The directional insensitivity is one of the main characteristics for magnetic polaritons. Also, the calculation and measurement have an excellent agreement on the large dip at 1728 cm^{-1}, which is MP2. Note that there is a small frequency shift for MP2 between 10° and

30 ° incidence, and it is mainly because the coupling with SPP at 10 ° incidence changes the MP2 condition a little bit. For 30 ° incidence, SPP (+1 order) shifts to 1898 cm^{-1} from the calculation, and the measurement confirms this with a smaller dip mainly due to the beam divergence. The last dip around 1250 cm^{-1} is nothing to do with MP or SPP, and was observed from a direct emittance measurement of an asymmetric Fabry-Perot cavity resonator in Section 4.3 and was discussed in Fig. 4.11. Due to the unique optical constants of SiO_2 in this region, the reflection coefficients at the air-SiO_2 and SiO_2-Au interfaces cancel with each other, resulting in a reflectance dip. Also, due to the coupling with this dip, the reflectance dip with MP1 is degraded compared with the much larger one at 10 ° incidence. Table 6.2 lists the resonance frequencies for MP1 from the reflectance measurements, the RCWA calculation, and the LC model for all three patterns for comparison.

Table 6.2 Resonance frequency for MP1 from measurements, RCWA calculation, and the LC model at room temperature

Frequency (cm^{-1})	**Pattern 1**	**Pattern 2**	**Pattern 3**
Measurement			
10 deg	1290	1408	1385
30 deg	1290	1406	1393
RCWA			
10 deg	1312	1396	1374
30 deg	1306	1394	1364
LC Model			
Air gap	1317	1420	1386
SiO_2 gap	1317	1419	1386

The RCWA calculation also demonstrates good agreement with the measurement for Pattern 2 for both incidences, as shown in Figs. 6.5(c) and 6.5(d) respectively. Since Pattern 2 has the same grating period with Pattern 1, the reflectance dips associated with the SPP should occur at the same frequencies. The calculation gives 1704 cm^{-1} and 1878 cm^{-1} for the SPP excitation suggested by the sharp dips in $10°$ and $30°$ incidence respectively, compared with 1728 cm^{-1} and 1898 cm^{-1} for Pattern 1. The slight difference is due to the coupling effect between SPP and MP2 in Pattern 1, and the small dip in Pattern 1 rather than the large and sharp one in Pattern 2 is also attributed to the same cause. However, the measurements only show small dips for the SPP due to the beam divergence. According to the previous theoretical studies, the strip width has more impact on the resonant conditions of MPs than the grating period, which was clearly demonstrated here. Note that Pattern 2 has a smaller width and the resonant frequency for MP1 shifts to higher frequencies compared with that for Pattern 1. The modeling and measurement results agree very well on the MP1 dip for both incidences. Also, the MP1 dip at $30°$ incidence is comparable with that the $10°$ incidence, thanks to the less coupling between SPP and MP1 in Pattern 2. The reflectance dip around 1250 cm^{-1} for the $30°$ incidence occurs again for Pattern 2 as well as Pattern 3, which is due to the same cause for Pattern 1.

Pattern 3 has a different grating period from the other two. The calculation indicates an abrupt change in the reflectance at 1420 cm^{-1} for the $10°$ incidence, as shown in Fig. 6.5(e). This is imputed to the excitation of SPP (-1 order) with $\Lambda = 6\,\mu m$. As a result, the right-hand side of the reflectance dip from the measurement experiences a sharp turn at this frequency and the curve is out of the harmonic shape. Besides, another

SPP is excited at 1950 cm^{-1} assisted by the wavevector from +1 diffraction order, which is sensed by the measurements as a small reflectance dip around the same location. On the other hand, the calculation clearly demonstrated that, the MP1 for Pattern 3 occurs at almost the same frequency with that for Pattern 2, since their strip widths are almost the same. When having the 30 ° incidence, the MP1 dip stays, while the SPP (-1 order) dip shifts to 1100 cm^{-1}. Note that MP2 dips for Pattern 2 and Pattern 3 at 30 ° incidence are pushed towards higher frequencies beyond 2000 cm^{-1} due to smaller strip width, which is the reason why they do not appear in the figures. Furthermore, MP2 strongly couples with SPP (+1 order) in the spectral range from 2000 cm^{-1} to 2500 cm^{-1}, and the modeling cannot predict well the measurement results considering the aforementioned approximations and factors. As a result, the large difference between the modeling and measurement from 1600 cm^{-1} to 2000 cm^{-1} as seen from Fig. 6.5(f).

Above findings from both measurements and calculation indicate that by changing the strip width, the reflectance dips or emittance peaks can be spectrally tailored to achieve coherent thermal emission control. Figure 6.6(a) provides a full scope on how the strip width affects the emittance at normal incidence from RCWA calculation. The geometric parameters for Pattern 1 was used for the calculation, and emittance from a total of 101 diffraction orders rather than the specular reflectance is presented as the contour with the brighter as the higher values. The frequency range is extended to 3000 cm^{-1} for demonstrating the behavior at higher frequency as well. First of all, two flat and sharp bands are clearly seen, which are associated with different branches of SPPs (±1 order for the lower-frequency one, and ±2 order for the lower-frequency one). As discussed above, SPP highly depends on the grating period and direction, and the

independence on the strip width is clearly shown in the figure. The lower resonance band associated with MP1 decreases with wider strips, which is consistent with the observation from the reflectance measurement of three different patterns. The peak emittance of MP1

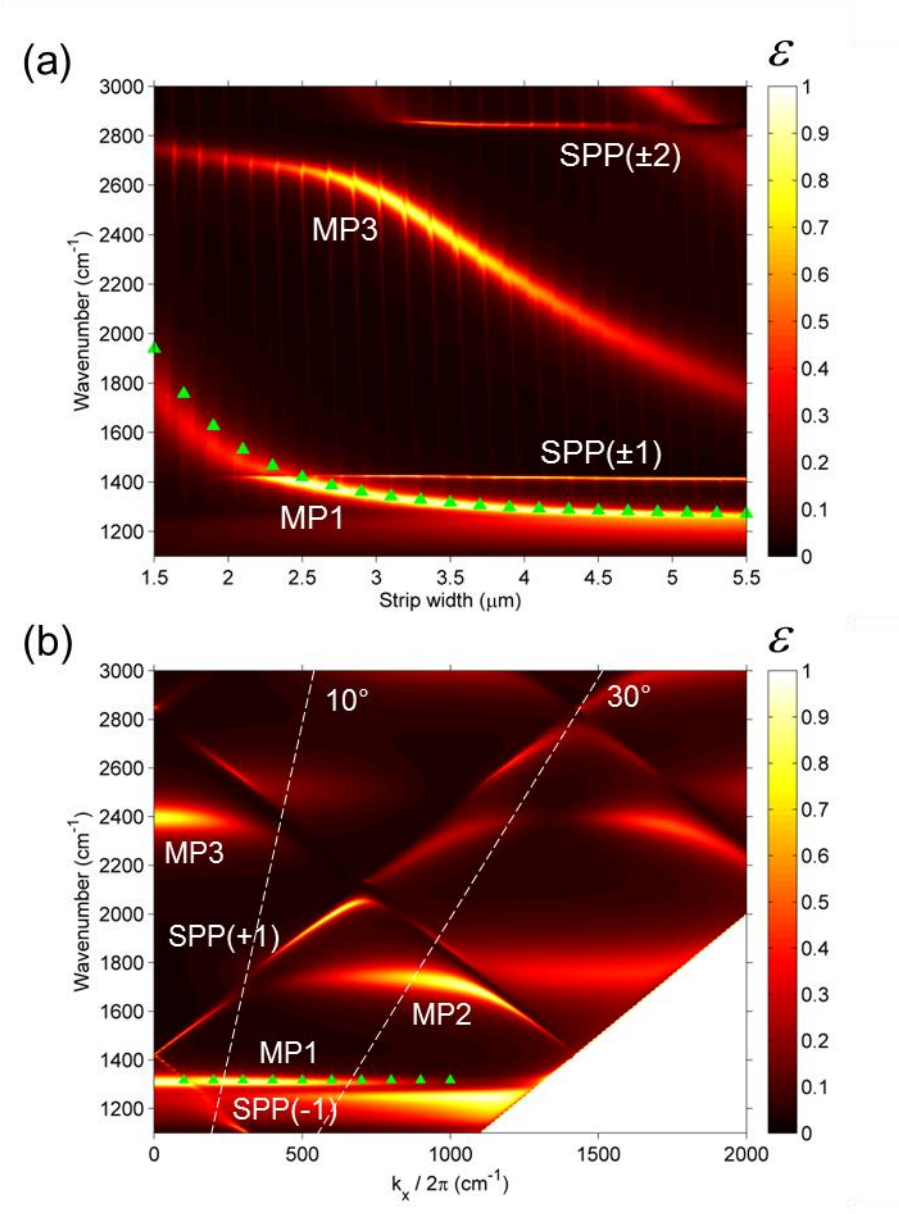

Figure 6.6 Contour plots of (a) the normal emittance as a function of wavenumber and strip width, and (b) the emittance from the ω-k_x dispersion. Triangles are the resonant conditions for MP1 predicted by Eq. (5.11). The calculation is from RCWA with parameters for Pattern 1.

is as close as to unit for strips wider than 2.5 μm but becomes lower for shorter strips after the interaction with SPP (±1 order). Moreover, the third harmonic mode of MPs occurs at higher frequencies, and the resonant condition in general decrease with larger strip width but is more sensitive for $w > 3\,\mu\text{m}$.

The LC circuit model shown in Fig. 5.21(b) can be used to verify the excitation of MP1, and Eq. (5.11) predicts its resonant conditions. The gap between neighboring Au strip in the structure shown in Fig. 6.4 is partially filled with SiO_2 and air. Table 6.2 lists the prediction by the LC model on the resonant conditions of MP1 for all three Patterns, considering the gap completely filled with either air or SiO_2. It turns out that the gap materials of either air or SiO_2 do not change the resonance frequencies, and those predicted values by the LC model agree well with the experimental and RCWA results. In addition, the LC model prediction with different strip width is also plotted as triangles in Fig. 6.6(a) for comparison with RCWA calculation, and matches well with each other. Recall that the LC model is based on the magnetic resonance, and the agreement undoubtedly verifies the physical mechanism as excitation of magnetic polaritons for the extraordinary emittance enhancement.

The dispersion relation presented in Fig. 6.6(b) reveals the behaviors of MPs and SPPs at different directions as well as their effects on the emittance. The geometry of Pattern 1 was used again for the calculation. Due to the periodicity of grating structures, multiple SPP branches are excited as inclined bright bands, indicating high dependence on both frequency and directions. These SPP resonance bands from RCWA match well with folded dispersion curves predicted by Eq. (2.33). On the other hand, the resonance associated with MP1 results in a flat dispersion curve, suggesting a diffuse-like emission

behavior; this is a unique characteristic due to the excitation of magnetic polaritons. The resonance condition predicted from the LC model as triangles also matches well the RCWA calculation, confirming the nature of magnetic resonance inside the structure. At higher frequencies, the second and third orders of MPs can be also excited. Note that the even order of MPs cannot be excited at normal direction due to the structure symmetry. Because of the interaction with multiple SPP branches, MP2 and MP3 resonance bands are divided into several parts, and the coupling is so strong when the MPs are in close proximity of SPPs such that their resonance conditions are somehow modified. In particular, emittance values at MP3 are only high for small angles near normal direction ($< 5°$), and then decreases a lot due to the coupling with the SPP (-2 order) for larger angles. On the other hand, the coupling with MP2 almost divides the SPP (+1 order) curve into half. As a result, the emittance values at SPP decrease a lot (reflectance increases) at $10°$ direction, which is also observed at 1728 cm^{-1} in Fig. 6.5(a). In addition, there is a bright resonance band below MP1 for angles larger than $25°$ or so, which is associated with the reflectance dips around 1250 at $30°$ incidence explained in Fig. 6.5. Since this resonance is very close to MP1, the emittance enhancement with MP1 is weakened at larger angles by their coupling effect.

6.3 Direct Observation at Elevated Temperatures

Though the reflectance measurements have clearly shown the coherent emission behavior at room temperature, for real-world applications the coherent emitters must work under high temperature environment where the properties may be different from room temperature. Therefore, the direct demonstration of coherent emission at elevated

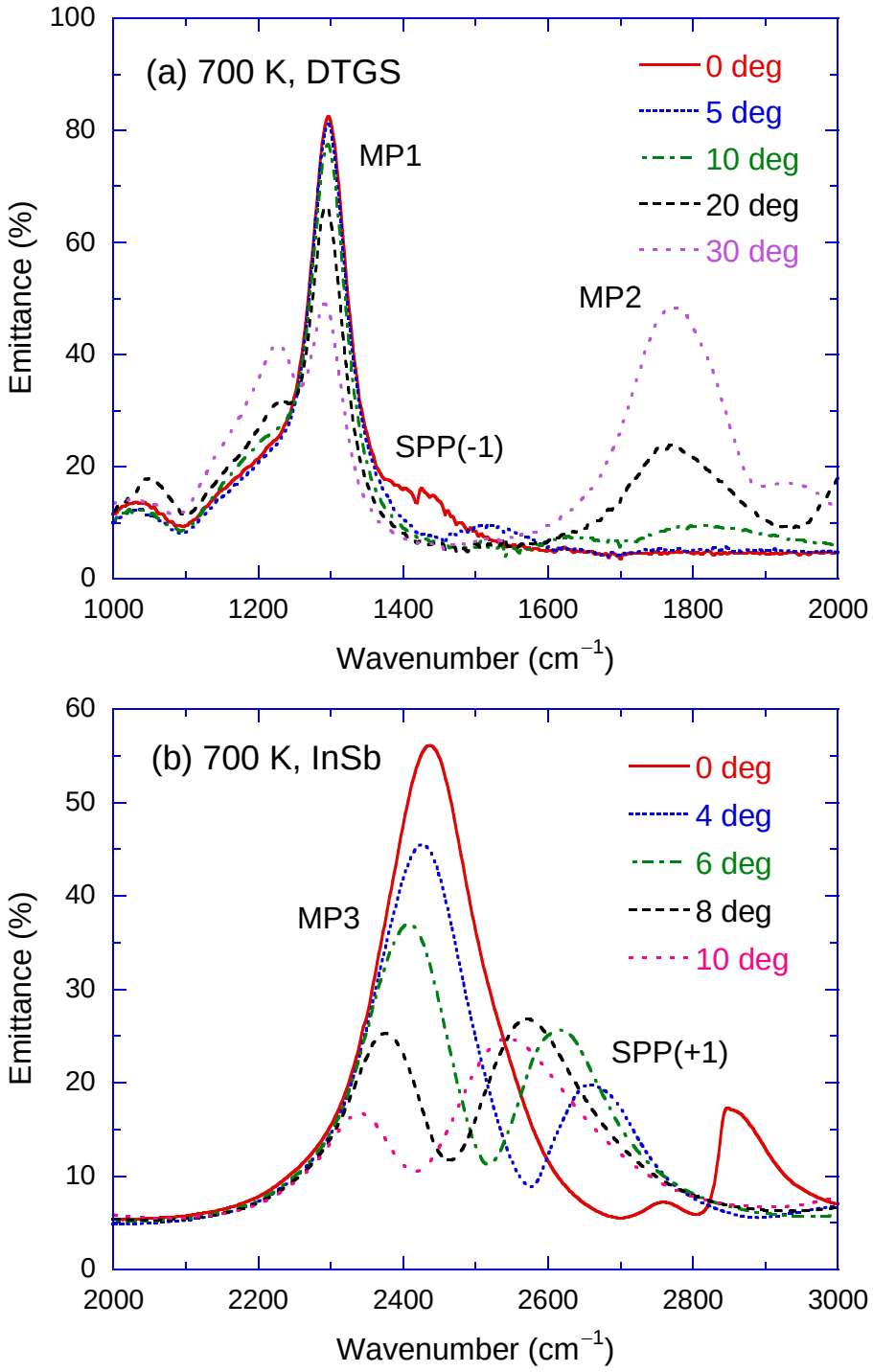

Figure 6.7 The emittance at 700 K for different directions measured with the high-temperature emissometer using (a) a DTGS detector and (b) an InSb detector. An IR polarizer is used and the results are for TM waves only.

temperature is necessary to address potential applications. In order to ensure the chemical stability at elevated temperatures, another sample was fabricated with a 40-nm Pt barrier layer deposited between the Ti and Au layers using the electron-beam evaporator to prevent the diffusion between Si and Au at high temperatures. This sample is used for the high temperature measurement and its geometry is almost the same with the Pattern 1 listed in Table 6.1. The high-temperature emissometry facility and measurement methods have been discussed in Section 3.3.

Figures 6.7(a) and 6.7(b) show the measured emittance at 700 K for different directions using the emissometry setup with different detectors, respectively. The DTGS detector gives good signal-noise ratio from 1000 cm^{-1} to 2000 cm^{-1}, whereas the InSb detector provides much better response from 2000 cm^{-1} to 3000 cm^{-1}. A large emittance peak appears at 1296 cm^{-1} with a maximum of as high as 0.82 at normal direction, and the peak maximum decreases but the peak location does not shift when the emission direction changes from 0 ° to 30 °. By comparison with Figs. 6.5(a) and 6.5(b), it is clearly that this emittance peak is associated with MP1, and the directional independence is also demonstrated at high temperatures. As discussed previously, the peak decreasing at larger angles is because of the interaction between the MP1 and the minor peak around 1250 cm^{-1}. Also, the emergence of the MP2 at 1769 cm^{-1} for normal direction to oblique angles is also directly observed, consistent with the measurements and theoretical calculations at room temperature. Figure 6.7(b) presents the strong coupling between the MP3 peak and SPP (+1 order) when they come closer with larger emission angles. At normal direction, the MP3 peak at 2437 cm^{-1} is far away from the SPP (+1 order) at 2847 cm^{-1}, and thus has an emittance peak as high as 0.56. However, due to its high sensitivity

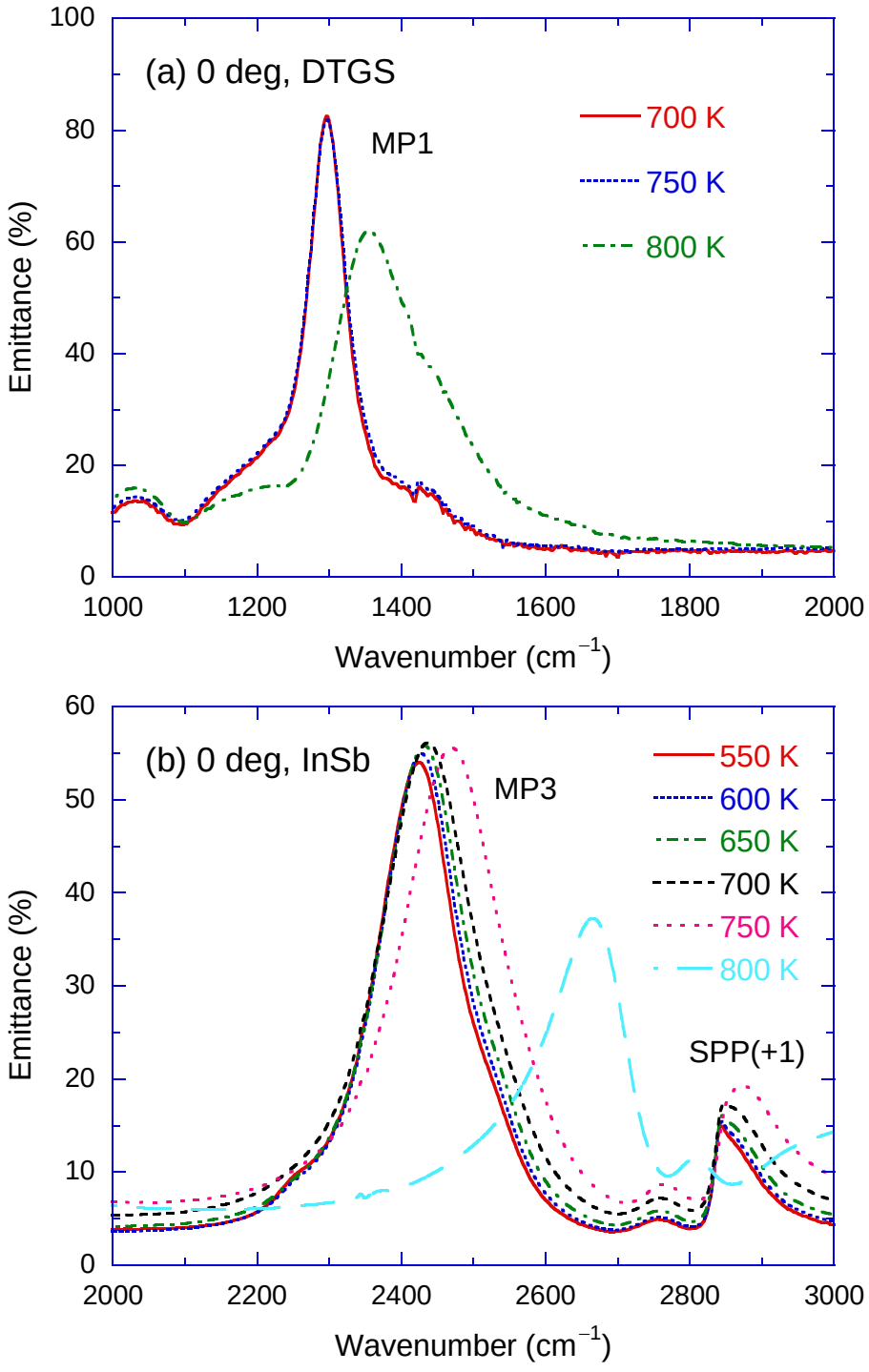

Figure 6.8 The normal emittance at different temperatures measured with the high-temperature emissometer using (a) a DTGS detector and (b) an InSb detector. An IR polarizer is used and the results are for TM waves only.

on the direction, the SPP (+1 order) shifts to lower frequencies and interacts with MP3. As a result, the MP3 peak decrease quickly to 0.17 with a 10° change and the peak location is pushed slightly to lower frequencies. Note that the coupling between different plasmonic modes has recently been a hot research area, and may find applications in optical detection and novel plasmonic devices [131-133].

Figure 6.8 presents how the normal emittance changes with the temperature from the direct measurements. Because of different detectors' detectivity, emittance was collected by the DTGS detector only for temperatures above 700 K, while emittance can be obtained from 500 K with the InSb detector, as shown respectively in Figs. 6.8(a) and 6.8(b). Amazingly, the emittance associated with the MP1 peak is almost the same for temperatures of 700K and 750K, and the emittance peak with MP3 little changes when the temperature increases from 550K to 700K. Though there is slightly peak increasing and peak shifting with the temperature, it is within the experimental uncertainty. The experimental observation clearly shows that the emittance associated with MPs little change with temperature, and the peak can be as high as 0.8 at high temperatures. Compared with other potential coherent emitters such as Fabry-Perot cavity resonators whose emittance peaks decrease at high temperatures due to increased scattering loss as discussed in Section 4.3, this is a great advantage to be a coherent emitter with high performance. However, the MP1 peak shifts and decreases significantly at 800 K, and the MP3 peak has a noticeable change at 750 K and a more significant one at 800 K. After examined under the microscope, the sample after heating was found to have some morphological change in the Au layer under the SiO_2 spacer. In other words, the optical property of the Au film has changed, which is believed to be responsible for the

degrading at 800 K. In fact, after the photolithography process during the sample fabrication, the color of the Au layer at the region where experienced UV-light exposure has a visible change, becoming darker compared with the unexposed region. Note that the Fabry-Perot cavity resonators were fabricated in a similar way as MP coherent emitter samples but without photolithography and lift-off processes, and were chemically intact at 800 K during the high temperature emittance measurements. Further investigation is needed to address this problem so that the MP coherent emitter could work properly at temperatures higher than 750 K.

To better understand the temperature effect on the MPs, the theoretical emittance at elevated temperatures was calculated using the RCWA coupled with the temperature-dependent Drude model for bulk Au's optical constants given by Eq. (4.2). At elevated temperatures, the plasma frequency is assumed unchanged, and the scattering rate has a linear dependence on the temperature, i.e., $\Gamma(T)/\Gamma_0 = T/300$, since the electron-phonon scattering dominates the scattering process at high temperatures. Note that the thicknesses for the Au film and Au grating strips are much larger than the penetration depth, so both can be assumed as bulk. The optical constants of SiO_2 are assumed independent of temperatures.

With the same geometric parameters for Pattern 1, the normal emittance at different temperatures is shown in Fig. 6.9. Four emittance peaks, associated with MP1, SPP (-1 order), MP3, and SPP (+1 order) can be seen respectively at 1316 cm^{-1}, 1424 cm^{-1}, 2422 cm^{-1}, and 2854 cm^{-1}, and the peak locations agrees quite well from the measurements. The increasing temperature has no influence on the peak locations at all, and the peak maxima little changes with the temperatures as well, which is consistent

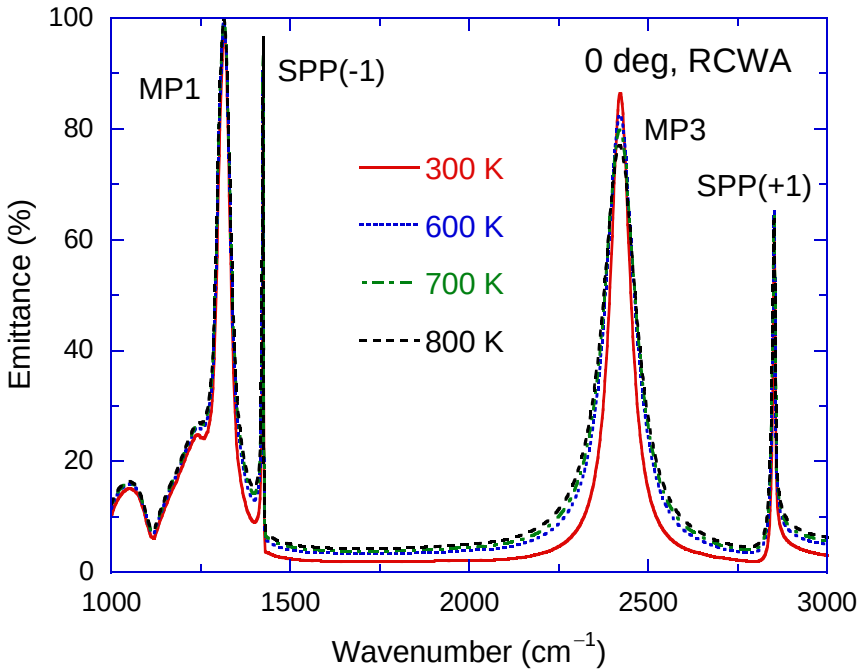

Figure 6.9 Theoretical calculation of the temperature effect on the normal emittance for the MP coherent emitters. The parameters for Pattern 1 are used for calculation.

with the experimental observation in Fig. 6.8. Note that the emittance has a close-to-unity at MP1 within the considered temperature range, and the MP3 peak gets a little bit broadening with slightly lowered maxima from the calculation, which is due to stronger scattering effect in the metals. Interestingly, the stronger scattering does not degrade the emittance peaks associated with MPs compared with ones caused by interference effect in the Fabry-Perot cavity resonators, indicating excellent performance as coherent thermal emitters at high temperatures. However, the measurements indicate that the peak maximum increases and the location shifts slightly at MP3 as the temperature goes high, which is different from the theoretical calculation. In fact, the changes from the measurements are very slightly, which is mainly due to the measurement uncertainties. Additional measurements also showed that the similar trend as the calculation at MP3 was obtained with other MP coherent emitter samples.

CHAPTER 7

CONCLUSION AND RECOMMENDATIONS

This dissertation theoretically and experimentally investigates the role of magnetic resonance and wave interference effects in tailoring thermal radiative properties of micro/nanostructures. The temporal and spatial coherence of thermal radiation of asymmetric Fabry-Perot resonance cavities is demonstrated at room temperature by measuring the spectral and angle-resolved reflectance using the FT-IR spectrometer and a laser scatterometer, respectively. Sharp reflectance dips are observed for both polarizations at several incidence angles. While the resonance frequencies are mainly determined by the cavity thickness, the phase shift due to reflection at the boundaries can modify the resonance frequency to some extend. The top Au film thickness dominantly affects the minimum reflectance or peak emissivity values. Narrow angular lobes of the emissivity are also shown by the angle-resolved reflectance measurement at λ = 891 nm, which indicates strong directional selectivity and spatial coherence of the sample. The measurement results can be well understood by a detailed theoretical model with fitted film thicknesses. The asymmetric Fabry-Perot resonators have a great advantage in terms of the fabrication as compared with the binary gratings and the truncated photonic crystal structures.

An emissometer facility is designed, built, and tested with a SiC wafer for direct measurements of the emittance in the infrared. While inexpensive, this setup allows directional-spectral emittance measurements for a given polarization at temperatures up to 800 K or even higher. A modified Fabry-Perot cavity resonator is fabricated for

spectral control of thermal emission at elevated temperatures. Proper barrier layers and a surface protection coating are included to achieve thermal and chemical stability. The direct emittance measurements of the structure at elevated temperatures demonstrate resonance features and wavelength selectivity. The broadening of the emittance peaks with increasing temperature is explained by the increased scattering rate in the Au films; such broadening may be advantageous in some energy conversion devices, such as TPV emitters. This study demonstrates the feasibility of using layered structures as wavelength-selective emitters at high temperatures.

Moreover, this dissertation unifies the direct and indirect methods in predicting thermal emission. This allows the thermal emission from and the brightness temperature of a multilayered structure with a nonuniform temperature distribution to be evaluated using the indirect method. The equivalence between the spectral directional emissivity and absorptivity of each layer can be viewed as the generalized Kirchhoff's law. Thermal emission and emissivity from each emitting layer in a Fabry-Perot resonance cavity are evaluated to demonstrate the equivalence of the direct and indirect methods. As a consequence of optical resonance, the enhancement in LDOS in SiO_2 cavity is nearly two orders of magnitude around 5000 and 10000 cm^{-1}, where the spectral emission peak occurs. The brightness temperature also reveals the emission peaks and can be used to characterize thermal emission from a nonuniform temperature structure.

Another structure studied in this dissertation is periodic gratings deposited on multilayered thin films. The physical mechanism of transmission/absorption enhancement in deep gratings is unambiguously identified as due to magnetic polaritons in this dissertation. This is supported by the fact that the resonance frequencies predicted

by the LC circuit model match well with those calculated by RCWA simulation. Furthermore, it is found that the MP resonance frequency is independent of the incidence angle θ and strip width w but depends strongly on the grating height h and slit width b. These features cannot be fully explained by coupled SPPs or the Fabry-Perot cavity resonance. Therefore, it can be concluded that MPs can be excited and are responsible for extraordinary optical transmission in double-layer nanoslit arrays. The electromagnetic field distributions visually show the distinct features of MPs as circulating electric currents and strong magnetic field confinement between the metallic strips. The magnetic responses can also explain the behavior at oblique angles, especially the unique characteristic of MPs as directional independence. The analytical prediction from the LC circuit model agrees well with the RCWA calculations with varying geometric parameters. The misalignment between the two nanoslit layers provides another way to tailor thermal radiative properties besides tuning the geometric parameters.

The existence of magnetic polaritons inside dielectric grating structures made of SiC is theoretically identified. Strong field localization can be achieved with magnetic polaritons, resulting in transmission enhancement or coherent thermal emission. The flat dispersion curve associated magnetic polaritons indicates that the resonance is omnidirectional. The formation of magnetic polaritons is assisted by phonons in polar materials rather than free charges in metals. The geometric effect on the magnetic resonance conditions offers guidance for tailoring the radiative properties of micro/nanostructures toward desired frequencies. The understanding on phonon-mediated magnetic polaritons may facilitate the design of novel energy conversion devices and metamaterials in the infrared region.

Based on the understanding of magnetic resonance, an innovative coherent thermal emitter is designed by excitation of magnetic polaritons. Multiple modes of the magnetic polariton have been identified according to the electric and magnetic fields distribution in the dielectric spacer. It is evident that the magnetic polariton can strongly interact with the surface plasmon, resulting in either enhancement or suppression of the emissivity for different magnetic polariton orders. In particular, a wavelength-selective and diffuse TPV emitter is envisioned by excitation of MPs in a nanostructure made of tungsten gratings with a SiO_2 spacer. This emitter design may enable high conversion efficiency and power throughput when paired with proper TPV cells.

Finally, this dissertation offers an experimental demonstration of coherent thermal emission by excitation of magnetic polaritons at both room and elevated temperatures from fabricated subwavelength grating structures. The resonance condition associated with magnetic polaritons depends on the strip width rather than the grating period, which offers a way to design coherent emitters whose emittance peaks can be tuned to a specific frequency of interest for particular applications. While interactions can exist between MPs and SPPs, the omnidirectional behavior for the MP emittance peaks is undoubtedly verified. The MP emittance peaks little change from room temperature to elevated temperatures up to 750 K with the Au gratings, and furthermore, the operating temperature can be increased using materials that are more stable at high temperatures.

The detailed analysis and experimental results in this dissertation not only enhance the understanding of the wave interference and magnetic resonance effect in achieving tunable coherent thermal emission and extraordinary optical transmission, but also facilitate future optimization design for their practical applications in energy

conversion systems, plasmonic devices, nanophotonics, and nanolithography. In the future, optimization of the metallic and dielectric materials with matched CTEs in asymmetric Fabry-Perot resonators is needed to reduce the thermal stress for applications at even higher temperatures. For the coherent emitter assisted by magnetic polaritons, other fabrication techniques such as nanoimprinting and e-beam lithography and suitable materials can be employed to build the coherent emitters with desired performance at working temperatures above 800 K. Magnetic polaritons in the 1D grating structures can only be excited for TM waves, which limits the performance in practical applications because of the nature of randomly polarized thermal emission. Therefore, the investigation of magnetic polaritons in 2D structures is needed with suitable computational methods such as 2D RCWA and FDTD. To further enhance the conversion efficiency and power throughput especially in TPV systems, the radiative heat transfer between a coherent emitter by excitation of magnetic polaritons and a TPV cell at nanometer distances should be explored. While challenges remain, the practical applications of the structures proposed in this dissertation and similar micro/nanostructures as engineered surfaces for energy harvesting will result in technological advances in the near future.

References

[1] Zhang, Z. M., 2007, *Nano/Microscale Heat Transfer*, McGraw-Hill, New York.

[2] Zhang, Z. M., Tsai, B. K., and Machin, G., 2010, *Radiometric Temperature Measurements: II. Applications*, Elsevier, Amsterdam.

[3] Porto, J. A., Garcia-Vidal, F. J., and Pendry, J. B., 1999, "Transmission Resonances on Metallic Gratings with Very Narrow Slits," Phys. Rev. Lett., **83,** p. 2845.

[4] Baida, F. I., and Van Labeke, D., 2002, "Light Transmission by Subwavelength Annular Aperture Arrays in Metallic Films," Opt. Commun., **209,** pp. 17-22.

[5] Lezec, H. J., Degiron, A., Devaux, E., Linke, R. A., Martin-Moreno, L., Garcia-Vidal, F. J., and Ebbesen, T. W., 2002, "Beaming Light from a Subwavelength Aperture," Science, **297,** pp. 820-822.

[6] Ebbesen, T. W., Lezec, H. J., Ghaemi, H. F., Thio, T., and Wolff, P. A., 1998, "Extraordinary Optical Transmission Through Sub-Wavelength Hole Arrays," Nature, **391,** pp. 667-669.

[7] Hesketh, P. J., Zemel, J. N., and Gebhart, B., 1986, "Organ Pipe Radiant Modes of Periodic Micromachined Silicon Surfaces," Nature, **324,** pp. 549-551.

[8] Srituravanich, W., Fang, N., Sun, C., Luo, Q., and Zhang, X., 2004, "Plasmonic Nanolithography," Nano Lett., **4,** pp. 1085-1088.

[9] Liu, Z. W., Wei, Q. H., and Zhang, X., 2005, "Surface Plasmon Interference Nanolithography," Nano Lett., **5,** pp. 957-961.

[10] Basu, S., Chen, Y.-B., and Zhang, Z. M., 2007, "Microscale Radiation in Thermophotovoltaic Devices - A Review," Int. J. Energy Res., **31,** pp. 689-716.

[11] Greffet, J.-J., Carminati, R., Joulain, K., Mulet, J.-P., Mainguy, S., and Chen, Y., 2002, "Coherent Emission of Light by Thermal Sources," Nature, **416,** pp. 61-64.

[12] Dahan, N., Niv, A., Biener, G., Gorodetski, Y., Kleiner, V., and Hasman, E., 2007, "Enhanced Coherency of Thermal Emission: Beyond the Limitation Imposed by Delocalized Surface Waves," Phys. Rev. B, **76,** p. 045427.

[13] Lee, B. J., and Zhang, Z. M., 2006, "Design and Fabrication of planar Multilayer Structures with Coherent Thermal Emission Characteristics," J. Appl. Phys., **100,** p. 063529.

[14] Lee, B. J., Chen, Y.-B., and Zhang, Z. M., 2008, "Surface Waves between Metallic Films and Truncated Photonic Crystals Observed with Reflectance Spectroscopy," Opt. Lett., **33,** pp. 204-206.

[15] Narayanaswamy, A., and Chen, G., 2004, "Thermal Emission Control with One-dimensional Metallodielectric Photonic Crystals," Phys. Rev. B, **70,** p. 125101.

[16] Lee, B. J., Chen, Y.-B., and Zhang, Z. M., 2008, "Transmission Enhancement Through Nanoscale Metallic Slit Arrays from the Visible to Mid-infrared," J. Comput. Theor. Nanosci., **5,** pp. 201-213.

[17] Veselago, V. G., 1968, "Electrodynamics of Substances with Simultaneously Negative Values of Sigma and Mu," Sov. Phys. Usp., **10,** p. 509.

[18] Pendry, J. B., Holden, A. J., Robbins, D. J., and Stewart, W. J., 1999, "Magnetism from Conductors and Enhanced Nonlinear Phenomena," IEEE Trans. Microwave Theory Tech., **47,** pp. 2075-2084.

[19] Linden, S., Enkrich, C., Wegener, M., Zhou, J. F., Koschny, T., and Soukoulis, C. M., 2004, "Magnetic Response of Metamaterials at 100 Terahertz," Science, **306,** pp. 1351-1353.

[20] Enkrich, C., Wegener, M., Linden, S., Burger, S., Zschiedrich, L., Schmidt, F., Zhou, J. F., Koschny, T., and Soukoulis, C. M., 2005, "Magnetic Metamaterials at Telecommunication and Visible Frequencies," Phys. Rev. Lett., **95,** p. 203901.

[21] Podolskiy, V. A., Sarychev, A. K., and Shalaev, V. M., 2002, "Plasmon Modes in Metal Nanowires and Left-handed Materials," J. Nonlinear Opt. Phys. Mater., **11,** pp. 65-74.

[22] Shalaev, V. M., Cai, W. S., Chettiar, U. K., Yuan, H. K., Sarychev, A. K., Drachev, V. P., and Kildishev, A. V., 2005, "Negative Index of Refraction in Optical Metamaterials," Opt. Lett., **30,** pp. 3356-3358.

[23] Zhou, J. F., Zhang, L., Tuttle, G., Koschny, T., and Soukoulis, C. M., 2006, "Negative Index Materials Using Simple Short Wire Pairs," Phys. Rev. B, **73,** p. 041101.

[24] Zhang, S., Fan, W. J., Panoiu, N. C., Malloy, K. J., Osgood, R. M., and Brueck, S. R. J., 2005, "Experimental Demonstration of Near-infrared Negative-index Metamaterials," Phys. Rev. Lett., **95,** p. 137404.

[25] Schurig, D., Mock, J. J., Justice, B. J., Cummer, S. A., Pendry, J. B., Starr, A. F., and Smith, D. R., 2006, "Metamaterial Electromagnetic Cloak at Microwave Frequencies," Science, **314,** pp. 977-980.

[26] Pendry, J. B., and Smith, D. R., 2006, "The Quest for the Superlens," Sci. Am., **295,** pp. 60-67.

[27] Pendry, J. B., 2000, "Negative Refraction Makes a Perfect Lens," Phys. Rev. Lett., **85,** pp. 3966-3969.

[28] Jacob, Z., Alekseyev, L. V., and Narimanov, E., 2006, "Optical Hyperlens: Far-field Imaging Beyond the Diffraction Limit," Opt. Express, **14,** pp. 8247-8256.

[29] Ortuno, R., Garcia-Meca, C., Rodriguez-Fortuno, F. J., Marti, J., and Martinez, A., 2009, "Role of Surface Plasmon Polaritons on Optical Transmission Through Double Layer Metallic Hole Arrays," Phys. Rev. B, **79,** p. 075425.

[30] Mary, A., Rodrigo, S. G., Martin-Moreno, L., and Garcia-Vidal, F. J., 2009, "Holey Metal Films: From Extraordinary Transmission to Negative-index Behavior," Phys. Rev. B, **80,** p. 165431.

[31] Li, T., Liu, H., Wang, F. M., Dong, Z. G., Zhu, S. N., and Zhang, X., 2006, "Coupling Effect of Magnetic Polariton in Perforated Metal/dielectric Layered Metamaterials and Its Influence on Negative Refraction Transmission," Opt. Express, **14,** pp. 11155-11163.

[32] Li, T., Wang, S. M., Liu, H., Li, J. Q., Wang, F. M., Zhu, S. N., and Zhang, X., 2008, "Dispersion of Magnetic Plasmon Polaritons in Perforated Trilayer Metamaterials," J. Appl. Phys., **103,** p. 023104.

[33] Shalaev, V. M., 2007, "Optical Negative-index Metamaterials," Nat. Photonics, **1,** pp. 41-48.

[34] Garcia-Vidal, F. J., and Martin-Moreno, L., 2002, "Transmission and Focusing of Light in One-dimensional Periodically Nanostructured Metals," Phys. Rev. B, **66,** p. 155412.

[35] Hibbins, A. P., Lockyear, M. J., and Sambles, J. R., 2006, "The Resonant Electromagnetic Fields of an Array of Metallic Slits Acting as Fabry-Perot Cavities," J. Appl. Phys., **99,** p. 124903.

[36] Sai, H., Kanamori, Y., Hane, K., and Yugami, H., 2005, "Numerical Study on Spectral Properties of Tungsten One-dimensional Surface-relief Gratings for Spectrally Selective Devices," J. Opt. Soc. of Am. A, **22,** pp. 1805-1813.

[37] Takakura, Y., 2001, "Optical Resonance in a Narrow Slit in a Thick Metallic Screen," Phys. Rev. Lett., **86,** pp. 5601-5603.

[38] Maruyama, S., Kashiwa, T., Yugami, H., and Esashi, M., 2001, "Thermal Radiation from Two-dimensionally Confined Modes in Microcavities," Appl. Phys. Lett., **79,** pp. 1393-1395.

[39] Sobnack, M. B., Tan, W. C., Wanstall, N. P., Preist, T. W., and Sambles, J. R., 1998, "Stationary Surface Plasmons on a Zero-order Metal Grating," Phys. Rev. Lett., **80,** pp. 5667-5670.

[40] Suckling, J. R., Hibbins, A. P., Lockyear, M. J., Preist, T. W., Sambles, J. R., and Lawrence, C. R., 2004, "Finite Conductance Governs the resonance Transmission of Thin Metal Slits at Microwave Frequencies," Phys. Rev. Lett., **92,** p. 147401.

[41] Chan, H. B., Marcet, Z., Woo, K., Tanner, D. B., Carr, D. W., Bower, J. E., Cirelli, R. A., Ferry, E., Klemens, F., Miner, J., Pai, C. S., and Taylor, J. A., 2006, "Optical TransmissionThrough Double-layer Metallic Subwavelength Slit Arrays," Opt. Lett., **31,** pp. 516-518.

[42] Cheng, C., Chen, J., Shi, D. J., Wu, Q. Y., Ren, F. F., Xu, J., Fan, Y. X., Ding, J. P., and Wang, H. T., 2008, "Physical Mechanism of Extraordinary Electromagnetic Transmission in Dual-metallic Grating Structures," Phys. Rev. B, **78,** p. 075406.

[43] Shvets, G., and Urzhumov, Y. A., 2006, "Negative Index Meta-materials Based on Two-dimensional Metallic Structures," J. Opt. A - Pure Appl. Opt., **8,** pp. S122-S130.

[44] Born, M., and Wolf, E., 1999, *Principles of Optics, 7th ed.*, Cambridge University Press, Cambridge, UK.

[45] Vaughan, J. M., 1989, *The Fabry-Perot Interferometer,* Adam Hilger, Philadelphia, PA.

[46] Schubert, E. F., Hunt, N. E. J., Vredenberg, A. M., Harris, T. D., Poate, J. M., Jacobson, D. C., Wong, Y. H., and Zydzik, G. J., 1993, "Enhanced Photoluminescence by Resonant Absorption in Er-doped SiO_2/Si Microcavities," Appl. Phys. Lett., **63,** pp. 2603-2605.

[47] Ben-Abdallah, P., and Ni, B., 2005, "Single-defect Bragg Stacks for High-power Narrow-band Thermal Emission," J. Appl. Phys., **97,** p. 104910.

[48] Celanovic, I., Perreault, D., and Kassakian, J., 2005, "Resonant-cavity Enhanced Thermal Emission," Phys. Rev. B, **72,** p. 075127.

[49] Hadley, L. N., and Dennison, D. M., 1947, "Reflection and Transmission Interference Filters," J. Opt. Soc. of Am., **37,** pp. 451-465.

[50] Laroche, M., Marquier, F., Carminati, R., and Greffet, J.-J., 2005, "Tailoring Silicon Radiative Properties," Opt. Commun., **250,** pp. 316-320.

[51] Zhang, Z. M., and Wang, L. P., 2011, "Measurements and Modeling of the Spectral and Directional Radiative Properties of Micro/Nanostructured Materials," Int. J. Thermophys., DOI: 10.1007/s10765-011-1036-5.

[52] Zhang, Z. M., Tsai, B. K., and Machin, G., 2010, *Radiometric Temperature Measurements: I. Fundamentals*, Elsevier, Amsterdam.

[53] Narayanaswamy, A., and Chen, G., 2005, "Direct Computation of Thermal Emission From Nanostructures," Annu. Rev. Heat Transfer, **14,** pp. 169-195.

[54] Narayanaswamy, A., and Chen, G., 2005, "Thermal Radiation in 1D Photonic Crystals," J. Quant. Spectrosc. Radiat. Transfer, **93,** pp. 175-183.

[55] Tsang, L., Njoku, E., and Kong, J. A., 1975, "Microwave Thermal Emission from a Stratified Medium with Nonuniform Temperature Distribution," J. Appl. Phys., **46,** pp. 5127-5133.

[56] Luo, C. Y., Narayanaswamy, A., Chen, G., and Joannopoulos, J. D., 2004, "Thermal Radiation from Photonic Crystals: A Direct Calculation," Phys. Rev. Lett., **93,** p. 213905.

[57] Basu, S., Zhang, Z. M., and Fu, C. J., 2009, "Review of Near-field Thermal Radiation and Its Application to Energy Conversion," Int. J. Energy Res., **33,** pp. 1203-1232.

[58] Park, K., Basu, S., King, W. P., and Zhang, Z. M., 2008, "Performance Analysis of Near-fieldThermophotovoltaic Devices Considering Absorption Distribution," J. Quant. Spectrosc. Radiat. Transfer, **109,** pp. 305-316.

[59] Fu, C. J., and Zhang, Z. M., 2006, "Nanoscale Radiation Heat Transfer for Silicon at Different Doping Levels," Int. J. Heat Mass Transfer, **49,** pp. 1703-1718.

[60] Lee, B. J., Park, K., and Zhang, Z. M., 2007, "Energy Pathways in Nanoscale Thermal Radiation," Appl. Phys. Lett., **91,** p. 153101.

[61] Basu, S., Wang, L. P., and Zhang, Z. M., 2011, "Direct Calculation of Energy Streamlines in Near-Field Thermal Radiation," J. Quant. Spectrosc. Radiat. Transfer, **112,** pp. 1149-1155.

[62] Lee, B. J., Wang, L. P., and Zhang, Z. M., 2008, "Coherent Thermal Emission by Excitation of Magnetic Polaritons between Periodic Strips and a Metallic Film," Opt. Express, **16,** pp. 11328-11336.

[63] Wang, L. P., Lee, B. J., Wang, X. J., and Zhang, Z. M., 2009, "Spatial and Temporal Coherence of Thermal Radiation in Asymmetric Fabry-Perot Resonance Cavities," Int. J. Heat Mass Transfer, **52,** pp. 3024-3031.

[64] Chen, G., 1997, "Wave Effects on Radiative Transfer in Absorbing and Emitting Thin-film Media," Microscale Thermophys. Eng., **1,** pp. 215-224.

[65] Baltes, H. P., 1976, "On the Validity of Kirchhoff's Law of Heat Radiation for a Body in a Nonequilibrium Environment," in *Progress in Optics,* ed. by E. Wolf, pp. 1-25, Elsevier, New York.

[66] Rytov, S. M., 1987, *Principles of Statistical Radiophysics,* Springer-Verlag, Berlin.

[67] Francoeur, M., Menguc, M. P., and Vaillon, R., 2009, "Solution of Near-field Thermal Radiation in One-dimensional Layered Media Using Dyadic Green's Functions and the Scattering Matrix Method," J. Quant. Spectrosc. Radiat. Transfer, **110,** pp. 2002-2018.

[68] Tsang, L., Kong, J. A., and Ding, K. H., 2000, *Scattering of Electromagnetic Waves: Theories and Applications,* Wiley, New York.

[69] Sipe, J. E., 1987, "New Green-Function Formalism for Surface Optics," J. Opt. Soc. of Am. B, **4,** pp. 481-489.

[70] Moharam, M. G., Grann, E. B., Pommet, D. A., and Gaylord, T. K., 1995, "Formulation for Stable and Efficient Implementation of the Rigorous Coupled-Wave Analysis of Binary Gratings," J. Opt. Soc. of Am. A, **12,** pp. 1068-1076.

[71] Fu, K., Chen, Y.-B., Hsu, P.-F., Zhang, Z. M., and Timans, P. J., 2008, "Device Scaling Effect on the Spectral-directional Absorptance of Wafer's Front Side," Int. J. Heat Mass Transfer, **51,** pp. 4911-4925.

[72] Valentine, J., Zhang, S., Zentgraf, T., Ulin-Avila, E., Genov, D. A., Bartal, G., and Zhang, X., 2008, "Three-dimensional Optical Metamaterial with a Negative Refractive Index," Nature, **455,** pp. 376-U332.

[73] Engheta, N., 2007, "Circuits with Light at Nanoscales: Optical Nanocircuits Inspired by Metamaterials," Science, **317,** pp. 1698-1702.

[74] Zhou, J., Koschny, T., Kafesaki, M., Economou, E. N., Pendry, J. B., and Soukoulis, C. M., 2005, "Saturation of the Magnetic Response of Split-ring Resonators at Optical Frequencies," Phys. Rev. Lett., **95,** p. 223902.

[75] Zhou, J. F., Economon, E. N., Koschny, T., and Soukoulis, C. M., 2006, "Unifying Approach to Left-handed Material Design," Opt. Lett., **31,** pp. 3620-3622.

[76] Liu, H., Li, T., Wang, Q. J., Zhu, Z. H., Wang, S. M., Li, J. Q., Zhu, S. N., Zhu, Y. Y., and Zhang, X., 2009, "Extraordinary Optical Transmission Induced by Excitation of a Magnetic Plasmon Propagation Mode in a Diatomic Chain of Slit-hole Resonators," Phys. Rev. B, **79,** p. 024304.

[77] Li, T., Li, J. Q., Wang, F. M., Wang, Q. J., Liu, H., Zhu, S. N., and Zhu, Y. Y., 2007, "Exploring Magnetic Plasmon Polaritons in Optical Transmission Through Hole Arrays Perforated in Trilayer Structures," Appl. Phys. Lett., **90,** p. 251112.

[78] Raether, H., 1988, *Surface Plasmons on Smooth and Rough Surfaces and on Gratings,* Springer-Verlag, Berlin.

[79] De Wilde, Y., Formanek, F., Carminati, R., Gralak, B., Lemoine, P. A., Joulain, K., Mulet, J. P., Chen, Y., and Greffet, J.-J., 2006, "Thermal Radiation Scanning Tunnelling Microscopy," Nature, **444,** pp. 740-743.

[80] Homola, J., Yee, S. S., and Gauglitz, G., 1999, "Surface Plasmon Resonance Sensors: Review," Sens. Actuators B, **54,** pp. 3-15.

[81] Park, K., Lee, B. J., Fu, C., and Zhang, Z. M., 2005, "Study of the Surface and Bulk Polaritons with a Negative Index Metamaterial," J. Opt. Soc. Am. B, **22,** pp. 1016-1023.

[82] Fu, C. J., Zhang, Z. M., and Tanner, D. B., 2005, "Planar Heterogeneous Structures for Coherent Emission of Radiation," Opt. Lett., **30,** pp. 1873-1875.

[83] Palik, E. D., and Ghosh, G., 1998, *Handbook of Optical Constants of Solids,* Academic Press, San Diego.

[84] Chen, Y.-B., Lee, B. J., and Zhang, Z. M., 2008, "Infrared Radiative Properties of Submicron Metallic Slit Arrays," J. Heat Transfer, **130,** p. 082404.

[85] Shen, Y. J., Zhu, Q. Z., and Zhang, Z. M., 2003, "A Scatterometer for Measuring the Bidirectional Reflectance and Transmittance of Semiconductor Wafers with Rough Surfaces," Rev. Sci. Instrum., **74,** pp. 4885-4892.

[86] Zhu, Q. Z., and Zhang, Z. M., 2005, "Correlation of Angle-resolved Light Scattering with the Microfacet Orientation of Rough Silicon Surfaces," Opt. Eng., **44,** pp. 073601-073612.

[87] Dahan, N., Niv, A., Biener, G., Gorodetski, Y., Kleiner, V., and Hasman, E., 2008, "Extraordinary Coherent Thermal Emission from SiC due to Coupled Resonant Cavities," J. Heat Transfer, **130,** p. 112401.

[88] Deblase, F. J., and Compton, S., 1991, "Infrared Emission Spectroscopy: A Theoretical and Experimental Review," Appl. Spectrosc., **45,** pp. 611-618.

[89] Markham, J., Kinsella, K., Carangelo, R., Brouillette, C., Carangelo, M., Best, P., and Solomon, P., 1993, "Bench top Fourier Transform Infrared Based Instrument for Simultaneously Measuring Surface Spectral Emittance and Temperature," Rev. Sci. Instrum., **64,** p. 2515.

[90] Marquier, F., Joulain, K., Mulet, J. P., Carminati, R., Greffet, J.-J., and Chen, Y., 2004, "Coherent Spontaneous Emission of Light by Thermal Sources," Phys. Rev. B, **69,** p. 155412.

[91] Del Campo, L., Pérez-Sáez, R. B., Esquisabel, X., Fernández, I., and Tello, M. J., 2006, "New Experimental Device for Infrared Spectral Directional Emissivity Measurements in a Controlled Environment," Rev. Sci. Instrum., **77,** p. 113111.

[92] Cagran, C., Hanssen, L., Noorma, M., Gura, A., and Mekhontsev, S., 2007, "Temperature-resolved Infrared Spectral Emissivity of SiC and Pt–10Rh for Temperatures up to 900 °C," Int. J. Thermophys., **28,** pp. 581-597.

[93] Monte, C., Gutschwager, B., Morozova, S., and Hollandt, J., 2009, "Radiation Thermometry and Emissivity Measurements under Vacuum at the PTB," Int. J. Thermophys., **30,** pp. 203-219.

[94] Wang, L. P., Basu, S., and Zhang, Z. M., 2011, "Direct Measurement of Coherent Thermal Emission from a Fabry-Perot Cavity Resonator," J. Heat Transfer, accepted.

[95] Zhang, Z. M., Hanssen, L. M., Datla, R. U., and Drew, H. D., 1996, "An Apparatus for Infrared Transmittance and Reflectance Measurements at Cryogenic Temperatures," Int. J. Thermophys., **17,** pp. 1441-1454.

[96] Incropera, F. P., Dewitt, D. P., Bergman, T. L., and Lavine, A. S., 2007, *Fundamentals of Heat and Mass Transfer*, Wiley, New York.

[97] Hopkins, P. E., Norris, P. M., and Stevens, R. J., 2008, "Influence of Inelastic Scattering at Metal-Dielectric Interfaces," J. Heat Transfer, **130,** p. 022401.

[98] Yu, J., Yee, A. L., and Schwall, R. E., 1992, "Thermal Conductance of Cu/Cu and Cu/Si Interfaces from 85 K to 300 K," Cryogenics, **32,** pp. 610-615.

[99] Spitzer, W. G., Kleinman, D. A., Frosch, C. J., and Walsh, D. J., 1960, "Infra-red Properties of Silicon Carbide," in *Silicon Carbide, A High Temperature Semiconductor,* ed. by J. R. O'connor and J. Smiltens, pp. 347-365, Pergamon, New York.

[100] Zhang, Z. M., and Lee, B. J., 2009, "Theory of Thermal Radiation and Radiative Properties," in *Radiometric Temperature Measurements: I. Fundamentals*, ed. by Z. M. Zhang, B. K. Tsai and G. Machin, pp. 74-132, Academic Press (an Imprint of Elsevier), Amsterdam.

[101] Siegel, R., and Howell, J. R., 2002, *Thermal Radiation Heat Transfer,* Taylor & Francis, New York.

[102] Lee, B. J., and Zhang, Z. M., 2009, "Indirect Measurements of Coherent Thermal Emission from a Truncated Photonic Crystal Structure," J. Thermophys. Heat Transfer, **23,** pp. 9-17.

[103] Laroche, M., Arnold, C., Marquier, E., Carminati, R., Greffet, J.-J., Collin, S., Bardou, N., and Pelouard, J. L., 2005, "Highly Directional Radiation Generated by a Tungsten Thermal Source," Opt. Lett., **30,** pp. 2623-2625.

[104] Lee, B. J., Zhang, Z. M., Early, E. A., Dewitt, D. P., and Tsai, B. K., 2005, "Modeling Radiative Properties of Silicon with Coatings and Comparison with Reflectance Measurements," J. Thermophys. Heat Transfer, **19,** pp. 558-565.

[105] Aspnes, D. E., Kinsbron, E., and Bacon, D. D., 1980, "Optical Properties of Au: Sample Effects," Phys. Rev. B, **21,** p. 3290.

[106] Johnson, P. B., and Christy, R. W., 1972, "Optical Constants of the Noble Metals," Phys. Rev. B, **6,** pp. 4370-4379.

[107] Flik, M. I., Zhang, Z. M., Goodson, K. E., Siegal, M. P., and Phillips, J. M., 1992, "Electron Scattering Rate in Epitaxial $YBa_2Cu_3O_7$ Superconducting Films," Phys. Rev. B, **46,** pp. 5606-5614.

[108] Lee, B. J., Khuu, V. P., and Zhang, Z. M., 2005, "Partially Coherent Spectral Radiative Properties of Dielectric Thin Films with Rough Surfaces," J. Thermophys. Heat Transfer, **19,** pp. 360-366.

[109] Automation Creations, Inc., 2009, "MatWeb, Your Source for Materials Information," http://www.matweb.com/

[110] Wang, L. P., Basu, S., and Zhang, Z. M., 2011, "Direct and Indirect Methods for Calculating Thermal Emission from Layered Structures with Nonuniform Temperatures," J. Heat Transfer, **133,** p. 072701.

[111] Bardati, F., and Solimini, D., 1984, "On the Emissivity of Layered Materials," IEEE Trans. Geosci. Remote Sens., **22,** pp. 374-376.

[112] Zhang, Z. M., and Basu, S., 2007, "Entropy Flow and Generation in Radiative Transfer Between Surfaces," Int. J. Heat Mass Transfer, **50,** pp. 702-712.

[113] Joulain, K., Carminati, R., Mulet, J.-P., and Greffet, J.-J., 2003, "Definition and Measurement of the Local Density of Electromagnetic States Close to an Interface," Phys. Rev. B, **68,** p. 245405.

[114] Basu, S., Lee, B. J., and Zhang, Z. M., 2010, "Near-Field Radiation Calculated With an Improved Dielectric Function Model for Doped Silicon," J. Heat Transfer, **132,** p. 023302.

[115] Wang, L. P., and Zhang, Z. M., 2009, "Resonance Transmission or Absorption in Deep Gratings Explained by Magnetic Polaritons," Appl. Phys. Lett., **95,** p. 111904.

[116] Yang, F. Z., and Sambles, J. R., 2002, "Resonant Transmission of Microwaves Through a Narrow Metallic Slit," Phys. Rev. Lett., **89,** p. 063901.

[117] Yuan, H. K., Chettiar, U. K., Cai, W. S., Kildishev, A. V., Boltasseva, A., Drachev, V. P., and Shalaev, V. M., 2007, "A Negative Permeability Material at Red Light," Opt. Express, **15,** pp. 1076-1083.

[118] Wang, L. P., and Zhang, Z. M., 2010, "Effect of Magnetic Polaritons on the Radiative Properties of Double-Layer Nanoslit Arrays," J. Opt. Soc. of Am. B, **27,** pp. 2595-2604.

[119] Lee, B. J., Chen, Y.-B., and Zhang, Z. M., 2008, "Confinement of Infrared Radiation to Nanometer Scales Through Metallic Slit Arrays," J. Quant. Spectrosc. Radiat. Transfer, **109,** pp. 608-619.

[120] Marquier, F., Joulain, K., and Greffet, J.-J., 2004, "Resonant Infrared Transmission Through SiC Films," Opt. Lett., **29,** pp. 2178-2180.

[121] Shen, S., Narayanaswamy, A., and Chen, G., 2009, "Surface Phonon Polaritons Mediated Energy Transfer between Nanoscale Gaps," Nano Lett., **9,** pp. 2909-2913.

[122] Rousseau, E., Siria, A., Jourdan, G., Volz, S., Comin, F., Chevrier, J., and Greffet, J.-J., 2009, "Radiative Heat Transfer at the Nanoscale," Nat. Photonics, **3,** pp. 514-517.

[123] Wang, L. P., and Zhang, Z. M., 2011, "Phonon-Mediated Magnetic Polaritons in the Infrared Region," Opt. Express, **19,** pp. A126-A135.

[124] Panina, L. V., Grigorenko, A. N., and Makhnovskiy, D. P., 2002, "Optomagnetic Composite Medium with Conducting Nanoelements," Phys. Rev. B, **66,** p. 155411.

[125] Francoeur, M., Vaillon, R., and Menguc, M. P., 2011, "Thermal Impacts on the Performance of Nanoscale-Gap Thermophotovoltaic Power Generators," IEEE Trans. Energy Convers., **26,** pp. 686-698.

[126] Chen, Y.-B., and Zhang, Z. M., 2007, "Design of Tungsten Complex Gratings for Thermophotovoltaic Radiators," Opt. Commun., **269,** pp. 411-417.

[127] Heinzel, A., Boerner, V., Gombert, A., Blasi, B., Wittwer, V., and Luther, J., 2000, "Radiation Filters and Emitters for the NIR Based on Periodically Structured Metal Surfaces," J. Mod. Opt., **47,** pp. 2399-2419.

[128] Sai, H., Kanamori, Y., and Yugami, H., 2005, "Tuning of the Thermal Radiation Spectrum in the Near-infrared Region by Metallic Surface Microstructures," J. Micromech. Microeng., **15,** pp. S243-S249.

[129] Lin, S. Y., Moreno, J., and Fleming, J. G., 2003, "Three-dimensional Photonic-crystal Emitter for Thermal Photovoltaic Power Generation," Appl. Phys. Lett., **83,** pp. 380-382.

[130] Boltasseva, A., and Shalaev, V. M., 2008, "Fabrication of Optical Negative-index Metamaterials: Recent Advances and Outlook," Metamaterials, **2,** pp. 1-17.

[131] Zentgraf, T., Zhang, S., Oulton, R. F., and Zhang, X., 2009, "Ultranarrow Coupling-induced Transparency Bands in Hybrid Plasmonic Systems," Phys. Rev. B, **80,** p. 195415.

[132] Jouy, P., Todorov, Y., Vasanelli, A., Colombelli, R., Sagnes, I., and Sirtori, C., 2011, "Coupling of a Surface Plasmon with Localized Subwavelength Microcavity Modes," Appl. Phys. Lett., **98,** p. 021105.

[133] Chen, J. X., Wang, P., Zhang, Z. M., Lu, Y. H., and Ming, H., 2011, "Coupling Between Gap Plasmon Polariton and Magnetic Polariton in a Metallic-dielectric Multilayer Structure," Phys. Rev. E, **84,** p. 026603.

VITA

LIPING WANG

Liping Wang was born in Hanshan, Anhui Province, China in 1982. He received his Bachelor's degree from the University of Science and Technology of China in 2004 and Master's degree from the Chinese Academy of Sciences in 2007, both in mechanical engineering. Liping entered the School of Mechanical Engineering at Georgia Tech in Fall 2007 as a PhD student, and since then he has been studying in Dr. Zhuomin Zhang's group in the area of nanoscale radiative heat transfer. His research focuses on selective control of radiative properties with micro/nanostructures by employing different physical mechanisms such as magnetic resonances and wave interference for energy-harvesting applications.

During his PhD study, he has published over 10 journal papers in *Applied Physics Letters*, *Optics Express*, *Journal of Heat Transfer*, and other peer-reviewed journals. He has also co-authored over 10 conference presentations, and has given several oral and poster presentations in international conferences, such as *14th International Heat Transfer Conference* and *2009 US-EU-China Thermophysics Conference – Renewable Energy*. He was invited to give a talk in *ASME 2011 International Mechanical Engineering Congress and Exposition* on November 2011 with awarded NSF student travel grants. Liping is a recipient of the 2010 Hartnett-Irvine Best Paper Award from the International Centre of Heat and Mass Transfer. In addition to the research experience, Liping Wang has also worked as a head graduate teaching assistant for the thermal-fluids labs of ME 4053 Mechanical Engineering System Laboratory since Spring 2010, and enjoyed the teaching and interactions with undergraduate students.